Geophysical models of Mount Etna, Sicily : its structural evolution and implications for slope stability

Thesis

Geophysical models of Mount Etna, Sicily: its structural evolution and implications for slope stability.

A thesis presented for the degree of Doctor of Philosophy

Paul Johann Röllin

BSc. MSc(Hons.)

University of Auckland, New Zealand.

Department of Earth Sciences

The Open University

Milton Keynes

United Kingdom

March 1996

RESEARCH DEGREES CENTRE

LIBRARY AUTHORISATION FORM

Please return this form to the The Research Degrees Centre with the two bound copies of your thesis to be deposited with the University Library.
All students should complete Part 1. Part 2 only applies to PhD students.

Student: Paul Rößlin PI: M7135588

Degree: PhD

Thesis title: Geophysical models of Mount Etna, Sicily: its structural evolution and implications for slope stability

Part 1 Open University Library Authorisation [to be completed by all students]

I confirm that I am willing for my thesis to be made available to readers by the Open University Library, and that it may be photocopied, subject to the discretion of the Librarian.

Signed: [signature] Date: 2/05/97

Part 2 British Library Authorisation [to be completed by PhD students only]

If you want a copy of your PhD thesis to be available on loan to the British Library Thesis Service as and when it is requested, you must sign a British Library Doctoral Thesis Agreement Form. Please return it to the Research Degrees Centre with this form. The British Library will publicise the details of your thesis and may request a copy on loan from the University Library. Information on the presentation of the thesis is given in the Agreement Form.

The University has agreed that your participation in the British Library Thesis Service should be voluntary. Please tick either (a) or (b) to indicate your intentions.

[a] ☑ I am willing for the Open University to loan the British Library a copy of my thesis. A signed Agreement Form is attached.

[b] ☐ I do not wish the Open University to loan the British Library a copy of my thesis.

Signed: [signature] Date: 2/05/97

Abstract

Mount Etna, Europe's largest active volcano, shows a long history of changing structure and environment, culminating in the modern volcanic edifice with its observed slope instability and region of past collapse (the Valle del Bove). The structure and evolution of the volcano and, more importantly, the Valle del Bove are poorly understood but have major effects on its present day behaviour. Several geophysical techniques have been used in order to determine new models for the sub-surface structure of the volcano, concentrating on the Eastern Flank and the Valle del Bove. The Valle del Bove is an important feature on the Eastern Flank. It measures 5 by 7 km and is 1200m deep at its maximum. Its formation and evolution are poorly understood and represent the main thrust of this work.

The primary work has been gravity and aeromagnetic surveys combined with 2.5-D and 3-D modelling to develop a better understanding of the sub-surface structures of the area. This work has identified several large gravity and magnetic anomalies indicating areas of contrasting geophysical properties. A 16mGal positive gravity anomaly over the Southern Wall of the Valle del Bove is interpreted as a large (volume = $38km^3$) high density ($2950\ kg\ m^{-3}$) body, related to the old Trifoglietto centre, possibly representing the ancient feeder system. A second high density body is seen under the present day summit region and is interpreted as an area of shallow level magma storage within the upper flanks of the volcano.

A negative gravity anomaly of 10mGal towards the coast, over the Chiancone sedimentary fan deposit, is interpreted as reworked debris flow material, derived from the Valle del Bove. The shape of the anomaly is strongly asymmetrical relative to the geographical extent of the deposit, with the centre of the anomaly sitting over its Northern extent. The resultant model of this material gives a thickness of 700m, with the material being deposited within a fault controlled basin, open to the sea. Such a shape suggests that a sizeable volume of material may be deposited off-shore. Below the Etnean volcanics lie sedimentary layers which slope in an easterly direction, providing a surface over which the Eastern Flank is free to slide.

Finite element modelling of the stress fields within the volcanic edifice and basement shows that the effects of sea-level variations and glaciations may be of a sufficient magnitude to affect the volcanic system, however, the time over which these changes occur may be more significant than the changes themselves. Similarly the Valle del Bove is shown to have had a significant effect on the stress patterns, and has resulted in a self-reinforcing process whereby the tension caused by the removal of mass encourages further collapse.

Palaeomagnetic measurements show that rotational failure has not been important in the formation of the Valle del Bove, and combined with the results of the other methods, show the Valle's formation to have been via a series of small piecemeal collapses, possibly relating to oversteepening of the walls following dyke emplacement.

These results are combined together to show that the Valle del Bove has been developing over much of the history of Etna, and is not a recent addition to the volcano.

Acknowledgements

My first and foremost thanks go to Prof. Geoff Brown who began this project and my biggest regret is that he was unfortunately unable to see the finish. Dr Hazel Rymer helped to pick up the pieces and continued to give help and advice through the last $3\frac{1}{2}$ years. Thank you. Funding for this work come under the guise of the EC funded Seavolc and Etnatec projects, among others. Drs Corrine Locke and John Cassidy provided the aeromagnetic data and gave assistance in the magnetic modelling. Drs Tim Rolph and John Piper were of great help in analysing the palaeomagnetic data. Tim did a great job in explaining what the data meant and how the equipment worked.

As for others to thank, the list seems endless - did I do any of this by myself?

In the beginning there was mum and dad and the rest of my family who have always been behind my attempts to avoid all forms of "real" work for the last 10 years - yes I have now finished school! Thanks for never questioning me about my career choices and always being there with love, food, money and of course, chocolate fish.

Then came John and Corrine who thought that they had gotten rid of me when I left Auckland - but they were wrong - thanks for putting up with my stupidity and for thinking me capable of a PhD in the first place.

And then came the UK - so many people so little time (sorry room)....

Jane, always there, you get the biggest thanks for keeping me going, putting up with late nights and constant stress and just being there with me dinner when I needed it. I guess this wouldn't be the pamphlet it is without your help and support.

In the field there was "There's a bright golden Haze on the meadow" Steve on the end of the radio to make even the rain seem fun - and don't even ask about his attempts at Italian - but I'll have a fish vodka. Dave "this piece of string will hold the landrover together for another year or two" Renouf and John "Dr Pedantic" Murray taught me all I know about landrover mechanics, whether I wanted to know or not. Ash, Jane(s), and Phil "water wallah" Gravestock all lent a hand as needed in the field. Of course the Landrover (RIP) itself should be thanked for making even the ride from the airport an adventure. And how can we forget Antonio and the Youth Hostel - who else would have done our washing!

Mean while back at the OU...

This pamphlet has benefited from a lot of discussions with a lot of people at various conferences and around the OU. The Volcano Geophysics Group Friday morning meetings

were always a good place for ideas, as were the pub lunches afterwards. H, Adam, John, Andy Pullen, Hazel and Ben were always there with helpful (and not so helpful) comments and advice. The Cock, Old Speckled Hen and Two Dogs must be thanked for many an enjoyable evening and new and interesting models.

The whores of Henders - Ash, Em, Penny and John - for making that house a place to be proud of (or at least the recycling bins) - and for keeping the neighbours guessing, big snogs babes!! H showed that there is someone sadder than I am and helped to get rid of beer cordial (and pretended to like it) and in this sado group comes Butty for hanging around with H far too long, and for making hockey a blood sport. Blando continued taking the piss even long after everyone else lost interest. Linda - did you know they've taken gullible out of the dictionary? Russell and Mike were always Russell and Mike. The Earthie football/hockey lot get a big smelly one for helping to make the bottom draw of my filing cabinet a no-go area.

Finally, did you know that the 1991-1993 lava flow on Etna could cover Milton Keynes to a depth of 0.5m?

$$Q \gg h$$

(where h and Q are unkown and have something to do with Stromboli).

Paul Röllin 1996

(At least the o wont fall over.)

PAGE/PAGES
EXCLUDED
UNDER
INSTRUCTION
FROM
UNIVERSITY

PAGE
NUMBERING
AS
ORIGINAL

Table of Contents:

Figure List:

Chapter 1

Chapter 2

Chapter 3

Chapter 4

Chapter 5

Chapter 6

Table List:

Chapter 1 Introduction and Aims

"...the universe was full of ignorance all around and the scientist panned through it like a prospector crouched over a mountain stream, looking for the gold of knowledge among the gravel of unreason, the sand of uncertainty and the little whiskery eight-legged swimming things of superstition." *Witches Abroad*, Terry Pratchett.

1.1. Introduction:

Mount Etna is Europe's largest active volcano and is located on Sicily's eastern coast (figure 1.1). It has been recognised for sometime that the Eastern Flank of the volcano represents an unstable or metastable zone, and poses a significant threat to the surrounding population due to potential slope failure [*EPOCH*, 1993]. Located in the centre of the Eastern Flank is the Valle del Bove, a collapse scar, measuring approximately 5 by 7km, and up to 1200m deep at its head.

Ground deformation measurements since the 1980's have shown that a major sector of the Eastern Flank is sliding down slope at an increasing rate [*EPOCH*, 1993], such accelerating downslope creep is considered a classic precursor to catastrophic slope failure [*Voight and Kennedy,* 1978]. If such slope failure involved part of the summit region, the sudden decompression of any near surface magma could produce a cataclysmic pyroclastic eruption similar to that of Mount St. Helens in May 1980 [*Voight et al.,* 1983]. Although there is little evidence for such a shallow level magma system on Etna today [*Murray*, 1990], the geology of the area suggests that this type of collapse event may have occurred several times in the past 20 000 years [*Guest et al.*, 1984; *McGuire*, 1982]. Such activity today would pose a significant hazard to the surrounding population.

Several models have been put forward in recent years to attempt to explain why and how the Eastern Flank is moving, and to describe the volcano-tectonic structure of the Mountain. The main result of this work has been to propose that a large (60°) sector of the Eastern Flank is decoupled from the rest of the volcanic mass. *Borgia et al.*, [1992] suggests that this sector is sliding seaward on an outward- and upward-ramping décollement

horizon at a depth of ca. 5km below the summit craters (approximately 2km below sea-level). An alternative model [*Lo Giudice and Rasà,* 1992] suggests that this movement is taking place at shallower depths (ca. <1km below sea-level), possibly along the boundary between the volcanic pile and the sedimentary basement.

A change in climatic conditions will have an effect on the stability of this flank in a number of ways. Changing sea-level, as has occurred throughout the Quaternary Period, will cause a change in stresses on the mountain, due to alternatively loading and unloading the flanks (rise and fall in sea-level respectively) thus causing compression / decompression of any magma chamber. Also increased erosion at times of changing sea-level will debuttres the flank, increasing its instability. A second and possibly more significant environmental effect may be the loading of the summit region by the build up of ice/snow during colder periods through the Quaternary. Again this causes alternating loading and unloading and thus may influence the behaviour of the volcano.

The main aim of this study is to use a variety of geophysical techniques to look at the Eastern Flank of Etna at several scales. From this a detailed picture of the structure and evolution of the Flank will be developed and thus the various theories trying to explain the observed instability can be tested, as can the causes of past failures, such as that leading to the formation of the Valle del Bove itself.

1.2. The Regional Geology and Structure of Mount Etna:

Sicily is located at the junction of the Eurasian and African plates. Two sites of Cainozoic volcanism are present on the island: the Iblean Mountains and Mount Etna. The Iblean Mountain Volcanics were erupted between the upper Miocene and the lower Pleistocene under shallow-marine and sub-aerial conditions, on a carbonate platform. Both low-K tholeiitic and alkali basalts are present, and this volcanism is linked to tensional movements located at the intersection of several major faults [*Chester et al.*, 1985]. Activity began on Etna in the middle Pleistocene with eruptions of tholeiitic basalts. The main bulk of the modern volcano is built up of alkaline products of trachy-basalt affinity [*Chester et al.*, 1985].

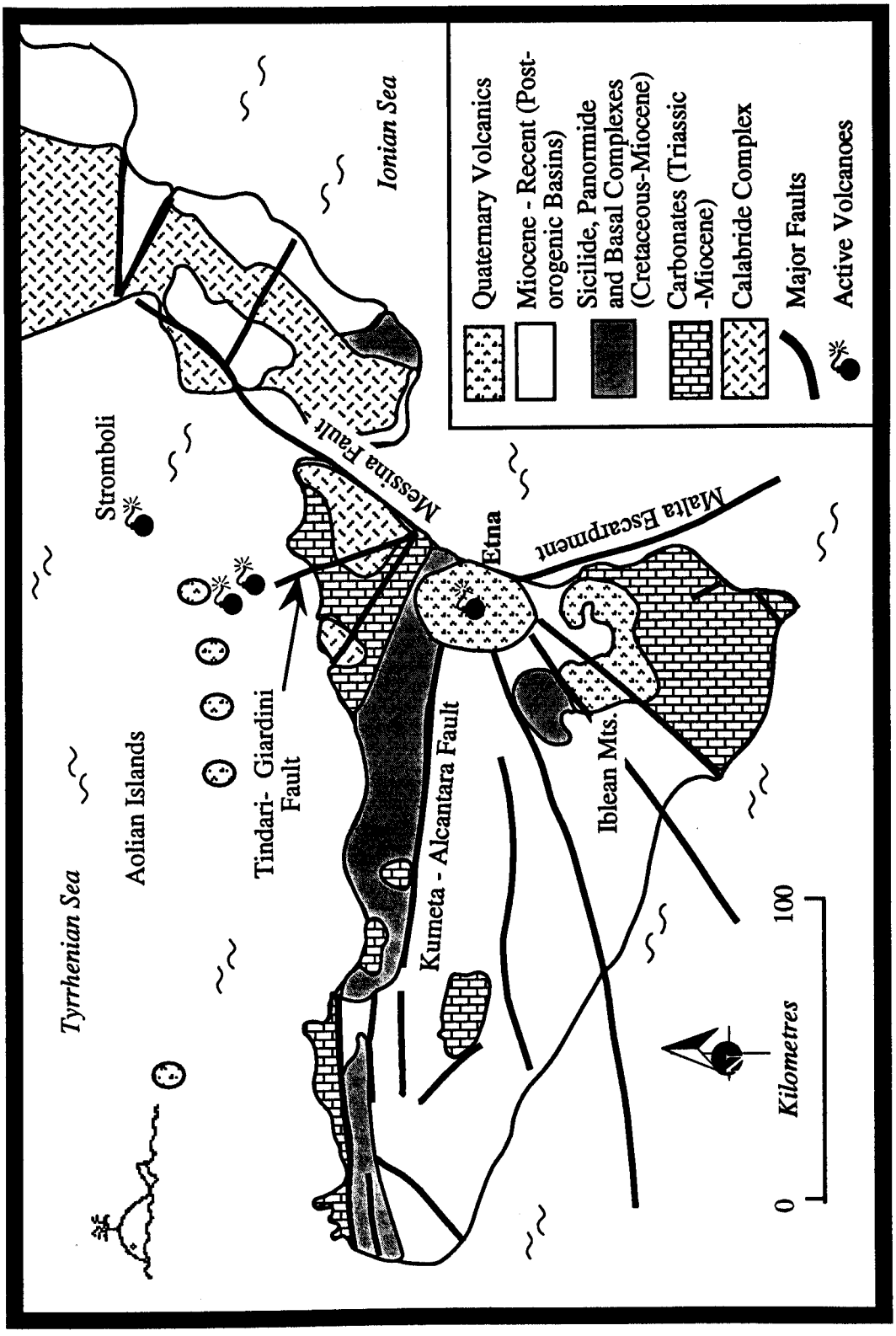

Figure 1.1. Simplified geological map of Sicily, showing the major structural units (from Chester et al. 1985).

Sicily itself is composed of several structural units, as shown in figure 1.1. The oldest unit is the Calabride Complex in the north-east. This unit forms the Peloritani

Mountains, is bounded by the Monte Kumeta - Alcantara Line in the south, and is composed mostly of granites, gneisses, schists and phyllites. A thin sequence of Miocene limestones and shales over lie this unit [*Chester et al.*, 1985].

The Sicilide Complex is composed of late Jurassic and younger flysch sediments. These are thrust over the Panormide Complex, which is predominantly composed of carbonates. In the Pliocene and lower Pleistocene northern Sicily was undergoing uplift while central Sicily was rapidly subsiding to form a number of post-orogenic basins. Later in the Pliocene to Pleistocene, tensional forces caused the reactivation of major faults in Sicily and Calabria [*Chester et al.*, 1985]. In the Etnean region the local geology consists of mid-Quaternary marine marly clays and more recent sands and conglomerates. The main outcrops of these deposits are to the South and East of the volcano, to the North and West are the allocthonous units of the Apenninian-Maghrebian chain, including the Sicilide and Panormide Complexes [*Labaume et al.*, 1990]. The extent to which these Quaternary clays (pre-Etnean clays) underlie the volcano is unclear. *Labaume et al.*, [1990] show that these clays have been deformed both as part of the emplacement of a nappe (the Gela nappe) during the Quaternary, and as Eastward shearing, possibly resulting from Eastwards sliding of a sedimentary apron. They see Mt. Etna as having grown on the active compressional front of the Apenninian-Maghrebian chain.

Sharp et al., [1980] have shown the Moho below Etna to be at a depth of ca. 27km, with average crustal thickness for Sicily being ca. 35km, thickening towards the North, but rapidly thinning below the Tyrrhenian Sea. They also identify an area of lower seismic velocity at approximately 20km which is interpreted as a zone of fractures, partly filled with magma, representing the low level storage system for the volcano. In addition to this low level storage many workers have suggested that magma is stored at high levels for periods of up to a year before an eruption occurs (e.g. *Wadge,* 1977; *Scott* 1983; *Armienti et al.,* 1984). The evidence for this has generally been geochemical in nature and has been used to suggest that this storage takes place within dykes in the top 1-2 km of the volcano. These dykes may be horizontally extending from the central crater area [*Tanguy and Kieffer* 1977]. While it has been shown that eruptions can be fed from shallow dykes travelling only a few

1 0 ' s o f

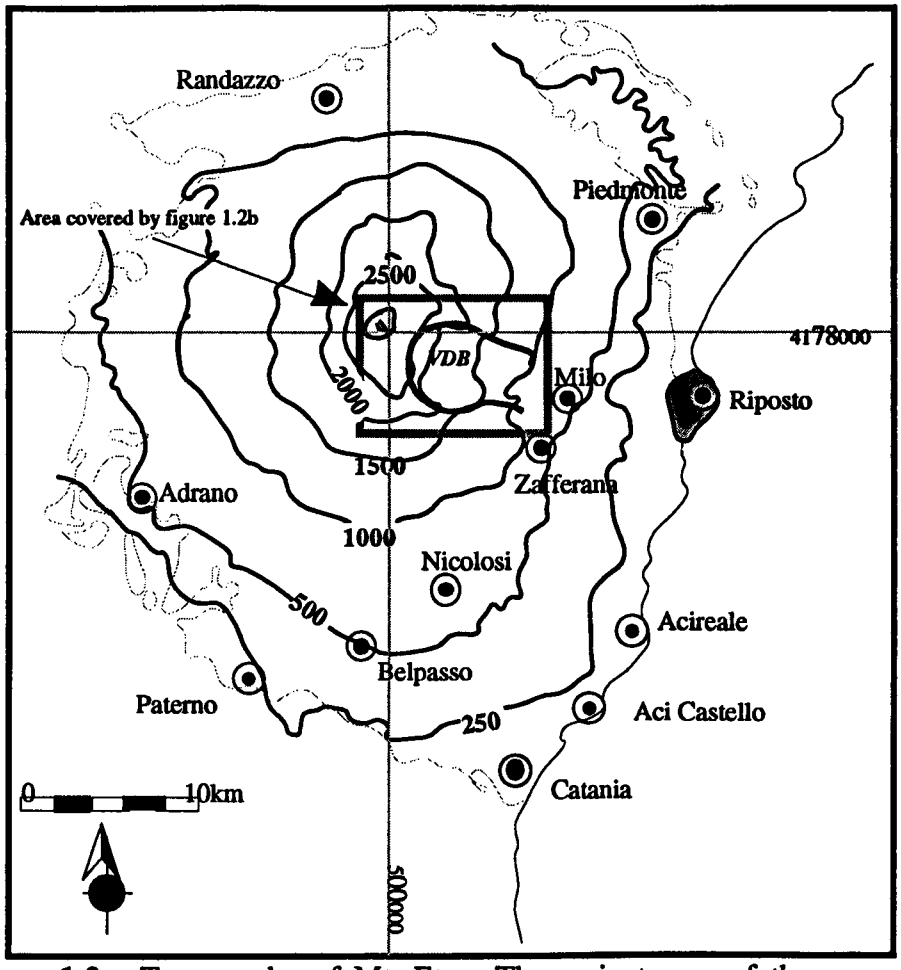

Figure 1.2a. Topography of Mt. Etna. The main towns of the area are shown together with the local grid coordinates for the summit craters. Contours are in metres. VDB = Valle del Bove; thin grey line = limit of volcanics. The shaded area represents the Chiancone deposit.

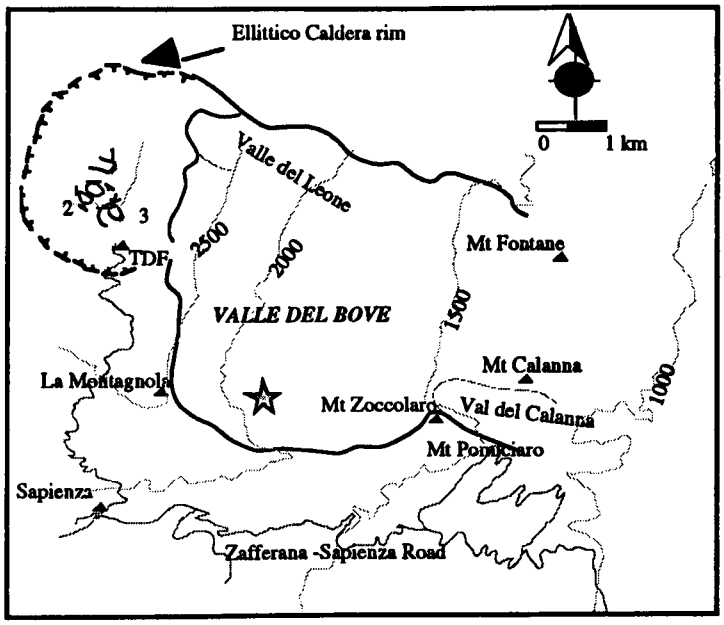

Figure 1.2b. Topography of the Valle del Bove. The Valle del Leone and the Val del Calanna form small depressions joining the Valle del Bove. Monte Zoccolaro and Monte Pomiciaro represent two points on the same promontory. 1 = Northeast Crater; 2 = Central Craters; 3 = Southeast Crater. The star represents the approximate location of the Trifoglietto Centre based on a number of reconstructions [*Cotelli et al.* 1994; *Calvari et al.*, 1994].

metres below the surface [*Wadge* 1980; *Tanguy* 1981; *Kieffer* 1983], long term storage at shallow levels encounters problems in that the dykes would be expected to solidify over the time spans postulated. Modelling ground deformation data recorded during eruptions, *Murray and Pullen* [1984] show that dykes may propagate horizontally from the central crater area, with the 1983 eruption being fed by a dyke extending from near the SE crater, with an upper surface at approximately 2450m asl. *Rittman* [1963; 1973] suggests that dykes propagate from a central vertical conduit to supply most eruptions, while eccentric eruptions are fed directly from a deeper source by near vertical conduits. *Wadge* [1977] gives a model for the Etna feeder system which shows a plexus of dykes at the base of the volcano (1-2 km a.s.l.) which acts as a magma reservoir. This agrees with the more recent work of *Dobran and Coniglio* [1996] who use non-equilibrium fluid flow models to derive a picture of the Etnean feeder system. The resultant model suggests that magma rises from a main reservoir at 8-9 km depth and encounters a structurally weak zone at 1-4 km below the summit, where it may accumulate for short periods of time. *Sanderson et al.,* [1983] interpret their measured gravity changes in terms of a dyke emplaced at about 1500m below the surface, up to six months before the (1981) eruption. Recent ground deformation and gravity monitoring of the volcano has provided some details on the transient magmatic system of the volcano but only limited information on the long term feeder system. Modelling of this data suggests that magma rises from depth (approx. 20 km) in a central conduit, dykes branch off at about 1 km depth and then travel horizontally until the surface is intersected and an eruption occurs [*Murray* 1990; *Rymer et al.* 1994]. No clear evidence is seen for a long term magma storage system at shallow levels [*Murray* 1990].

Recent work has divided the eruptive history of Etna into four stages, the first being the beginning of activity approximately 500 000 years B.P., with the extrusion of sub-marine tholeiitic basalts into a marine gulf that extended partly over the present area of the volcano [*Gillot et al.*, 1994]. These form pillow lavas, hyaloclastic breccias and shallow intrusions, and are exposed around Aci Castello - Aci Trezza (see figure 1.2 for location) [*Romano*, 1982]. The second period represents a switch from fissure type eruptions to the building of strato-cones of alkaline composition. The main exposure of this period is located near the town of Paternò (the Paternò neck) and has been dated at 168 000 years [*Gillot et al.*, 1994]. Following a possible hiatus in activity, the third period is represented

by differentiated lavas and intense eruptive activity, characterised by the large polygenic Trifoglietto centre (80 000 years, [*Gillot et al.*, 1994]). The Trifoglietto centre has been placed in the area now occupied by the Southern Wall of the Valle del Bove. It is possible that it was during this stage that a proto-Valle del Bove formed. The fourth period is represented by the development of the modern centre, beginning around 34 000 years ago [*Gillot et al.*, 1994], this last phase has been divided into the Ancient and Modern Mongibello. Ancient Mongibello begins with eruptions from the Zoccolaro centre, erupting lavas in the area of Monte Zoccolaro, and ends with the collapse of the Ellittico caldera and subsequent formation of the Leone caldera. The Ellittico caldera appears to have occupied the area now covered by the Modern Mongibello deposits of the present eruptive centre, while the Leone caldera appears to have erupted lava flows from a centre near Pizzi Deneri, which then ponded in the area of the collapsed Ellittico centre [*Guest et al.*, 1984]. Table 1.1 summarises the stratigraphy of the eruptive products of Etna. The overall impression of this eruptive history is the gradual movement of the eruptive centre in a Northwesterly direction; from Aci Castello to the present summit region. The location of these centres are shown on figure 1.2 and 1.3.

There is only limited evidence for major pyroclastic producing eruptions during the history of Etna, thus the caldera collapses that have occurred (e.g. Ellittico) are interpreted as representing erosional/structural collapse rather than classical caldera collapse. Generally caldera collapses produce large amounts of pyroclastic material while within the modern summit region post-eruptive collapse is seen to occur in coincidence with the withdrawal of magma from the central conduit. The Ellittico caldera may have formed this way - removal of magma from below causing collapse, with erosion aiding the processes.

On the Eastern coast line of Etna is located the Chiancone deposit (figure 1.3). This is an area of sandy conglomerates deposited in an approximate fan shape. The material is a mixture of large basaltic blocks mixed with fine grained ash and sandy material. Sedimentological structures within the deposit show a fluvial origin for the bulk of the deposit, while some matrix-supported units indicate emplacement as mud flows, these structures are consistent with the origin of the material as landslide debris. Dating of carbonised wood within the Chiancone gives an age of 5460 yrs. B.P. [*Kieffer* 1979], more recent work gives 7590±130 years for the base of the exposed material [*SEAVOLC* 1996].

The inferred source area for this unit appears to be the Valle del Bove. Forming the western boundary of this deposit is the Timpe Fault system. The faults making up the Timpe appear to be the landward continuation of the Malta Escarpment. Immediately North and South of the Chiancone they form large fault scarps of up to 100m, while within the Chiancone they are more subdued features [*Stewart et al.,* 1993]. Movement on these faults appears to be both strike-slip and dip-slip, downthrown to the East. Superimposed on this downthrowing to the East is a regional uplift, seen by uplifted marine terraces, of up to 11m in the last 7700 years [*Stewart et al.,* 1993]. *Stewart et al.,* interpret this regional movement as indicating an asymmetric updoming of the pre-Etnean basement, show Etna siting on material which is itself up lifting and sloping towards the East.

Table 1.1. Stratigraphy of the Etna Area (after *Chester et al.*, 1985; *Gillot et al.*, 1994; *McGuire*, 1982)

Units	Centres	Description	Events	Approximate Age (years B.P.)
Recent Mongibello	Present Centre	Includes historic Eruptions, Mainly Hawaiites	Minor Collapse in summit area.	
	Piano	Mainly Hawaiites	Caldera Collapse Formation of Valle del Bove	5000
Ancient Mongibello	Leone	Hawaiites, basic Mugearites	Caldera Collapse	6000
	Ellittico	Hawaiites, Mugearites, Benmoreites	Caldera Collapse	15 000.
	Belvedere	Hawaiites, basic Mugearites		
	Vavalaci	Hawaiites, Mugearites, Benmoreites	Caldera Collapse	
	Zoccolaro			
Trifoglietto	Trifoglietto II	Basic Mugearites, Mugearites	Major Phreatomagmatic Activity	34 000 - 80 000
Pre-Trifoglietto	Calanna	Poorly exposed - Hawaiites	Major Caldera Collapse	100 000
	Trifoglietto I	Poorly Exposed	Caldera Collapse	
		Tholeiitic Basalt	Intrusive neck on Southern Flank	
Alkali Olivine Basalt	Paternò Cone	Alkali Olivine basalt	Eroded Cone	168 000
	(Adrano)	Sub-aerial Tholeiitic Basalts		300 000
	(Aci Castello / Aci Trezza)	submarine Tholeiitic Basalts and Intrusives		500 000

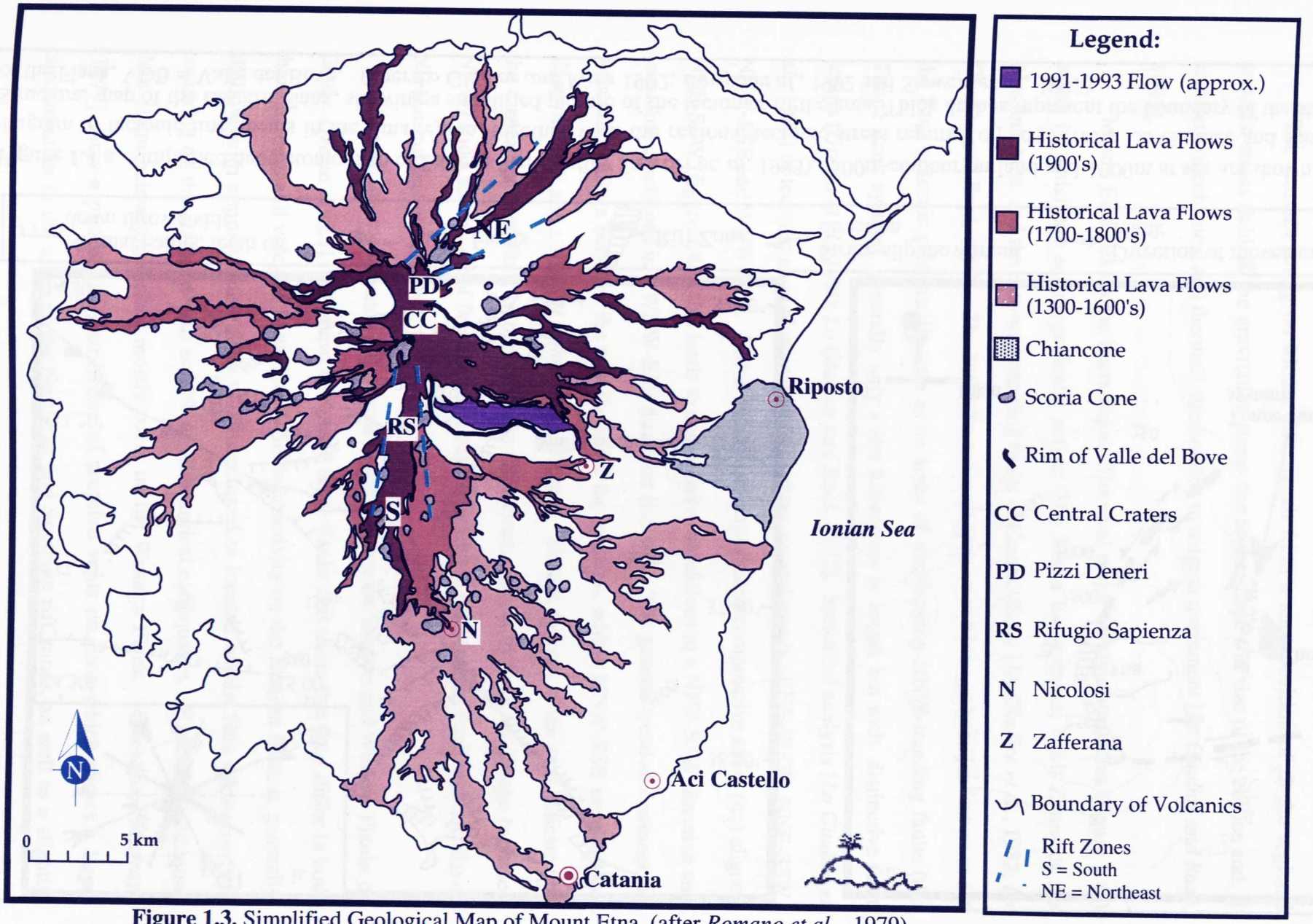

Figure 1.3. Simplified Geological Map of Mount Etna (after *Romano et al.*, 1979).

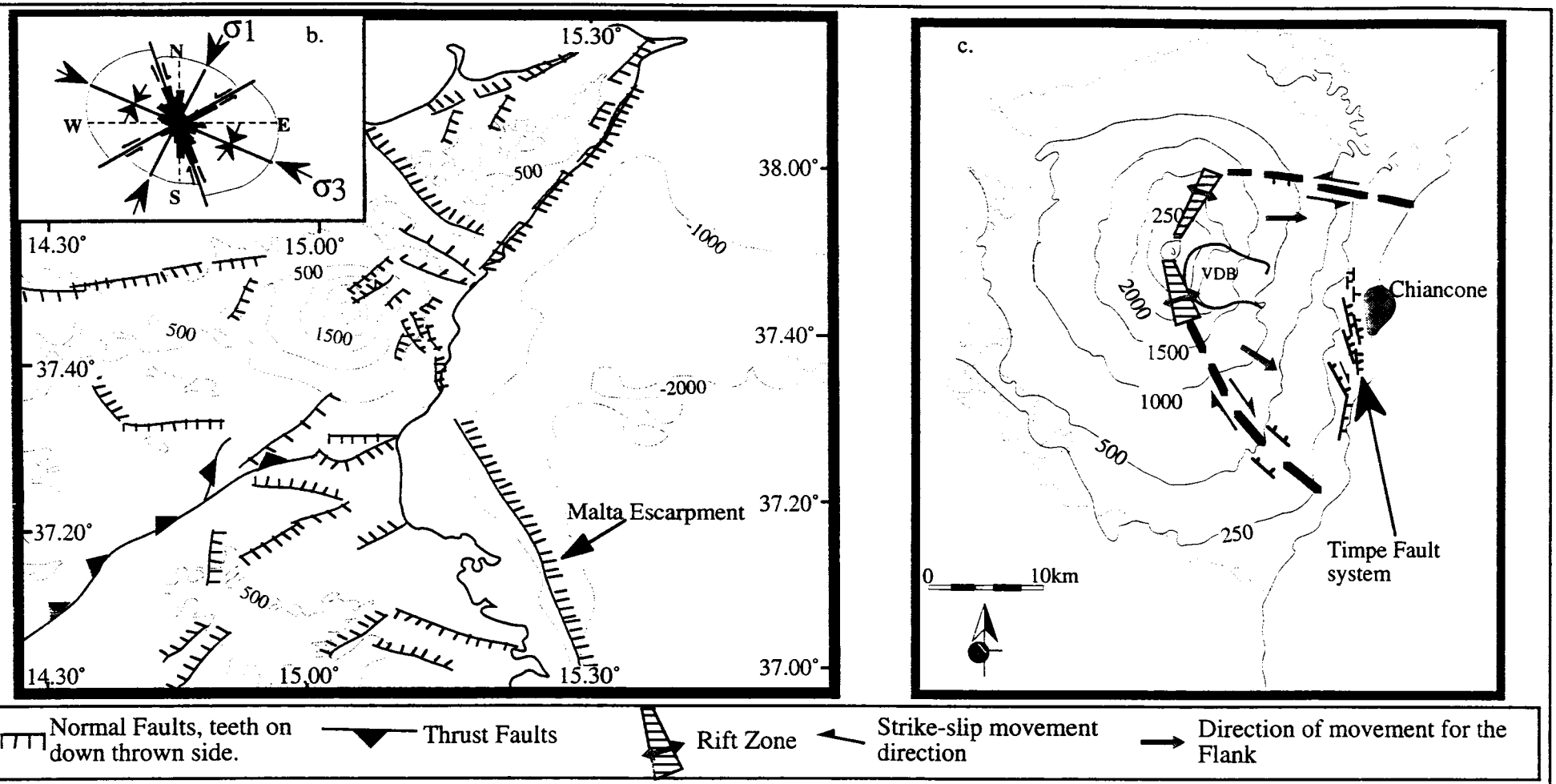

Figure 1.4 a. Simplified neotectonic map of Eastern Sicily (after *Stewart et. al.* 1993). 500m contour on land and 1000m at sea are shown. **b.** Rose diagram of tectonic lineaments in the Etna region, together with the regional tectonic stress regime (σ_1, σ_3) (from Lo Giudice and Ràsa 1982). **c.** Structural map of the Eastern Flank, showing a simplified picture of the tectonics of the area. Thick dashes represent the boundary of the sliding sector of the Flank, VDB = Valle del Bove. (after *Lo Giudice and Ràsa* 1992; *Borgia et al.*, 1992 and *Stewart et al.*, 1993).

1.2.1. Regional Stress Field:

The stresses acting on Mount Etna result from a superposition of ① the regional tectonic stress field, ② the gravitation stress due to the shape and size of the edifice and, ③ transient (mechanical and thermal) stresses due to magma movement [*Lo Giudice and Rasà,* 1992].

Mount Etna lies on the intersection of several major tectonic structures (figure 1.4a) many of which are seismogenically active: The Malta Escarpment; Fault Zones of the Messina Area; and the east-west trending faults of Central Sicily [*Lo Giudice et al.*, 1982; *Lo Giudice and Rasà,* 1992]. The Malta Escarpment appears to be the only major feature to cut the Etna volcanic pile, and is seen as an array of overlapping NNW-trending faults (the Timpe Fault system), generally only a few kilometres in length but with distinctive fault scarps [*Gresta et al.*, 1990; *Lo Giudice and Rasà,* 1992]. Statistical analysis [*Lo Giudice et al.*, 1982] of tectonic and volcanic structures show several trends : ENE-WSW, NNE-SSW, NNW-SSE and WNW-ESE. These result from a maximum compressive stress (σ_1) aligned NNE-SSW (figure 1.4b), this leads to compressive conditions in a NNE-SSW direction and tensional conditions in a WNW-ESE direction (i.e. σ_3). The general trend of seismogenic structures differs between the two flanks of the volcano, with a NNW-SSE trend on the Eastern Flank and a NE-SW trend on the Western. Recent surveys of the area indicate that the coastal parts of Etna, in particular the Chiancone, are cut by both the Timpe (oriented NNW) and a second set of faults approximately parallel to the Messina Fault with a strike of NE [*Lanzafame et al.*, 1996].

Several other noticeable differences occur between the Eastern and Western Flanks of Etna. *Gresta et al.*, [1990] have compared these flanks and show that they differ in both their tectonic and volcanic behaviour. Seismic activity on the Eastern flank is generally shallow with approximately 80% of all earthquakes located within 5km of the surface occurring on this flank, as well as 80% of all historical earthquakes. Events located more than 10km below the surface mostly occur on the Western Flank. *Guest and Murray,* [1979] show a plot of the distribution of eruptive vents on Etna which shows a large concentration in the areas of the Northeast and Southern rift zones, as well as a slightly

greater number on the rest of the Eastern Flank relative to the Western Flank. They also note that eruptions on the Eastern Flank occur approximately once every 50 years while on the Western Flank the time period is approximately 200 years. The Valle del Bove shows relatively few eruptive vents, but this may be due to the covering of older centres by the deposits of younger ones, due to the confining effect of the Valle walls [*Guest and Murray*, 1979]. The larger number of eruptions occurring on the Eastern Flank suggests that the higher degree of tectonisation on this Flank facilitates shallow level magma intrusion. [*Gresta et al.*, 1990].

The consideration of all these factors has lead to the formation of a volcano-tectonic model suggesting that the Eastern Flank can be seen as a structural domain decoupled from the rest of the volcanic body and undergoing gravitational sliding towards the east [*Borgia et al.*, 1992; *Lo Giudice and Rasà,* 1992]. This movement occurs between two fault zones : a left-lateral, oblique slip (to the north) and a right lateral, oblique slip (to the south). On the volcanic edifice itself these fault zones can be seen as represented by the NE and SE rift zones (respectively). The area bounded by these fault zones is characterised by shallow seismicity, representing both discrete low magnitude events and continuous creep [*Lo Giudice and Rasà,* 1992]. The depth of the basal slip plane has been placed at between 1km and 5km below sea-level, that is either the volcano/basement contact or within the underlying sediments [*Borgia et al.*, 1992; *Lo Giudice and Rasà,* 1992]. Located between these two rift zones is the large collapse structure of the Valle del Bove (figure 1.3).

1.2.2. Geology and Structure of the Valle del Bove

The Valle del Bove consists of a series of coalescing amphitheatre-shaped depressions, producing a large sub-circular hollow approximately 5km in diameter, opening out towards the sea (East) with a total length of approximately 7km. Its maximum depth is about 1200m at the head of the Valle, south-east of the main summit craters, becoming shallower towards the east.

Much of the southern wall represents deposits of the ancient Trifoglietto centre, with numerous exposed dykes. These dykes represent the Calanna, Trifoglietto and Zoccolaro units, as well as two major dykes sets of post-Trifoglietto origin. These post-Trifoglietto

dykes show orientations of NE/SW and NW/SE [*McGuire*, 1982]. Both the Northern and Southern walls of the Valle show numerous normal faults with orientations ranging from NE-SW to E-W, with the down thrown side being in the direction of the Valle. Some of these faults can be traced to old centres (e.g. the formation of the Ellittico Caldera) while many show signs of being still active [*Calvari et al.*, 1994; *Coltelli et al.*, 1994]. The western wall of the Valle is cut by a series of almost parallel normal faults, oriented approximately N-S, interpreted as linked to the gravitational stresses resulting from the presence of the Valle [*Calvari et al.*, 1994] (figure 1.5a).

The origin of the Valle del Bove has been much debated with glacial erosion [*Vagliasindi,* 1950], fluvial processes [*Lyell,* 1858], volcanic activity and volcano-tectonic collapse [*Klerkx* 1970; *Klerkx and Evrard* 1970] all being cited. *Habesch* [1985] critically discusses each of these hypotheses and concludes that the Valle del Bove is unlikely to have originated from any one single process, rather several individual events and processes have acted together. He suggests that volcanic activity, small landslides and fluvial erosion have all played a part in the formation of the Valle.

Glacial erosion can be discounted, as although Etna would have had permanent snow fields during past glacial episodes it is unlikely that the snow line was ever depressed enough to allow large glaciers to form [*McGuire*, 1982]. Recent work by *Neri et al.*, [1995] has suggested the presence of significant ice layers on the summit region during previous glaciations, however no evidence is seen for the formation of extensive glaciers.

One possible method for the formation of the Valle is as the result of large scale caldera collapse or explosive eruption (c.f. Mount St. Helens). Assuming the Valle to be a caldera, *McGuire*, [1982] suggests that its structure (highly irregular and strongly scalloped walls) indicates formation by a more violent and piecemeal process than that which formed the smaller Etna calderas (e.g. Ellittico). He concludes that the distribution of volcanic deposits lying outside of the Valle indicate formation by landslides triggered by volcanic explosions. His model can be summed up as an initial phreatic/phreatomagmatic explosion of the old Trifoglietto centre (ca. 20 000 years B.P.), followed by enlargement through gravitational collapse and erosion.

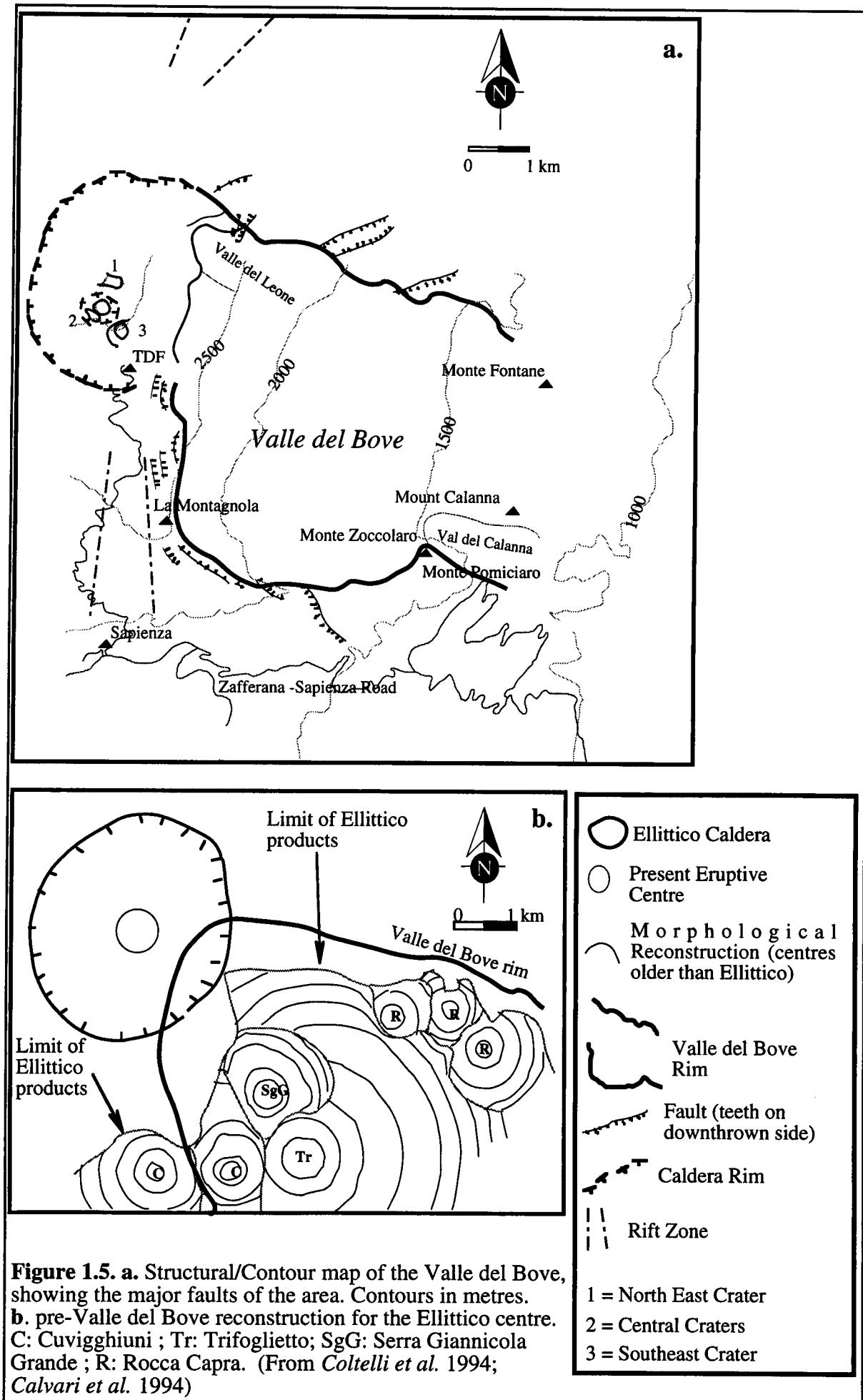

Figure 1.5. a. Structural/Contour map of the Valle del Bove, showing the major faults of the area. Contours in metres. **b.** pre-Valle del Bove reconstruction for the Ellittico centre. C: Cuvigghiuni ; Tr: Trifoglietto; SgG: Serra Giannicola Grande ; R: Rocca Capra. (From *Coltelli et al.* 1994; *Calvari et al.* 1994)

An alternative model is proposed by *Guest et al.*, [1984], in which each of the individual depressions making up the Valle formed by one major movement and were subsequently enlarged by small-scale mass movements. They found no direct evidence to link the formation of the Valle to any known episode of explosive volcanism. Its location on the unbuttressed sea-ward side of the volcano in the angle between the Northeast and the Southern Rift zones and also between the orthogonal set of dykes exposed in the Valle walls, is evidence for formation by slope failure under gravitational stresses [*Guest et al.*, 1984]. The pattern of fault scarps (Timpa) downslope, are indicative of seaward slumping of the Flank.

The most probable scenario for the Valle del Bove's formation, based on published models, appears to be that of *Habesch* [1985] where several processes have acted either together or separately to produce the structures seen today. Initial collapse due to volcanic or tectonic forces has then been enlarged by erosional and further tectonic/volcanic action.

Two recent geological studies of the Valle [*Calvari et al.*, 1994; *Coltelli et al.*, 1994] have reinterpreted many of the deposits and structures exposed in the walls of the Valle, and provide new reconstructions and eruption histories for the area. Two phases in the volcano's activity are identified; the first being dominated by eruptions from small volcanic centres located in the Valle's north-eastern sector, the second beginning with the formation of the Ellittico stratovolcano, followed by caldera collapse and the formation of the present day volcano. These new reconstructions suggest that the Trifoglietto centre was the first of many to build up within the area now occupied by the Valle del Bove, the last being the Cuvigghiuni centre, the products of which have been attributed to three distinct vents which were active until approximately 34000 years B.P. (figure 1.5b). This unit has been included within the Trifoglietto sequence in the past and has been so treated in table 1.1. Also included within the Trifoglietto unit have been the deposits of the Serra Giannicola Grande centre which was active between the time of the Trifoglietto and the Cuvigghiuni centres. Following this the feeding system appears to have moved towards the north-west, building up the Ellittico stratovolcano, which subsequently underwent caldera collapse. The modern summit zone is located within, and covers over, the Ellittico caldera. The older centres of the Valle del Bove region have had an important morphological influence on the

deposits of the Ellittico caldera; the lack of Ellittico products within the Southern wall of the Valle indirectly implies the presence of significant topographical features in this area during the eruption of the Ellittico lavas [*Calvari et al.*, 1994; *Coltelli et al.*, 1994], preventing them from flowing towards the east and Southeast, this in turn implies that the Valle could not have existed in its present form at this time (figure 1.5b).

Horizontal ground movement during dyke emplacement in 1983 and 1985 resulted in a 2.8m eastward displacement of a block of the western wall of the Valle del Bove [*McGuire et al.*, 1990], if the total thickness of dykes exposed within the Valle is considered, a West to East extension of 500m has occurred over the last 34 000 years, giving a rate of 1.3cm/yr [*Borgia et al.*, 1992]. The linear shape of the present western rim (figures 1.2b and 1.5a) indicates that north-south aligned slope failure has occurred in the past, thus dyke-induced collapse appears to be an important agent in the continuing enlargement of the Valle [*McGuire et al.*, 1990]. One consequence of the existence of the Valle del Bove is the generation of a superficial stress regime such that repeated injections of north-south oriented dykes adjacent to the western rim will occur preferentially [*McGuire and Pullen,* 1989]. This alteration of the stress regime only occurs in the upper parts of the edifice, at depth the tectonic stress regime will dominate. Shallow magma intrusion leads to dilation of the Western Wall of the Valle del Bove and to slope instability and failure of the cliff wall, causing a progressive westward migration of the western rim [*McGuire et al.*, 1990].

When compared to modern deposits, older Etnean lavas show a change in petrology, which has been linked to the formation of the Valle del Bove: pre-Valle del Bove lava is consistent with the presence of a high level magma storage area within the volcanic pile, whereas post-formation lavas appear to have risen directly from a deep level source. This suggests that the formation of the Valle changed the stress field of the volcano such that high level storage of magma can no longer take place [*Guest et al.*, 1984].

There are still many questions concerning the Valle del Bove which are unanswered, such as the time period for formation, its effect on activity and whether or not it is still growing. To answer these questions is one of the aims of this study.

1.3. Volcanic Instability:

Many volcanoes around the world have been recognised as having had large scale slope failures occur in their history e.g. Mauna Loa (Hawaii), Piton de la Fournaise (Réunion), Etna, as well as numerous stratovolcanoes [*Borgia et al.*, 1992; *Francis and Self*, 1987; *Lénat et al.*, 1989; *Lipman et al.*, 1988], suggesting that collapse of part of the edifice may be a common stage in volcano evolution. In the case of the Hawaiian Islands and Réunion large submarine landslide deposits are recognisable [*Lénat et al.*, 1989; *Lipman et al.*, 1988]. *Borgia*, [1994] puts forward the theory that collapse is an integral part of a volcano's life cycle. In this model a volcano moves through five phases: building, compressing, thrusting, intruding and spreading. As the volcano builds up it exerts an ever increasing load on the crust causing large compressive stresses to build up. These compressive forces limit magma movement, allowing for the build up of large magma chambers, possibly leading to large caldera forming eruptions. The thrusting phase begins with the formation of a basal décollement; thus the stress changes, with compression in the summit region and tension in the basal region, encouraging intrusion of material to form basal intrusive complexes. Finally the mass builds to the point when spreading takes over as the predominant force, it is within this phase that the *Borgia et al.*, [1992] model places Etna. These phases may repeat and overlap. Collapse may occur in any of the final three phases. Such collapse may be related to a number of factors, both environmental and volcanic. Environmental factors may be regional or local in extent, ranging from small scale creep related to processes such as freeze-thaw to large scale erosion following sea-level changes or ice build-up. Such variations in scale of the causative process will result in a corresponding variation in the scale of the resultant slope movements. Volcanic factors may also vary in scale, from small movements relating to dyke emplacements [*McGuire et al.*, 1991; *McGuire et al.*, 1990], to large scale sector and dome collapse (e.g. Mt. Saint Helen's 1980 eruption).

1.3.1. Mechanisms of Slope Failure:

Slope failure can occur on many scales and involve a number of different mechanisms, therefore it is important to be consistent in the terms used. The term landslide is generally used to describe all types of slope movement which have the following properties:

1. Gravity is the principal force involved.
2. Movement is moderately rapid.
3. Movement may include falling, sliding and flowing.
4. The plane or zone of movement is not identical with a fault.
5. Movement is down and out with a free face.
6. The displaced material has well-defined boundaries and usually involves only limited portions of the hillside.
7. The displaced material may include parts of the regolith and/or bedrock.

[*Hansen*, 1984]

Landslides can be divided into several categories depending on the mechanism and scale of the failure, these are described in table 1.2. In the case of the Valle del Bove the most likely failures to occur are either a slide or topple. In a rock slump (see table 1.2) movement is rotational in nature and due to forces causing a turning moment about some axes above the centre of gravity of the unit. The rupture (or décollement) surface will be concave upwards. If the slide is translational (a rock slide or rock block slide) movement is along an approximately planar surface, frequently controlled by the structure of the material (e.g. a bedding plane). For a rock topple, movement occurs about a pivot point below the centre of gravity of the unit, such movement will generally result from the oversteepening of a free face [*Hansen*, 1984]. Given the geometry of the Valle del Bove, a translational slide is unlikely (see figure 1.6), rather either a rock slump or topple is the most likely mechanism. Figure 1.6 shows the relative geometry of each type of failure in relation to the Valle del Bove. In the case of a rotational movement the décollement surface is most likely to be located towards the Central Crater area. Non-rotational movement in the form of toppling would result from outward movement of the walls (for example, following dyke

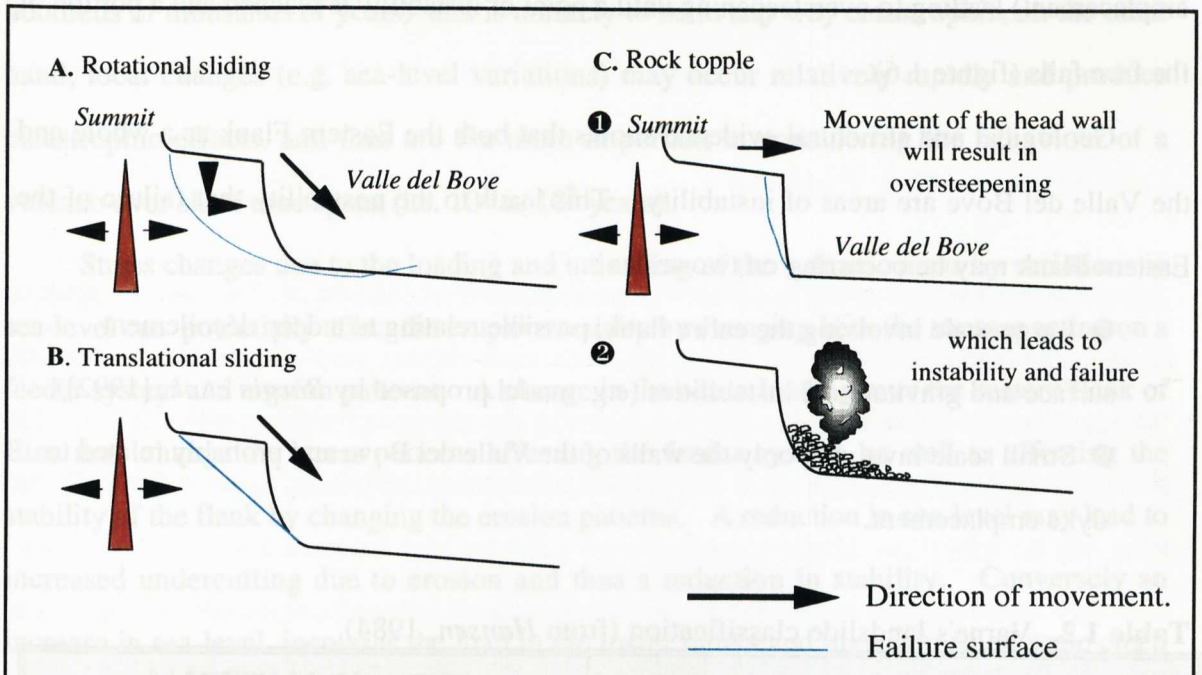

Figure 1.6 . A cartoon of possible mechanisms of failure for the walls of the Valle del Bove. Injection of material under the summit region forces out the walls of the Valle del Bove which may respond in one of the ways shown. Definition of terms follows table 1.2.

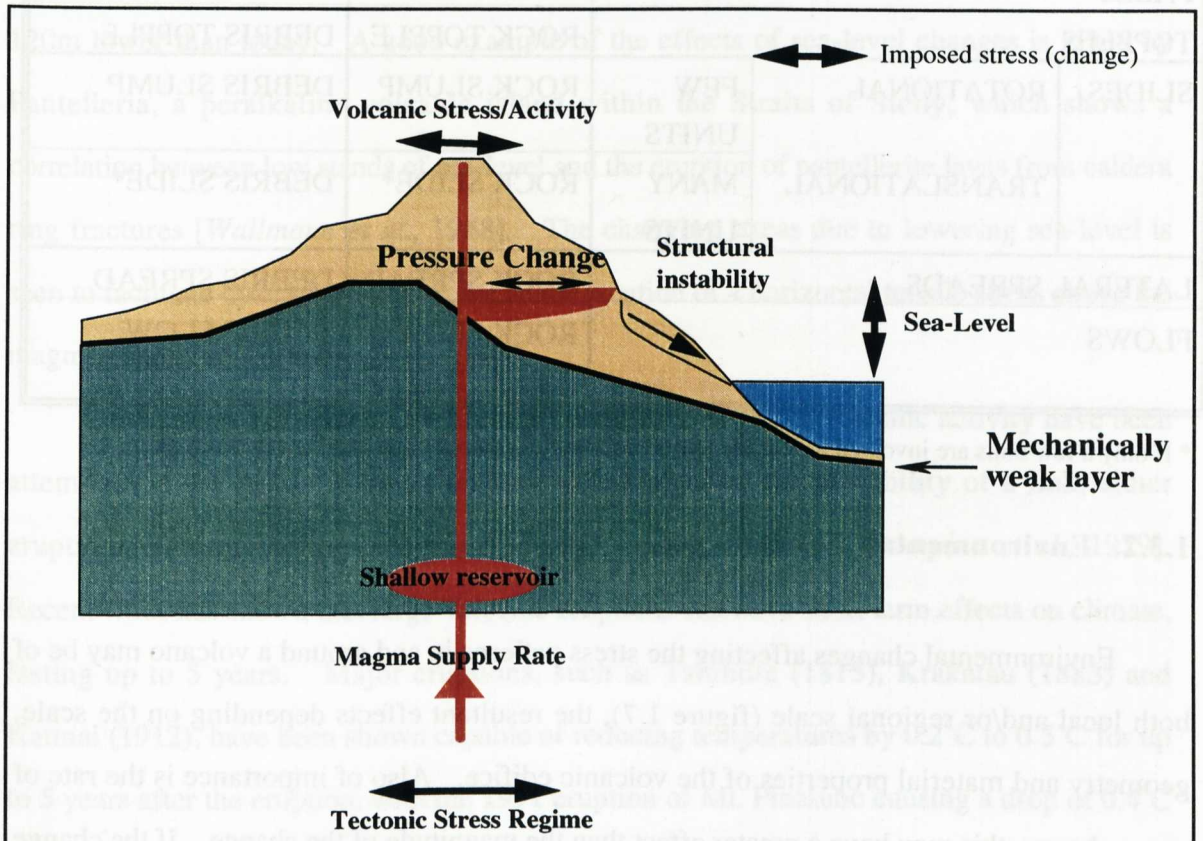

Figure 1.7. Environmental influences on a volcanic edifice. Such influences may be on any number of scales and relate both to the volcano itself as well as its surrounding area.

emplacement) leading to oversteepening until a point of instability is reached and a portion of the face fails (figure 1.6).

Geological and structural evidence shows that both the Eastern Flank as a whole and the Valle del Bove are areas of instability. This leads to the possibility that failure of the Eastern Flank may be occurring on two scales :

❶ Large scale involving the entire flank, possible relating to a deep décollement surface and gravitational instabilities (e.g. model proposed by *Borgia et al.*, [1992]).

❷ Small scale involving only the walls of the Valle del Bove and probably related to dyke emplacement.

Table 1.2. Varne's landslide classification (from *Hansen*, 1984).

TYPE OF MOVEMENT			TYPE OF MATERIAL	
			BEDROCK	ENGINEERING SOILS
FALLS			ROCK FALL	DEBRIS FALL
TOPPLES			ROCK TOPPLE	DEBRIS TOPPLE
SLIDES	ROTATIONAL	FEW UNITS	ROCK SLUMP	DEBRIS SLUMP
	TRANSLATIONAL	MANY UNITS	ROCK SLIDE*	DEBRIS SLIDE*
LATERAL SPREADS			ROCK SPREAD	DEBRIS SPREAD
FLOWS			ROCK FLOW (DEEP CREEP)	DEBRIS FLOW

* If only a few units are involved then these terms become Rock Block slide and Debris Block slide.

1.3.2. Environmental Effects:

Environmental changes affecting the stress patterns in and around a volcano may be of both local and/or regional scale (figure 1.7), the resultant effects depending on the scale, geometry and material properties of the volcanic edifice. Also of importance is the rate of stress change, this may have a greater effect than the magnitude of the change. If the change occurs over a long time period then the system will have time to equilibrate with the new stress fields, however this will not be the case for a rapid change. For example, a change in regional stress will affect the deep structures of the volcano, possibly leading to a change in the feeder system. Such a large scale change will occur over a long time period (i.e. tens to

hundreds of thousands of years) and is unlikely to be in any way catastrophic, on the other hand, local changes (e.g. sea-level variations) may occur relatively rapidly and produce catastrophic effects, and thus are the more important in considering the behaviour of a volcano over short time spans (i.e. 10^1 to 10^3 years).

Stress changes due to the loading and unloading of the volcanic mass by variations in sea-level can potentially affect the eruptive activity by changing both the stresses acting on a feeder system and erosion patterns. A change in the ocean loading over the eastern flank of Etna may change the stress patterns affecting the feeder system, as well as affecting the stability of the flank by changing the erosion patterns. A reduction in sea-level may lead to increased undercutting due to erosion and thus a reduction in stability. Conversely an increase in sea-level, increases the load in the lower flanks and may stop small scale creep from occurring, this would then lead to a build up of stresses within the upper flanks and may lead to a large scale catastrophic failure. Sea-level fluctuations of up to 120m have occurred in Etna's history [*Fairbanks*, 1989; *SEAVOLC*, 1996], with sea-level at 20ka being 120m lower than today. A good example of the effects of sea-level changes is given by Pantelleria, a peralkaline volcanic island within the Straits of Sicily, which shows a correlation between low stands of sea-level and the eruption of pantellerite lavas from caldera ring fractures [*Wallmann et al.*, 1988]. The changing stress due to lowering sea-level is seen to facilitate dyke propagation, due to the creation of a horizontal tensile stress above the magma chamber [*Wallmann et al.*, 1988].

Correlations between major sea-level changes and global volcanic activity have been attempted in the past. Various authors have suggested the possibility of a link, either eruptions causing cooling or climate change causing eruptions [*Rampino et al.*, 1979]. Recent work has shown that large volcanic eruptions can have short term effects on climate, lasting up to 5 years. Major eruptions, such as Tambora (1815), Krakatau (1883) and Katmai (1912), have been shown capable of reducing temperatures by 0.2°C to 0.5°C for up to 5 years after the eruption, with the 1991 eruption of Mt. Pinatubo causing a drop of 0.4°C [*Jakosky*, 1986; *McCormick et al.*, 1995; *Self et al.*, 1981]. On the scale of single volcanoes such as Mt. Etna, correlations between changes in eruption style and palaeoclimate have been noted [*Duncan et al.*, 1984]. Episodes of phreatomagmatic and laharic activity on

Etna have been related to environmental rather than magmatic changes. These variations in eruptive style appear to relate to variations in precipitation (i.e. colder, wetter conditions).

1.4. Aims of the Project:

The overall aim of this project is to understand the structure of the Eastern Flank of Mount Etna and the effect of changing conditions, both climatic and volcanic, on its stability. The secondary purpose is to investigate the failure occurring on the Eastern Flank at present and in the past and thus produce a model for the formation of features such as the Valle del Bove and the Chiancone deposit. This is achieved by:

❶ Detailed gravity and aeromagnetic surveys to determine the shallow to medium structures of the Eastern flank, with special emphasis on the Valle del Bove and Chiancone areas. This will provide controls on the subsurface geology.

❷ The use of palaeomagnetics to determine the degree of rotation of dykes exposed within the Valle del Bove, to place constraints on the style of movement within the Valle.

❸ Finite element stress modelling to determine the effect of changing conditions on the volcanic edifice. The subsurface models derived from the gravity and aeromagnetic data help constrain these models.

❹ The Global Positioning System (GPS) to locate the gravity stations and the establishment of a small deformation network on the lower slopes of the volcano to provide a measure of present day movement and instability.

1.5. Methodologies:

The numerous methods used in this study are complementary in that each relates to a particular aspect of the overall problem and each focuses on a different scale. Thus, by combining the various techniques it is possible to build up a more detailed picture than with any one technique on its own. For example, the palaeomagnetic study was used to investigate the movement of individual rock units (in this case dykes), while gravity, aeromagnetics and GPS provide information on the physical properties of rocks for the whole area. Finite element modelling was used to investigate large scale environmental

factors such as sea-level change and ice cover, and their effect on the stress regime within the whole volcano.

1.5.1. Palaeomagnetics:

Palaeomagnetism provides a method for determining whether rotation has occurred, thus distinguishing between possible failure mechanisms in the Valle del Bove. Failure of this area may be occurring by rotational (e.g. rock slides) or non-rotational means (e.g. rock topples); palaeomagnetic measurements should provide evidence for one or the other. If rotational failure has occurred then we can expect bodies within the walls of the Valle to be rotated about some axis. In order to determine if this has occurred, samples were collected for palaeomagnetic analysis from several of the dykes exposed in the southern and western walls of the Valle. As these features are ≤20 000 yrs in age we would expect their palaeo-declination and -inclination to be similar to today's, allowing for secular variation. Rotation of the dykes by an amount greater than the secular variation would be measurable.

The large number of dykes outcropping on the western and southern walls of the Valle del Bove provide an excellent source of samples for palaeomagnetic work. The high content of ferrous minerals (2% by volume magnetite phenocrysts [*McGuire*, 1983]) means that the dykes have a strong magnetic intensity, and thus a well preserved magnetisation relating to the Earth's field at the time they cooled below their blocking temperature (T_B), the temperature at which the magnetisation is frozen into the mineral.

The present day geomagnetic field for Etna has a declination of approximately 0° and an inclination of approximately 55°. Palaeomagnetic work in the area shows that over the last 800 years these values have varied by ±20° for the declination, and ±10° for the inclination [*Rolph and Shaw,* 1986]. As it is impossible to know the true field direction at the time the dykes gained their magnetisation we must assume that such values are typical for the past 20 000 yrs, and thus a declination and inclination outside the ranges of 340°-020° and 45°-65°, respectively, would suggest that rotation has occurred.

Palaeomagnetism is commonly used to measure rotation of bodies on both the continental and local scale (e.g. *Patrascu et al.*, 1994; *Perrin et al.*, 1994; *Saribudak et al.*, 1991). Work on Mt. Etna to date has concentrated on the younger (dated) lava flows in

order to study aspects of the geomagnetic field and secular variation (e.g. *Rolph and Shaw,* 1986; *Tanguy,* 1970). Only one study has looked at the older material, again this was in an effort to study the secular variation and as a possible dating tool for the dykes sampled [*Griffiths*, 1983]. *Griffiths*, [1983] collected samples from a number of dykes outside the Valle del Bove and found he was able to divided them into groups on the base of their palaeo-polar positions, although dating them by this method was not possible. No rotation was found in these samples, but as they are from outside of the Valle del Bove this would be expected.

1.5.2. Global Positioning System:

The Global Positioning System (GPS) represents a method for the determination of accurate locations anywhere on the Earth by the use of satellites. If the position of the satellite is known, as well as the distance from each satellite to observer then the intersection of this distance sphere for three satellites gives the location of the observer. Three satellites are needed to solve for the three unknowns: latitude; longitude; elevation [*Hofmann-Wellenhof et al.*, 1993].

GPS has been used for two parts of this study: i) as a tool for locating gravity stations; ii) to set up a deformation network on the lower parts of the Valle del Bove.

As accurate station locations are needed for gravity data reduction, GPS has an advantage over traditional methods of locating oneself, in that, in a relatively quick time it gives latitude, longitude and elevation, often in places where maps are of limited use (e.g. the featureless Valle del Bove; see Chapter 4). In the case of the deformation network, a series of stations have been set up on the lower flanks of the Valle del Bove with the aim of investigating slope movement through time (Chapter 3). The network is centred on the town of Milo and includes Monte Fontane and Monte Pomiciaro.

A second, smaller, deformation network was set up on the island of Stromboli (figure 1.1) in order to study the response of the island to the continual input of magma due to the continuous activity on the island over the last 2000 years [*Francis et al.*, 1993]. Measurements of the surface response over time may help develop models for the replenishment of the island's magma system.

GPS is now commonly used in gravity surveys (e.g. *Balde et al.*, 1991; *Lin et al.*, 1992) , geoid determination, and in geodetic networks where it is coming to replace more traditional methods such has EDM. For ground deformation networks GPS offers the potential for much greater line lengths than EDM, with similar accuracy (e.g. *Nunnari and Puglisi*, 1994; *Nunnari and Puglisi*, 1995). GPS is now being used as a continuous recording method for volcano monitoring as well as repeat deformation surveys.

1.5.3. Gravity and Aeromagnetics:

A gravity survey can be used to map out subsurface density contrasts by measuring perturbations in the Earth's Gravitational field at the surface.

Gravity has been widely used as a tool for studying volcanoes (e.g. *Yokoyama,* 1974; *Williams and Finn* 1985; *Rymer and Brown,* 1986; *Hallinan,* 1991; *Hallinan,* 1993) as such bodies generally show large variations in subsurface density. Typically, basaltic volcanoes give positive anomalies associated with high density intrusive bodies, contrasting with younger near surface uncompacted material [*Rymer and Brown,* 1986]. The previous gravity studies of Mt. Etna [*Klerkx and Evrard,* 1970; *Loddo et al.,* 1989; *Neumann et al.,* 1985] show a large circular anomaly centred on the southern wall of the Valle del Bove. Seismic tomography shows this area to be a seismic velocity high [*Hirn et al.*, 1991] which has been interpreted as being caused by a high density body, possibly representing a magma feeder system for the ancient Trifoglietto centre.

Gravity data (298 new stations) and 3-dimensional modelling of the structures have been used to investigate the structure of the Valle del Bove and the influence this may have on the stability of the Eastern Flank.

An aeromagnetic survey was carried out in the summer of 1994, the data were collected and processed by C. Locke and J. Cassidy (Auckland University, New Zealand). The data were collected using a total field proton precession magnetometer, at an elevation of approximately 3300m. The volcano was covered by several flight lines, concentrating on the summit region and the Eastern Flank. These data are used in conjunction with the gravity data in the computer modelling.

1.5.4. Finite Element Modelling:

"The Finite Element Method is a computer-aided mathematical technique for obtaining approximate numerical solutions to the abstract equations of calculus that predict the response of physical systems subjected to external influences." [*Burnett*, 1987]

The above quote summarises the principle of the finite element method; in its most basic form this method offers a numerical approach by which general differential equations can be solved in an approximate manner, but, rather than looking for an approximation over the whole region, the region is divided into smaller parts - *finite elements*. It is over these small finite elements that the approximation is carried out [*Akin*, 1986; *Ottosen and Petersson*, 1992]. For this study finite element analysis is used in the determination of stress states within the volcanic edifice given a variety of scenarios.

Early work in this field typically used Mogi models or variations on them as a tool for investigating volcanic stresses (e.g. *Bianchi et al.*, 1987; *Dieterich and Decker*, 1975; *Mogi*, 1958; *Murray and Pullen*, 1984; *Paul et al.*, 1987) however these are inappropriate or at least incomplete for volcanic situations as they assume elastic and homogenous material as well as, often, spherical sources which are unlikely to occur in volcanic environments. Several recent studies have applied finite element programs to the study of volcanic phenomena with a large degree of success. *Paul et al.*, [1987] have retro-predicted the 1980 collapse and eruption of Mt. St. Helens by the use of finite element modelling, while [*Borgia*, 1994] has made extensive use of such modelling in the investigation of the growth of volcanic structures. The success of these models depends on the availability of reasonable physical properties for the material being studied, thus a good understanding of the volcano's geology and structure is needed. More commonly it has been applied to slope stability and other geotechnical problems (e.g. *Emery*, 1978).

All finite element work in this study has been carried out using ELCUT, a relatively simple program which only allows 2-dimensional static linear stress analysis to be carried out. ELCUT was downloaded from the Higher Education National Software Archive at Lancaster University and installed on an IBM-PC compatible computer (A. Pullen, pers. comm.). It is a very user-friendly system and therefore little familiarisation time is needed.

Both the pre- and post-processors are quick and simple to use, with post-processing allowing for a number of stress directions and deformation patterns to be viewed. The version used here is a demonstration version and is limited to 250 nodes or elements. As Elcut is 2-D, the calculations have been carried out assuming plain strain. In plain strain it is assumed that the body is infinite in the z (out of the page) direction and that the load is applied normal to this direction, also, the load does not vary in this direction. All cross sections are identical therefore any arbitrary x-y section can be used.

Chapter 2 Palaeomagnetic Data.

2.1. Introduction:

Palaeomagnetic samples have been collected for a limited number of dykes outcropping within the Valle del Bove, in order to look for possible rotation of the material, expected if the collapse of the Valle was by sliding. Numerous dykes are exposed throughout the walls of the Valle, with the best and most accessible exposures being on the Western and Southern walls. It is from these walls that the samples have been collected. Attempts were made to collect samples from further down the Valle around Monte Calanna, however all access routes to the Monte itself have been covered by the 1991-1993 flow, and no suitable sites were found elsewhere in this area. No samples were collected from the North wall of the Valle due to problems of access to this area and the lower number of outcropping dykes. However if the formation of the Valle del Bove was associated with rotational movement, material within all walls would be expected to show the effects, also more recent movement appears concentrated in the Southern and Central regions of the volcano, thus causing movements in the Southern and Western walls of the Valle. Again if this recent movement is rotational, it should be detectable with palaeomagnetism. The majority of dykes in the Valle have dips of greater than 75°. Modelling of modern dyking events suggests that most are emplaced vertically [*Murray and Pullen,* 1984; *Rymer et al.,* 1994], and assuming that this applies in the past, we can say that any rotation that has occurred must be limited, thus only a sufficient number of samples to test the hypothesis were collected. As previously published data for locations surrounding the Valle (figure 2.1) are available and give control samples for areas which are expected to be non-rotated, the number of samples collected is limited. Rotation about a horizontal axis will alter the declination of the samples, while rotation around a vertical axis will alter the inclination. Rotation leading to collapse is expected to show as occurring around both a vertical and horizontal axis.

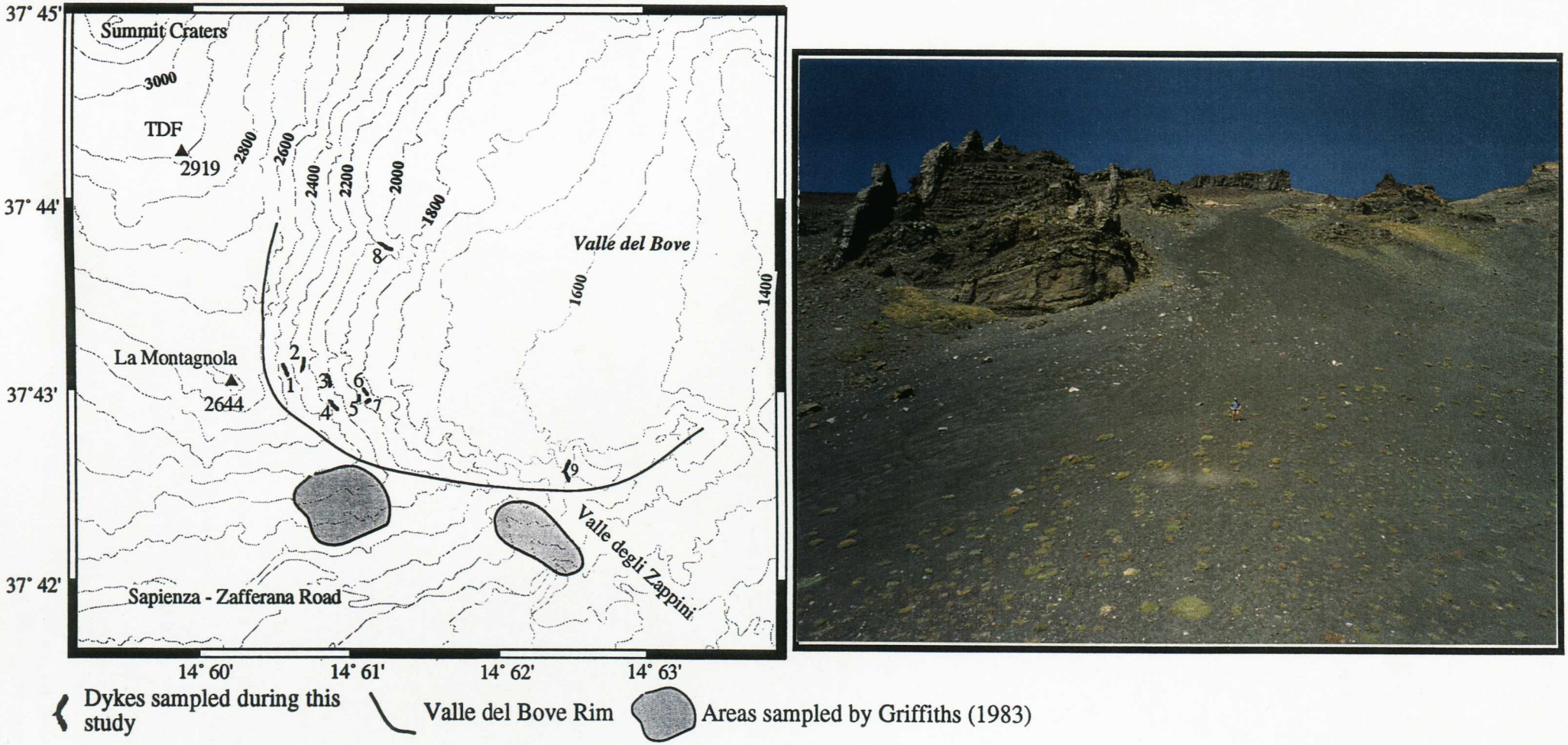

Figure 2.1. a. Location map for palaeomagnetic samples. Dyke numbers are as per table 2.1. Contours in metres **b.** Photo showing typical exposure of dykes on the Southewestern wall of the Valle del Bove. This photo was taken from the area of dykes 6 and 7.

2.2. Field Methods:

Cores were collected using a two-stroke chain saw engine modified to take 2.5cm drill bits, with a water feeding system for cooling (figure 2.2a). Drill bits were 15cm in length but full length cores were rarely collected due to fracturing of the rock. In heavily fractured dykes only one or two cores were collected (e.g. dyke 1), due to the fracture spacing causing the core to brake while still in the hole, this causes problems with orienting the samples, giving values of dubious quality. In such cases where the orientation data was poor samples were not analysed In several cases full length cores were collected and up to 7 cores taken from a single dyke (e.g. dyke 3). See table 2.1 for a full list of cores collected.

Within a dyke, sample sites were selected on the basis of ease of operations, with the only prerequisite being to try to collect cores from the full length of the outcrop.

Table 2.1. Dykes sampled and cores collected. For the location of each dyke see figure 2.1

DYKE	ORIENTATION (STRIKE / DIP)	NUMBER OF CORES	NUMBER OF SAMPLES ANALYSED
1	145°/90°	1	0
2	020°/90°	2	0
3	162°/88°E	7	3
4	137°/86°E	4	3
5	002°/85°E	3	2
6	154°/88°E	5	3
7	162°/85°E	2	2
8	107°/90°	4	3
9*	041°/82°SE	1	1
9*	015°/80°W	4	2

* Dyke 9, located at the top of the Valle degli Zappine, showed a change in strike along its length, therefore it was decided to sample from both sections.

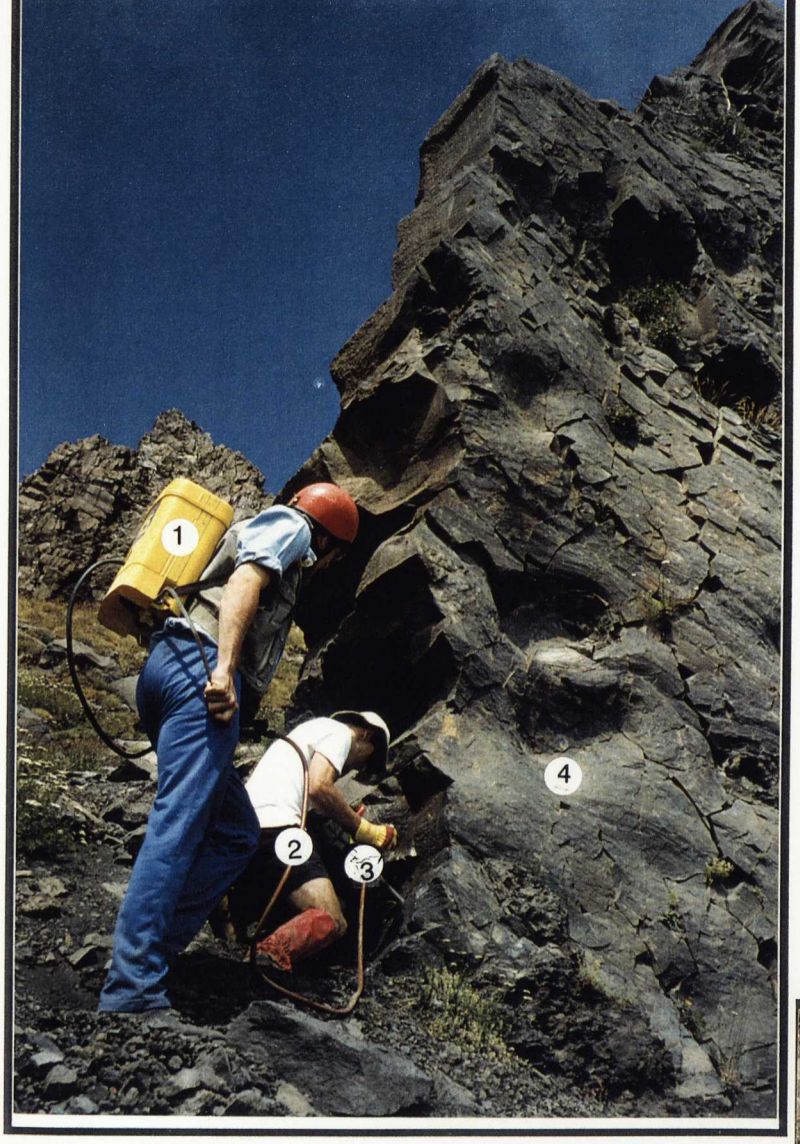

1 = Water tank

2 = Hose

3 = Drill

4 = Typical dyke

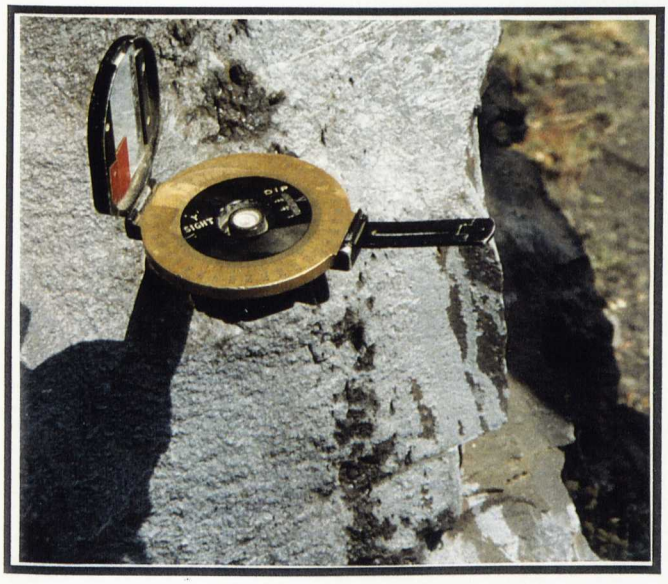

Figure 2.2 **a**. This photo shows the drill as used in the field. The bit is cooled by the use of a hand pumped water tank connected by the hose.
b. The sun compass, shown from two views: i) the top showing the mirror reflecting the sun onto the dial ready for a reading to be made of the Y-sight. The dip is read when the bubble in the centre shows the compass head to be level. ii) A side shot showing the compass held in the rock by the tube which is inserted over the core.

No samples from dyke 1 or 2 were analysed due to doubts over the quality of the orientation data.

The cores were oriented before removal from the hole (i.e. while still partly attached to the dyke) by the use of a sun compass (see figure 2.2b). The sun compass consists of a brass tube which fits over the core, attached to a circular plate with a spirit level. When this plate was level, a dip for the core was taken from the marker on the top. The orientation of the core relative to the sun was read from a graduated circle on the top of the plate by lining up the shadow reflected from the mirror, with the 0 on the plate and reading off the "Y-sight" at the indicated mark. A careful note of the time was taken in order that the azimuth measured from the sun could be converted into a direction east of true north. The direction of the sun, relative to the horizontal plane and geographic North at a site, may be calculated from the angle between the sun's direction and the equatorial plane, (the sun's declination), and the angle between the meridians containing the site and the sun, (the local hour angle). The declination and local hour angle for the samples in this work were calculated by a program available at the Geomagnetism Laboratory, Liverpool University. These are then used to convert the Y-sight into values East of True North (Y-ETN).

Once the orientation details had been recorded a brass wire was used to scratch a reference mark on the core using a groove in the top of the tube of the sun compass as a guide. Upon removal of the core from the hole this scratch mark was made permanent with a waterproof marker pen. This reference line is then used to establish a co-ordinate system for the core (figure 2.3)

2.3. Laboratory Methods:

2.3.1. Rock Magnetism:

The theory behind the palaeomagnetic method is outlined in Appendix C. The natural remanent magnetisation (NRM) is the permanent magnetism preserved in the rock, and is given by the resultant vector of the primary magnetisation, acquired when the rock formed, and the secondary magnetisation, acquired during subsequent geological time [*Piper,* 1987]. Several forms of primary and secondary magnetisation can occur in rocks, however within

the scope of this work only three are important (TRM, IRM and VRM) and these are outlined below.

The primary magnetisation of igneous rocks forms by the cooling of the rock from high temperatures through the blocking temperatures of the magnetic minerals (this is the thermoremanent magnetisation, TRM). The blocking temperature is the temperature at which the magnetisation becomes frozen into the mineral.

Secondary magnetisation may be produced when a rock is subjected to a local magnetic field. The magnetisation acquired will be defined by the hysteresis behaviour of the rock, and if the field is large enough a saturation magnetisation may be reached. This is the isothermal remanent magnetisation (IRM) and is the residual magnetisation left after an external field is applied to and then removed from a magnetic material. A large IRM over a local area will be produced by a lightning strike, which essentially represents a strong line current and creates a circular field about the point of impact. Such lightning-induced IRM in rocks are recognised by their large, unstable, low-coercivity magnetisations, confined to no more than a few square metres of outcrop. A time dependent IRM (a viscous remanent magnetisation, VRM) can be acquired by rocks exposed to the Earth's magnetic field for a period of time. VRM results from the thermal vibrations of the lattice, causing domain walls to shift slightly and irreversibly, resulting in the expansion of domains oriented close to the ambient field direction [*Piper*, 1987].

For the material sampled for this study the primary TRM is the main component of the NRM. This is clear from the insignificant change seen in the magnetisation directions for most samples following demagnetisation (see section 2.3.3). Thus secondary components such as IRM and VRM have only a small effect which varies from sample to sample.

2.3.2. Measuring the NRM:

19 samples in total were analysed from 7 dykes. Each core was cut into ca. 2.5cm lengths, producing a length/diameter ratio of approximately 1. Such a shape for the sample reduces the errors in the measurement procedure. The idealised situation is that of a uniformly magnetised sphere, such that its magnetisation can be represented by a simple dipole at its centre with a magnetic moment of:

$$\text{magnetic moment} = \frac{4}{3}\pi r^3 M$$

where M = volume magnetisation

r = sample radius [*Collinson*, 1983]

Such a sample would require only 2 readings for the determination of its NRM. As a sphere is not a practical sample shape, it is preferred to approximate it with any shape for which the external field departs as little as possible from that of a dipole of equivalent magnetic moment at the sample centre. An approximately equidimensional cylinder (a core with length to diameter ratio of 1) will approach such requirements [*Collinson*, 1983].

Analysis was carried out at the Geomagnetism Laboratory at Liverpool University, using a MINISPIN fluxgate magnetometer connected to a BBC computer (figure 2.4a). The MINISPIN measures two orthogonal horizontal components of magnetisation for a sample. Samples were measured in 6 orientations, for each of the 6 orientations used, 2 components are measured, thus 4 measurements (2 +ve, 2 -ve) of each of the axes of the core (X_c, Y_c, Z_c) are obtained. A standard sample was run for calibration at the beginning of each day.

As each sample is rotated in within the fluxgate, a DC output signal is produced, which is proportional to the component of the magnetic moment of the sample which is parallel to the principle axis of the fluxgate. By rotating the specimen at 6 Hz, a sinusoidal output signal of that frequency is obtained. The amplitude and phase of this signal provides a measure of the magnitude and direction of the horizontal component of magnetisation for the sample. For each revolution, 128 samples of the output signal are measured and stacked. Fourier analysis is used to obtain the amplitude and phase of the 1st harmonic, which is expressed as North and East components relative to the principle axis of the system. For N revolutions of the sample for each orientation, the signal-to-noise ratio (SNR) is improved by $\sqrt{N}$.

The use of the 6 orientations improves the SNR and reduces the effects of sample inhomogeneity. The declination and inclination of the sample is then calculated by converting between the core reference system (X_c, Y_c, Z_c) and the geographical system, using Y-ETN and the dip of the core.

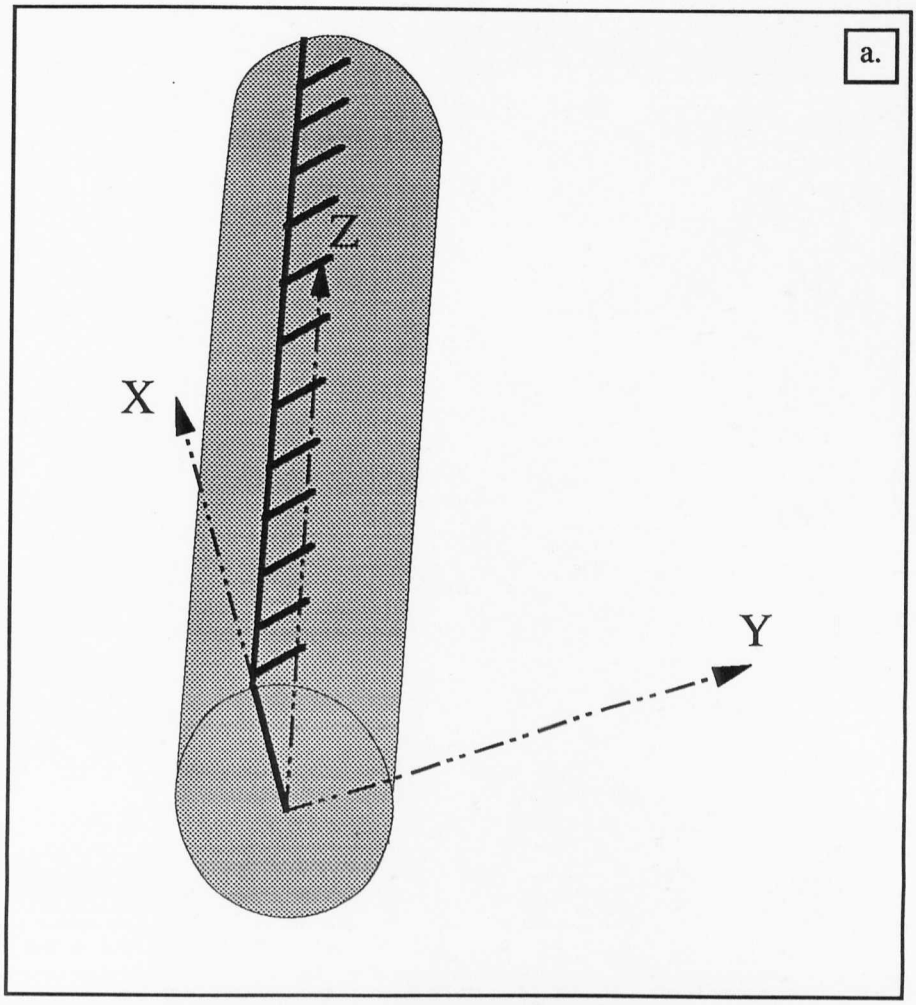

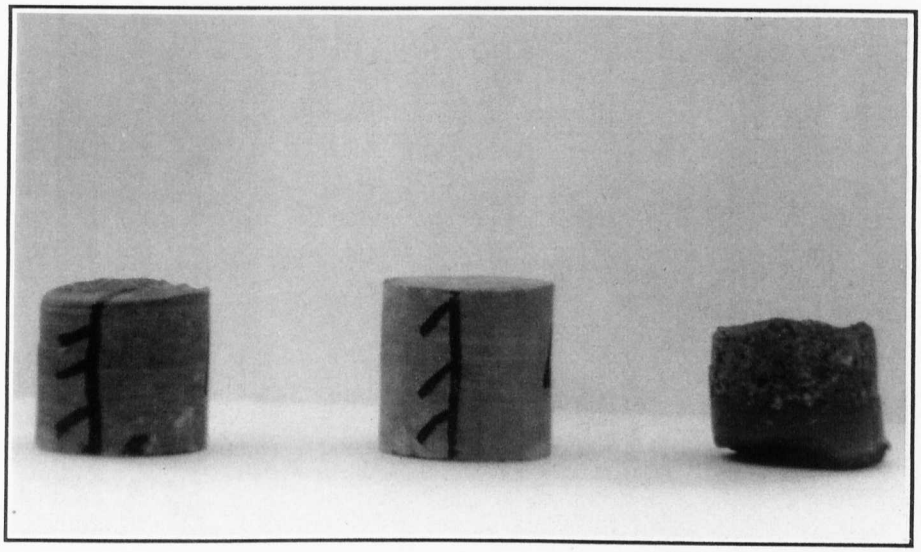

Figure 2.3. **a.** The coordinate system used in the orientation of cores. Dotted lines show the three axes along which measurements are made; the heavy solid lines represent the marks made on the core at the time of collection. Z is along the core into the rock; X and Y define the plane at right angles to the long axis of the core.
b. This photo shows one of the cores after being cut into the correct size for measurement. Each of the left hand samples are 2.5cm in height. The right hand sample shows the contact between the dyke (the base of the sample) and the wall rock.

2.3.3. Demagnetisation:

In order to more accurately determine the direction of the primary NRM, magnetic cleaning techniques are used. Such techniques rely on the secondary magnetisation having a lower stability than the primary. Secondary magnetisation is removed by the application of sufficient energy to overcome the magnetostatic energy of alignment within the affected magnetic domains, leaving them randomly oriented.

Alternating frequency (AF) demagnetisation was carried out at the Liverpool University Geomagnetism Laboratory for this work. In this method the demagnetisation is achieved by cycling the sample through hysteresis loops of progressively greater amplitude, corresponding to an applied peak (magnetic) field of H_{max}.

For single domain (SD) grains with a coercive force $H_c < H_{max}$, their magnetic moments will tend to "follow" the decreasing alternating peak field, H, until $H<H_c$. At this time the domain moments become locked in random directions within the rock. Multi-domain particles behave slightly differently from SD grains but the effect is similar: particles of certain coercive force will be effectively demagnetised or left with residual moments with random directions. These particles will then no longer contribute to the NRM of the rock due to effective self-cancelling in the random directions [*Collinson*, 1983].

Progressively increasing H_{max} leads to particles or domains of successively higher coercive force being randomised or demagnetised. Changes in the intensity and direction of the NRM allow remanences of differing stability to be distinguished [*Collinson*, 1983].

While removing secondary magnetisation effects, AF demagnetisation must avoid imparting any spurious magnetisation to the sample. Spurious magnetisation may result from either a direct magnetic field acting on the sample, (producing an anhysteretic magnetisation, ARM), or be an IRM resulting from non-sinusoidal effects of the AF waveform. Direct magnetic fields may arise from incomplete removal of the effects of the Earth's ambient field or harmonics within the AF waveform [*Collinson*, 1983; *Piper*, 1987]. The effect of the ambient field was removed by the use of a low-field coil surrounding the demagnetising coil and sample (figure 2.4b), which was used to cancel out the Earth's field at the start of each day and checked several times during the course of the day.

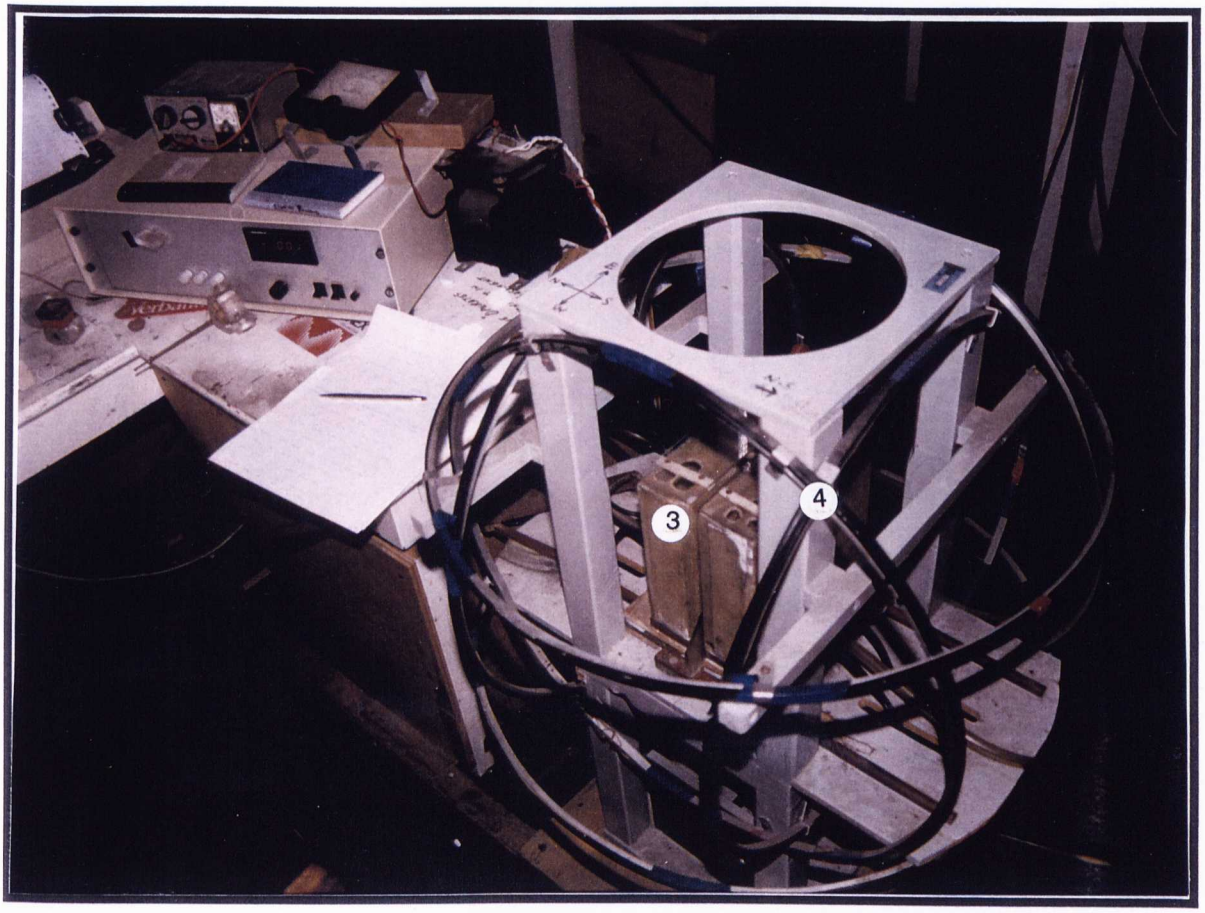

Figure 2.4 a. MINSPIN Fluxgate magnetometer (1) and computer (2) for measuring the NRM of the cores. **b.** Demagnetisation equipment. The sample sits within the centre of the coil (3), while the large outer-coil (4) is used to neutralise the Earth's magnetic field.

During demagnetisation the sample is continuously tumbled about 2 or 3 axes which results in:

❶ Reducing any possible ARM (due to randomising the direction);

❷ Allow the demagnetising field to act along as many axes as possible, i.e. if θ is the angle between the magnetisation direction and the applied demagnetising field, then all grains with magnetisation less than $H_{max}\ \theta$ will be demagnetised, i.e. $H_c < H_{max}\ \theta$.

Each sample was progressively demagnetised, using steps of 100 gauss (10 gauss = 1 milliTesla), from 0 to 1000 gauss. The results are displayed on the computer screen for each step, thus giving an indication of the quality of the data, i.e. how much secondary magnetisation was present.

2.4. Demagnetisation Results:

The resultant declinations and inclinations obtained after demagnetisation were plotted on orthogonal plots and a final direction for the magnetisation vector was determined, together with a measure of the spread of the data (the Maximum Angular Deviation, M.A.D.). The M.A.D. is a measure of the precision of the best vector fit (the best fit values for declination and inclination). The closer the M.A.D. is to 1.0, the better the fit of the vector. The M.A.D. reflects the amount of secondary magnetisation affecting the sample, thus for samples such as 803A and 904C, the value of M.A.D. are high (17 and 8 respectively, figure 2.5), where as, in general most of the samples show values in the region of 1-4, thus indicating very little to no secondary magnetisation. Figure 2.5 shows the plots for all samples.

Orthogonal (or Zijderveld) plots are obtained by projecting the NRM vector onto two orthogonal planes, one horizontal and one vertical [*Piper,* 1987]. Such plots allow the illustration of both magnitude and direction for the sample. This is done by considering the data in terms of the three axes x (referred to as North), y (East) and z (vertically downward). A vector of magnitude J is then the resultant of three orthogonal components :

$$x = J\cos D\cos I$$

$$y = J\sin D\cos I$$

$$z = J\sin I$$

Where D = Declination,

I = Inclination.

Thus, as the rock is progressively demagnetised, these projections will trace out paths defined by the collective changes in D, I and J. If the NRM vector comprises only a single component, its magnitude will be progressively reduced by demagnetisation, but its direction will remain the same. Therefore the projections on the orthogonal plot will migrate along two straight lines toward the origin (e.g. the plots for 401A, 501A, 903C). If the magnetisation is multicomponent then the demagnetisation path will again trace out a straight line, but will not go through the origin. Many of the plots of figure 2.5 show paths which change direction as they are demagnetised, this shows that various components of the NRM are being removed (e.g. 301A, 803A, 904C). In most cases this secondary magnetisation is removed within one or two steps of the demagnetisation, although some samples do show a more convoluted path.

Several of the plots of figure 2.5 are shown with the first one or two demagnetisation steps removed. This is done for plots where the initial steps show an obvious secondary magnetisation (e.g. 803A) which causes an error in the estimation of the mean vector and an over estimation of the M.A.D. In the case of both 803A and 804A the secondary magnetisation seen in the initial stages of demagnetisation appears to be an IRM induced by a lightning strike. These samples were collected from a very prominent dyke on the Western wall of the Valle, an area prone to lightning strikes. As can be seen in the case of 803A, ignoring this low intensity IRM improves the M.A.D. considerably. Sample 605A shows a direction approximately 180° from all the other samples, this was determined to be due to an error in the placing of the sample in the spinner magnetometer, i.e. the sample was placed into the magnetometer upside down, and therefore this sample has been removed from the data set for the purpose of analysis.

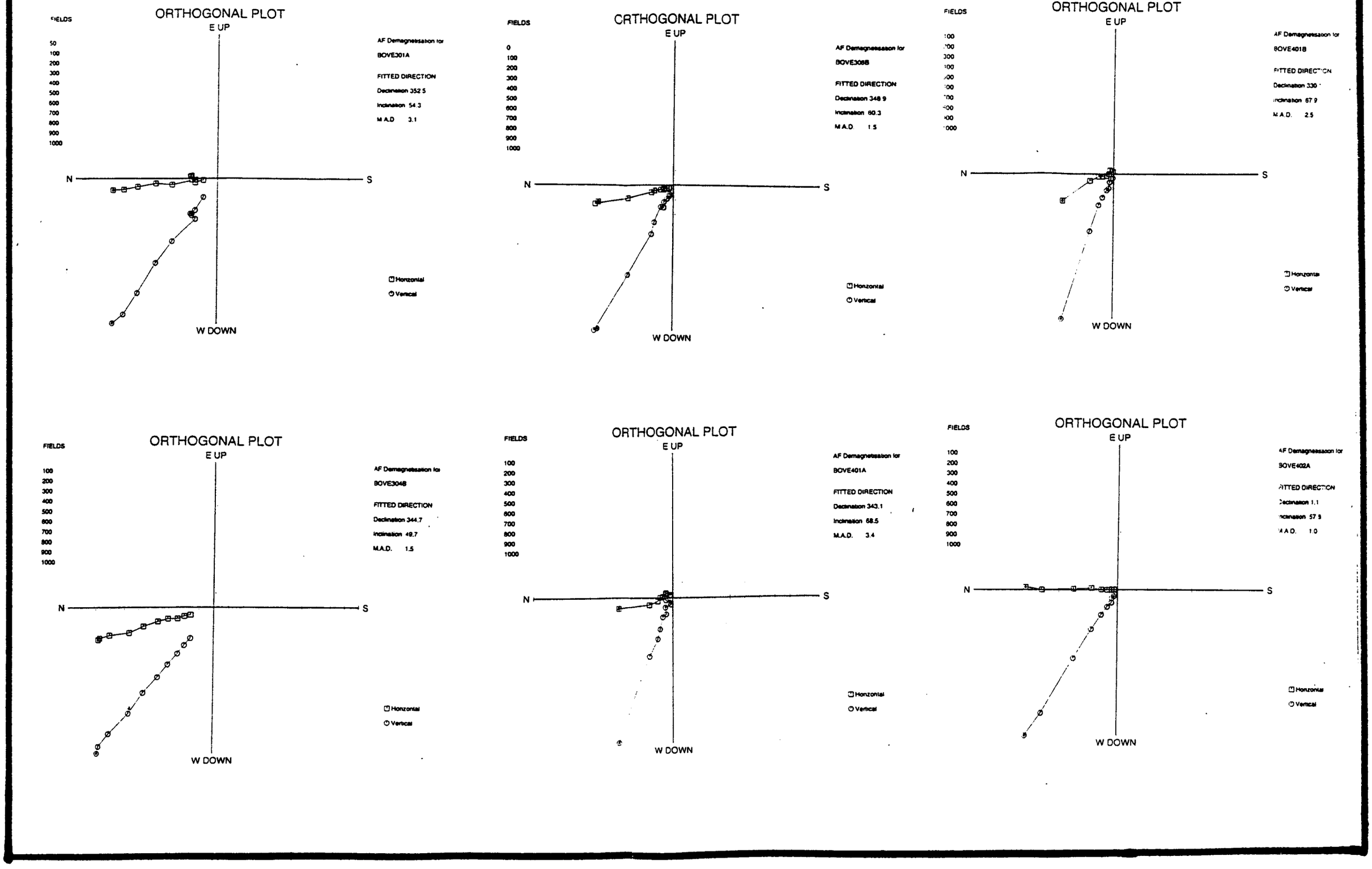

Figure 2.5. Orthogonal (or Zijderveld) plots for all samples analysed. Each plot represents the demagnetisation path of a single sample. The demagnetisation steps are shown on the left and the best fit directions on the right, for each plot. Samples numbers are given as BOVExxxL, where the first number represents the dyke the sample came from, the next two numbers represent the number of the core from that dyke and the letter represents where in the full length core the individual cylinder is from, e.g. BOVE301A = dyke 3, core 01, cylinder A, i.e. the first cylinder cut from the core.

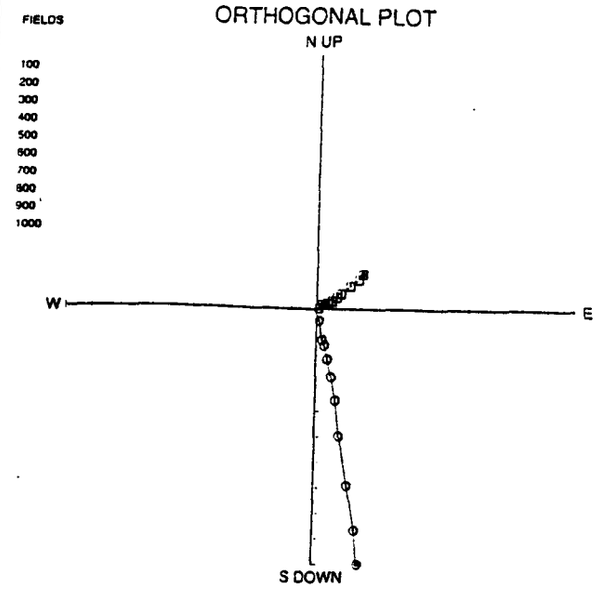

AF Demagnetisation for
BOVE501A

FITTED DIRECTION
Declination 53.0
Inclination 77.1
M.A.D. 1.0

Horizontal
Vertical

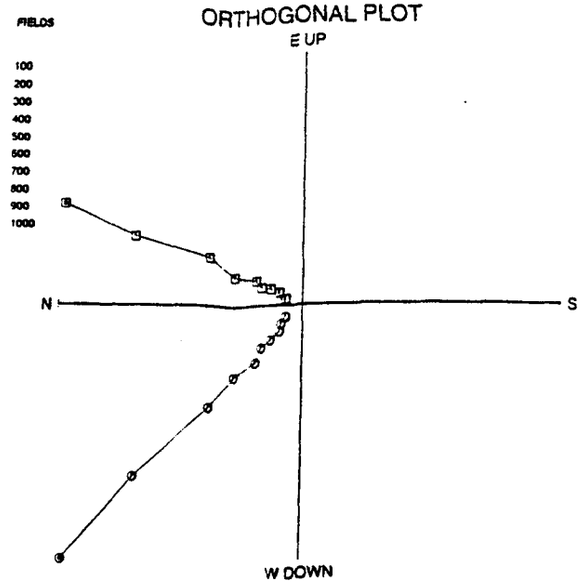

AF Demagnetisation for
BOVE504D

FITTED DIRECTION
Declination 22.0
Inclination 43.3
M.A.D. 2.1

Horizontal
Vertical

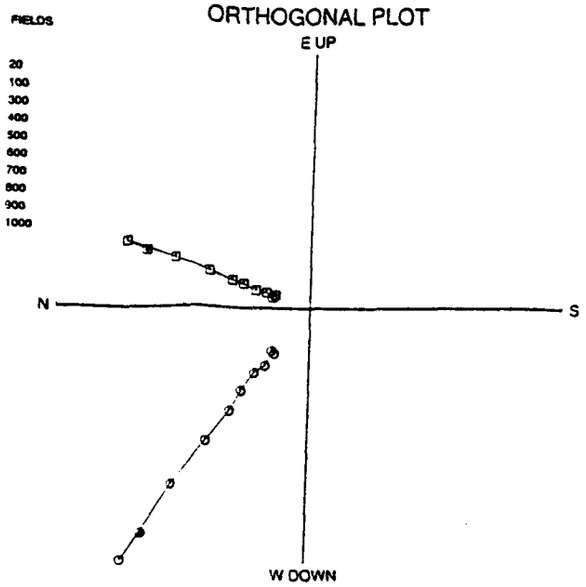

AF Demagnetisation for
BOVE702A

FITTED DIRECTION
Declination 19.7
Inclination 52.9
M.A.D. 1.5

Horizontal
Vertical

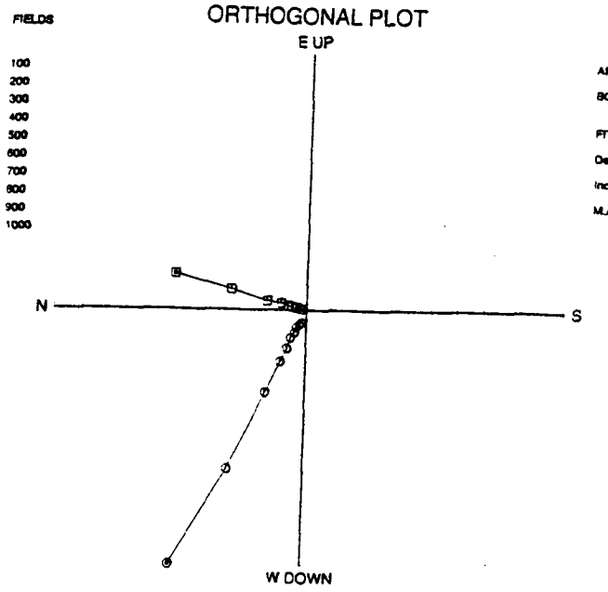

AF Demagnetisation for
BOVE502C

FITTED DIRECTION
Declination 14.8
Inclination 61.5
M.A.D. 1.2

Horizontal
Vertical

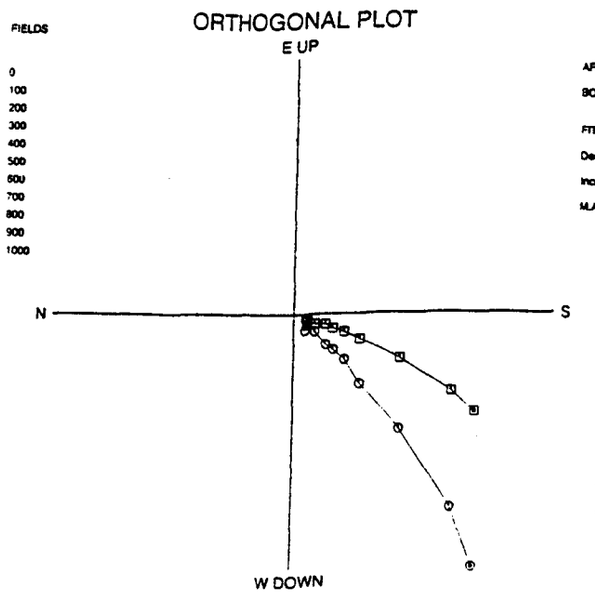

AF Demagnetisation for
BOVE505A

FITTED DIRECTION
Declination 208.9
Inclination 50.9
M.A.D. 3.5

Horizontal
Vertical

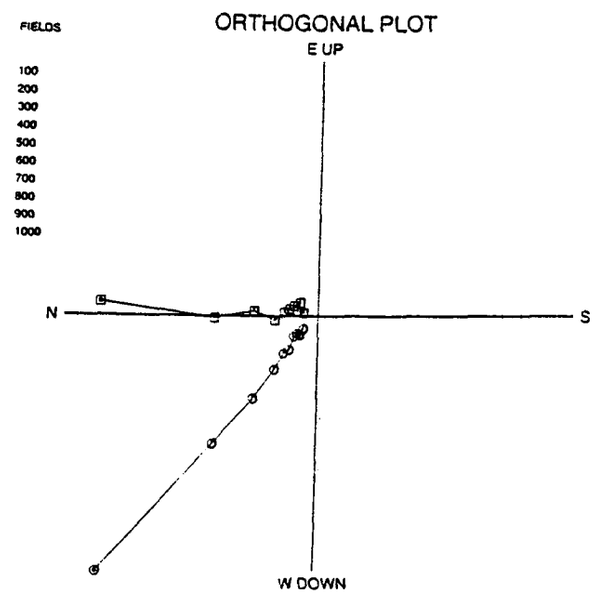

AF Demagnetisation for
BOVE802A

FITTED DIRECTION
Declination 1.1
Inclination 50.1
M.A.D. 3.7

Horizontal
Vertical

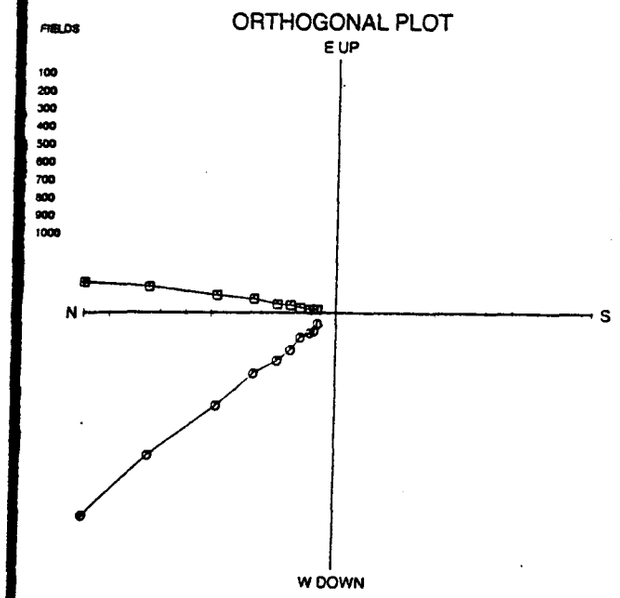

AF Demagnetisation for
BOVE601A

FITTED DIRECTION
Declination 7.1
Inclination 38.1
M.A.D. 1.6

Horizontal
Vertical

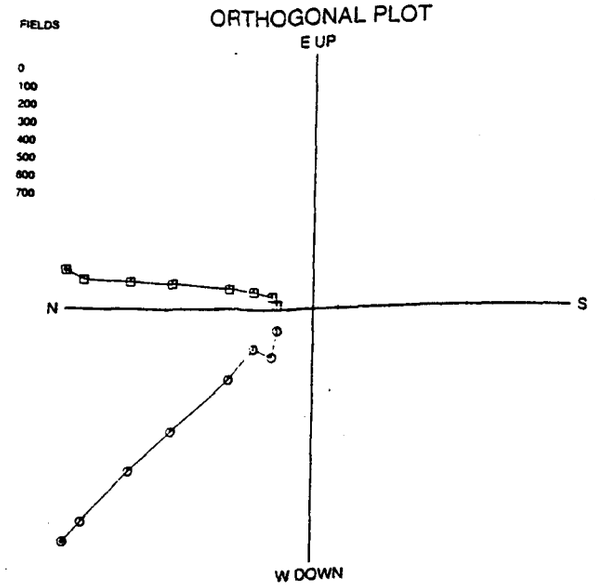

AF Demagnetisation for
BOVE701B

FITTED DIRECTION
Declination 6.6
Inclination 43.1
M.A.D. 3.4

Horizontal
Vertical

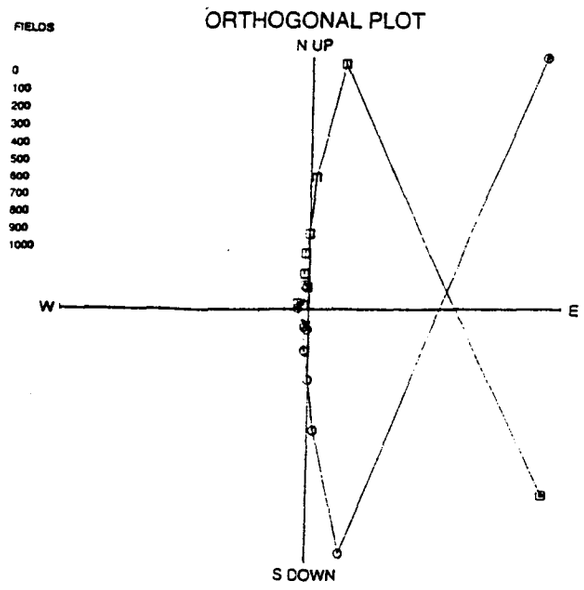

AF Demagnetisation for
BOVE803A

FITTED DIRECTION
Declination 152.5
Inclination -45.5
M.A.D. 17.8

Horizontal
Vertical

ORTHOGONAL PLOT

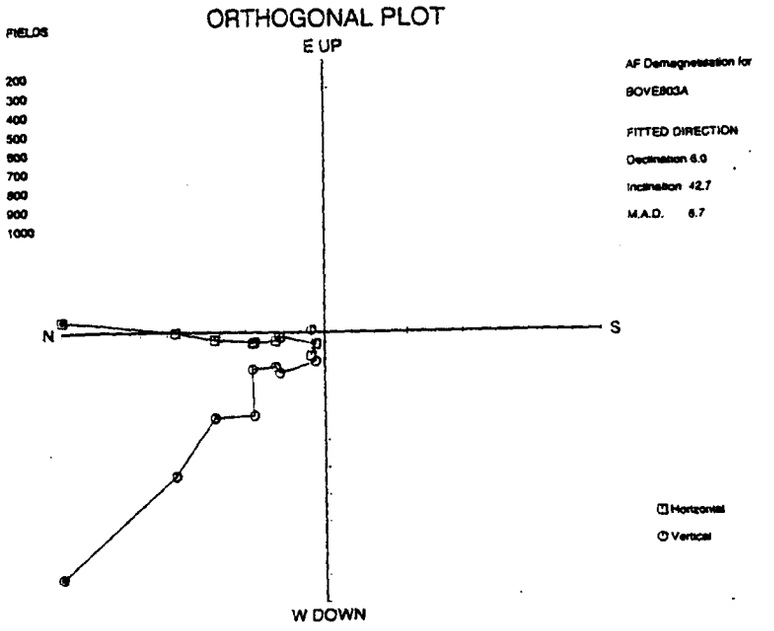

ORTHOGONAL PLOT

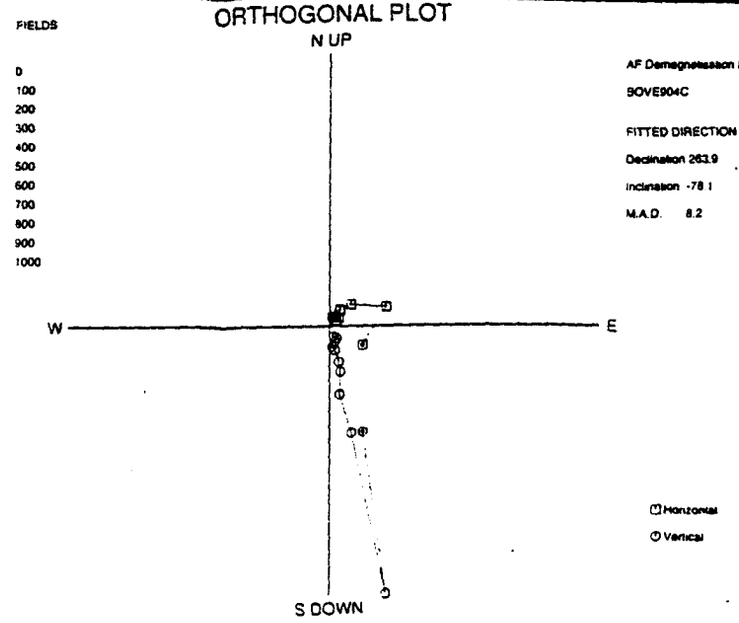

ORTHOGONAL PLOT

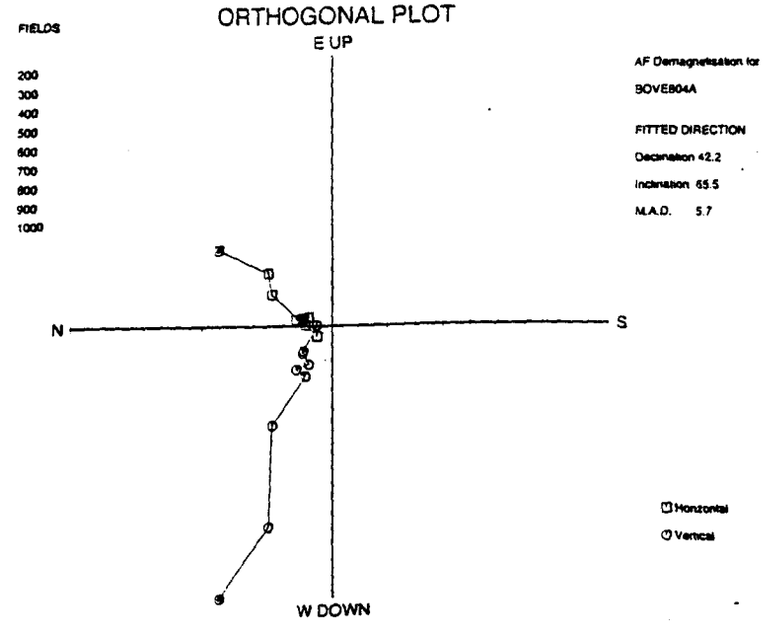

ORTHOGONAL PLOT

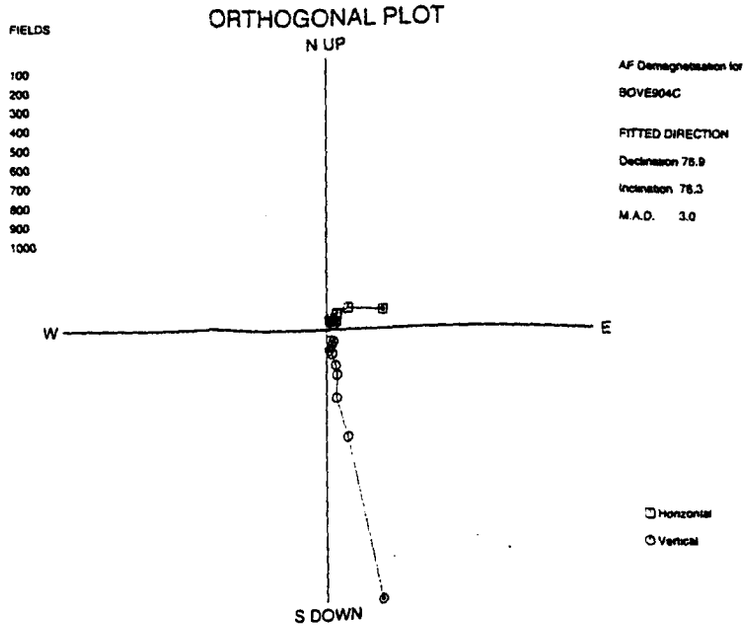

ORTHOGONAL PLOT

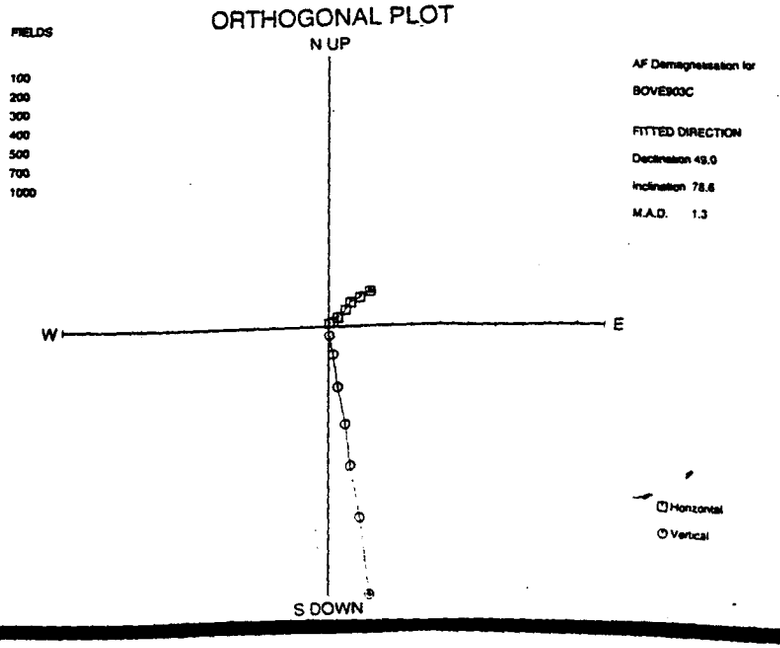

ORTHOGONAL PLOT

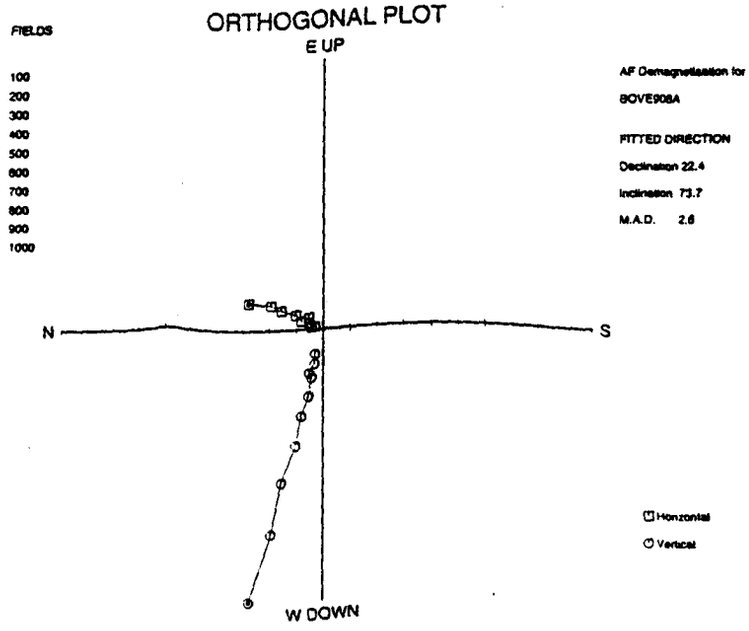

Table 2.2. Declination and Inclination for each sample.

SAMPLE	DECLINATION	INCLINATION	M.A.D.
301A	352.5	54.3	3.1
304B	344.7	49.7	1.5
306B	348.2	60.2	1.5
401A	343.1	68.5	3.4
401B	330.1	67.9	2.5
402A	1.1	57.8	1.0
501A	53	77.1	1.0
502C	14.8	61.5	1.2
601A	8	36.9	1.6
604D	22.1	42.6	2.1
605A	208.9	50.9	3.5
701B	6.6	43.1	3.4
702A	19.7	52.9	1.5
802A	1.1	50.1	3.7
803A	6	42.7	17.8/6.7*
804A	42.2	65.5	5.7
903C	43.1	77.2	1.3
904C	41	74.9	8.2/3.0*
906A	26.8	64.7	2.6

* Two values for the M.A.D. are obtained when plots are made using, first, all demagnetisation steps and second, ignoring the first 1 or 2 steps. Where two values are given for the M.A.D. the second value relates to the given declination and inclination.

The magnetisation vectors of table 2.2 have been plotted on a stereo plot (figure 2.6) to show better their relationship with each other. A mean vector for the whole data set has also been plotted. This vector has been calculated using Fisher statistics, which define the distribution of points on a sphere. An individual direction may be expressed in terms of its directional cosines l, m, n, where:

$$l = \text{cosD cosI}$$

$$m = \text{sinD cosI}$$

$$n = \text{sinI}$$

where D and I are the declination and inclination of the direction [*Collinson*, 1983].

The mean declination and inclination are then given by:

$$\tan D_m = \frac{\sum_{i=1}^{N} m_i}{\sum_{i=1}^{N} l_i}$$

$$\sin I_m = \frac{\sum_{i=1}^{N} n_i}{R}$$

where $R = \sqrt{(\sum l_i)^2+(\sum m_i)^2+(\sum n_i)^2}$

Fisher, [1953] has described a probability distribution for points on a sphere of the form:

$$P = \frac{\kappa}{4\sinh\kappa} \exp(\kappa \cos\psi) \sin\psi \; d\psi$$

where ψ is the angle between the true mean direction and one of the N vectors and κ is the precision parameter (a measure of the scatter of the vectors).

The best estimate, k, of the precision parameter κ is:

$$k = \frac{(N-1)}{(N-R)}$$

The higher the value of k the more tightly grouped the data set. $\kappa = 0$ ($k \rightarrow 1$) implies a random group [*Fisher*, 1953].

A measure of the accuracy of the mean direction can be expressed as the semi-angle, α, of a cone about the observed mean, within which the true mean lies, with probability (1-P).

$$\cos \alpha_{(1-P)} = 1 - \frac{N-R}{R}\left[\left(\frac{1}{P}\right)^{\frac{1}{N-1}} - 1\right]$$

(for $k > 3$).

For P=0.05, this means that there is a 95% probability that the observed mean is within α° of the true mean [*Collinson,* 1983].

The data of table 2.2 and figure 2.6a show a mean vector of : declination = 7.7°; inclination = 60°; $\alpha_{95} = \pm 6.7^{\circ}$. These numbers lie within the range described by the secular variation of the area (T. Rolph, pers. comm. 1994; [*Rolph and Shaw,* 1986]), thus suggesting that no rotation of these dykes has occurred. For this area the secular variation pattern is approximately: declination = 0°±20°; inclination = 55°±10°. In order to better test this, previously published data from an area believed unlikely to show any rotation [*Griffiths*, 1983] was included (figure 2.6b; figure 2.1 shows approximate location sites for this data) and the mean for the total data set calculated. The results are: declination = 4°; inclination = 59°; $\alpha_{95} = \pm 3.6^{\circ}$. Again these results are clearly within the region described by secular variation. Also of note is the way the data set of this study plots within the spread of *Griffiths*, [1983] data.

2.5. Summary and Conclusions:

The present day magnetic field at Mount Etna has a declination of 0° and an inclination of 55°. The mean values calculated from both data sets (this work and *Griffiths*, 1983) show no significant variation from this value, and are clearly contained within the range of values due to secular variation. As we do not know the paleopolar position to any better than the secular variation (±20°, declination; ±10°, inclination) we are limited in our interpretation.

Figure 2.6a shows a much tighter grouping of data than 2.6b. This is due to the smaller number of samples used and the narrower age range of the samples. All samples collected as part of this study are post-Trifoglietto in age (pers. comm. M.Wright, 1993), excluding dyke 9, which appears to be older, while a large proportion of dykes sampled by *Griffiths* [1983] are likely to be Trifoglietto or older (based on location and orientation). Therefore there is possibly an age gap of up to 10 000 years between the two sample groups. Such a large time span would cause the increased spread seen in the data.

As the dykes and flows sampled by *Griffiths*, [1983] are located outside the Valle del Bove, they should represent the control samples, i.e. it is reasonable to expect that dykes in

this area would not have undergone rotation during failure of the Valle del Bove area. Therefore, as all samples plot together and lie close to the present day field values, given the assumption that the secular variation is approximately symmetrical about a mean value of 0° / 55°, it is concluded that the dykes of the Valle del Bove have not undergone rotation, either vertical or horizontal. However this does not preclude the possibility of significant translation movement. Pure translational movement, or translation with a small amount of rotation would not be detectable by palaeomagnetism, thus we can discount the possibility that failure of the upper flanks of the Valle del Bove has occurred by large scale rock slides, but rock topples and possibly small scale slides are possible. From this it is possible to say that oversteepening of the walls of the Valle appears to have been the main cause of failure since the formation of the dykes sampled, i.e. within the last approximately 20 000 years. The present exposures of dykes resultis from the retreat of the Valle del Bove walls.

It is difficult, given the uncertainties, to be sure that no rotation has occurred during the formation of the Valle del Bove. It is likely that individual collapses would undergo rotation, giving the scalloped shape of the resultant valleys. The Valle walls rest at angles of between 20° and 30° at present, however this is only the apparent angle, the true slope may be steeper but is masked by scree and post-failure volcanic deposits. Given this situation, maximum angles of rotation are likely to be within the 20° to 30° range, which is at the limit of detection within this work. The results of this study suggest that any rotation that has occurred is not deep seated and that the movement of the upper sections of the Eastern Flank as a whole, occurs by translational rather than rotational means.

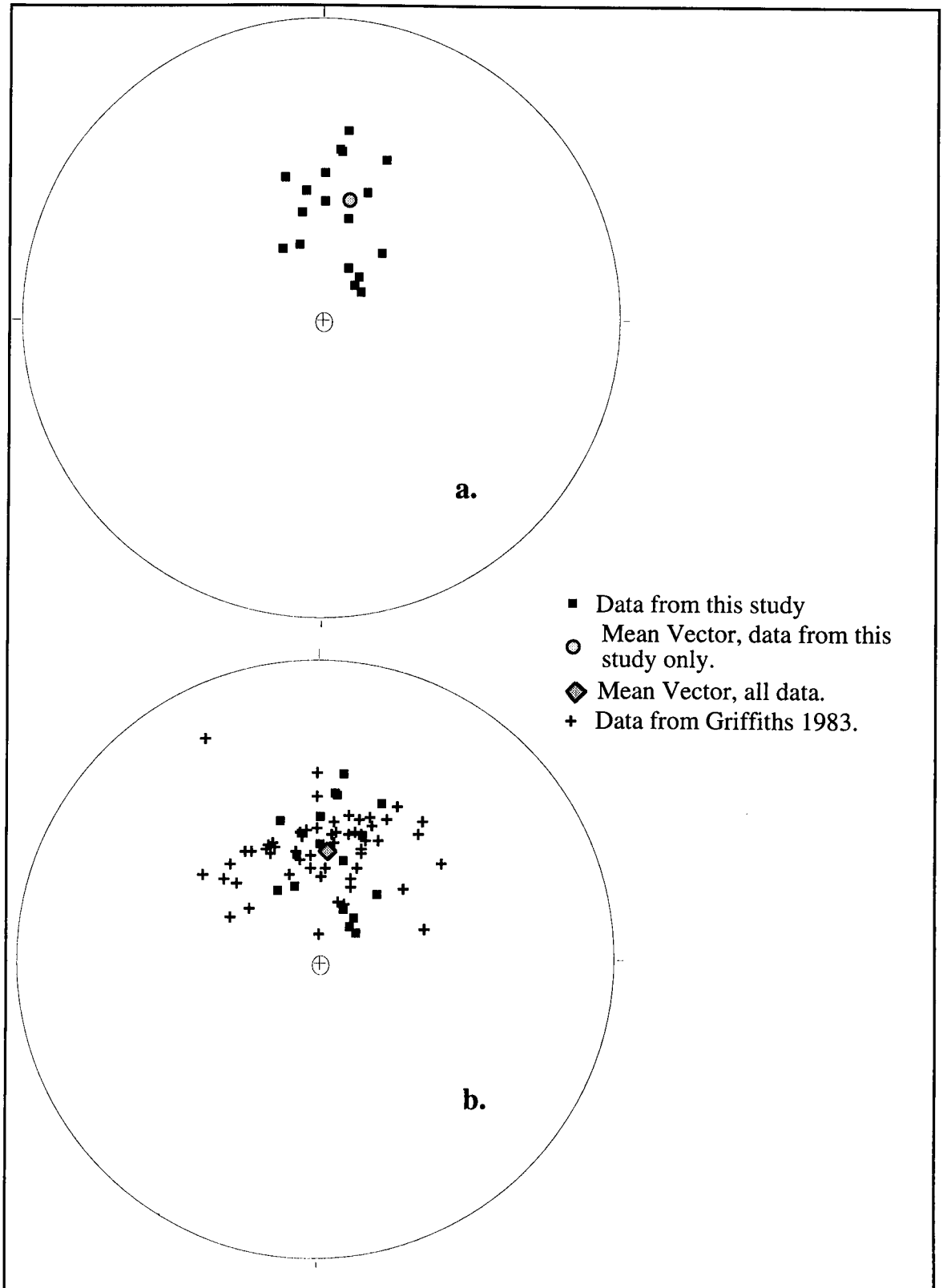

Figure 2.6. Stereoplots of palaeomagnetic data.
a. Data collected as part of this study, with mean vector.
b. Data from this study together with data from Griffiths (1983) with mean vector for all data.

Chapter 3 The Global Positioning System Technique

3.1. How it Works:

PS uses a constellation of 21+3 satellites, i.e. 21 "working" satellites plus 3 spare, in orbits such that at any time, 4 satellites should be visible from anywhere on the globe. The satellites are in nearly circular orbits at a distance of 20 200 km and a period of 12 sidereal hours. These 24 satellites are deployed in six orbital planes, 4 satellites per plane, inclined at 55° [*Hofmann-Wellenhof et al.*, 1993]. If the range from the satellite to the centre of the Earth (ρ^S) and the range from the GPS receiver to the satellite (ρ) are known, then the range from the receiver to the centre of the Earth (and hence its location) can be determined (figure 3.1).

3.1.1. Finding yourself:

The co-ordinates, in space (ρ^S), relative to the centre of the Earth, for each satellite can be determined from the ephemerides broadcast by the satellite. An observer, anywhere on the globe, using a receiver with a clock set precisely to GPS system time, can determine the true distance or range to the satellite from the time taken for a signal to travel from the satellite to the receiver. For each satellite the range will define a sphere, centred on the satellite, thus ranges to 3 satellites would be required to solve for the 3 unknowns (latitude, longitude, elevation). The intersection of the three spheres gives the location of the receiver [*Hofmann-Wellenhof et al.*, 1993].

Standard GPS receivers use simple crystal clocks, thus introducing a time error and this in turn will cause the range to the satellite to be either shorter or longer than the true range; such a range is referred to as the pseudo-range (R). The pseudo-range equals the true range (ρ) plus (or minus) an extra amount ($\Delta\rho$) due to the clock error (or bias), δ.

$$R = \rho + \Delta\rho = \rho + c\delta$$

where c = velocity of light.

The clock error means that in order to determine positions on the Earth's surface four range spheres are required to solve for the four unknowns; the 3 positional components and the clock bias [*Hofmann-Wellenhof et al.*, 1993]. So in order to calculate accurate positions, 4 satellites are required.

Given a single receiver the accuracy of measured locations are dependent on:

- ☞ Accurate knowledge of the position of each satellite;
- ☞ Accuracy of pseudo-range measurements;
- ☞ Geometry of the satellite constellation.

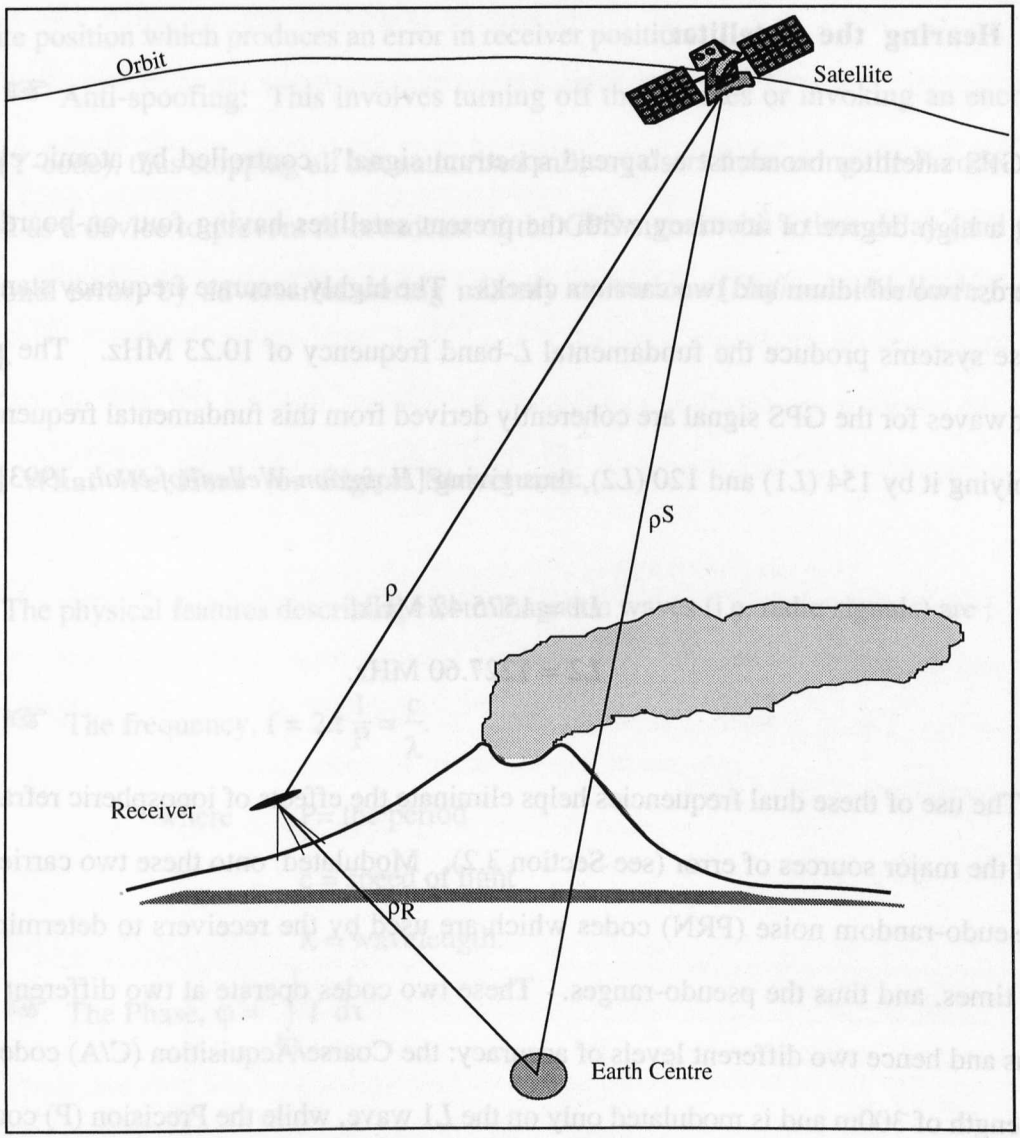

Figure 3.1. Satellite-Receiver geometry for GPS.
ρ^S = Satellite - Earth Centre distance;
ρ_R = Receiver - Earth Centre distance;
ρ = Range for Receiver-Satellite

Effects due to the first two points can be over come by the use of two receivers and differencing the pseudo-ranges for a given satellite to each receiver. Geometric effects cannot be overcome by differencing, therefore consideration of the constellation geometry is necessary. The satellite geometry is measured with respect to the observing site by a factor known as the Geometric Dilution of Precision (GDOP; the lower the value of the GDOP the better the satellite geometry). If we consider a body formed by the interaction of the site-satellite vectors with the unit sphere centred at the observing site, then the larger the volume of this body, the better the satellite geometry and the smaller the GDOP [*Hofmann-Wellenhof et al.*, 1993].

3.1.2. Hearing the Satellite:

GPS satellites broadcast a "spread spectrum signal", controlled by atomic clocks, giving a high degree of accuracy, with the present satellites having four on-board time standards: two rubidium and two caesium clocks. The highly accurate frequency standards of these systems produce the fundamental *L*-band frequency of 10.23 MHz. The actual carrier waves for the GPS signal are coherently derived from this fundamental frequency by multiplying it by 154 (*L*1) and 120 (*L*2), thus giving [*Hofmann-Wellenhof et al.*, 1993]:

$$L1 = 1575.42 \text{ MHz};$$
$$L2 = 1227.60 \text{ MHz}.$$

The use of these dual frequencies helps eliminate the effects of ionospheric refraction, one of the major sources of error (see Section 3.2). Modulated onto these two carriers are two pseudo-random noise (PRN) codes which are used by the receivers to determine the travel times, and thus the pseudo-ranges. These two codes operate at two different wave lengths and hence two different levels of accuracy: the Coarse/Acquisition (C/A) code has a wavelength of 300m and is modulated only on the *L*1 wave, while the Precision (P) code has a wavelength of 30m and is modulated on both the *L*1 and *L*2 waves. As GPS has been developed by the US. military the C/A code is the one reserved for civilian use, while the P-code is for military use. However while the system is still being developed P-codes are

available for all users. As well as these codes several data messages are also modulated onto the carrier waves (the navigation messages): satellite ephemerides, ionospheric modelling coefficients, status information, system time and satellite clock bias, and drift information [*Hofmann-Wellenhof et al.*, 1993]. The US. Government also adds two other features to deny full civilian use of the system, these are:

☞ Selective availability: This is a form of accuracy denial resulting from "dithering" the satellite clock frequency so as to prevent accurate instantaneous pseudo-ranges being determined. This only affects single receiver systems, differential (two-receiver) systems largely eliminate this error [*Hofmann-Wellenhof et al.*, 1993]. A second method of degrading the accuracy is to truncate the navigation messages, thus giving an error in the satellite position which produces an error in receiver position.

☞ Anti-spoofing: This involves turning off the P-codes or invoking an encrypted code (Y-code), thus stopping all but authorised military users from using the P-code. This is used as a device to prevent re-broadcast of the GPS signal with a time delay (and thus a positional error) by adversaries during military operations [*Hofmann-Wellenhof et al.*, 1993].

3.1.3. What We Hear (or Signal Structure):

The physical features describing electromagnetic waves (i.e. radio signals) are :

☞ The frequency, $f = 2\pi \frac{1}{P} = \frac{c}{\lambda}$.

where P= the period

c = speed of light

λ = wavelength.

☞ The Phase, $\varphi = \int_{t_0}^{t} f \, dt$

Therefore, taking a signal with constant frequency, and an initial phase $\varphi(t_0) = 0$, travelling over a distance, ρ, the phase equation for the signal arriving at the receiving site is:

$$\varphi = f(t-t_\rho) = f(t - \frac{\rho}{c}).$$

where t_ρ = time taken for the signal to propagate over the distance ρ.

As the GPS satellites are orbiting with a mean (radial) velocity of approximately 3.9km s^{-1} [*Hofmann-Wellenhof et al.*, 1993] the Doppler effect must be taken into account. However, with respect to a stationary terrestrial observer, there is zero radial velocity at the point of closest approach, and therefore no Doppler shift in frequency, while maximum Doppler shift occurs as the satellite crosses the horizon. For the *L*1 frequency of approximately 1.5 GHz, the Doppler shift is 4.5×10^3 Hz, and thus a phase change of 4.5 cycles occurs after 1 millisecond, corresponding to a range error of 90cm [*Hofmann-Wellenhof et al.*, 1993]. The effect of this is taken into account by the receiver software.

The fundamental frequency, f_0, is derived from the onboard atomic clocks, and the carrier wave frequencies, *L*1 and *L*2, represent multiples of f_0. Modulated onto these carrier waves are the codes giving the navigation messages and the satellite clock readings. These codes are formed by combining a sequence of +1 or -1, representing the binary values 0 or 1, with the carrier wave, resulting in a biphase modulation, due to a 180° shift in the phase of the carrier wave at each change in state (see figure 3.2) [*Hofmann-Wellenhof et al.*, 1993].

Table 3.1 gives a summary of the signal components and their frequencies. The two codes used to transmit the satellite clock readings have the frequencies of: C/A code = $f_0/10$; P-code = f_0. The C/A code is repeated every millisecond, while the P-code is repeated approximately every 266.4 days.

Table 3.1. Components of the satellite signal (after *Hofmann-Wellenhof et al.*, 1993)

Component		Frequency (MHz)
Fundamental Frequency	f_0	10.23
Carrier, *L*1	$154f_0$	1575.42
Carrier, *L*2	$120f_0$	1227.60
P-Code	f_0	10.23
C/A-Code	$f_0/10$	1.023
Navigation message	$f_0/204600$	50Hz

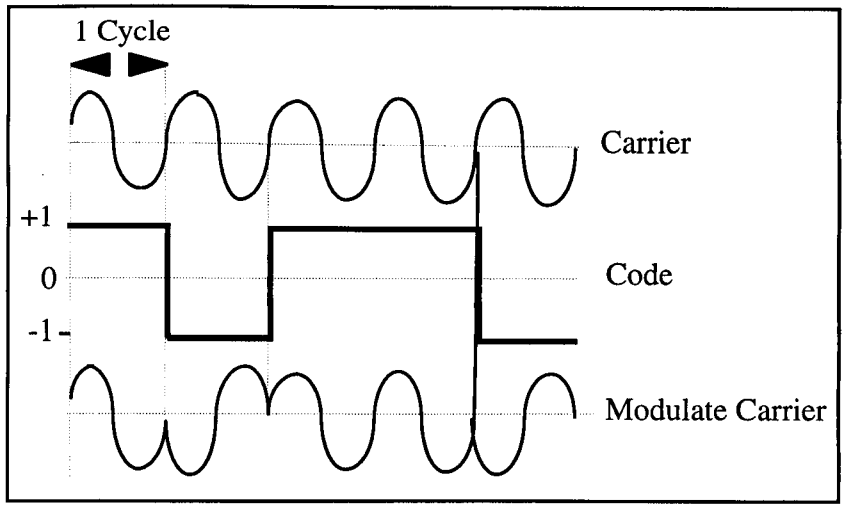

Figure 3.2. Biphase modulation of carrier wave (after *Hofmann-Wellenhof et al.* 1993).

Given the wave equation for the unmodulated wave as:

$$Li(t) = a_i \cos(f_i t),$$

then the modulated carriers can be denoted by :

$$L1 = a_1 P(t)D(t) \cos(f_1 t) + a_1 C/A(t)D(t) \sin(f_1 t)$$

$$L2 = a_2 P(t)D(t) \cos(f_2 t)$$

where, P(t) = state sequence of the P-code

D(t) = state sequence of the navigation message

C/A(t) = state sequence of the C/A-code.

3.1.4. The Calculations:

There are two ways of calculating the pseudo-range between the satellite and the receiver, either from time or phase differences, both based on comparison between received signals and receiver generated signals.

The simplest way of determining the pseudo-range is using the transit time for the signal from the satellite to receiver (code pseudo-range). This transit time can be measured by correlating identical PRN (pseudo-random noise) codes generated by the satellite and receiver. The receiver creates a replica of the PRN codes and shifts it in time until maximum correlation occurs [*Leick*, 1990]. If we take the time, t^S, as the time the signal left the satellite and the time, t_R, as the time the signal arrived at the receiver, then Δt is the difference between the clock readings.

$$\Delta t = t_R - t^S = [t_R(GPS) - \delta_R] - [t^S(GPS) - \delta^S] = \Delta t(GPS) + \Delta\delta$$

where: δ^S and δ_R = clock delays with respect to GPS system time [*Hofmann-Wellenhof et al.*, 1993].

δ^S, the satellite clock bias can be modelled by a polynomial, the coefficients of which are transmitted in the first subframe of the navigation message, thus $\Delta\delta$ equals the negative receiver clock delay. The pseudo-range, R, can then be calculated [*Hofmann-Wellenhof et al.*, 1993]:

$$R = c\,\Delta t = c\,\Delta t(GPS) + c\,\Delta\delta = \rho + c\,\Delta\delta.$$

This method is affected by atmospheric delays (see Section 3.2) and produces a crude location known as the navigation solution. Generally this location (horizontal co-ordinates) is in error by up to 100m for the C/A code, or 30m for the P-code [*Leick*, 1990].

An alternative method for calculating the pseudo-range is by using the phases of the incoming signal (phase pseudo-range). In this case, the difference between the phase of the signal from the satellite, measured at the receiver, and the phase of the oscillator within the receiver at epoch t, is used to calculate the distance [*Leick*, 1990].

If we take the phase of the received carrier to be $\varphi^S(t)$, with frequency f^S, and $\varphi_R(t)$ to be the phase of the reference signal generated by the receiver, with frequency f_R, then:

$$\varphi^S(t) = f^S\,t - f^S\,\frac{\rho}{c} - \varphi_0^S$$

$$\varphi_R(t) = f_R\,t - \varphi_{0R}.$$

Thus the beat phase $\varphi_R^S(t)$ is given by:

$$\varphi_R^S(t) = \varphi^S(t) - \varphi_R(t) = - f^S \frac{\rho}{c} - f^S \delta^S + f_R \delta_R + (f^S - f_R)\, t.$$

where the initial phases are: $\varphi_0^S = f^S \delta^S$, and $\varphi_{0R} = f_R \delta_R$ [*Hofmann-Wellenhof et al.*, 1993].

As the difference between f^S, f_R, and the fundamental frequency f_0 is below the noise level (approximately 10^{-4} Hz) the above equation can be written as [*Hofmann-Wellenhof et al.*, 1993]:

$$\varphi_R^S(t) = -f \frac{\rho}{c} - f\, \Delta\delta.$$

When the receiver is turned on at epoch $t_0 = 0$, the instantaneous fractional beat phase is measured, and the initial integer number (N) of cycles between satellite and receiver is unknown. However if no loss of lock occurs during tracking of the satellite, N (called the integer ambiguity) remains the same and the beat phase at epoch t is:

$$\varphi_R^S(t) = \Delta\varphi_R^S \Big|_{t_0}^{t} + N$$

where $\varphi_R^S(t)$ = the fractional phase at epoch t, augmented by the number of integer cycles since initial epoch, t_0 [*Hofmann-Wellenhof et al.*, 1993].

From the preceding two equations we can derive an equation for the phase pseudo-range:

$$-\Delta\varphi_R^S = \frac{1}{\lambda}\rho + \frac{c}{\lambda}\Delta\delta + N$$

where λ = signal wavelength, ρ = distance between the satellite at epoch t (time of emission) and the receiver at epoch $t+\Delta t$ (time of reception) [*Hofmann-Wellenhof et al.*, 1993].

As the phase can be measured to better than 0.01 cycles, this method allows for millimetre to centimetre precision in range determination.

3.1.5. Differential GPS:

Under a differential system, two or more receivers are used simultaneously to observe the satellites. This gives several advantages over single receiver systems. One receiver, the reference, remains stationary throughout the survey while other receivers, the rovers, move between the points whose locations are needed. The results are then calculated as relative positions between the reference and each rover station, giving a baseline length. This removes the problems due to atmospheric effects as the signal to the two receivers can be considered to have travelled through the same atmosphere, and, as absolute co-ordinates are not calculated, the accuracy is not down-graded by features such as selective availability. In order to determine accurate absolute co-ordinates it is necessary that at least one station, preferably the reference station, has known values for latitude, longitude and elevation. If these are not known it is possible to over come some of the errors in the signal by recording for long periods of time (e.g. up to 10 hours) such that the effects of selective availability are averaged out [*Leica*, 1992]. Such a system has been used for this study (see Section 3.3.).

3.2. Errors and Other Problems:

Many of the error sources associated with GPS have already been mentioned, the main ones being summarised in table 3.2.

Most satellite and receiver errors are removed in the differential method of surveying, thus in this type of work atmospheric effects and random noise account for the main error sources. Under differential GPS, if the baselines are kept short (<15km) most atmospheric effects are minimal and therefore can be discounted, as the signal to the two receivers can be said to have travelled through the same atmosphere [*Leica*, 1992]. Large elevation differences have a similar effect to long baselines as the signals may pass though significantly different atmospheres.

3.2.1. Atmosphere:

If we consider that the GPS signals are a group of electromagnetic waves propagating through space, we find that the carrier waves (*L*1, *L*2) have a velocity of v_{ph} while the codes propagate with a group velocity of v_{gr}. In a non-dispersive media these velocities are equal (and equal c, the velocity of light). However in a dispersive media, such as the ionosphere (50 to 1000km above Earth), these velocities can be seen to become non-equal ($v_{gr} < v_{ph}$). This results in a delay in the code measurements and an advance in the carrier phase. Therefore calculated code pseudo-ranges are too long and calculated phase pseudo-ranges are too short [*Hofmann-Wellenhof et al.*, 1993].

Table 3.2. Summary of error sources in GPS surveying.

Source	Effect
Satellite	Orbital errors Clock bias
Signal Propagation	Atmospheric effects: -Ionospheric refraction -Tropospheric refraction
Receiver	Antenna phase centre variation Clock bias

Ionospheric effects vary with sunspot activity as well as seasonal and diurnal variations, and are thus difficult to model. The error produced by ionospheric refraction can largely be removed by the use of dual frequencies (*L*1 and *L*2) and short baselines.

The non-ionised part of the atmosphere (the troposphere) also affects the measurements, although this part of the atmosphere is non-dispersive, and therefore velocity is no longer frequency dependent, these effects include small changes in the velocity of the waves due to water content. Here there is no difference between *L*1 and *L*2 velocities, and therefore dual frequency measurements will not remove tropospheric effects. Unlike the ionosphere however, the troposphere can be adequately modelled and therefore its effects

removed. For a full account of all atmospheric effects see [*Hofmann-Wellenhof et al.*, 1993].

3.2.2. Bouncing Signals (Multipath):

Multipaths occur when the signal reaches the receiver by more than one path. This is generally due to the reflection of the signal off surfaces near the receiver, such as walls, roads etc. This causes an error in the pseudo-ranges due to phase off-sets occurring, the effect is reduced when both $L1$ and $L2$ frequencies are used. It is impossible to remove these effects, thus it is important to choose station locations such that these effects are reduced or some form of shielding used.

3.3. Field Methods for this Study:

GPS has been used in this study for 2 distinct applications: 1. Locating of gravity stations; 2. Measurement of ground deformation. It has been used for a location tool due to its ease of operation, its speed and its accuracy. However only part of the gravity survey has been located by this method, for approximately half of the stations, maps and altimeters have been used due to the unavailability of the GPS system early in the work (see Chapter 4). For ground deformation work it has the advantage over other measurement methods (e.g. EDM) in that line of sight is not needed and baseline lengths are relatively unimportant. Thus over moderately long baselines (>3km) it produces results as accurately as EDM work but without the need for line of sight. The field technique differs for each application as each has its own acceptable limits on accuracy and time taken. The ground deformation data requires a greater degree of accuracy than does the gravity data.

For this study the Wild GPS 200 system, which is a differential method using P-codes, has been used, requiring two receivers, one acting as a reference the other as the rover. Each receiver consists of a controller and a sensor (figure 3.3). The controller has a keypad and an LCD screen to display and enter survey parameters and station names, while the sensor is, at its most basic, an antenna for receiving the satellite signal.

There are several possible ways to collect data using a differential GPS system. When, as in this study, the measurements are taken by two stationary receivers the survey is termed a static survey [*Leica*, 1992]. When only a short time is used for measurements by the rover (5 to 10 minutes) the method is termed rapid static. Traditional static surveying requires long observation times (up to several hours), however with the appropriate software (e.g. the Wild SKI Static Kinematic software) this can be cut significantly [*Leica*, 1992]. The use of rapid static survey techniques allowed for a large number of stations to be measured in a short amount of time, thus increasing data coverage.

For all the GPS work in this study several factors are common, the survey parameters were set within the controller for both the reference and rover stations such that measurements were only made if GDOP ≤ 8 and if 4 or more satellites were visible above 15° from the horizon. The reason for the 15° cut-off is that the lower in the sky the satellite is, the greater the atmospheric effects i.e. the nearer to horizontal the line between the satellite and the sensor, the greater the volume of atmosphere the signal must pass through.

All stations (for both gravity and ground deformation work) were located in positions likely to keep the interference to a minimum. Locations near trees, tall buildings and other objects which obscure the sky were avoided.

At the end of each day the data were downloaded from the memory card within the controller onto a laptop computer, and then a brief analysis of the data was made using the SKI software (see next section). No analysis was carried out in the field as the controller is only capable of showing the navigation solution which may be in error by up to 100m in all directions.

3.3.1. Gravity Station Location:

A single reference point was used for the entire survey for the collection of the gravity station locations. The point chosen was located near the gravity station SAP, close the Sapienza, in a position away from the public; as the equipment is left alone for long periods of time it is necessary to ensure that passer-bys cannot interfere with it. Due to these restrictions baselines could not be kept small, and thus range up to 25 km. The aim of keeping baselines small is that the assumption of similar atmosphere for reference and rover

is maintained. If baselines are long then this is not necessarily true and errors due to atmospheric effects are increased. However, since for gravity data reduction, the aim was rapid and accurate location and elevation data for all stations, an error of up to ±10m in location is acceptable. As elevations determined by the use of altimeters have an error of ±5m, due to the poor quality of benchmark data in the area, (see Chapter 4), the increase in elevation errors due to long baselines was not considered a problem.

The sensor (i.e. the GPS antenna for receiving the satellite signal) was set up on a tripod over each gravity station, and the gravity measurement taken while the satellite data was collected (see figure 3.3).

3.3.2. Ground Deformation Network:

A small network of stations located in the Eastern end of the Valle del Bove, around the town of Milo (figure 3.4), has been established for the purposes of investigating ground movements which may be occurring in this unstable region. Two sets of measurements of this network have been carried out, one in July 1994, the other, December 1994, also one baseline was re-measured during July 1995. For the December measurements repeat measurements and two base stations have been used, giving at least two measurements for all stations, however for July 1995 only one base station was used but repeat measurements were carried out. The use of more than one base station provides for both an error check and the determination of movement vectors, as any movement occurring along baselines can be seen in two directions. Where only one base station has been used it is only possible to determine the magnitude of movement along the azimuth of the line between the station and the (single) base. For this part of the work a high degree of accuracy was required and therefore baselines are short (all < 5 km) and observation times relatively long (up to 30 minutes). One station, Milo Top, corresponds to a point used by several other workers on Etna as a GPS reference point (e.g.*EPOCH*, 1993; *Nunnari and Puglisi*, 1994). The station locations were picked so as to show movement occurring at the bottom of the Valle del Bove, i.e. to detect movement in the Milo area, based on the assumption that Bloody Flies is in a stable area relative to all the other stations, and that, relative to Milo, Monte Pomiciaro and Fontane are also stable.

1 = antenna	2 = battery	3 = controller	4 = tripod	5 = gravimeter

Figure 3.3. GPS station set up and equipment.
a. This photo shows the setting up of a GPS point. The antenna is placed on the tripod and connected to the battery and the controller. Station particulars (name etc) are entred into the controller, which also records the satellite data.
b. Set up for a gravity station. The GPS equipment is set up as for 3.3a with the gravimeter under the tripod.

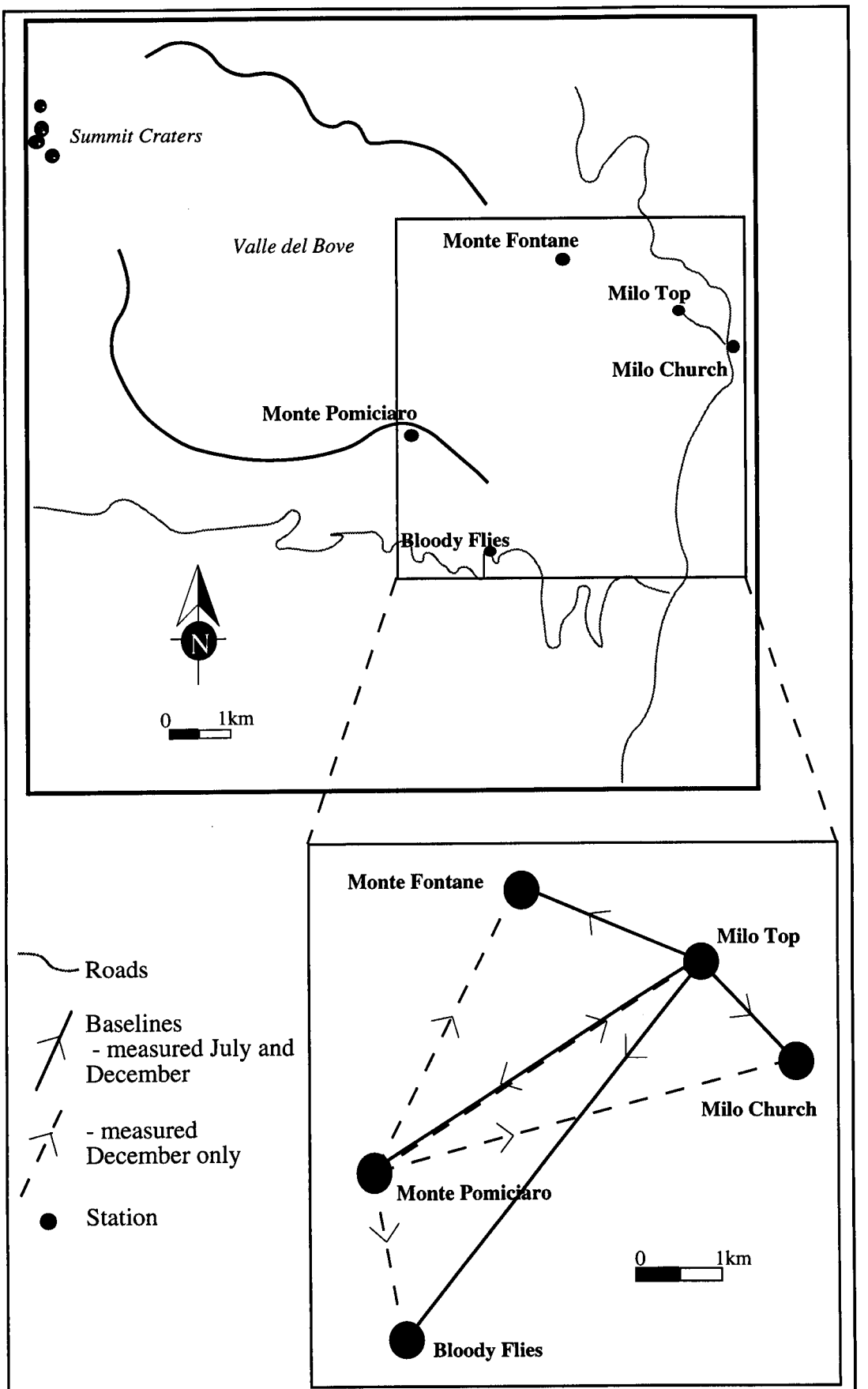

Figure 3.4. The Milo deformation network.

3.4. Getting the Numbers Out (Data Processing):

The Leica Wild SKI software package is a Windows based system and processes the data by taking the user through a series of steps:

- ☞ Importing the data;
- ☞ Data Processing;
- ☞ View/Edit results;
- ☞ Datum Transform;
- ☞ Network Adjustment.

3.4.1. Locating of Gravity Stations by GPS:

The raw data are imported into the system directly from the Wild controller internal memory card. Co-ordinates are calculated initially in the WGS-84 reference system. WGS-84 is a geocentric ellipsoid of revolution, defined by the parameters of table 3.3. This is the standard terrestrial co-ordinate system used by GPS [*Hofmann-Wellenhof et al.*, 1993]. In order to relate this to the local system (for Etna this is the Universal Transverse Mercator (UTM) system using the International Spheroid) the co-ordinates of at least one point must be known. For this study no points were known as accurately as required, therefore the Single Point Processing Mode was used. This mode allows the co-ordinates of a single point to be determined to within ±10m, but only when data have been collected for more than 2 hours. As the reference station was left recording for 10+ hours every day it was possible to obtain an accurate solution. This gives absolute co-ordinates still in WGS-84, thus the latitude and longitude are correct, but the elevations are relative to the WGS-84 ellipsoid, not mean sea-level (the geoid). In order to calculate elevations relative to sea-level several points with known elevations were used (elevations from J. Murray, unpublished data, and the Obsevio Vesuvious levelling network). These points had errors of ±5m, and thus, this limits the accuracy of the final calculated heights. Co-ordinates of

these points were also available but of no greater accuracy than the GPS Single Point solution and therefore they were not used to constrain the data.

The first step of the calculation is to select the reference station, the system then calculates positions relative to this point. The results are displayed and can then be either stored for keeping or discarded. In general, given short baseline lengths and sufficient time for recording the data, the integer ambiguity will be solved. However, as the majority of baselines were long and recording time kept to a minimum, ambiguities were not always solved and thus errors were slightly increased. Error ellipses for the calculated results, as determined by the SKI system, were generally of ±0.5m or less. As the error in the position of the reference station was ±10m, this small additional error can be ignored.

Once the results have been calculated they can be viewed in map form using the View/Edit part of the program, this allows for editing of information (e.g. station names) and for the general coverage of the data (important for the distribution of the gravity stations) to be assessed.

The data can be left in WGS-84 co-ordinates or converted to the local grid system using Datum Transform. For the gravity data reduction, latitude and longitude are required so it was felt to be unnecessary to convert the locations to UTM co-ordinates, however the heights must be relative to sea-level (i.e. the geoid) rather than the WGS-84 ellipsoid. The geoid and ellipsoid are related by:

$$h = H + n$$

where: h = ellipsoidal height;

H = orthometric height (height above mean sea-level);

n = geoidal height (undulation). [*Hofmann-Wellenhof et al.*, 1993]

Thus if the geoidal undulation (i.e. the geoid - ellipsoid separation) is known then the orthometric elevation can be calculated from the ellipsoidal elevation. In the case of this study n was unknown but values of H were available for a number of stations and thus n was calculated and used to deduce the elevation of all stations. This is the final stage of processing for the gravity data, and the resultant data set consists of each stations latitude, longitude and height above sea-level.

The final results for the gravity station locations have errors of ±10m for both North-South and East-West position and ±2.5m elevation. This accuracy is considered sufficient for this work (see Chapter 4). Datum Transform was used in order to produce the gravity maps of Chapter 4 in the local grid co-ordinates, this produces maps which are easier to read and of a useful scale, relative to latitude and longitude.

Table 3.3. Spheroid Parameters.

Parameter	WGS-84	International Spheroid
a (semi-major axis)	6 378 137m	6 378 388m
f (spheroidal flattening)	1/298.257 2221	1/297
e^2 (square of spheroidal eccentricity)	0.006 694 379	0.006 722 670

3.4.2. Ground deformation network:

The ground deformation network data covered much smaller baseline lengths than the gravity data and therefore ambiguities were always solved and more accurate results obtained. In several cases initial calculations failed to resolve ambiguities, in these case the data was examined for possible cycle-slips or other problems. In certain situations satellites with a large number of cycle-slips or time windows where cycle-slips occurred were removed and the positions re-calculated; in all but one case this improved the results and allowed the ambiguities to be solved. A cycle-slip generally occurs where the receiver loses contact with the satellite for a short period of time and thus misses part of the beat-cycle count. The SKI software lets the user deal with this in several ways: if the cycle-slip is short and ambiguities resolved it can be ignored; where the cycle slip is for an extended length of time, but only affecting one or two satellites, the signal for these satellites can be ignored (effectively turning off the satellite) or if it is occurring in a number of satellites, the time-span over which it occurs can be "windowed out", i.e. the software will not use data collected within that window of time.

The deformation network data contains much smaller errors than the gravity data as the absolute positions are not required; repeat measurements give errors of ±8mm in baseline lengths and ±58mm in elevations for the July 1994 measurements; ±11mm and ±38mm for the December 1994 measurements.

The data for the Milo network has been reduced in a different manner to the rest of the GPS data, the steps used follow those of *Elwell*, [1995]. As two separate data sets are available, and it is the change between them that is of interest, they have been processed so as to make them directly comparable. The initial stages follow those for the gravity data, however following the initial solving of ambiguities and the production of relative co-ordinates, the network has been taken into Network Adjustment, to carry out a least squares' adjustment on the data and determine the baseline vector lengths with a 95% confidence limit, that is, the network is adjusted so as to produce values for the baseline which fall within the given error ellipses with a confidence level of 95%. It is changes in these baseline vectors which will show ground movement directions and magnitudes.

However, as only one set of baseline vectors are available for the July 1994 data (i.e. only one base station was used) it is impossible to determine the true 2 dimensional movement from the baseline changes only. In order to determine these 2 dimensional vectors of movement the data has been taken into Datum Transform.

By carrying out a transformation of the data collected in December 1994, using the co-ordinates of the base station for July 1994, we can see the 2 dimensional movement. This has the effect of constraining the point Milo Top to the same co-ordinates in both data sets. The choice of Milo Top results from it being a base station and thus having a significantly longer recording time than the other stations. This additional recording time increases the accuracy of the co-ordinate determination. However it should be noted that *any* station could have been used with no significant difference seen in the results. If no movement has occurred then the transformed December points will lie directly over the July points. Movement will show as an offset in the points. The results of this work are discussed in chapter 5.

Chapter 4 Gravity and Aeromagnetics

4.1. In the Field:

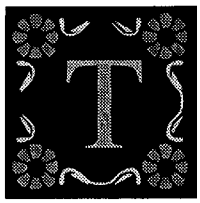

he principal aims of the gravity survey are to build up a picture of the structures underlying the Eastern Flank, and more importantly the Valle del Bove and the Chiancone deposit. By developing a good understanding of the sub-surface features of these areas we can develop better models for the formation of the Valle del Bove as well as the instability of the Eastern Flank as a whole. Thus the main concentrations of gravity stations are around the Valle del Bove and the Chiancone (figure 4.1). The station distribution of these areas is approximately 1 station per km^2, becoming more spread out further from the Valle del Bove. Individual station locations were picked on the basis of ease of operations - covering the greatest ground within the shortest time - and thus tend to follow roads and tracks. For approximately half the stations (labelled B in Appendix A), GPS was used in order to determine position (latitude and longitude) and elevation. For all other stations, 1:10,000 and 1:25,000 maps were used for position while elevations were determined by the use of two barometric altimeters (see Appendix A). GPS was only used for half the survey as it was unavailable during the early part of the study. It has the advantage over the use of maps and altimeters in its greater degree of accuracy and speed of operation. Also over the upper parts of the volcano and within the Valle del Bove, the use of maps as a location tool would have been impossible due to the lack of clear, permanent features and the age of many of the available maps. The gravity data were collected using a LaCoste and Romberg G-model gravimeter (G-513).

While the altimeters were being used continual looping was necessary to determine the change in air pressure during the day, as no continuously recording altimeter was available. This meant returning to a base station once every two hours, therefore gravity was also re-measured at these stations several times a day in order to check for instrument drift and mechanical tares [*Rymer,* 1989]. With GPS it is not necessary to return to a base station, so

repeat gravity readings were made whenever possible during the day. A single base station, Nicolosi, was used to tie together the various daily bases. Nicolosi was chosen as it is an absolute gravity station and also linked to the microgravity monitoring networks present on the volcano [*Rymer et al.*, 1993; 1994].

Repeated measurements at several stations give the reading error for the gravity data as ±25 μGal (1 μGal = 10^{-3} mGal = 10^{-8} m s^{-2}). Several tares occurred during the survey time of up to 100 μGal (although this is an extreme value), and if it was not possible to remove these, based on repeat readings of stations, then further data at the affected stations were collected at a later date.

4.3. Data Reduction:

The first stage of gravity reduction is the removal of daily tidal effects. These result from the movement of mass associated with the tidal bulge of the Earth tides [*Baker*, 1984]. This effect is removed by using calculated values for the Earth tides, taken from a FORTRAN program based on *Brouke et al.*, [1972]. The observed gravity (g_{obs}) is then the difference between the tidally corrected values for the field stations and Nicolosi.

In order to produce a map of the gravity anomalies, reduction of the data was carried out following the standard methods (e.g.*Kearey and Brooks*, 1991; *Telford et al.*, 1990). The Bouguer Anomaly (BA) is defined as:

$$BA = g_{obs}+FC-BC+TC\pm LC$$

where: g_{obs} = observed gravity value relative to the station at Nicolosi, corrected for tidal variations;

FC = free-air correction;

BC = Bouguer correction;

TC = terrain correction;

LC = latitude correction.

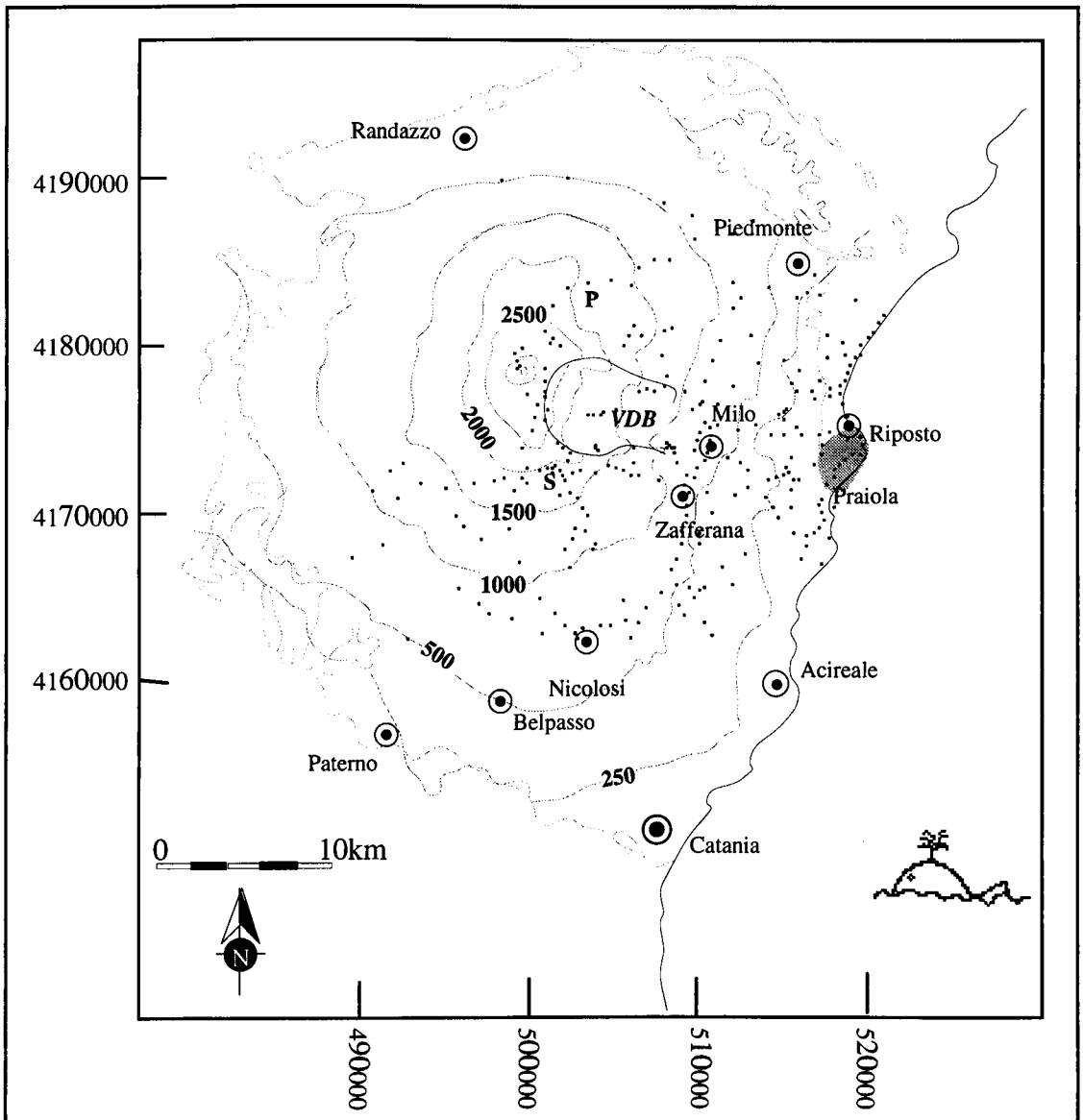

Figure 4.1. Gravity station location map. Dots mark the locations of the gravity stations established in this study. Also shown are the approximate extent of the Valle del Bove (VDB) and the Chiancone (shaded area). The limits of the volcanic deposits are shown by the thin grey line; contours are in metres. The local 10km grid squares are shown for reference. S= Sapienza; P = Piano Provenzana.

4.3.1. Free-Air Correction:

As gravity varies with height it is necessary to correct the stations to a single datum plane, in this case sea-level. The first stage is to carry out the free air correction using the standard Free Air Gradient, FAG = 0.3086 mGal m^{-1}.

$$\therefore \quad FC = 0.3086h \text{ mGal}$$

where h = the elevation of the station above the datum plane (in metres).

This correction implies that between the station and the datum is "free air", i.e. no mass, thus it is necessary to adjust this correction with the Bouguer correction.

Errors in the FC result from two sources: i) errors in the elevation; ii) errors in the FAG. Where altimeters have been used the error in relative height between the daily base and the field station is approximately ±2m (see appendix A), while for the GPS data it is ±0.5m. However absolute heights relative to sea-level are not available to an accuracy of better than ±5m so the true error is obtained by combining these two errors and is ±5.3m, this gives an error of ±1.6 mGal. The second source of error, variations in the FAG, is difficult to determine as no measurement of the gradient were made in the course of this study. The actual value for this gradient will depend on a number of local factors such as terrain and the local Bouguer Gravity anomaly, thus it is likely to be quite variable over the study area. Two measurements of the FAG on Etna have been published: one is from the Serra la Nave Observatory (1750m a.s.l.; approximately 2.5km SW of the Sapienza) with a value of 0.2994 mGal m^{-1} [*SCIENCE*, 1994]; the other has been measured at the summit area (approx. 3000m a.s.l.), and gives a value of 0.365 mGal m^{-1} [*Rymer*, 1994]. The variation between these values and the theoretical value results from the effect of the local topography and local gravity anomalies. No values for the FAG are available for the coastal areas where, given the relatively flat topography, it is expected to be closer to the theoretical value. Rather than use a number of values for different parts of the survey it was decided to use the theoretical value. The possible effects of an incorrect FAG will depend on where the stations is and the local FAG, however the effects of this will cancel in the computer modelling of the final reduced data.

4.3.1.1. Choice of Datum Plane:

The relative values of gravity between stations is unaffected by the choice of datum plane. For this study, the datum plane has been chosen as sea-level, which therefore means that the base station (Nicolosi) has a non-zero value.

4.3.2. Bouguer Correction:

The BC represents a correction to the FC, i.e. this correction replaces the "missing" mass from the FC. The correction is based on the gravitational attraction of an infinite slab:

$$BC = 2\pi G\rho h \times 10^5 \text{ mGal.}$$

where ρ = chosen reduction density (in kg m^{-3});

G = Universal Gravitational Constant (6.67×10^{11} m^3 kg^{-1} s^{-2});

h = elevation of the station above the datum plane in metres.

As the BC relies on elevation it is also affected by the ±5.3m uncertainty in the height data, giving an error of ±0.59 mGal.

The final value for both the Bouguer and Terrain Corrections are dependent on the choice of reduction density and the local topography. Given the extreme range of elevations in this survey (sea-level to over 3000m a.l.s.) the final values for these two corrections will also be extreme, and therefore care must be taken with them, thus the correct choice of density is important.

4.3.2.1. Reduction Density:

The use of an incorrect reduction density may result in the failure to remove topographic effects completely from the gravity data, especially in regions of extreme topography, thus determination of the correction density can be very important. The Nettleton method of density

determination relies on correlation between gravity and terrain: by reducing the gravity data we should be removing all terrain effects in order that the anomalies seen are solely due to sub-surface density changes. Thus the reduction density resulting in the least correlation between terrain and gravity is considered the best choice [*Telford et al.,* 1990]. For a topographical feature of a given density, x, a gravity high will be created if a reduction density, y, has been chosen such that y<x, and vice versa, thus it is important to remove such effects. However in cases where the subsurface distribution of anomalous mass (i.e. the targets of interest) coincides with topography, there is the possibility of removing the feature of interest by using this method [*Williams and Finn,* 1985]. In an attempt to choose the best density for this study several plots of the data reduced using a number of densities versus height have been plotted (figure 4.2). A correlation between topography and gravity can be seen in all of these plots, however that for densities of 2400 kg m^{-3} and 2670 kg m^{-3} the correlation appears to be the smallest. This general correlation is not unexpected as the density structure of Mt. Etna is likely to be very complex and much of its topography will directly relate to sub-surface features and thus densities.

For this survey 2670 kg m^{-3} has been chosen as the most appropriate reduction density. This density was chosen as being the a good representative value of crustal rocks and, as it is the structures of the edifice itself we are interested in, it is appropriate to remove the basement effects. Previous workers have used both this density [*Loddo et al.,* 1989] and the lower value of 2400 kg m^{-3} [*Neumann et al.,* 1985]. However, this lower value is likely to be close to the value for the density of the volcanic deposits [*Loddo et al.,* 1989], and thus an inappropriate choice for a reduction density. As the final aim of this work is to use the gravity data in modelling, the choice of reduction density is less important if the models are constructed with a background density equal to the reduction density, although a reasonable density must be used if the models are to reflect reality.

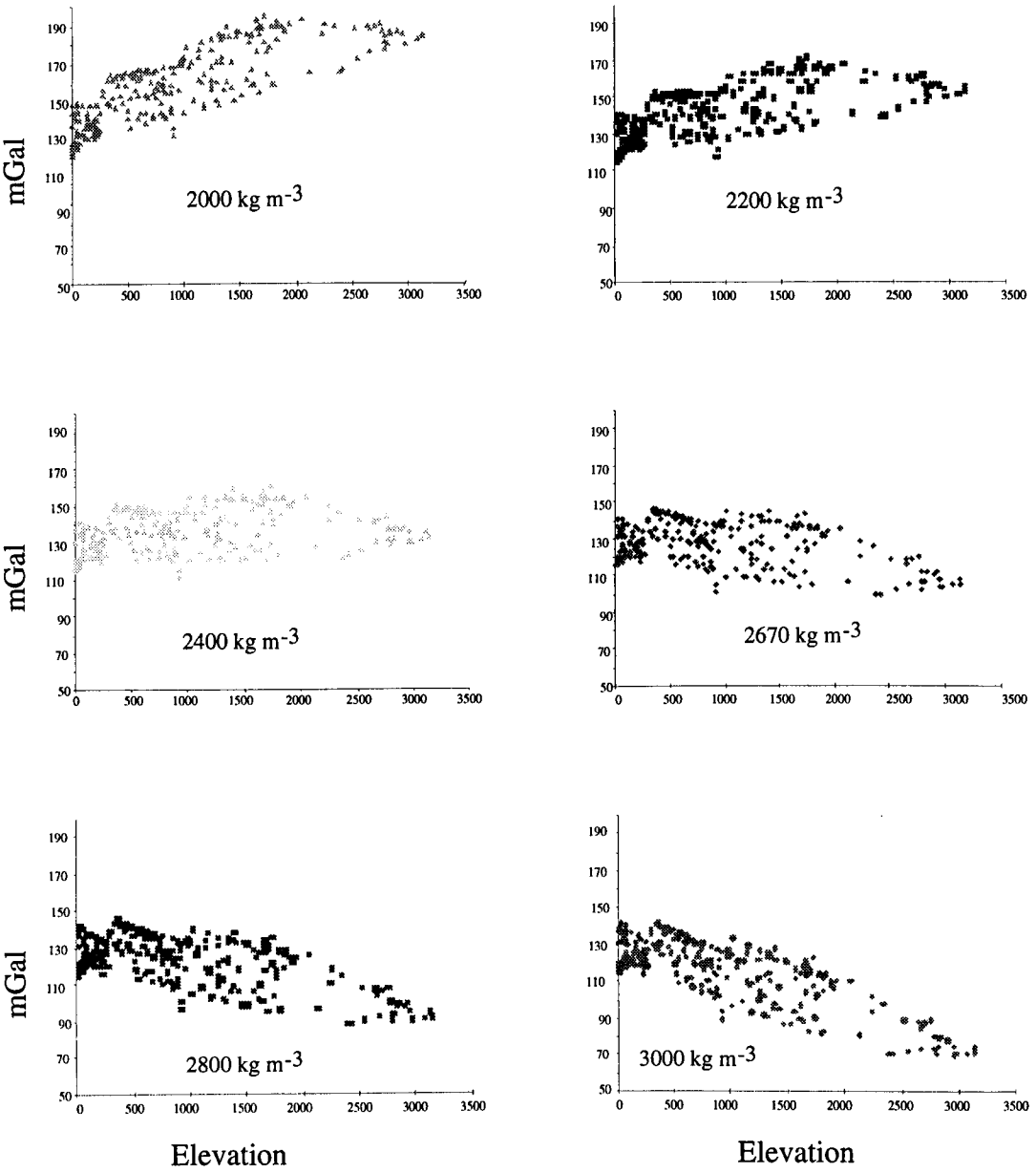

Figure 4.2. Bouguer corrected gravity vs. station elevation. These plots show all the data reduced using a number of densities (2000kg m^{-3} to 3000kg m^{-3}) in order to determine which is the best choice of reduction density. Based on these, 2670kg m^{-3} appears to be the best choice as it shows the least correlation with topography. Although 2400kg m^{-3} also shows little correlation with topography this value is very close to the expected density of the volcanic deposits and is thus an inappropriate reduction density

4.3.3. Terrain Correction:

The terrain correction (TC) is carried out in order to correct for the effect on the measured gravity values of hills and valleys. For this study the TC was calculated by the method of *Hammer*, [1939]. In this method the region around the station, out to a large distance (generally 22km) is divided into zones (labelled A-M) with each zone being of a greater radius than the preceding one, each zone is then divided into a number of compartments and the "average" topography within each compartment is estimated (table 4.1 gives the inner and outer radius and number of compartments of each zone). Topographic data for zones E-M were taken from 1:50 000 and 1:100 000 maps of the area by using an overlay marked with the zones, with the TC being calculated within a computer spreadsheet from the equation [*Hammer*, 1939]:

$$T_{ij} = \frac{2\pi G\rho}{n_i}(R - r + \sqrt{r^2 + h^2} - \sqrt{R^2 + h^2}) \times 10^5 \text{ mGal}$$

where : T_{ij} is the terrain correction for the j^{th} compartment of the i^{th} zone;

n_i = the number of compartments in the zone;

R = the outer radius of the zone;

r = the inner radius of the zone;

ρ = the chosen reduction density;

h = elevation difference between compartment and station.

Station locations were usually chosen such that zone A was always an area of 0 height difference, in certain cases this was not possible (e.g. due to sloping ground) and for these stations the method of *Sandberg*, [1958] was used, in this method the terrain effect is determined for a slope of a given inclination, the values being read from prepared tables. The terrain effects for zones B-D were determined in the field by estimating the elevation out to 170m in 3 stages. The zones were divided into 4 (B) and 6 (C & D) compartments and the height difference between the station and points 10m (B), 35m (C) and 100m (D) away was estimated for each compartment, effectively giving an average height difference for each zone.

Topography for the outer zones of J-M is similar for closely grouped stations, therefore elevations were defined only once for each group. The diameters of these groups are shown in table 4.1. These diameters were determined by trial and error; by determining the area over which no significant change in the TC occurred (significant being considered 0.2 mGal or greater).

Repeat estimations of the terrain corrections were carried out for 5 stations in order to provide a measure of the error in the technique. The error has been taken as the average difference between these repeat measurements, and is ±0.4mGal.

Table 4.1. Inner (r) and outer (R) radii and number of compartments (n) for Hammer zones A-M. Grouping size refers to diameter of groups of stations used in the determination of "average topography".

Hammer Zone	R (km)	r (km)	n	Grouping Size (km)
A	2m	0m	-	-
B	17m	2m	-	-
C	53m	17m	-	-
D	170m	53m	-	-
E	0.39	0.17	8	-
F	0.90	0.39	8	-
G	1.54	0.90	12	-
H	2.64	1.54	12	-
I	4.51	2.64	12	-
J	6.73	4.51	16	1
K	10.0	6.73	16	1
L	14.9	10.0	16	3
M	22.1	14.9	16	3

4.3.3.2. Cutting the Bouguer Slab:

Hallinan, [1991] shows that failure to take the Terrain Correction out to a great enough distance results in a significant underestimation of the total TC. He shows that for a station

2000m above the average terrain, this effect can lead to a false anomaly of -10 mGal being created when the TC are stopped at 22km. As Mt. Etna is a solitary mountain, descending from 3200m to sea-level to the East and down to 100-500m on the other flanks (at 22km), a significant number of stations are several hundred metres above the average terrain, i.e. stations on the upper flanks of the volcano. For all these stations, truncating the terrain correction too soon would create a significant false anomaly. This anomaly is due to the presence of the Bouguer slab at this distance, but there being no real mass, i.e. over compensation for the free air correction (figure 4.3). *Hallinan*, [1991] avoids this problem by continuing the terrain correction out to 221km, beyond which there is no appreciable effect. The necessity of continuing terrain corrections to such distances can be avoided if the Bouguer slab is truncated at the same distance as the terrain corrections. Such truncation will greatly reduce the possible error from failure to carry out "full" terrain corrections. This method is only applicable to situations such as Etna where there are no sizeable bodies (i.e. other mountains) close enough to produce a significant terrain effect, that is a terrain effect greater than the error in the method. Out to 50km from the summit of Etna the terrain is generally below 600m above sea level, and thus below the majority of the gravity stations in this survey, therefore failure to carry out terrain corrections to this distance would produce a sizeable error if the usual Bouguer slab is used. However this is reduced by using a Bouguer disk of radius 22km around each station. The gravitational attraction (BD) for this Bouguer disk is that of a vertical cylinder:

$$BD = 2\pi G\rho \, (h + r - \sqrt{h^2 + r^2}) \times 10^5 \text{ mGal}$$

where: r = the outer radius of the disk (i.e. 22km for this case) in metres;

h = the elevation of the station (m a.s.l.).

In this situation stations below the level of the surrounding terrain will be left with a residual effect not accounted for, any errors resulting from this are likely to be much less than those due to failure in carrying out "full" terrain corrections. This effect will be greatest for the coastal stations where there is a significant elevation difference between the station (near sea-level) and the terrain beyond 22km to the west (i.e. the lower areas of the Western Flank of

Etna). A second effect arises due to the Ionian Sea, as this is composed of water with a density of approximately 1000kg m^{-3} it represents a slight mass deficit (relative to the reduction density of 2670kg m^{-3}). The magnitudes of both these effects can be determined by the use of the terrain correction formula, with appropriate density values and radii of 22km to infinity (taken here as 200km, beyond which effects will be negligible), such calculations give maximum possible effects of 0.5mGal for the effect of the Western Flank and 0.8mGal for the effect of the sea, both these values are for stations at or near sea-level. Also both effects are negative, i.e. they both represent mass deficits (hills above a station have the same effect as valleys below the station). Thus coastal effects may have a false anomaly of approximately -1mGal added to their true gravity anomaly. However, this is a maximum effect and is less than the likely error in estimating the full terrain corrections out to these distances as the available topographic and bathymetric data is very poor.

4.3.4. Latitude Correction:

As the Earth is a non-spherical rotating body the acceleration due to gravity (g) will vary with North-South position (i.e. latitude). As the Polar radius is less than the equatorial radius gravity is greater as we move northwards for the Northern Hemisphere. This effect is calculated using the International Gravity Formula 1967 (see *Telford et al.*, 1990):

$$g_\phi = g_0 (1+0.005278895 \sin^2\phi + 0.000023462 \sin^4\phi)$$

where g_ϕ = the value of gravity at latitude ϕ;

g_0 = 978031.8 mGal (value of g at the equator)

The latitude correction is then the difference in g_ϕ between the station and Nicolosi, and is positive (negative) if the station is to the south (north). The error in the LC is due to errors in locating the stations in the North-South direction, and depends on the local gradient in the gravity field, this gradient for Etna is 0.8 mGal per km. For stations where GPS has been used this error has ±10m, for all other stations it is ±50m, thus the error in the LC is ±0.04 mGal at its maximum.

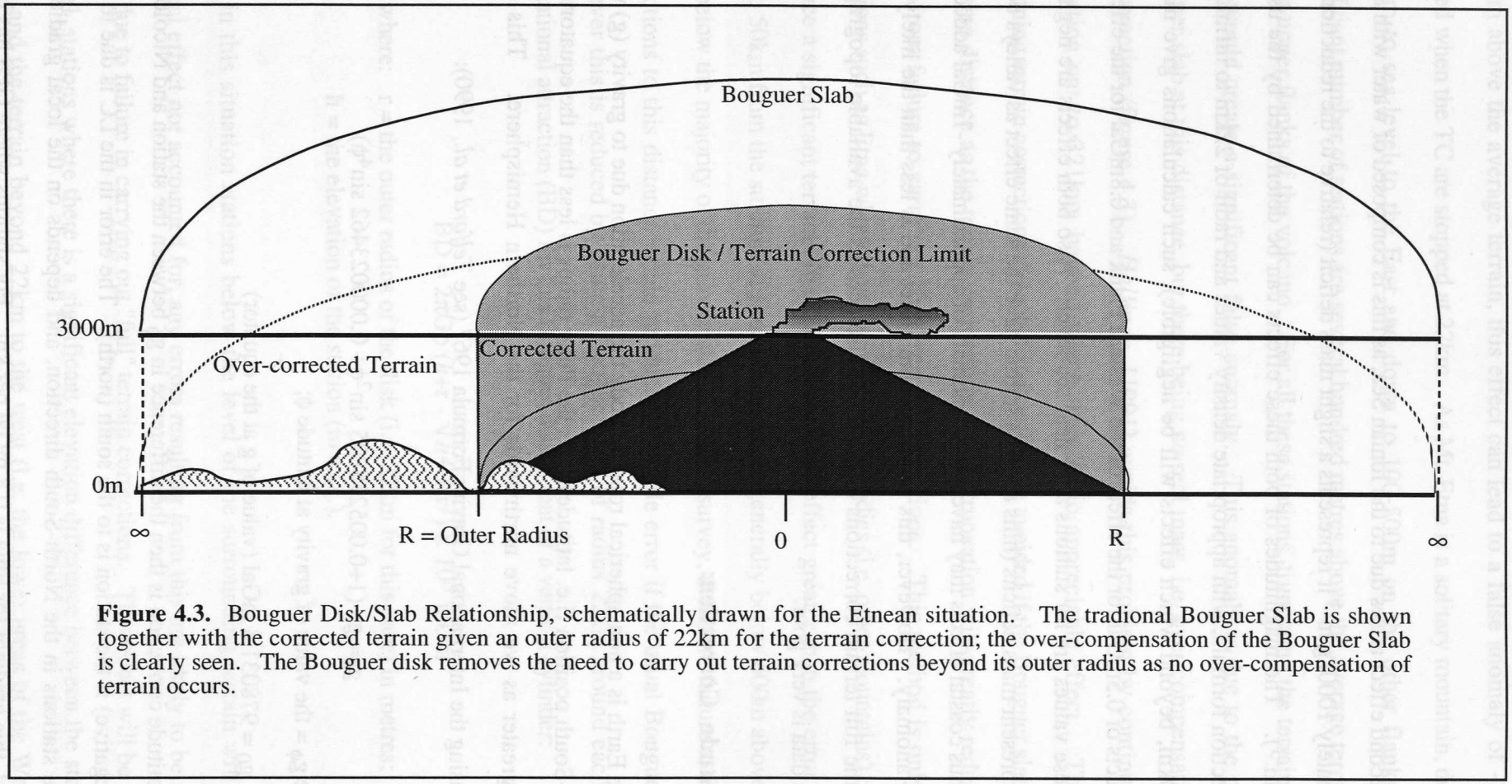

Figure 4.3. Bouguer Disk/Slab Relationship, schematically drawn for the Etnean situation. The tradional Bouguer Slab is shown together with the corrected terrain given an outer radius of 22km for the terrain correction; the over-compensation of the Bouguer Slab is clearly seen. The Bouguer disk removes the need to carry out terrain corrections beyond its outer radius as no over-compensation of terrain occurs.

4.4. Summary of Errors:

Table 4.2 summarises the errors in the gravity data. Most of these errors relate to field practices and therefore are calculated from repeat readings. In the case of the terrain corrections the method for determining the topography is highly subjective and therefore operator error is a significant effect. An attempt to determine the possible error in this correction was made by carrying out full terrain corrections (A-M zones) twice for several stations. It is the average difference from these repeats which is considered the error in the terrain correction.

Table 4.2. A summary of Errors in the observed gravity data.

	"Field" Error	Gravity Error (mGal)
Raw Data	±0.02 mGal	±0.02 mGal
Free-Air Correction	±5.3 m	±1.6 mGal
Bouguer Correction	±5.3 m	±0.59 mGal
Terrain Correction	±0.4 mGal	±0.4 mGal
Latitude Correction	±50 m	±0.04 mGal
TOTAL		**±1.7 mGal**

4.5. Aeromagnetic data:

Aeromagnetic data refers to magnetic field readings continuously collected by trailing a magnetometer behind an aircraft. The data are collected along a set of lines - the flight lines - at either a fixed ground clearance or at a set elevation above sea-level. Flight line spacing and direction will vary depending on the scale and orientation of the features of interest. In this case the data were collected in the summer of 1994 along several approximately North-South flight lines by C. Locke and J Cassidy (University of Auckland, New Zealand). These lines are linked by a tie-line running East-West as well as several cross over points where a number of lines meet (figure 4.4 shows the flight lines).

This survey was carried out so as to be complementary to the gravity survey, covering similar areas but concentrating on the Valle del Bove.

4.5.1. Data Collection:

In order to avoid the magnetic effects of the aircraft (in this case a helicopter) the sensing element of the magnetometer is housed within a cylindrical container (the *bird*) and towed some distance behind. The data were collected with a total field proton-precession magnetometer, trailing the helicopter by 20 to 30 m. Such a magnetometer measures the total field and is relatively unaffected by the irregular movement of the bird in flight, also, as each reading is effectively instantaneous the affect of in-flight wobble and other movement is minimal.

The flight line pattern will affect the data in the same way as all data collection: the tighter the pattern (i.e. the closer the lines), the better the definition of anomalous areas. The flight lines shown in figure 4.4 are only approximate, the true flight lines (plotted by the co-ordinates of the sample points) are shown together with the data in figure 5.7. It was attempted to fly at a constant elevation of 3300m, although this was not always possible. Elevation and location for each sample point was determined by GPS, the data automatically logged together with the magnetic data. The error in position for each sample point is: ±100m horizontal and ±150m vertical. A data point was collected approximately every 5 seconds along the flight lines, giving a total of approximately 1600 sample points.

Aeromagnetic data must be corrected for several effects, the principal one being the diurnal variation in the geomagnetic field. This is measured by the use of a base station magnetometer and the variations removed from the data. For this survey a base magnetometer was set up near the Northern Wall of the Valle del Bove, at the point the helicopter took off from. Secondary corrections account for any differences in measured values at points where the flight lines cross (cross over points). Differences at cross over points are forced together by a least-squares adjustment.

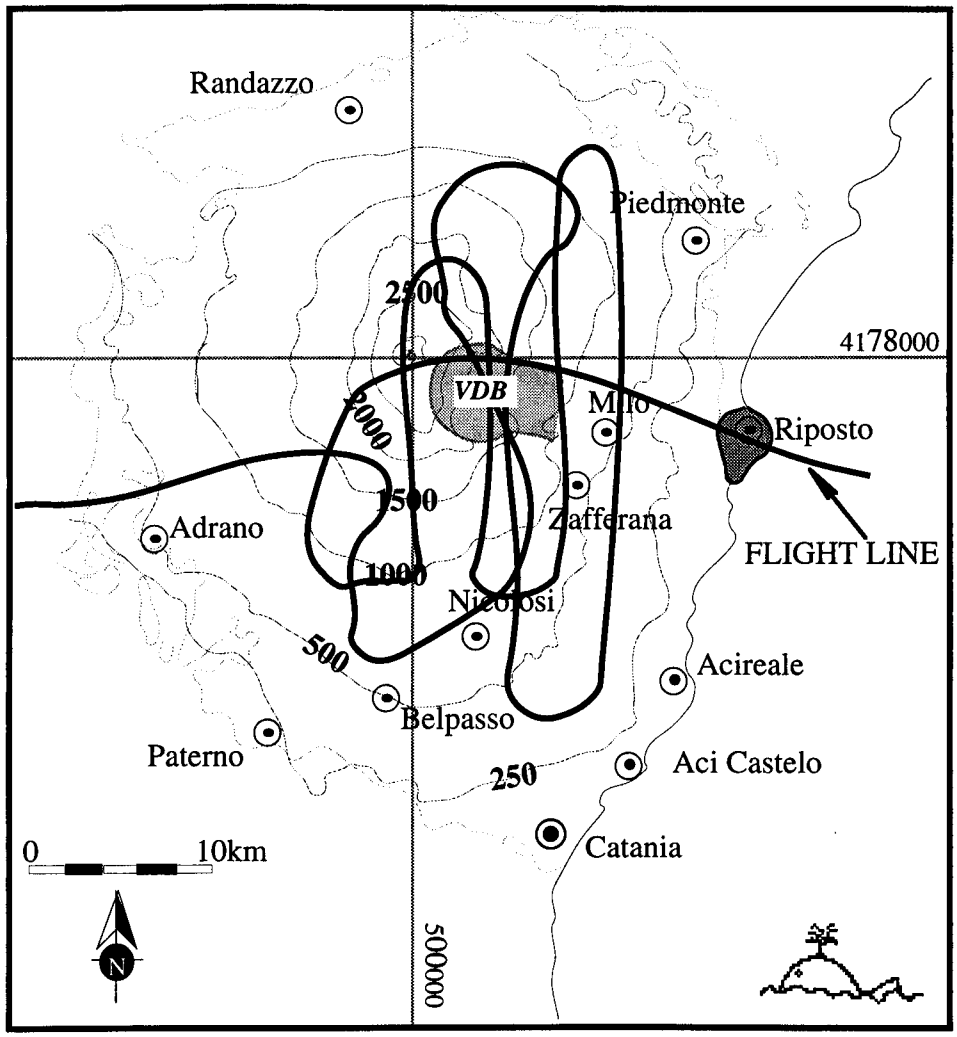

Figure 4.4. Aeromagnetic flight lines. This figure shows the approximate position of the flight lines in relation to the topography of Etna. The extent of the volcanics is given by the thin grey line, VDB = Valle del Bove; dark shadded region repesents the Chiancone deposit

The final step is the removal of the geomagnetic field by subtraction of the International Geomagnetic Reference Field (IGRF) model. This model defines the theoretical undisturbed magnetic field at any point on the Earth's surface [*Kearey and Brooks*, 1984]. The removal of these effects produces the final data set allowing for the identification of any anomalous areas (discussed in section 5.3).

Chapter 5 Results and Interpretations

5.1. Ground Deformation Results:

easurements carried out on the upper slopes of the volcano have shown that movement occurs in association with eruptions [*Murray.* 1990], and over short time periods may result in a significant movement of the upper slopes of the Valle del Bove [*McGuire et al.*, 1991]. Whether or not this movement is then transferred downslope is uncertain. In addition to this possible source of movement, the lower parts of the Valle del Bove as well as the town of Milo rest on steep fault scarps (the Timpe Faults) which are composed mostly of pyroclastic and volcaniclastic material. This material can be expected to be unstable, and thus this slope must be considered unstable. In an attempt to monitor this instability a small network of stations has been set up around Milo, this network is shown in figure 3.4 (see appendix B for station location maps). Two sets of measurements were made; one in July 1994, the other December 1994. The results are shown in tables 5.1 and 5.2.

The initial assumption for this network is that, relative to the floor of the Valle, points such as Monte Pomiciaro and Bloody Flies are stable; while Milo should represent an area of instability. Elevation changes are more difficult to measure due to the increase in error in elevation determination in GPS; however such changes are also expected. Given the errors discussed in chapter 3 changes in horizontal distances of greater than 10mm and elevation changes of greater than 60mm should be detectable.

The final data for the Milo Network suggests that some movement has taken place with several baselines increasing in length and one (Milo Top to Milo Church) decreasing (table 5.3). This gives the overall impression of a slight movement of the station Milo Top down slope. However, as only one set of measurements relative to Monte Pomiciaro has been made to date it is impossible to be certain of the true movement vectors based on these baseline lengths. Figure 5.1 shows a somewhat different result, with no clear direction of movement being seen. This diagram shows the result of performing a datum transform on

the December data set, using the July 1994 Milo Top co-ordinates. Also shown are the error ellipses for the stations. As can be seen, for no station does movement outside the boundaries of the error ellipse occur. The smaller error ellipses for December result from better constraints due to the use of two base stations.

Table 5.1. GPS results for Milo Network JULY 1994.

STATION	REFERENCE STATION	BASELINE LENGTH	HEIGHT DIFFERENCE (m)
Milo Church	Milo Top	1445.435	-157.507
Milo Church	Milo Top	1445.443	-157.565
Mt. Fontane	Milo Top	2113.158	399.550
Mt. Pomiciaro	Milo Top	4186.755	593.039
Bloody Flies	Milo Top	5101.262	281.970

Table 5.2. GPS results for Milo Network DECEMBER 1994.

STATION	REFERENCE STATION	BASELINE LENGTH (m)	HEIGHT DIFFERENCE (m)
Milo Church	Milo Top	1445.425	-157.461
Milo Church	Milo Top	1445.436	-157.499
Mt. Fontane	Milo Top	2113.180	399.689
Bloody Flies	Milo Top	5101.273	282.056
Mt. Pomiciaro	Milo Top	4186.764	593.138
Milo Top	Mt. Pomiciaro	4186.757	-593.120
Milo Church	Mt. Pomiciaro	4677.450	-750.579
Mt. Fontane	Mt. Pomiciaro	3410.543	-193.414
Bloody Flies	Mt. Pomiciaro	1805.660	-311.122

Table 5.3. Changes in Baseline Length and Elevation, July to December 1994.

BASELINE	ΔLINE LENGTHS[1] (mm)	ΔHEIGHT DIFFERENCE[1] (mm)
Milo Top - Milo Church[2]	-8.5	-56
Milo Top - Mt. Fontane	22	139
Milo Top - Mt. Pomiciaro[2]	5.5	9
Milo Top - Bloody Flies	11	86

1. A negative number indicates shortening in line length/reduction in height difference;
2. Average values have been used for these stations.

One point to note is that the method of determining the co-ordinates by constraining one point effectively forces that point to be the "stable" reference point. Thus if all stations have moved relative to each other and at the same time the chosen reference point has moved the results will become increasingly complicated and at the same time it will appear as if the base station has not moved. Results seen by other workers in this area [*SCIENCE*, 1994]

show Milo has moved 3cm towards the South-East (approximately along the bearing of 110°) between September 1993 and 1994. The main difference in the two data sets being the larger data coverage of the SCIENCE report showing that this movement occurs over the whole of the Eastern Flank (movement varies from 1 to 3cm, and North-East to South-East in direction) over the same time period. Thus if we consider only the baseline changes (table 5.3), the lines in the direction of the slope (i.e. Monte Pomiciaro-Milo Top; Bloody Flies-Milo Top; Monte Fontane-Milo Top) appear to increase in length, while the up-slope line (Milo Church-Milo Top) appears to reduce in length, then it appears as if Milo Top is in fact moving down slope. However by forcing the two different data sets to have the same co-ordinates for Milo Top this result is lost within the error ellipses, and possibly hidden by the relative movement of the other stations. Bloody Flies was located outside the area of the Valle del Bove in the hope that it would be in a (relatively) stable area, if this is the case then the movement vectors of figure 5.1 can be interpreted as Milo Top moving downslope, together with Monte Pomiciaro and Monte Fontane (ignoring the error ellipses for the moment). Measurements made in July 1995 of the baseline Bloody Flies-Milo Top shows no changes since December 1994 (J. Murray, unpublished data).

No attempt has been made to consider the 3 dimensional movement by considering elevation changes as well as positional changes. Data from *SCIENCE*, [1994] shows no significant elevation changes.

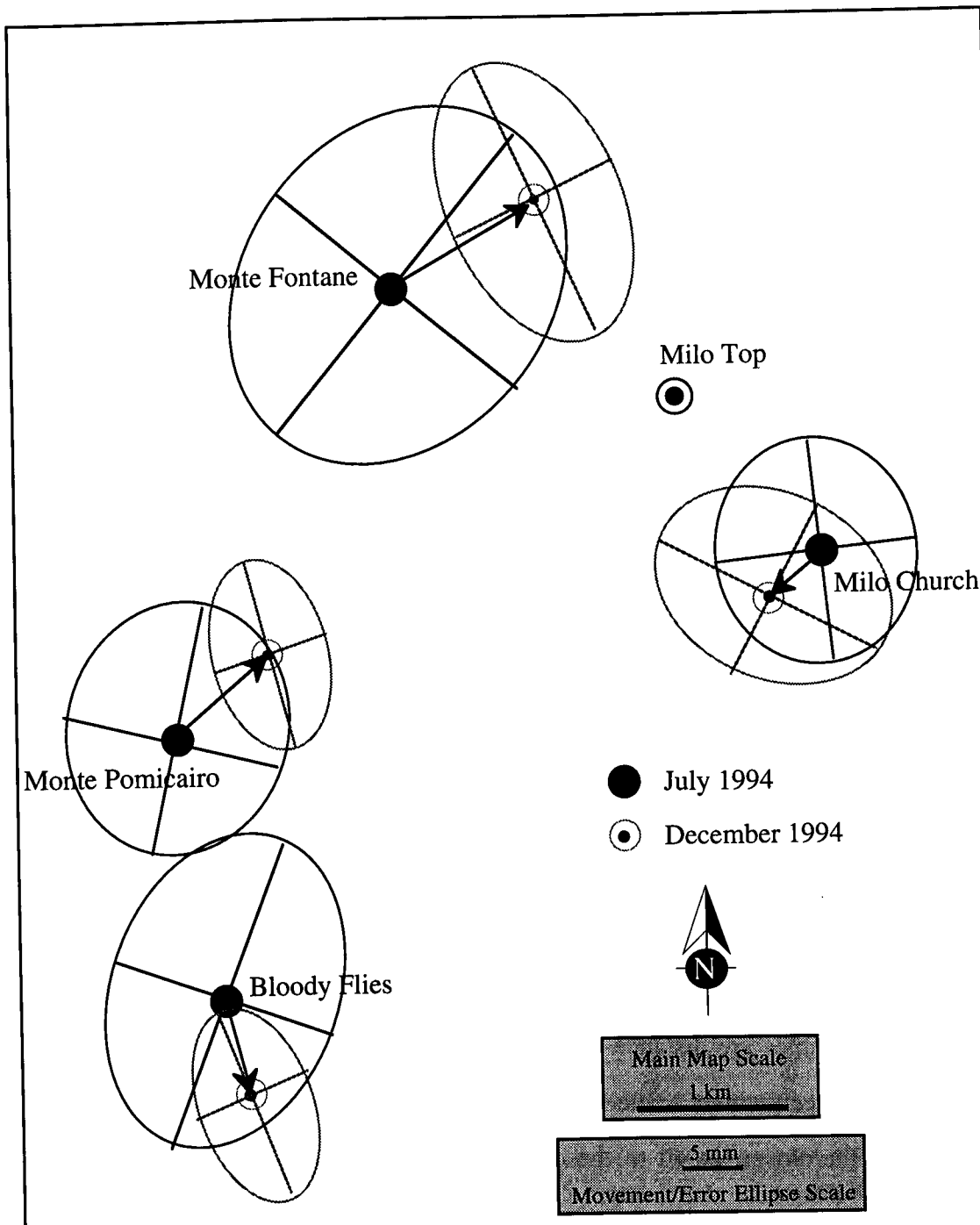

Figure 5.1. Results of the Milo Deformation Network, July-December 1994. The two sets of co-ordinates have been calculated by the use of the Datum Transform part of the Ski software, by holding the co-ordinates of Milo Top fixed. The resultant movement is indicated by the arrows, the scale of the error ellipses and the movement vectors are the same.

5.2. Gravity Data:

This section describes the results obtained from the gravity data of chapter 4. These results will be used for computer modelling (chapter 6) together with the aeromagnetic data.

5.2.1. The Bouguer Anomaly Map:

In order to study the Bouguer Anomaly, contour maps were prepared using UNIMAP (figure 5.2), which is an interactive package for the contouring and display of spatial (x,y,z) data [*UNIRAS*, 1990]. In order to contour the data it is necessary to create a regular grid from the irregular data set. The program allows the user to specify the parameters used to produce this grid: grid size (node spacing); interpolation method; interpolation parameters. For this work the bilinear interpolation method was chosen (*UNIRAS*, [1989] gives the specifics of the interpolation procedures). This method assigns the value for each station to the nearest grid node; where several stations are close to the same node, the distance weighted average value is used. For nodes where no value has been assigned the nodal points with values are used to calculate the function value. The search radius chosen limits the distance to which the valueless nodes may look for node(s) with a value; within the search area the values are distance-weighted. The search radius limits the amount of interpolation between widely scatted data (i.e. greater than the grid size): the smaller the search radius the closer the fit to the observed data, although gaps may occur in the contours. Quadratic interpolation is then used to smooth the interpolated grid. Several initial maps were drawn using no smoothing and small search radii, this allowed for the detection of erroneous points in the data, several of which were detected and then either corrected where appropriate or removed.

Figure 5.2b shows raw Bouguer Anomaly data (i.e. the reduced gravity data) plotted as a 2-D line contour map using the local UTM grid references, derived by the use of the Datum Transform part of the SKI softwere. This data set was interpolated with a search radius of 2km, thus producing some holes in the coverage. UNIMAP can also be used to produce 3-D maps with the gravity data draped over topography (figure 5.2c), this allows for the analysis of the relationships between the Bouguer anomaly and the topography.

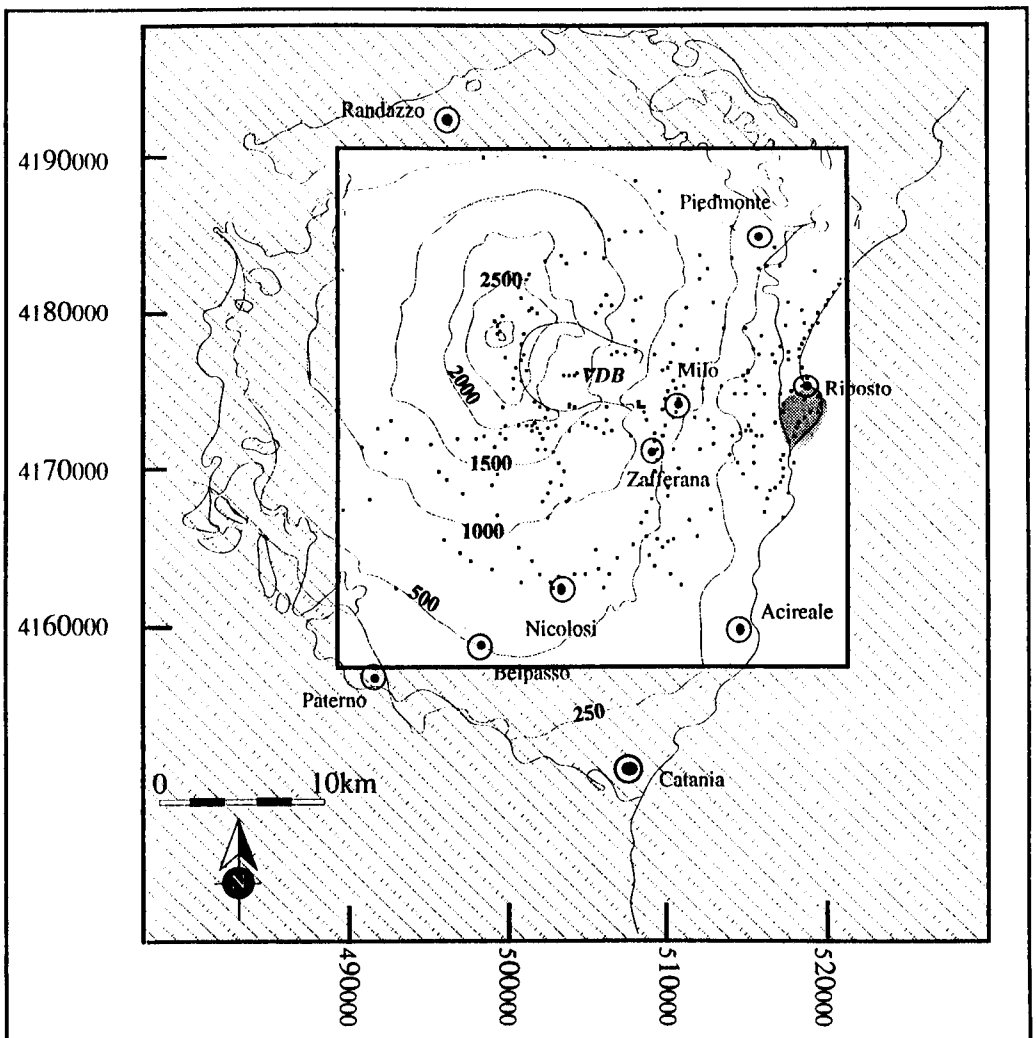

Figure 5.2. Gravity Data

a. The highlighted area of this map corresponds to the area covered by all the gravity contour maps (figures 5.2 b&c, 5.3 and 5.6.). Dots represent the gravity stations; VDB = Valle del Bove

b. (overleaf) Bouguer Anomaly map for the data set of this study. The stations are marked by dots. A rough North-South gradient can be seen in this data. Contours are in mGals.

c. (overleaf) Bouguer anomaly data draped over the topography. The correlation between the Summit region and an area of low gravity is clearly seen, although this is the only correlation seen between topography and gravity in the figure. Colours show the gravity values in mGals

Figure 5.2b: Bouguer Anomaly Map

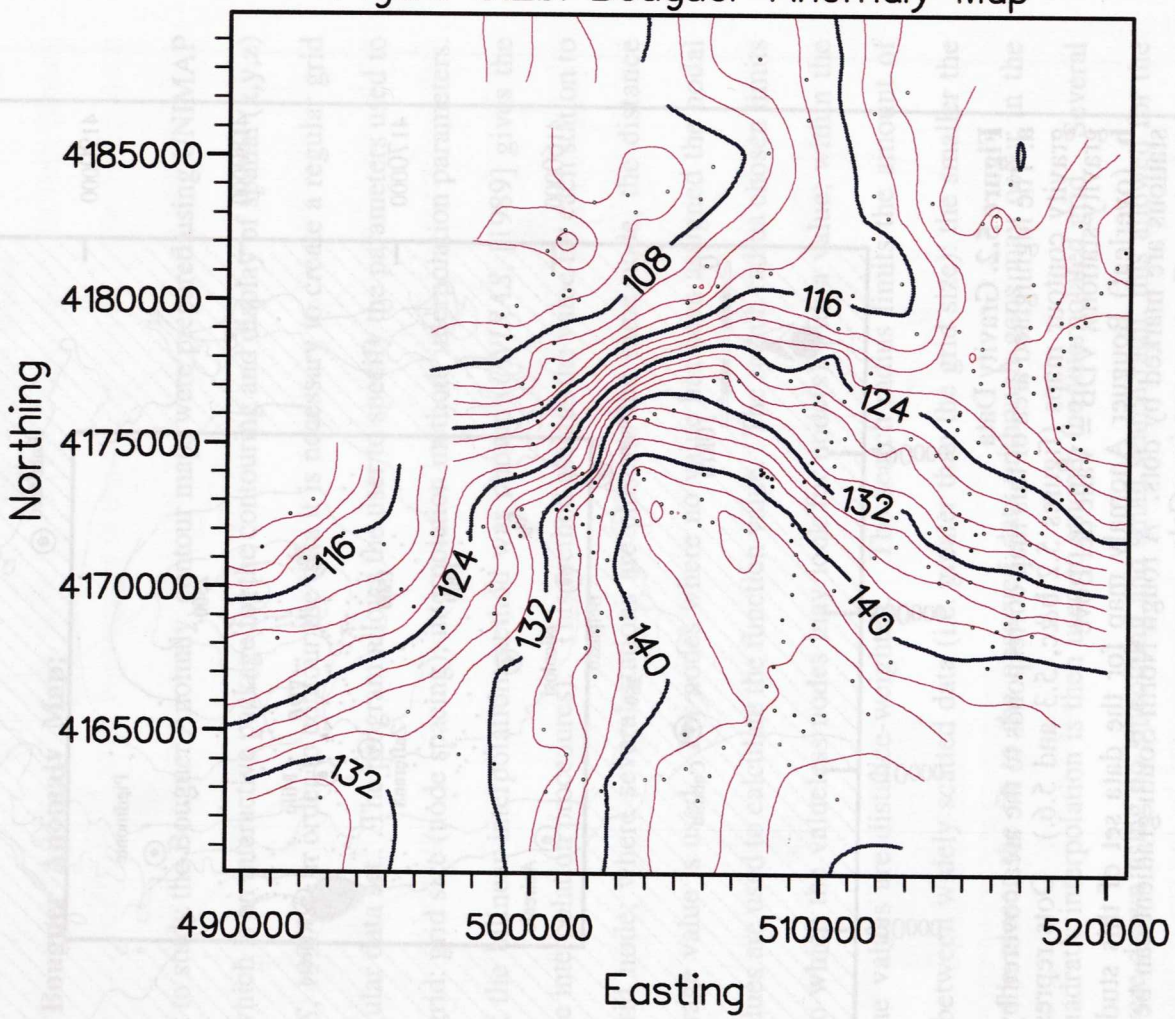

Figure 5.2c. Bouguer Anomaly draped over topography

View from the SW

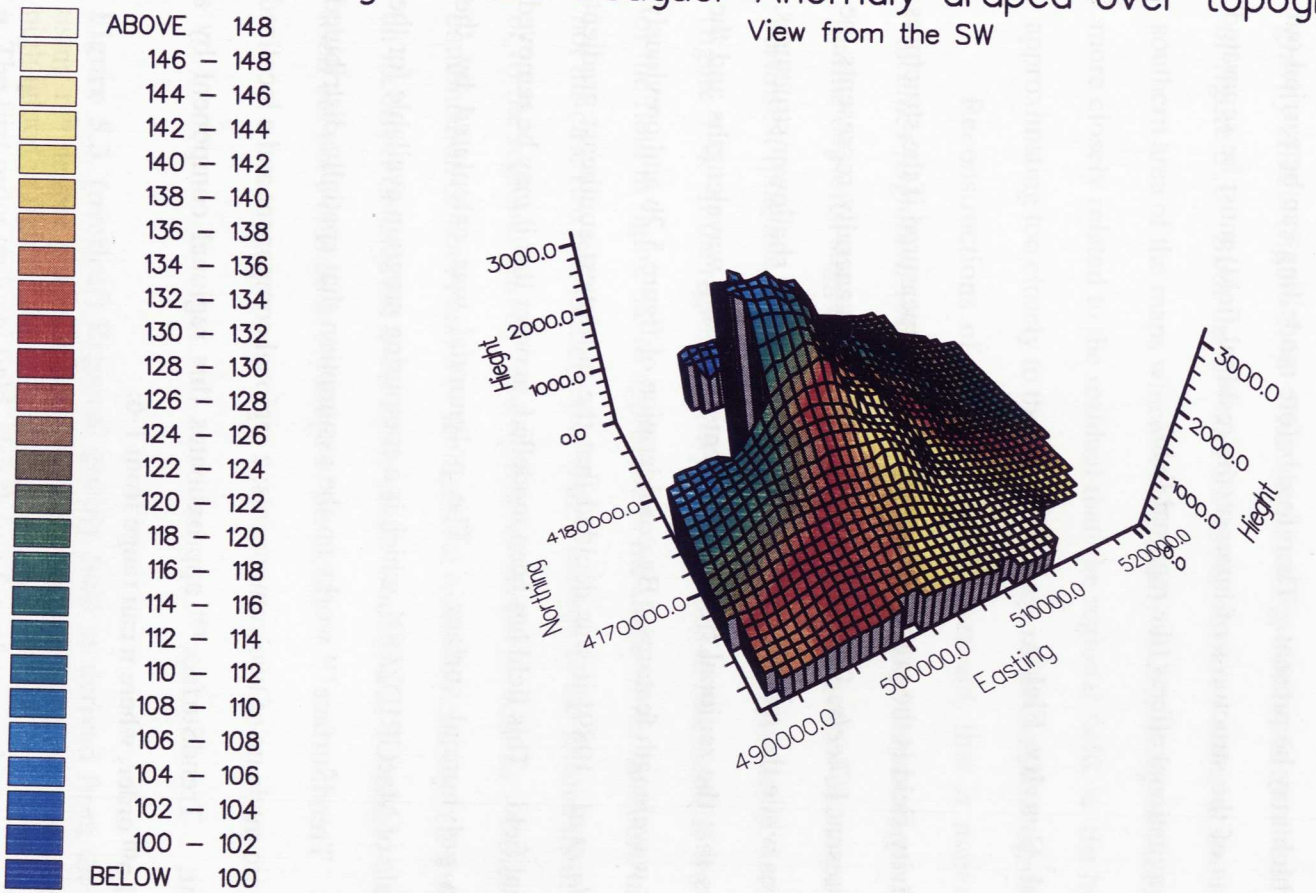

The main feature of the Bouguer map is the north-south gradient, with gravity clearly decreasing in a northwards direction. This gradient is discussed in the next section. The other point that comes to light in figure 5.2c is the strong negative anomaly associated with the upper flanks of the volcano. One possible explanation for this feature is the use of an incorrect density in the reduction of the data, however as this is the only place where such a correlation between topography and gravity occurs it seems more likely that this is a real affect of the low density material of which the summit is composed. A strong positive anomaly is also seen in the central and Southern parts of the Eastern Flank.

The strong gradient in the data causes problems in the analysis of the maps and masks any local anomalies which may be present. Therefore before modelling can be carried out the gravitational effects of the structures of interest (the residual field) must be separated from the broad scale gravitational effects (the regional field).

5.2.2 The Regional Gravity Field:

The regional gravity field is the gravity field that would be measured if the structures of interest were not present [*Skeels*, 1967] i.e. the regional field generally represents the deeper, larger structures while the residual field represents the smaller shallower structures. In general, this means that the regional field is represented by long wavelengths and the residual field by short wavelength features. By consideration of figure 5.2b and previously published data [*Loddo et al.*, 1989] it was decided that the northwest-southeast gradient represented the regional field. This field has been modelled, in order that it may be removed from the data, by a polynomial surface. The polynomial was calculated by the TrendSurface™ module of MacGRIDZO™, which is a contouring program available for the Macintosh computer. TrendSurface™ works on the assumption that spatially distributed data (i.e. x, y, z data) are made up of two components: a regional component and a localized (residual) component. TrendSurface™ approximates this regional component by a polynomial surface of n^{th} order, where n can range from 1-6:

$$1^{st} \text{ order: } z = c_i + c_j x + c_k y$$

$$2^{nd} \text{ order: } z = c_i + c_j x + c_k y + c_l x^2 + c_m xy + c_n y^2$$

etc.

where c_{i-m} = are constants.

Once a polynomial surface has been chosen TrendSurface™ will calculate the residual value for each data point within the data set.

Polynomial surfaces with n = 1 to 3 were determined for the data set in this work (figure 5.3). *Loddo et al.*, [1989] shows a regional field based on data covering a larger area than this study and therefore (possibly) better representing the border scale regional gravity effects (figure 5.4). This shows strong similarities to the 1st order polynomial field of figure 5.3. Both the 2nd and 3rd order surfaces show a strong circular shape in the southern area of the maps which is also clearly visible in figure 5.2b, and is interpreted to be more closely related to the residual than the regional field, ie. the higher order surfaces are approximating too closely to the whole data set, rather than the regional component alone.

Reconstructions of the sub-Etnean basement, that is material directly below the volcanics [*Ogniben*, 1966; *Stewart et al.*, 1993] based on outcrops of pre-Etnean Quaternary marine deposits, suggests that the sediments are present at elevations of up to 1100m in the northwest (possible as high as 1300m NW of the summit area), decreasing towards the sea (figure 5.5). If the regional gravity field was due to this material we would expect the shape of the field in figure 5.3 to approximate the shape of the contours in figure 5.5. As this is not the case two possiblities exist: i) the contours of the sediments in figure 5.5 are incorrect or ii) the regional gravity field represents deeper structures. Other possibilites included a combination of both i and ii or an incorrect reduction density. If the data was reduced with an incorrect density the most likely result would be of a change in values and the gradient itself but not a change in the shape of the field.

Figure 5.3. (overleaf) Regional gravity field as derived from the data set of this study using n^{th} degree polynomials. The area covered by these maps corresponds to the area highlighted in figure 5.2a.
a. The first order regional field, also shown for reference, is the coast line.
b. The second order field.
c. The third order regional.

Figure 5.3a First order regional field

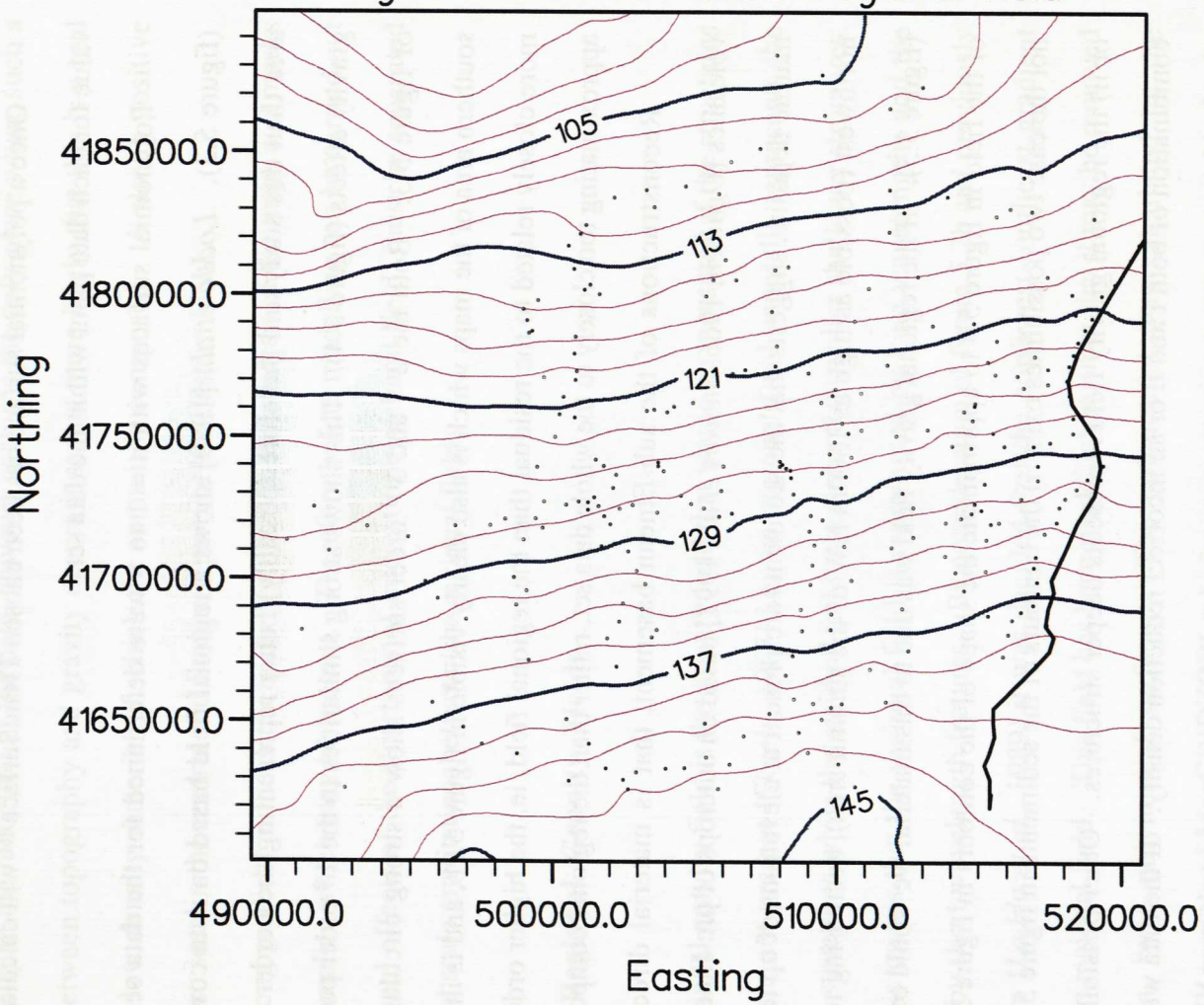

Figure 5.3b: Second order regional field

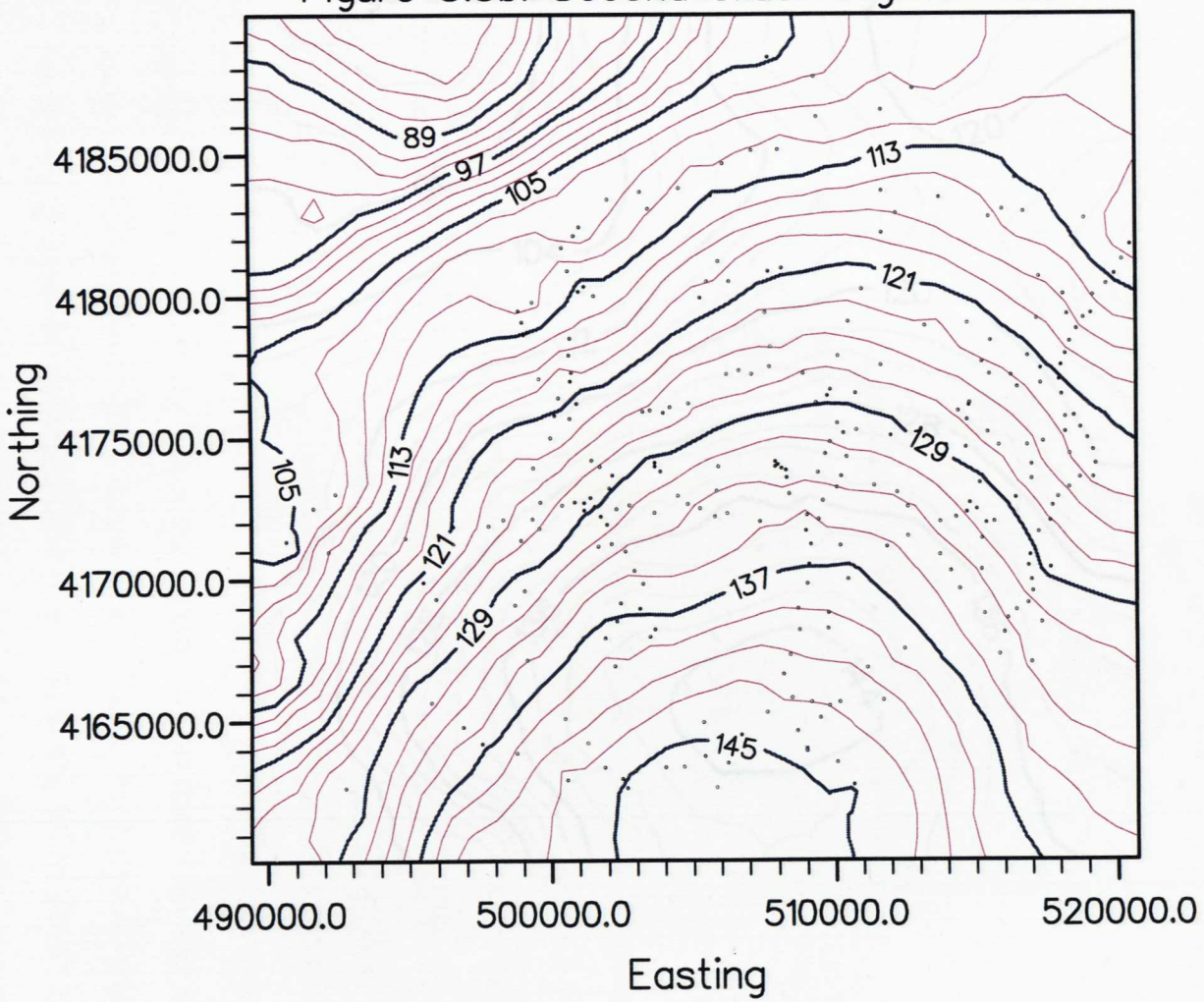

Figure 5.3c: Third order regional field

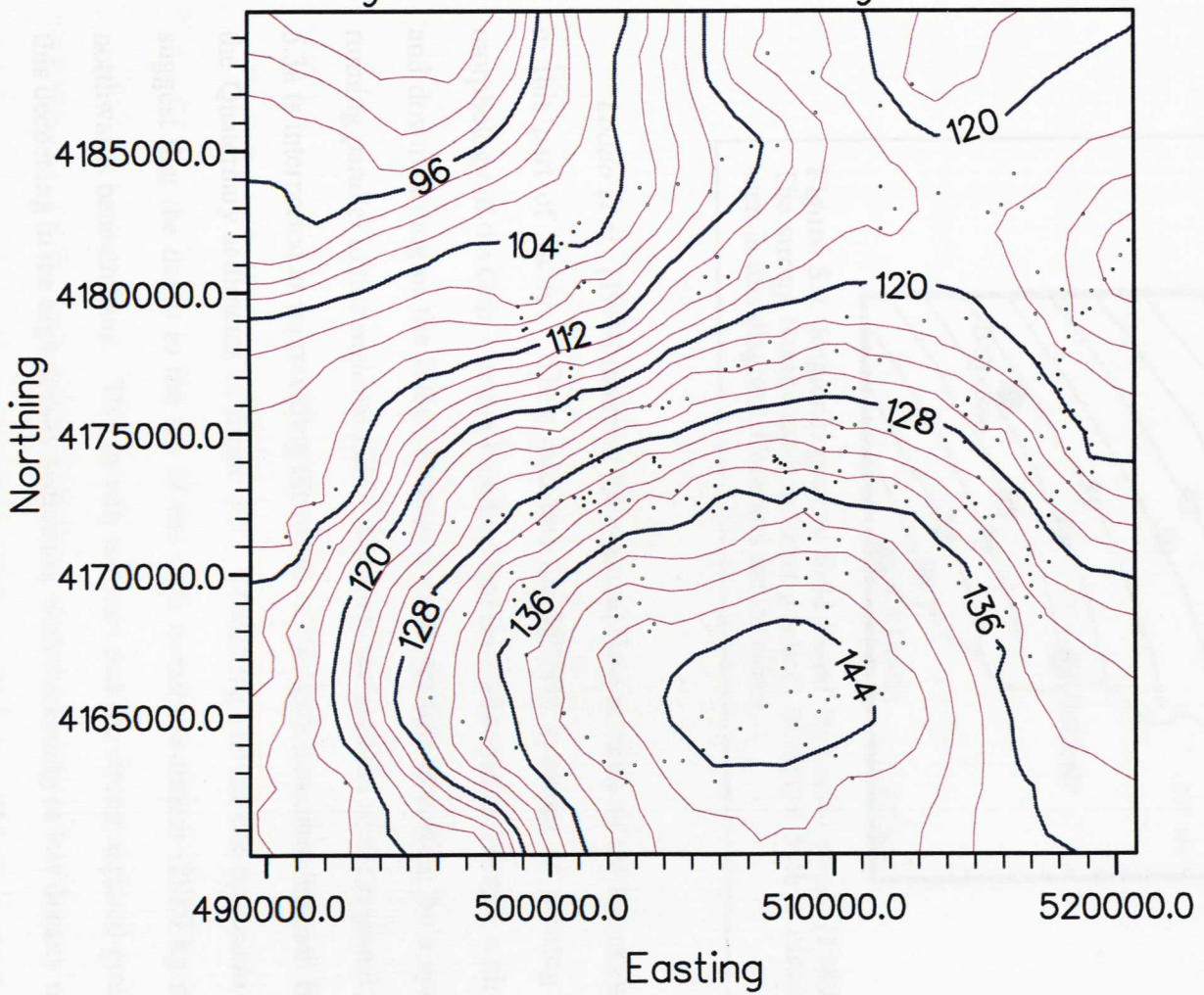

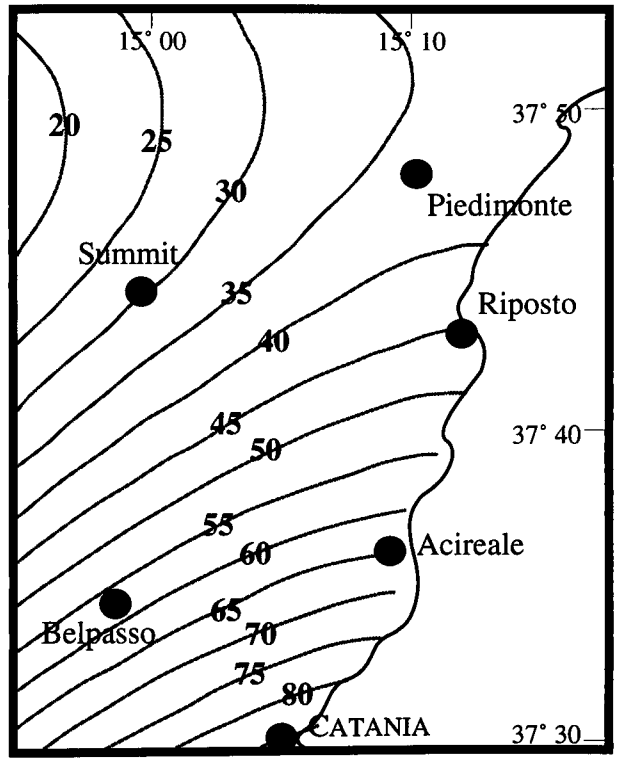

Figure 5.4. Regional gravity field based on *Loddo et al.*, [1989]. The strong Northwest-Southeast gradient of figure 5.2b is clearly seen in this diagram. Contours are in mGals.

Loddo et al., [1989] interpret the regional field in terms of the basement morphology in this part of Sicily. They interpret the SE-NW gradient as relating to the broad morphology of the Gela-Catania Foredeep and the Caltanissetta Trough, with the stretching and downwarping of the Iblean Plateau northwestwards occurring by a system of faults running parallel to this regional field. Similarly the gradient of the regional field of figure 5.3a is interpreted as representing the shape of the deep basement beneath Etna i.e. below the Quaternary sediments of figure 5.5. Modelling carried out by *Loddo et al.*, [1989] suggest that the depth to the top of the high density sediment (2920 kg m^{-3}) increases northwards beneath Etna. This in turn suggests that the strong regional gradient relates to this deepening in the high density sediments, with thickening in low density material, which may be either Etnean volcanics or low density sediments. This is supported by borehole data collected several kilometres northwest of Etna which shows that low density sediments (2500 kg m^{-3}) are present at 4000m depth [*Caupano et al.*, 1993] while on the Eastern and

Southern Flank of Etna *Loddo et al.,* [1989] show high density sediments (2920 kg m^{-3}) at less than 2km depth.

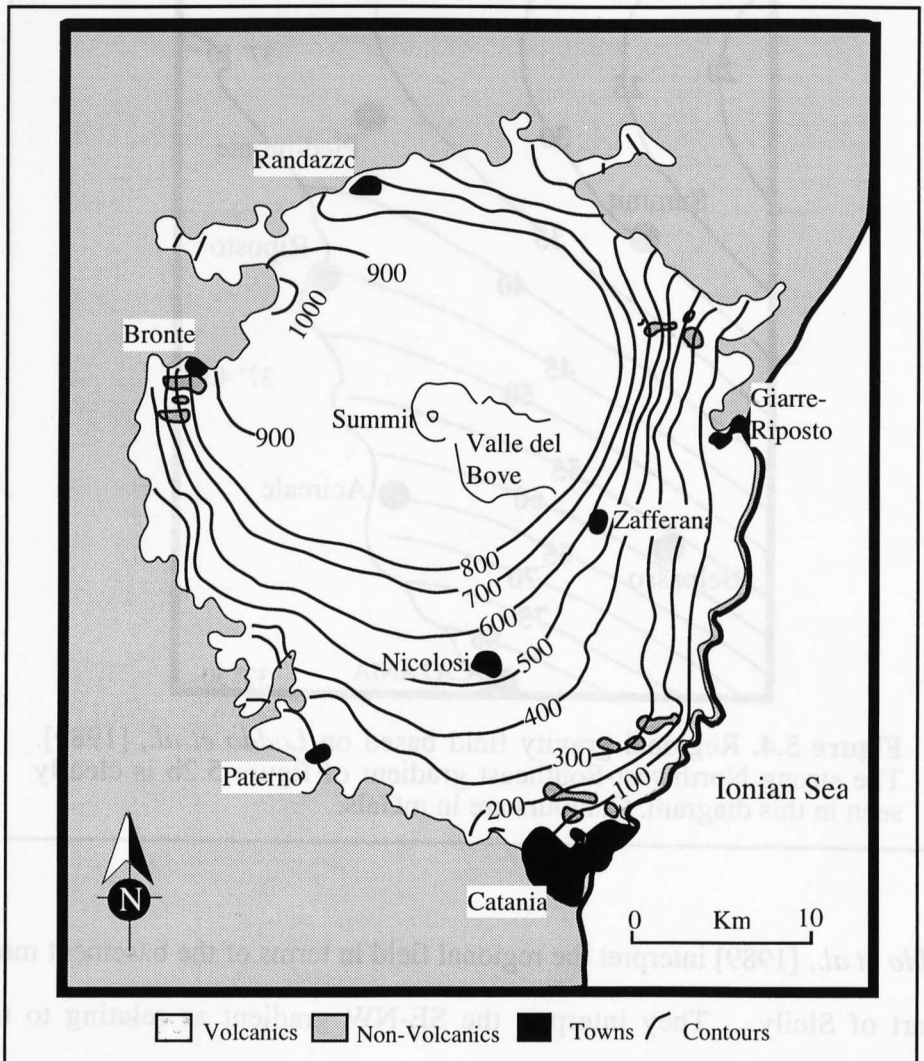

Figure 5.5. Contour map of the sedimentary basement of Etna (the Quaternary marine clays), after *Stewart et al.,* [1993]. It is important to note that this map is drawn from very limited evidence, based on outcrops within the volcanic pile.

5.2.3. The Residual Field:

Once the regional field has been removed from the data the residual field should represent the gravity signature of the structures of interest, in this case the sub-surface structure of the edifice. The residual anomaly map of figure 5.6 is that resultant from the removal of the 1st order surface, which was chosen as the most representative of the regional structure.

Figure 5.6 shows a number of features worth noting:

☞ A positive anomaly (+16 mGal) associated with the Southern half of the Valle del Bove;

☞ A negative anomaly (-10mGal) associated with the summit region;

☞ A second negative anomaly (-10 mGal) associated with the Chiancone deposit.

The anomalies associated with both the summit region and the Valle del Bove are visible to some extent, but poorly defined, in previously published works [*Loddo et al.*, 1989; *Neumann et al.*, 1985], this poor definition is in part due to the large regional coverage of these surveys and hence the low station density around the Valle del Bove and upper Flanks of the volcano. The 14 stations covering the floor of the Valle del Bove in this study help to better constrain the shape of the anomalies. These two features can be explained in terms of the low density summit material producing an area of low gravity, and a high density body leading to an area of high gravity, this body appears to coincide with the seismic velocity high zone of *Cardaci et al.*, [1993] and *Hirn et al.*, [1991].

The Chiancone deposit has not shown up as a significant anomaly in previously published work, although in the map of *Loddo et al.*, [1989] there is a small low in the area of Riposto. The greater station density of the present study allows for better definition of this anomaly. On figure 5.6 the outline of the Chiancone deposit has been included. As can be seen the anomaly and the deposit do not directly overlie, that is, the centre of the geographical extent of the material does not coincided with the centre of the anomaly. The shape of the anomaly is interpreted as representing the shape of the structure which the Chiancone has infilled. Thus the Chiancone must have been deposited in a deep basin, the deepest parts of which are either along the coast or off-shore, as there is no off-shore gravity data available it is impossible to completely constrain the shape of both the anomaly and the causative structure. Computer modelling of the gravity data allows for a more detailed interpretation than simply "looking at the map" and is covered in the next chapter.

Figure 5.6. (overleaf) Residual gravity field. This figure shows the residual field derived by subtracting figure 5.3a from 5.2b and therefore allows for the identification of local anomalies such as the low near the coast and the high over the Valle del Bove. The area of this map is as for figure 5.2a. The outlines of the Valle del Bove, the Chiancone deposit and the coast line are shown by the blue lines.

Figure 5.6: Residual Gravity Field

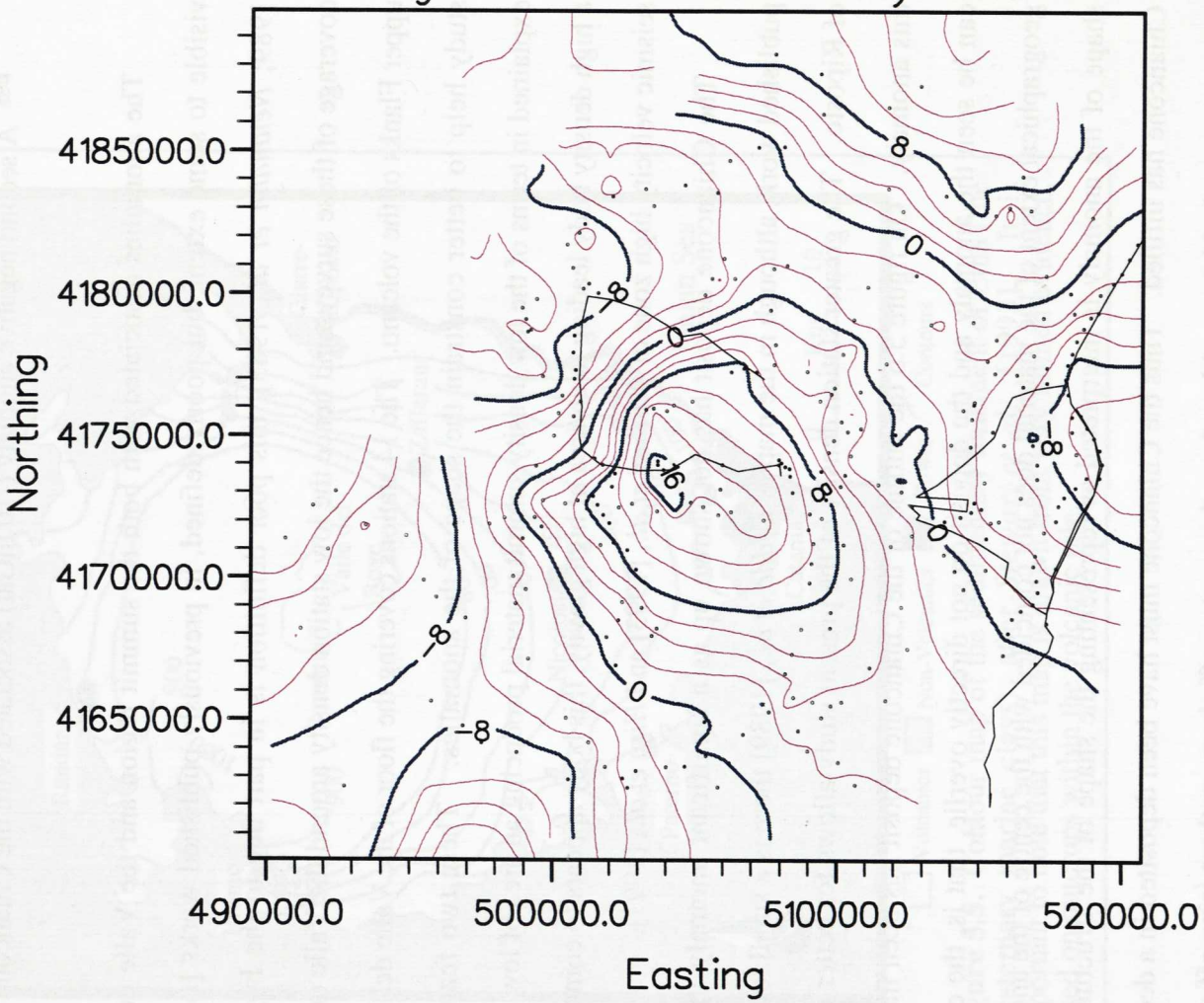

5.3. Aeromagnetic Results:

The aeromagnetic data have been plotted within UNIMAP, in a similar manor to the gravity data, this allows for the identification of areas of anomalous structures. In this case there is no need to remove any regional effects, once the reference geomagnetic field has been removed, and thus the data is available for interpretation immediately. The main feature of figure 5.7 is the strong anomaly associated with the summit region of the volcano. Such a bipolar anomaly, with the positive part to the south and the negative part to the north, is caused by a normally magnetised body, i.e. a body whose direction of magnetisation is approximately parallel to the present day's geomagnetic field. It is likely that the magnetic effect of the summit scoria deposits will be low as they will be normally magnetised but lying in random orientations, thus largely self-cancelling. The strong anomaly associated with the summit region may result from material at depth which is also normally magnetised.. The palaeomagnetic work on Etna suggests that this is the case for the majority of the material making up the exposed deposits. This aeromagnetic anomaly suggests that this also holds for the material at depth below the summit, thus all the upper parts of the volcano may be considered as young (<40 000yrs.). Several excursions of the geomagnetic field have occurred during the time that Etna has been active, with the youngest being at approximately 46 000 yrs ago [*Levi et al.,* 1990], but there is no evidence of significant deposits being present which show magnetic properties relating to these excursions.

The geomagnetic field is significantly more complex than the gravity field, being composed of several components (gravity has only one - vertical), as are the anomalies due to magnetic bodies. Unlike gravity, the shape of magnetic anomalies may bear no relationship to the shape of the causative body and therefore interpretation of magnetic anomalies can be significantly more difficult. Due to the difference between the two fields it is very rare for an area of a gravity anomaly to correspond directly to a magnetic anomaly, thus direct comparison of figures 5.6 and 5.7 does not aid interpretation.

The aeromagnetic data will be combined with the gravity data in the computer modelling (chapter 6), providing an additional constraint, helping to ensure that the models are not too unrealistic

Figure 5.7: (overleaf). Aeromagnetic data. This map shows the aeromagnetic data used in the 2.5-D modelling, together with the position of the flight lines. The strong anomaly associated with the summit region is clearly visible, while there is no clear expression for other significant anomalies of figure 5.6. The Valle del Bove, Chiancone and coast line are shown for reference. Contours are in nT.

Figure 5.7: Aeromagnetic anomaly map.

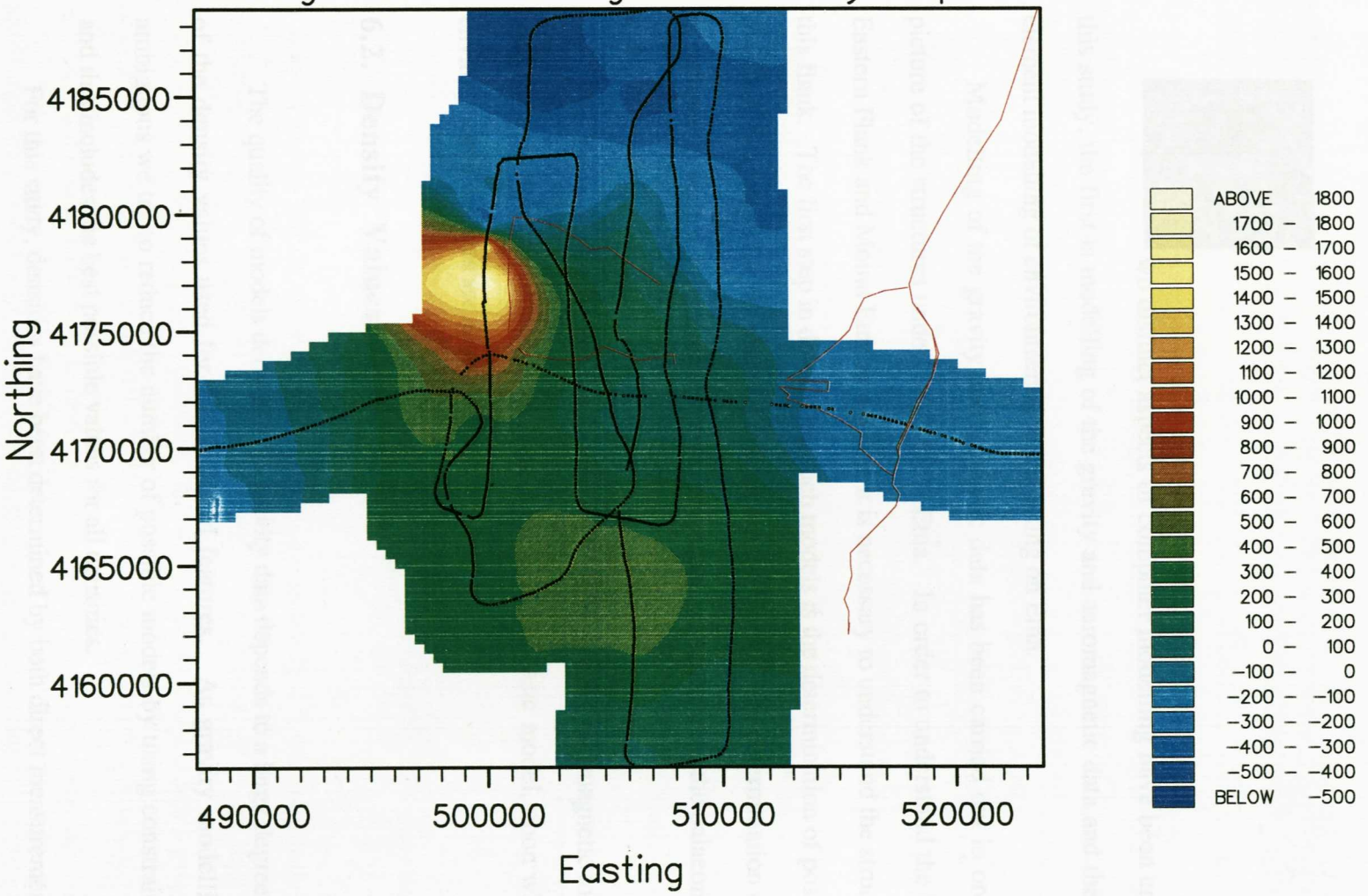

Chapter 6 Computer Modelling

6.1. Introduction:

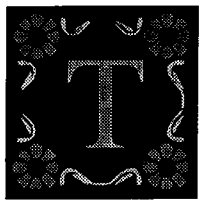

wo distinct aspects of computer modelling have been carried out within this study, the first is modelling of the gravity and aeromagnetic data and the second is finite element modelling of environmental forces acting on Etna.

Modelling of the gravity and magnetic data has been carried out in order to develop a picture of the structures underlying Mount Etna. In order to understand the behaviour of the Eastern Flank and Mount Etna as a whole it is necessary to understand the structures making up this flank. The first step in developing such models is the determination of possible density and magnetic properties for the material making up the Flank. The determination of density values is outlined in section 6.2, while magnetic properties are taken from the palaeomagnetic work or published data.

The finite element modelling follows on from the gravity and magnetic modelling in that it uses the structures developed from these models as the basic model, upon which a variety of environmental changes are allowed to act.

6.2. Density Values:

The quality of models derived from gravity data depends to a large degree on the reliability of the density values used for the modelled features. As gravity modelling is inherently ambiguous we try to reduce the number of possible models by using constraining information and this includes the best possible values for all densities.

For this study, densities have been determined by both direct measurement of samples and by the use of Nettleton profiles. The wet and dry densities were measured for a number of samples from the Trifoglietto system (M. Wright, pers. comm. 1992), possibly representing the

high density body seen on the Bouguer Anomaly map. Table 6.1 summarises the various densities and their sources.

Table 6.1. Summary of Rock Densities for the Etna region.

Location	Rock Type	Density[1] (kg m^{-3})	Source
Santa Caterina	Recent Mongibello[2]	2188 ± 95 (b)	G. Brown pers. comm.
		2158 ± 95 (b)	ditto
Praiola (Chiancone)	Debris flow deposits	2405 ± 85 (b)	This Study, Nettleton
Valle del Bove	Cumulate	2910 (d); 2950±5 (w)	This Study, Direct Meas.
Valle del Bove	Recent Lava	2487 ± 75 (b)	This Study, Nettleton
Summit	Pyroclastics and recent lava flows	1939 ± 95 (b)	ditto
Etnean volcanics		2470 (b)	*Loddo et al.*, [1989]
(sub-Etnean Sediments)	Allocthonous flysch	2570 (b)	*Loddo et al.*, [1989]
ditto	Allocthonous flysch	2680 (b)	*Loddo et al.*, [1989]
ditto	Massive flysch; carbonates	2920 (b)	*Loddo et al.*, [1989]
West of Etna	Allocthonous material	2400 (w)	*Caupano et al.*, [1993]
West of Etna	Carbonates (≈4000m depth)	2500 (w)	*Caupano et al.*, [1993]

1 Densities are either wet (w), dry (d) or in-situ bulk (b); errors are given where known.
2 Volcanic deposits ranging in age from 8000 b.p. to the XIV century, comprising lava flows and pyroclastics.

6.2.1. Measuring the Densities:

The Nettleton method is a graphical approach using a gravity profile measured over the feature for which the bulk density is required. For this study one Nettleton profile was undertaken, using 6 stations in a stream cut through a coastal section of the Chiancone deposit. Gravity was measured at each station and relative heights determined by the use of a total station EDM. This gravity data was reduced to a datum (the level of the lowest station has been used) in the same manner as the full gravity data set, including Bouguer and terrain corrections using a standard density of 2670kg m^{-3}, the choice of density here does not affect the calculation. The

reduced gravity and height measurements were then plotted (figure 6.1), and a best fit line drawn through the data. The gradient (S) of this line can be used to derive the density of the material comprising the section:

$$S = \frac{\Delta g}{\Delta h} = 0.3086 - 2\pi G x 10^5 \rho$$

$$\therefore 0.3086 - S = 2\pi G x 10^5 \rho$$

$$\therefore \rho = \frac{0.3086 - S}{2\pi G x 10^5}$$

where ρ = the density to be determined (in kg m^{-3});

Δg, Δh = gravity and elevation change along the profile;

G = Gravitational Constant (6.67 x 10^{-11} m^3 kg^{-1} s^{-2}).

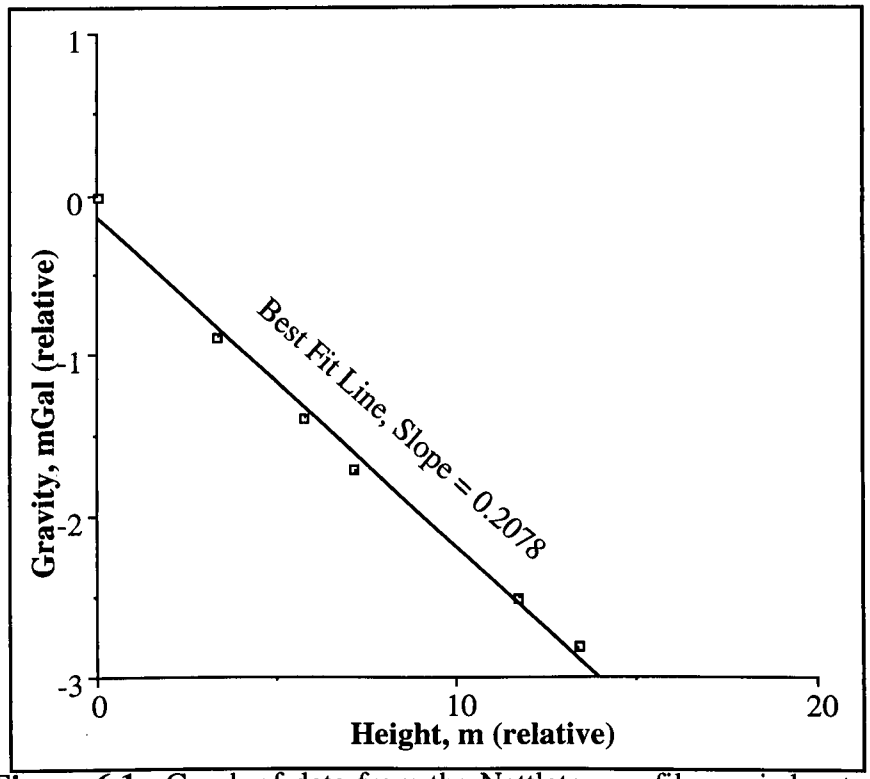

Figure 6.1. Graph of data from the Nettleton profile carried out at Praiola on the Chiancone deposit. The best fit line of the data is shown together with its slope (0.2078; $r^2 = 0.9$). This gives a density of 2405 kg m^{-3} for this material.

Several other bulk densities were determined by using groups of stations from the main gravity data set and plotting them against height; one in the Valle del Bove, over part of the 1991-1993 flow, and the other covering the summit region, using stations from the Sapienza (SAP) to Piano Provenzana (S14) (figure 6.2). The densities determined from these profiles are shown in Table 6.1. The data for the summit region shows a remarkably tight grouping, which suggests that the bulk density (1939 ± 95 kg m^{-3}) of this area is constant with height. Geological maps of the area show an older caldera structure (the Ellittico Caldera) at approximately 2500 m above sea level (southern flank) to 2700 m a.s.l. (northern flank) (*Romano et al.*, [1979] and figure 1.5a), these elevations correspond to 600m and 800m above the Sapienza level (the station SAP is the 0m level in the left-hand graph in figure 6.2, and is located at the Sapienza). The present active vents have developed within this caldera structure. If the two groups of gravity data are used separately to derive densities of inside and outside the caldera structure (figure 6.3), the values found do not differ significantly, given the errors, from the above value: 1899 ± 50 kg m^{-3} for material inside the caldera structure and 2073 ± 200 kg m^{-3} for material outside (the errors given are based on errors in the calculated slope). The material exposed at the surface does not differ significantly (a mixture of scoria and lava flows) and thus this change may reflect sub-surface structures, with denser material at depth, thus affecting the lower parts of this data set more than the upper parts. The errors given for the densities and the lower R^2 values for the inner and outer plots suggests that for the modelling it may be best to use the combined value of 1939 ± 95 kg m^{-3} as the best representative density for this area.

Samples of material collected in pyroclastic deposits around the Southern wall of the Valle del Bove have been used to derive densities. These samples are dense, crystalline material and have been interpreted as a cumulate material related to the feeder system for the Trifoglietto centre (M. Wright, pers. comm. 1992). The densities of the samples were measured by the use of Archimides principle, comparing the weight in air with the weight in water. This allowed the wet (water saturated pore space) and dry (air-filled pore space) densities to be calculated:

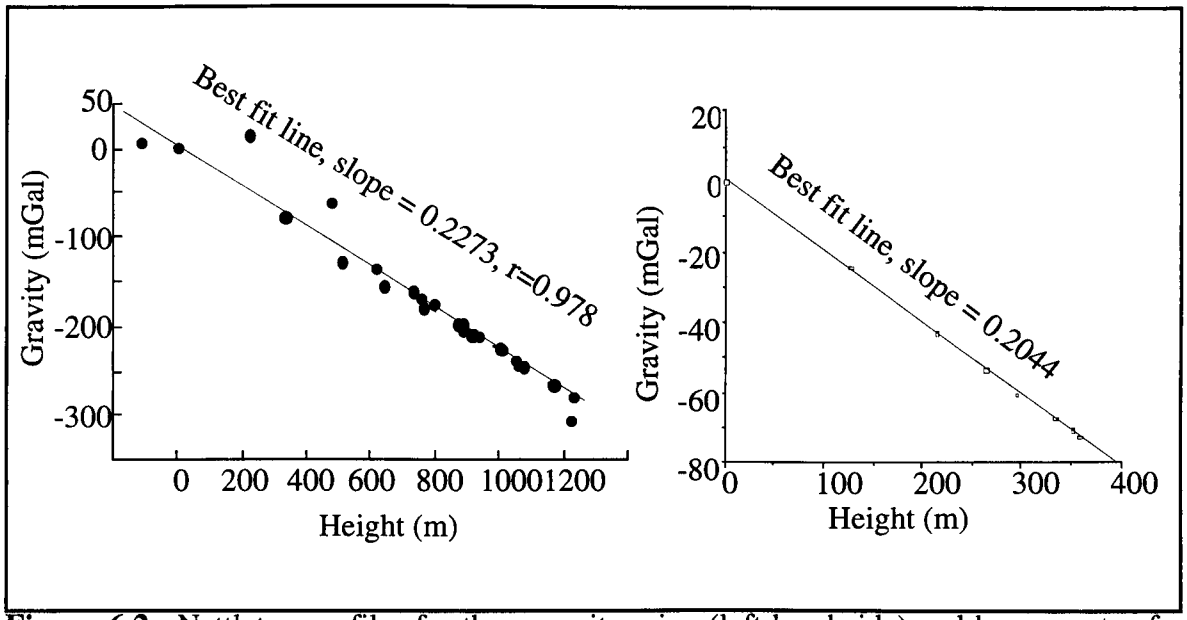

Figure 6.2. Nettleton profiles for the summit region (left hand side) and lower parts of the Valle del Bove. The greater spread in the summit data reflects the larger aerial coverage of this data, although the best fit line still gives a reasonable estimation for the slope, and hence the density (the point (0,0) is the station SAP at the Sapienza).

$$\rho_d = \frac{M_a}{M_{a'} - M_w}$$

$$\rho_w = \frac{M_{a'}}{M_{a'} - M_w}$$

where ρ_d, ρ_w = the dry and wet density respectively;

M_a = dry mass in air;

$M_{a'}$ = water saturated mass in *air*;

M_w = water saturated mass in *water*.

In effect the bottom line of these equations gives the volume of the sample.

As the natural setting for the parent body is at depth and thus likely to be below the water table, it is assumed that the water saturated density best represents the in-situ value.

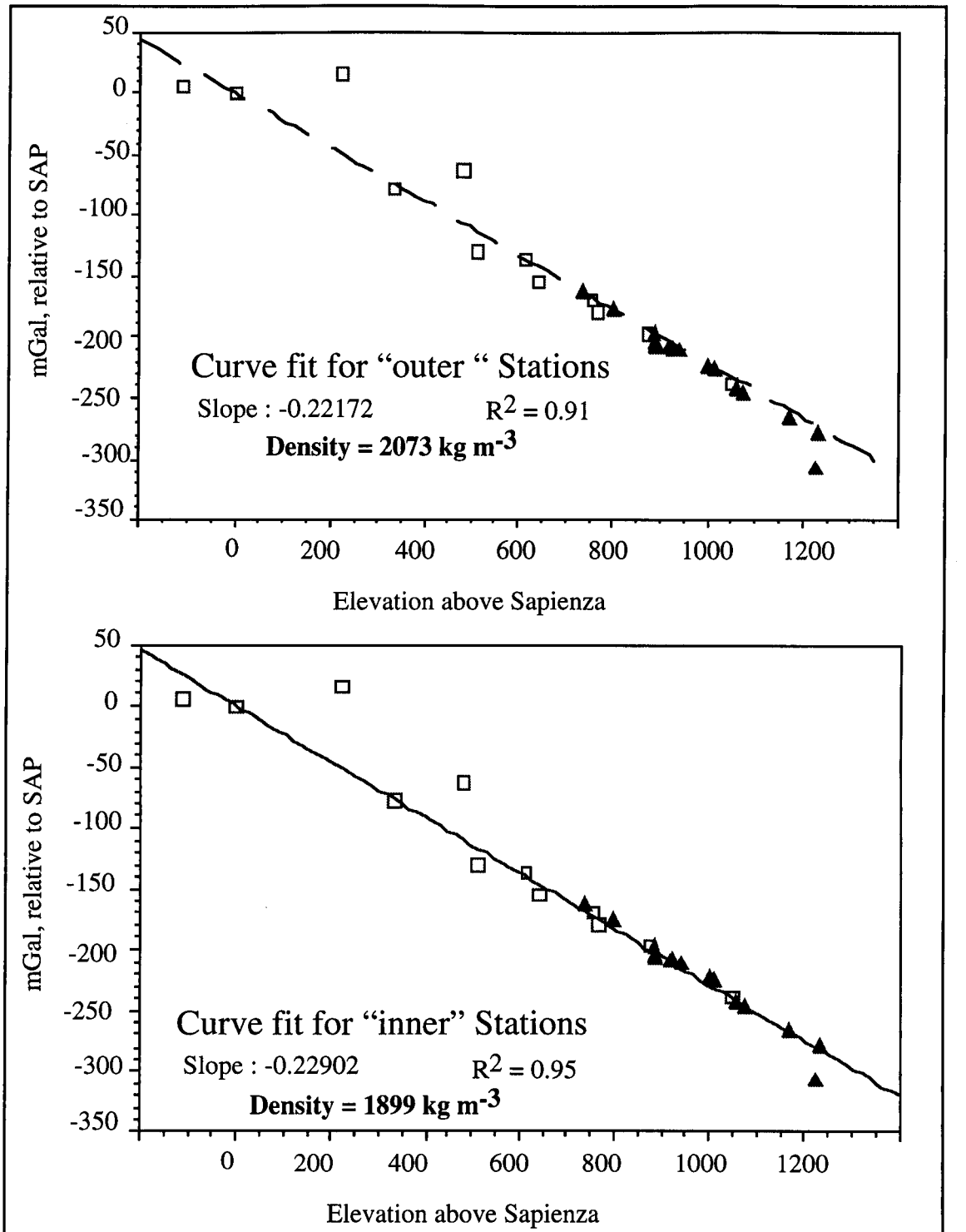

Figure 6.3. Nettleton plots for the summit gravity stations. Inner is defined as those stations which lie within the outline of the old caldera structure; Outer stations lie outside this structure. The slope, regression factor and calculated density are given for each plot.

Table 6.2. Density measurements of samples from the Trifoglietto Centre. Densities are in kg m^{-3}, as are the errors. Sample numbers are from M.Wright pers. comm. Errors are derived from repeat measurements. The average wet density is the one used in the modelling.

Sample	Wet Density	Error	Dry Density	Error
7	2764	35	2717	35
10a	3097	21	3066	25
6	2820	17	2759	21
9'	2964	2	2888	3
9''	2966	2	2907	4
1a'	2932	4	2880	7
1	2965	2	2940	1
4	3137	3	3117	4
9	2947	8	2907	5
6b	2923	2	2884	5
Average	**2951**	**4.5**	**2907**	**4.9**

6.3. Gravity and Magnetic Models:

The main aim of the gravity and magnetic modelling is to build up a picture of the subsurface structures of the Valle del Bove and Chiancone area as well as the Eastern Flank in general. To this end three profiles were used, covering the main features of this area: A-A' cuts the summit and the upper reaches of the Valle del Bove; B-B' covers the Southern wall of the Valle del Bove and the Chiancone; C-C' covers the central part of the Valle del Bove and the Chiancone. The orientations of the profiles were chosen so as to pass through the regions with the greatest data coverage as well as the main parts of the relevant anomalies (figure 6.4).

GRAVMAG, an interactive 2.5-D (2 and $\frac{1}{2}$ dimensional) gravity and magnetic modelling program, designed by the British Geological Survey [*Pedley*, 1991], was used for the initial modelling. A 2.5-D program differs from a 2-D program in that it allows the user to define a *half-strike* , this is the distance that the model polygons extend in the third (unseen) dimension (figure 6.5). This provides a constraint on the third dimension, which is essential in building up an accurate picture of subsurface bodies (e.g. sub-volcanic intrusions, collapse structures,

feeder systems) which are very much 3-dimensional in shape. For the purpose of gravity modelling it is possible to consider any feature with a half-strike of greater than 5 km to be 2-dimensional (i.e. increasing the half-strike beyond 5 km has a negligible effect on the calculated gravity values), therefore the sedimentary basement can be considered as 2-D but the upper parts of the volcanic edifice cannot.

GRAVMAG constructs the subsurface geology based on user-defined interlocking polygons, each with its own density and half-strike. The polygons are then modelled in terms of their density contrast with the background material, thus spurious topographic effects due to an incorrect choice of reduction density are removed by making the background density equal to the reduction density. GRAVMAG allows the shape, density and half-strike of the individual polygons to be changed easily, thus changing the calculated gravity. The user decides when the fit of observed and calculated gravity is "close enough" to consider the model "correct". Gravity modelling is inherently ambiguous and therefore all available constraints have been used to control the modelling. This includes careful consideration of the surface geology and published geophysical surveys (e.g. *Cardaci et al.*, 1993; *Hirn et al.*, 1991; *Loddo et al.*, 1989; *Neumann et al.*, 1985).

Three dimensional gravity modelling has also been carried out using the program GRAV3PLH, a FORTRAN program for the VAX, developed by *Soengkono*, [1990], based on the algorithm of *Barnett*, [1976]. This program calculates the gravitational effect of an arbitrary shaped polygon, which is specified by a "top", a "bottom" and a number of slices between. Each slice must have the same number of vertices and the body is constructed by joining vertices to make triangular facets. GRAV3PLH allows the construction of a body or bodies of any orientation and independent of topography, thus it can be used to calculate the gravitational effect of isolated bodies at depth. The 3-dimensional modelling has been much more limited in extent than the 2.5-D; rather than attempting to model the entire Eastern Flank in 3-D, only the major features of the 2.5-D models have been included (see section 6.6).

Figure 6.4. (overleaf). Location map for the profiles used in the 2.5-D modelling. The profiles (marked A-A', B-B', C-C') are plotted on the residual gravity map (figure 5.6), Together with the approximate position of the Valle del Bove (1) and the Chiancone (2). S = Summit; Sap = Sapienza; N = Nicolosi; Contours are in mGal.

Figure 6.4: Gravity model profiles

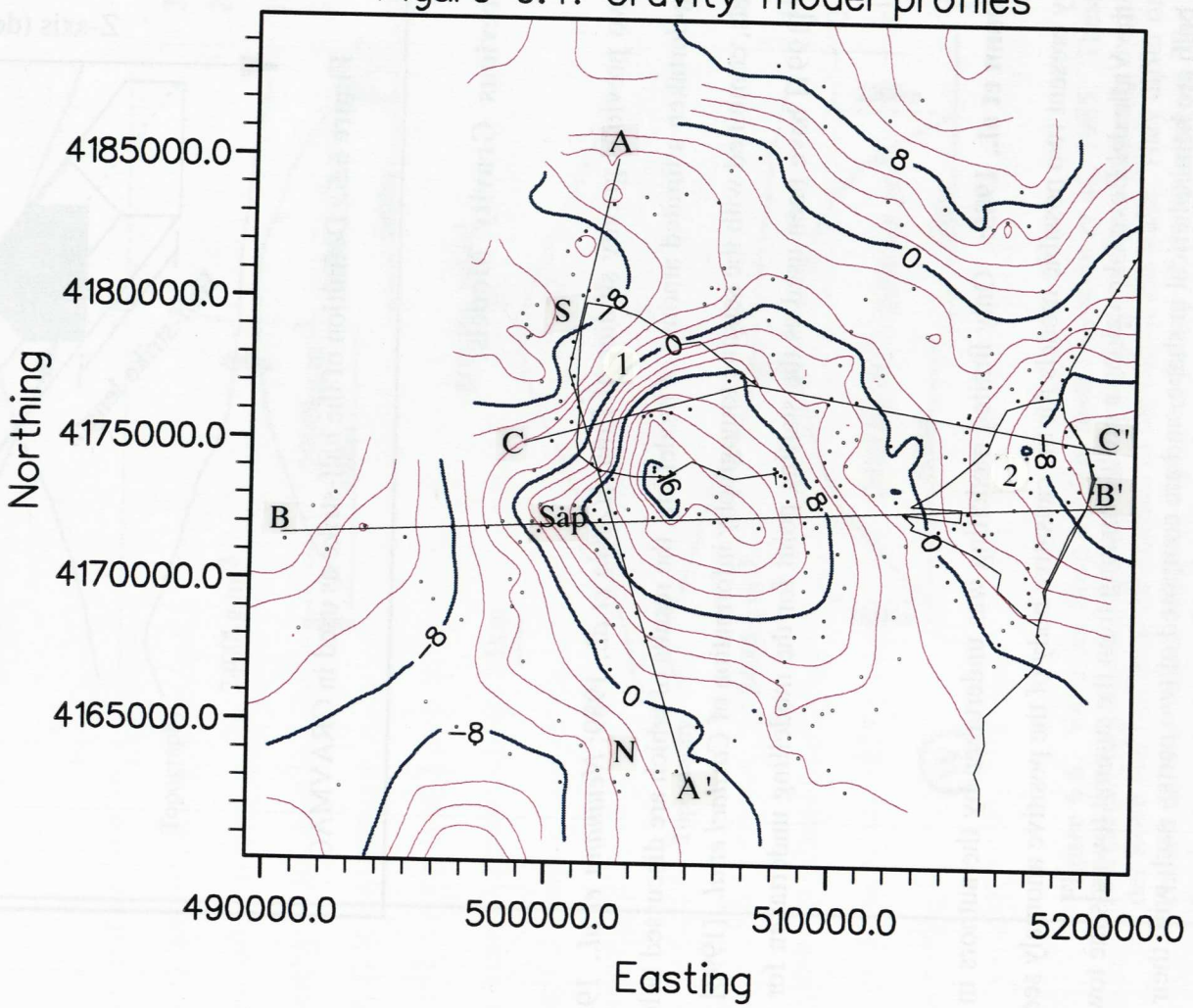

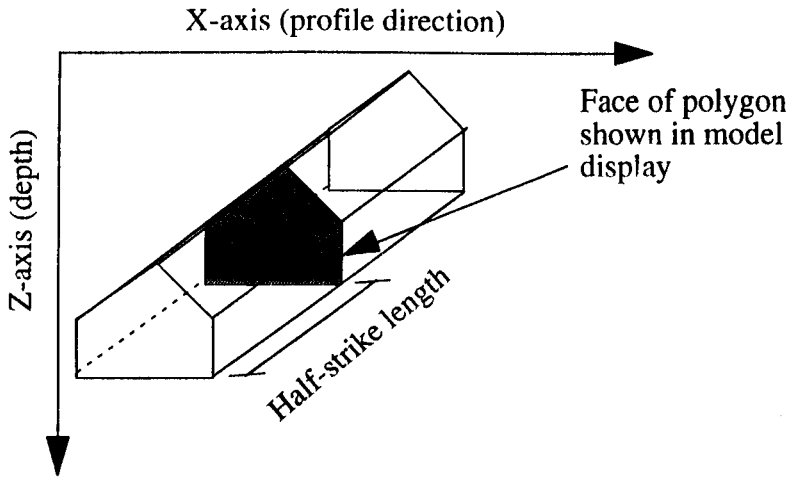

Figure 6.5. Definition of the half-strike as used in GRAVMAG.

6.3.1. Previous Gravity Models:

The two previous gravity studies of Etna, [*Loddo et al.*, 1989; *Neumann et al.*, 1985] have both undertaken a limited amount of modelling, the results of which are discussed below. These models, combined with the seismic tomography information of *Cardaci et al.*, [1993] and *Hirn et al.*, [1991] have been used as the starting point for the modelling undertaken for this study.

Neumann et al., 1985: Only limited modelling was undertaken by the authors in this case. They present two possible models for the causative body of the positive anomaly seen in the area of the Valle del Bove taken along a profile running from the summit towards the town of Zafferana; both are hemispherical in shape, and are composed of two parts - each with their own density contrasts (figure 6.6). The only difference between the two models is the chosen density contrasts, and hence the depth to the top of the body, but in both cases the depth to the top is less than 1 km below the surface and the density values chosen are between 2860 kg m^{-3} and 2990 kg m^{-3}. By the use of a number of East-West profiles across Etna, they have also estimated the thickness of the volcanic material, and hence basement morphologies. The results

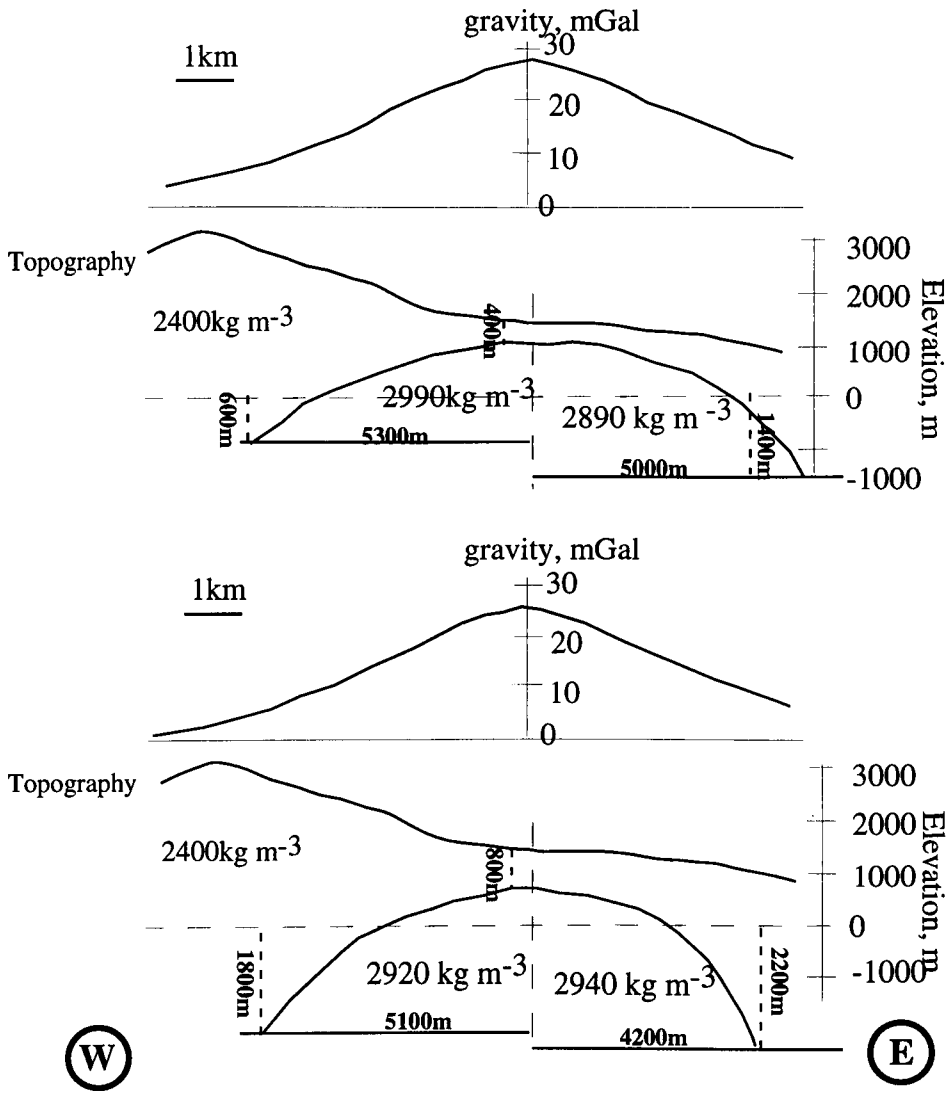

Figure 6.6. Valle del Bove models from *Neumann et al.,* 1985. These models represent two possible explanations for the large positive anomaly over the Valle del Bove and run from the summit to the end of the Valle. They differ only in the chosen density values and thus depths to the top of the structures. The densities used are consistent with the interpretation of this body representing a frozen magma chamber or similar structure.

are in reasonable agreement with those obtained by *Ogniben*, [1966] using hydrological information (figure 6.7), and show the sediments sloping strongly in an Eastwards direction (i.e. towards the sea), with the highest point (ca. 1300m a.s.l.) coinciding with a point Northwest of the summit region, rather than directly below the central craters. These diagrams differ somewhat from *Stewart et al.,* [1993] (figure 4.8), the difference possibly resulting from

the different data sets used. *Stewart et al.,* base their diagram on outcrops of Quaternary marine clays within the volcanic edifice, which are extremely limited in extent, thus their basement map requires a large amount of interpolation, producing a much simplified model. Secondly the extent to which Etna is underlain by these clays is not clear (see models of *Loddo et al.,* 1989) thus the figure of *Stewart et al.,* may be creating contours on a feature which is not continuous.

Loddo et al., 1989: The gravity modelling carried out in this study was much more extensive than that undertaken by *Neumann et al.,* [1985]. A number of profiles across Etna were modelled in combination with deep dipole geoelectric soundings, allowing for the construction of a 3-D block model of the basement. No attempt was made to model structures occurring within the volcanic edifice itself - rather this was given a single density value of 2470 kg m^{-3}, which is similar to that found in the present study for the modern Etnean lavas. Their models are entirely of basement structures, which have been useful in the present attempts at modelling as a constraint on the shape, position and density of the sub-Etnean basement. They show a number of areas of differing density lying below Etna; densities range from 2470 kg m^{-3} to 2920 kg m^{-3}, these values are based on the results of the geoelectric soundings, a process which produces values with large errors (up to ±500kg m^3 is possible [*Angenheister* 1982]). Underlying most of the Eastern flank, at a depth of 2 km below sea level is material of a density of 2920 kg m^{-3}, however immediately below the volcanics the situation is much more complicated (figure 6.8). One of their models cuts the Chiancone deposit and shows low density and resistivity material to a depth of approximately 300m below sea-level. As the Chiancone contains a large amount of clay-like material (A. Morrell, pers. comm. 1995) it is likely to have a low resistivity, and a density of 2405 kg m^{-3} has already been determined (section 6.2), the most likely interpretation is that this low resistivity material represents the Chiancone, thus giving a thickness in the order of ca. 400 m (when surface expression is included).

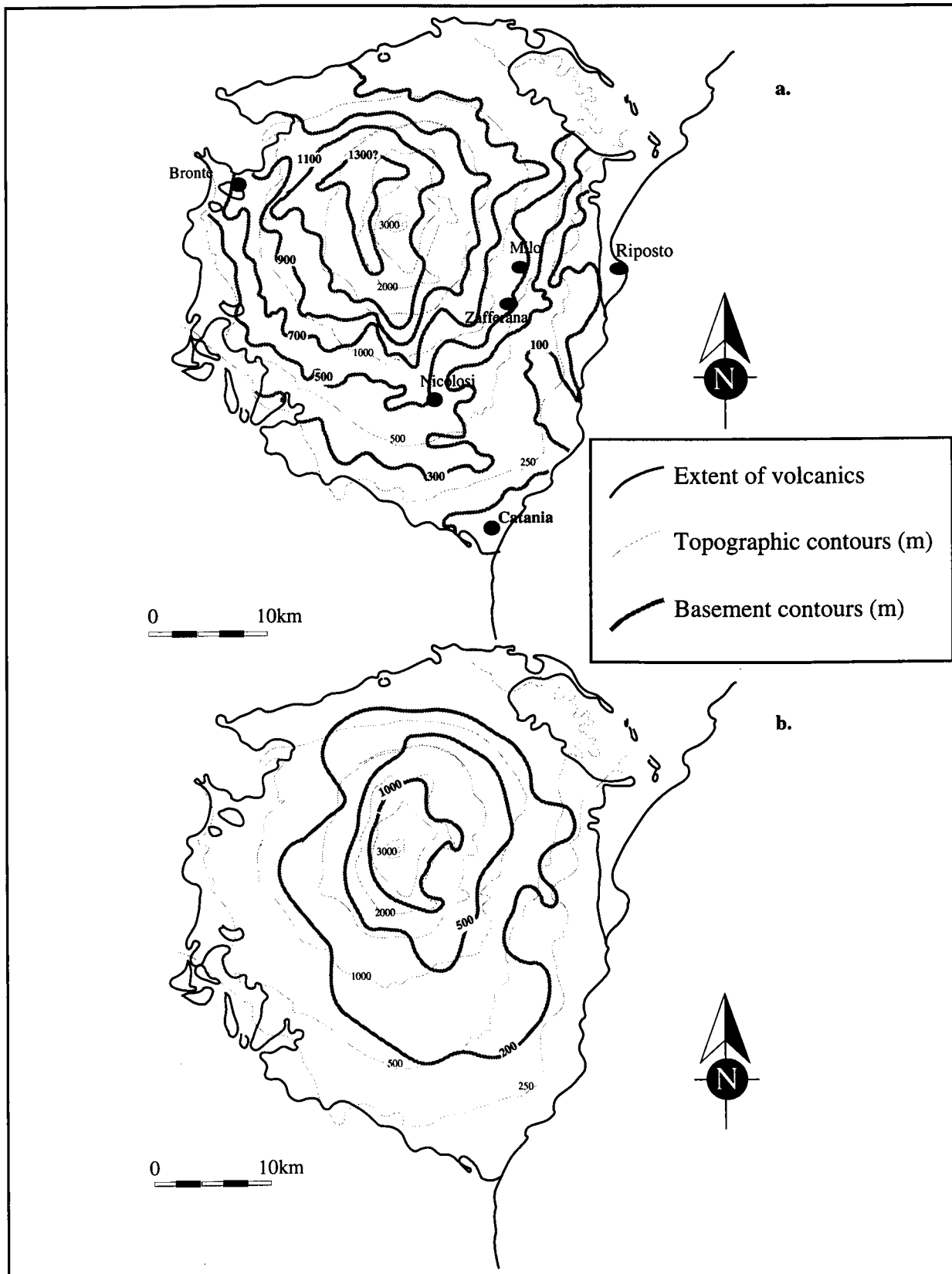

Figure 6.7. Sub-Etnean basement morphology. **a**. Basement morphology based on *Ogniben* [1966] using hoydrological data. **b**. Morphology based on the gravity models of *Neumann et al.*, [1985]. Both models show similar structures, with a slope towards the east, and a slight ridge of material extending SE from the summit.

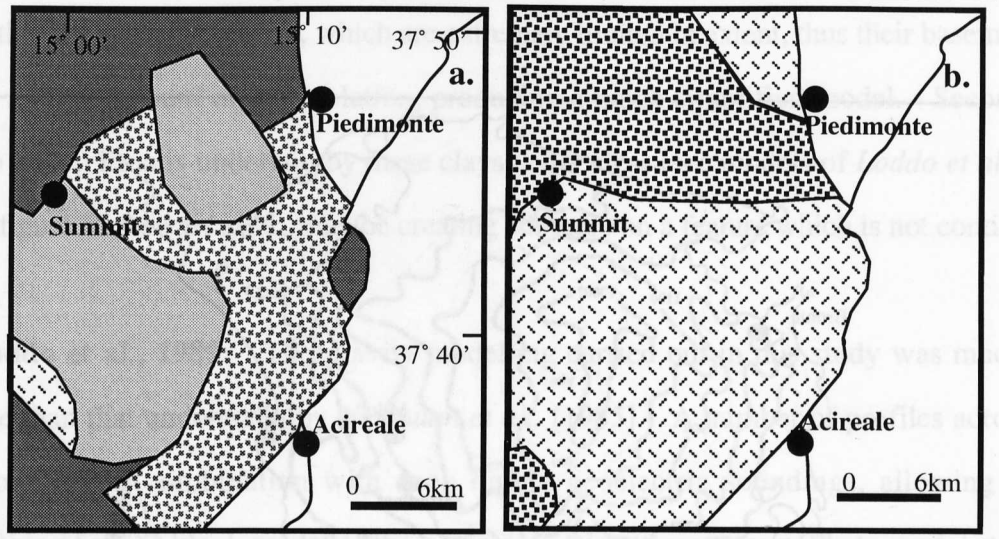

Figure 6.8: Resistivity and density models of Loddo et al., 1989.
a. Model representing material lying directly below the Etnean volcanics.
b. Model at 2km depth.

Seismic Tomography: The seismic tomography data available provides good starting points for the gravity modelling described below. The studies by *Cardaci et al.*, [1993] and *Hirn et al.*, [1991] show a large zone of positive velocity anomaly at shallow depth below the southern wall of the Valle del Bove. This anomaly extends to below sea-level from its top at approximately 1 km above sea-level, with dimensions of approximately, 3 km depth by 10 km diameter. Both sets of authors have interpreted this feature in terms of an old, cooled magma system, the positive velocity anomalies indicating a relativity high density.

6.4. 2.5-D Modelling:

The main aim of the 2.5-D modelling was to develop a detailed picture of the sub-surface structures of the volcano as well as to build a starting point for the less detailed but more representative 3-D modelling. The three profiles chosen are shown on figure 6.4, they were

positioned so as to pass through the main features of the Bouguer Anomaly map as well as cutting areas with the greatest data coverage. Using the actual data collected, rather than reading values from the contour maps, removes any fear of "data creation" which may occur in the contouring processes. Although the Bouguer Anomaly map (figures 5.2; 5.6) was carefully selected and all inputs controlled such that the possibility of creating false anomalies was kept to the minimum, the possibility does still exist. Thus only the true anomalies are modelled and no possibility exists that false anomalies resulting from poor selection of contouring criteria are included. Each profile is discussed individually below, and the main results are then summarised.

Density values used in the three profiles are based on table 6.1, with a background density of 2670 kg m^{-3} (= the reduction density). The positions of the profiles were partly chosen so that each would help constrain the other two, therefore at all stages of the modelling the models were checked for inter-profile consistency. The base of the models has been arbitrarily chosen at approximately 4 km below sea-level; below this level any further bodies have little or no affect on the computed gravity values. Each model is individually described below and the individual properties of the polygons for each model are given in table 6.3.

Problems may arise in 2.5-D modelling when profiles are not completely straight, due to space considerations i.e. the program assumes a straight line, and calculates the effects of the half-strike accordingly. Non-straight profiles will cause inaccuracies in the regions of the bends due to the squeezing/extending of the bodies at this point. The effects of this have been kept to a minimum both by keeping the bends as close as possible to 180°, while still cutting the relevant features, and by the use of 3-D modelling as an extension of the gravity modelling. The use of 3-D modelling of significant bodies removes any inaccuracies in the 2.5-D modelling of these features.

The labelling of the polygons in the three profiles (figures 6.9, 6.10, 6.11, and table 6.3,) have been kept consistent, thus, for example, I_1 in each figure refers to the same body.

The error in the gravity data is approximately ±1.7 mGal, thus a difference between the calculated and observed anomalies equal to or less than this is considered as a good fit.

6.4.1. Choice of Physical Properties:

The physical properties of the polygons appearing in all three profiles were always kept the same; any change was made to all three profiles at once, thus adding another constraint to the modelling process.

Density values were taken from table 4.3, while half-strike values were based on available geological information, care being taken with regards topography (i.e. bodies which do not outcrop are constrained in their half-strike so that they do not outcrop in the models). Magnetic data was taken from both published and unpublished work. Total field magnetisation values have been used and are based on susceptibility values from *Griffiths*, [1983], and remanent magnetisation values from data collected in this study (for the palaeomagnetic work) and T. Rolph, unpublished data.

6.4.2. Profile A-A´:

The aim for this profile was to study the summit region and the southern flank of the volcano. Data are extremely limited on the northern flank and therefore the profile was not extended significantly in this direction. The profile cuts through the summit anomaly, but only cuts through the side of the main Valle del Bove anomaly. As the model is only 2.5-D, failure to cut through the centre of the anomaly means that the reliability of the calculated anomaly is reduced, as the half-strike is likely to be overestimated on one side of the profile and underestimated on the other. As can be seen in figure 6.9, the calculated values for the gravity anomaly are slightly too large, possibly due to over estimation of the half-strike. As the profile does cut across the main part of the summit area it is considered that the model is correct in this region, with appropriately chosen half-strikes. The main feature of the model is the number of high density bodies (labelled I_1 to I_5) representing bodies underlying the Valle del Bove (I_1) and the summit region (I_{2-5}). The material under the summit region is interpreted as a large pipe structure (I_2) leading up to a roughly circular body (I_3) which in turn has two small pipe-like bodies extending towards the summit craters (I_4, I_5). I_2 is interpreted as representing a possible

feeder system/zone of dykes, the depth limit for this intrusive body has been placed at the sedimentary-volcanic contact as extending this body below this level makes no difference to the calculated anomaly, and its geometry is likely to become increasingly complex with depth. The final shape of this body has been determined from both the need to fit the calculated to observed data (i.e. this shape gave the best fit) and reasonable assumptions concerning the geometry of any possible feeder system.

The three units marked with an L represent volcanic deposits, with L_1 refereeing to the modern surface lava flows and L_2 and L_3 representing older material at depth. The summit deposits (S) are composed of a mixture of aa lava flows and pyroclastics and thus have a low density (1940 kg m^{-3}). Se indicates sedimentary material.

Finally, this model shows a strong southwards slope within the sedimentary basement, descending from approximately 1000m north of the summit area to approximately sea level at the end of the profile (c. 20km south of the central craters).

Table 6.3. Summary of physical properties used in the gravity and magnetic modelling. Polygon numbers are as used in figures 6.9, 6.10 and 6.11.

Polygon Number	Half-Strike km (A-A')[1]	Half-Strike km (B-B')	Half-Strike km (C-C')	Density kg m^{-3}	Total Magnetisation[2] A m^{-1}
S	0.75	-	0.75	1940	0.1
L_1	1	0.75	1.5	2400	5
L_2	3	-	3	2150	0.1
L_3	3	2	-	2200	3
I_1	2	3	3	2950	8
I_2	0.5	-	-	2800	10
I_3	0.75	-	0.75	2750	10
I_4	0.1	-	-	2750	10
I_5	0.1	-	-	2750	10
I_6	-	1	-	2800	8
C	-	3	3	2400	0
Se_1	25	25	25	2920	0
Se_2	25	25	25	2500	0

1. - indicates that polygon is not present in this profile.
2. Data from *Griffiths*, [1983]; T. Rolph, unpublished data.

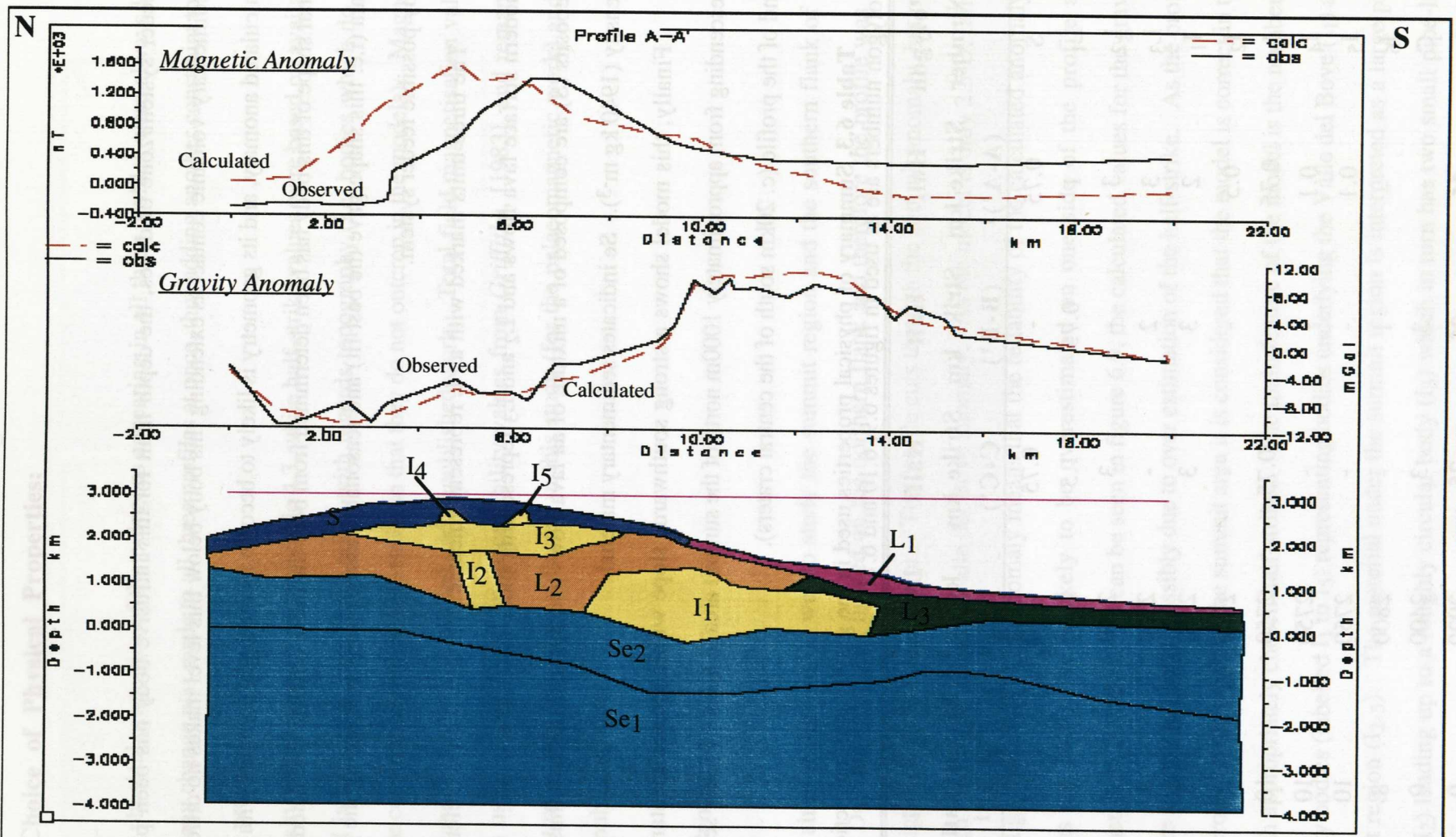

Figure 6.9. Gravity model along profile A-A'. This profile crosses the summit region and shows a number of significant sub-volcanic bodies. Also clearly seen is a Southwards slope to the sedimentary basement. Physical properties for the bodies are given in table 6.3.

6.4.2. Profile B-B´:

Profile B-B' was chosen so as to cover the Southern Wall of the Valle del Bove and thus the main part of the associated anomaly. It also extends to the coast and thus cuts both the Timpa fault system and the Chiancone as well as cutting the surface expression of the Southern rift zone, an area with a large concentration of satellite cones and other eruptive vents. Initial models ignored this feature but fitting the data proved difficult, thus a high density body (I_6) representing a possible zone of dyking was added, greatly improving the fit of the anomalies. A slight downward offset is seen in Se_2, in the area of the Timpe Fault System (labelled TF in figure 6.10) however given the uncertainties in the modelling no real significance can be placed on this feature. The surface expression of the faults are as fault-scraps up to several 100 m in height, thus they are major features and as such it is to be expected that they should be visible in the gravity data. This lack of clear expression may result from a lack of a density contrast across the faults. This may occur if they cut only the volcanic material, which in turn suggests that they are strongly listric in nature, possible following the sediment/volcanic contact at depth, however it should be noted that this interpretation is based on very little evidence. *Stewart et al.,* [1993] suggest that horizontal movement is more important on these faults than vertical, such movement would result in no density contrast across the faults and thus is undetectable using gravity. The Chiancone (C) appears as a wedge of material thickening towards the East (sea-wards).

The fit of the aeromagnetic anomalies is much improved compared with profile A-A' with the general shape and values of the calculated anomaly agreeing closely with the observed data. In general it is easier to fit gravity data than magnetic data (due to the greater complexity of the magnetic field), thus in this case as the gravity data fits extremely well it is consider that the model is a reasonable representation of reality.

6.4.3. Profile C-C´:

Profile C-C' extends from just south of the summit region to the coast, covering similar features to B-B'. Half-strikes and polygon shapes for B-B' and C-C' were constantly checked

for consistency. Again this profile covers both the Timpa fault system and the Chiancone, and again no clear expression for the Timpa faults (TF in figure 6.11) is seen, while the Chiancone (C), is modelled as a wedge, with a maximum thickness of approximately 700m, thickening seawards. Lying below the scoria deposits of the summit region is the southward continuation of the body I_3 from profile A-A'. The Valle del Bove appears as a region full of fresh lava flows (density = 2400 kg m^{-3}) overlying lower density (2200 kg m^{-3}) older lava/volcanic material. Typically, explosive caldera collapse, as has been envisaged for the formation of the Valle del Bove (e.g. *McGuire*, 1982), results in the accumulation of low density material in the caldera floor, this then gives negative gravity anomalies [*Rymer and Brown,* 1986]. The density of the material seen in this area does not rule out caldera collapse, however no associated structures, e.g. boundary faults etc., are seen. This lack of structures adds support to a more peaceful method of formation.

6.5. Synthesis of 2.5-D modelling Results:

While it is possible to interpret the structures of the region based on each profile separately, the best results are obtained when all three profiles are consider together. When this is done the large high density body marked I_1 stands out as the most prominent feature. This body has a highly irregular shape and appears to almost have sunken into the underlying sediments (profiles A and C show this clearer than B). Of the other high density bodies, possibly those underlying the summit are the most important after I_1. The density values used for these bodies (I_2 to I_5) are significantly less than for I_1, giving the impression that these areas represent zones of intrusions or accumulations of dense lava flows mixed with lower density material, thus they may be best described as zones of dyking rather than true intrusive bodies. Body I_6 also fits into this category, and is interpreted as an area of dyking associated with the Southern Rift Zone.

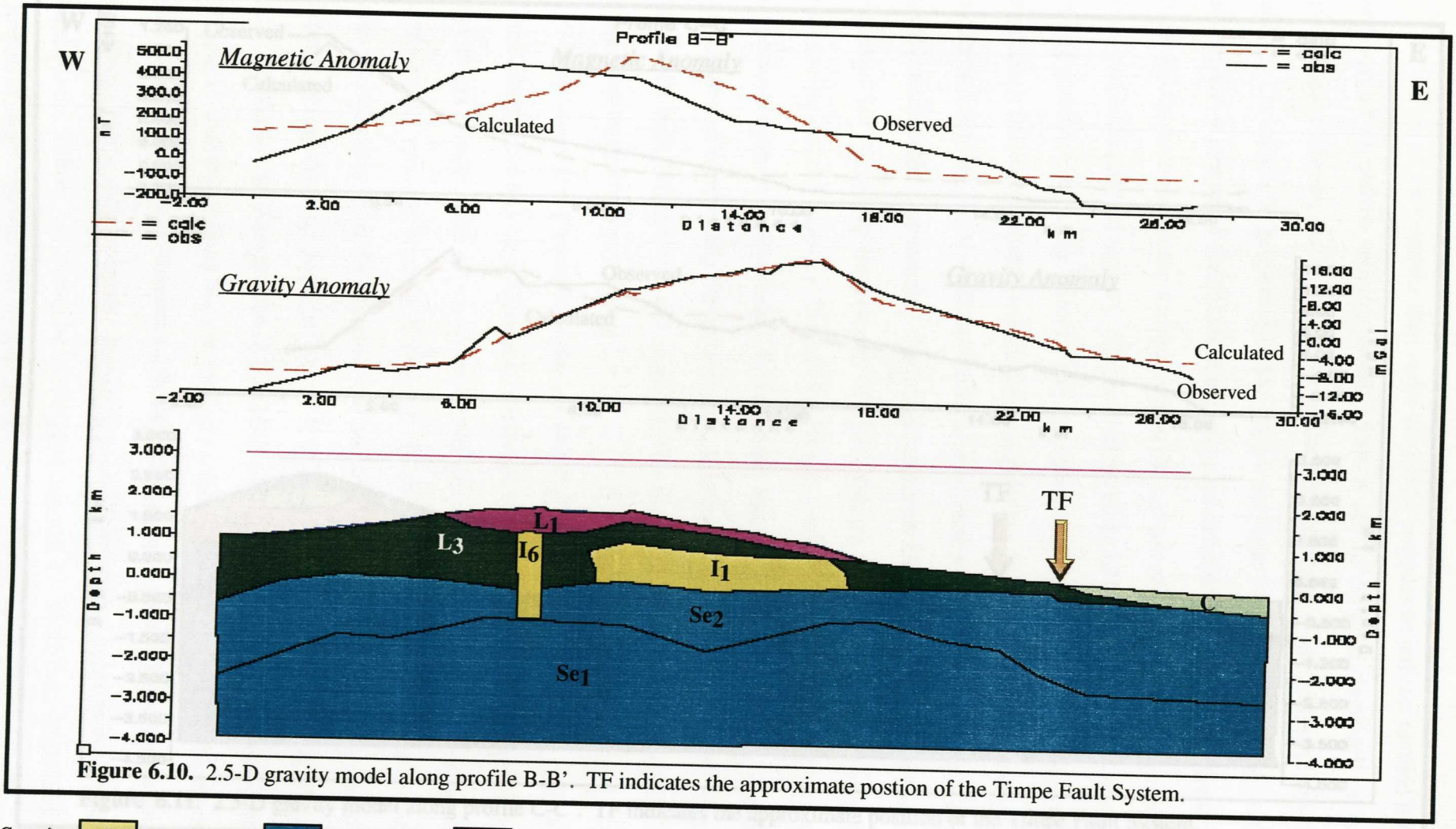

Figure 6.10. 2.5-D gravity model along profile B-B'. TF indicates the approximate postion of the Timpe Fault System.

S Scoria | I Intrusives | Se Sediments | L Modern Lava Flows | L Older Volcanics | C Chiancone | Aeromagnetic Flight Line

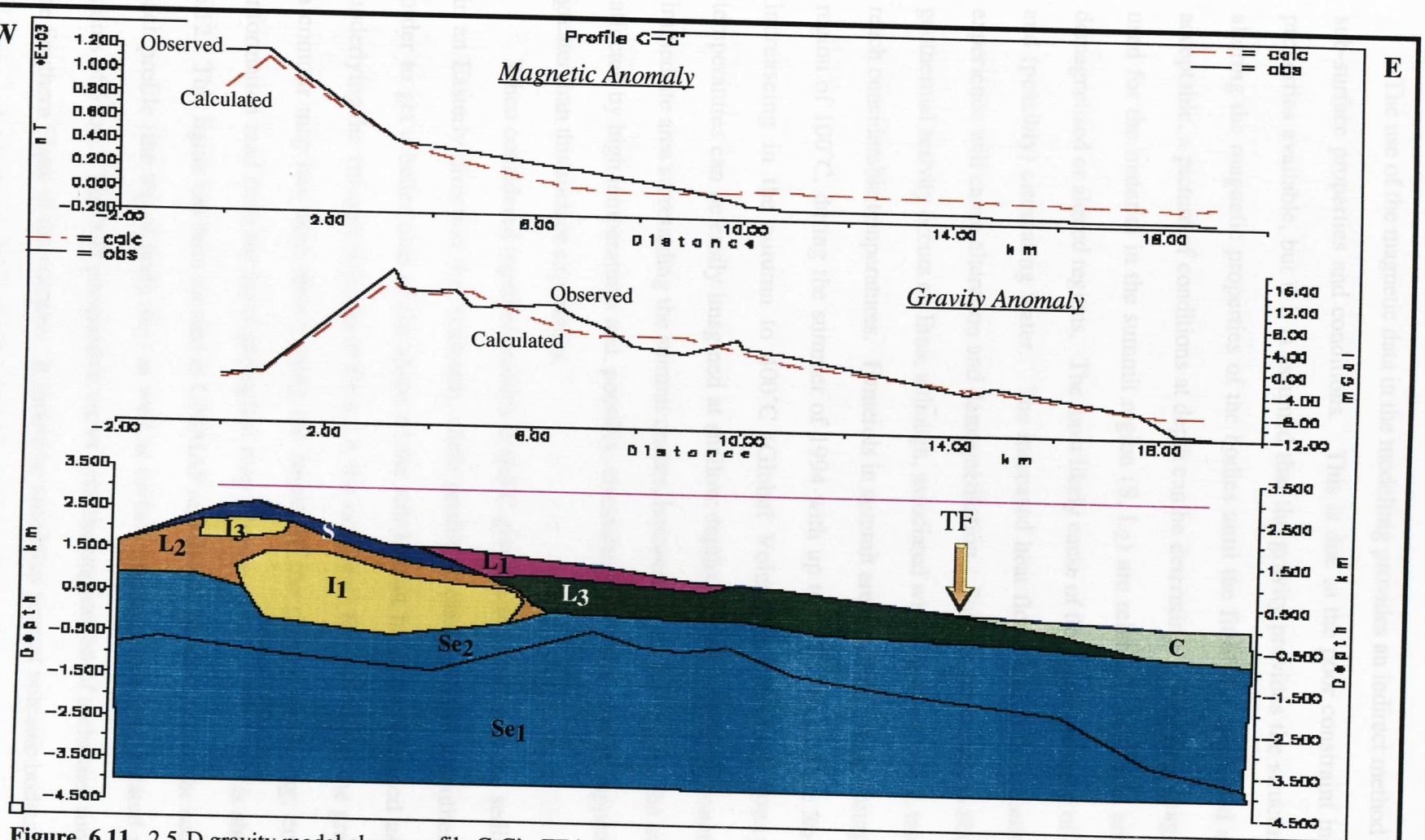

Figure 6.11. 2.5-D gravity model along profile C-C'. TF indicates the approximate position of the Timpe Fault System.

S Scoria | I Intrusives | Se Sediments | L Modern Lava Flows | L Older Volcanics | C Chiancone | Aeromagnetic Flight Line

The use of the magnetic data in the modelling provides an indirect method for determining sub-surface properties and conditions. This is due to the poor constraint in terms of these properties available, but if it is assumed that the gravity provides the structural controls, by altering the magnetic properties of the bodies until the fit of the calculated and observed is acceptable, a picture of conditions at depth can be determined. The final magnetic properties used for the material in the summit region (S, L_2) are relatively low, and are suggestive of demagnetised or altered regions. The most likely cause of this is the presence of heated material and (possibly) circulating water. The increased heat flows which this material is likely to experience will cause alteration and demagnetisation. Surface observations show that limited geothermal activity occurs on Etna, although, associated with eruptive activity, isolated areas can reach considerable temperatures. Fumerols in summit area reached average temperatures in the region of 100°C, during the summer of 1994 with up to 312°C around the Southeast crater, increaseing in the autumn to 400°C (Global Volcanism Network, 1994), and higher temperatures can be easily imagined at shallow depths. Such activity is concentrated in the immediate area surrounding the summit craters, however, from the models, the area of material affected by high temperatures and, possibly, circulating hot water at depth appears to be much greater than this surface expression.

When considered together profiles B and C give the impression of the sediments sloping in an Easterly direction (i.e. seaward), while profile A clearly shows a southerly slope. In order to get a better idea of the shape of the sub-Etnean basement (defined as the material underlying the volcanic deposits of Etna, i.e. the sediments Se_2 and Se_1 of the gravity models), a contour map has been drawn using the results of the gravity modelling, combined with information read from the local geological map [*Romano et al.*, 1979], and is shown in figure 6.12. This figure has been created in UNIMAP and shows the elevation of the sediments along each profile (the top of body Se_2) as well as surface geology data, interpolated with a search radius of 5 km. The 3-D perspective views give the impression of a channel running through the Southern Flank of the volcano. It should be noted that several volcanic bodies are present in this area and it is these which may be causing this channel, i.e. as the data is spatially limited the influence of large features may appear greater in these plots than is the case in reality. The

impression of the body I_1 "sinking" into the sediments on the bases of profiles A and C is reinforced by these maps, showing quite clearly the resultant depression. No attempt is made here to distinguish between I_1 sinking into underlying sediments or intruding into both the sediments and volcanics, such differentiation is impossible given the available data. The body I_6 represents a higher density area within both the sediments and the over lying volcanics and thus no "depression" or hole in the sediments appears in figure 6.12 due to this body, however it may be causing a slight lowering of the sediments in the models, thus reinforcing the impression of a channel.

Care must be taken in interpreting diagrams such as figure 6.12 as they are based on spatially limited data, however, even with this consideration in mind, it is clear that the sediments slope towards the East, with a large basin structure present on the eastern coast. This basin is now occupied by the Chiancone deposit, together with other low density volcanics (parts of L_2 and L_3). The second point to note is the similarity between these maps and those of earlier workers [*Ogniben*, 1966; *Neumann et al.,* 1985]. In agreement with the earlier work, the highest point of the sediments does not lie directly below the summit, rather it is slightly displaced northwards; also the maximum elevation (approximately 1300m a.s.l.) agrees with *Ogniben*, [1966]. One other feature common in the two maps is a ridge of material descending down the Southern Flank, from the summit area towards Nicolosi. One possible interpretation of such a feature is as a response to rifting. If a rift zone is located over ductile to semi-ductile material, the act of pulling apart the volcanic material results in an upwelling of the underlying material [*van Wyk de Vries*, 1995]. As this ridge of sediments coincides with the Southern Rift Zone, this would appear to support such a model. Sediments outcropping around the Etna region appear to be highly brittle limestones and sandstones, however their behaviour at depth is unknown. The pre-Etnean marine clays [*Labaume et al.*, 1990] would be expected to be ductile and thus respond in this manner, however as their extent, thickness and physical properties are unknown it is difficult to be certain. The modelling of this study has not accounted for these marine clays on the bases of the models of *Loddo et al.,* [1989] who suggests that their extent under the volcanics may be limited, this may have caused the thickness of the Etnean volcanics

to be slightly overestimated, however this effect is considered small due to the likely limited extent of the deposits.

The origin of the Chiancone deposit is believed to be closely linked to the Valle del Bove, and therefore understanding this deposit is an important part of this study. Figure 6.13 shows an isopach map for this deposit based on the gravity models and the plots of figure 6.12. The overall shape is of a basin open to the sea, the maximum thickness of the deposit does not coincide with the centre of its geographical extent, but rather lies in the northern part, thus the deposit is highly asymmetrical. It can be seen that the deposit is very thick, up to 700m at one point, with the thickest area occupying a trench-like shape, open to the sea. One problem with this model is the location of the deposit on the coast, preventing gravity data being collected to the East, thus the eastern edge of the model is poorly constrained and therefore this thickness is a maximum. Even taking this into account it is clear that the deposit must continue off shore, however the volume of material deposited offshore is impossible to estimate.

One consideration in attempting to explain the Chiancone as the resultant deposit due to the formation of the Valle del Bove is that the volumes should be similar, although if a significant fraction of the Chiancone lies off shore then it is to be expected that the Valle del Bove volume should be greater. Volume estimates for both features have been made; the Chiancone volume was determined by calculating the volume of half kilometre grid cells, using the thicknesses derived from figure 6.13; the volume of the Valle del Bove has been estimated in a similar way, using the 1:50 000 map of the area and the 1 km grid, with the thickness of the missing material being estimated from the reconstruction of *McGuire*, [1982] and the present day topography (from the 1:50 000 scale map). Thus the volume determined for the Valle del Bove is only an approximation and it also does not take into account the infill of modern volcanic deposits (i.e. it is an underestimation of the initial volume, following formation).

The resultant volumes are:

Valle del Bove Volume: 13.2 km^3

Chiancone Deposit Volume: 9.7 km^3

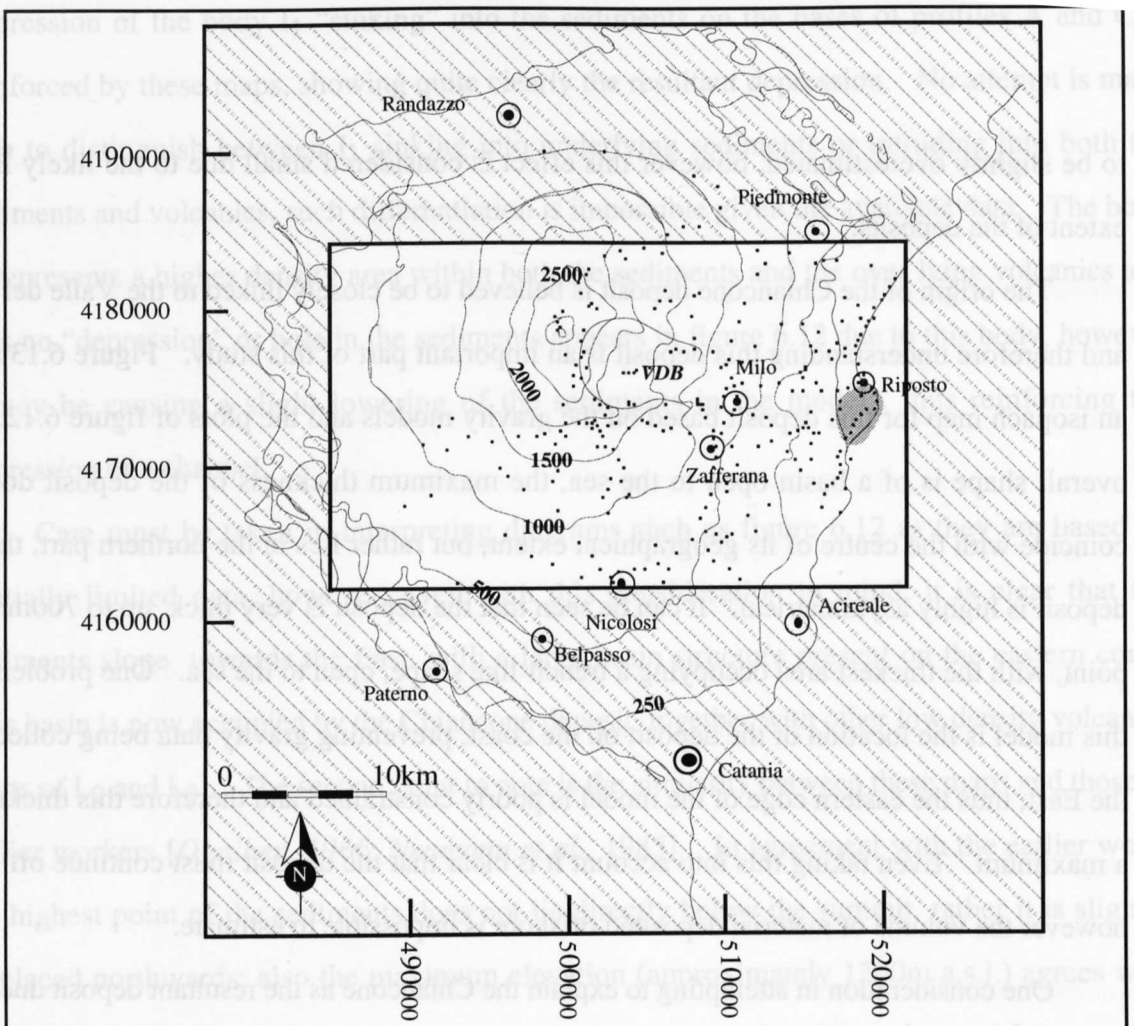

Figure 6.12. Maps of the sedimentary layers underlying the Etna volcanics. These maps are based on the results of the 2.5-D gravity modelling combined with geological information taken from *Romano, et al.* [1979].

a. The highlighted area shows the region covered by the maps of 6.12b and 6.12c. Dots represent the gravity stations; contours are in metres

b. Contour map of sediment/volcanic contact. The structures of the surface of the sediments is clear seen as a slope towards the East and a slight ridge running SE from the summit region. The colours represent 100m bands (see key). The black line represents the coast line. S = Summit; C = Chiancone; The depression in the area of the body I_1 (from the gravity models) is visible (I). Contours in metres.

c. 3-dimensional surface plot looking from the Southwest. This plot shows clearly the general eastwards slope, and the basin structure occupied by the Chiancone deposit, also visible is a slight ridge running southwards from the summit (S) towards Nicolosi (N). $I = I_1$ from the gravity models.

Figure 6.12b: Sub–Etnean sedimentary morphology.

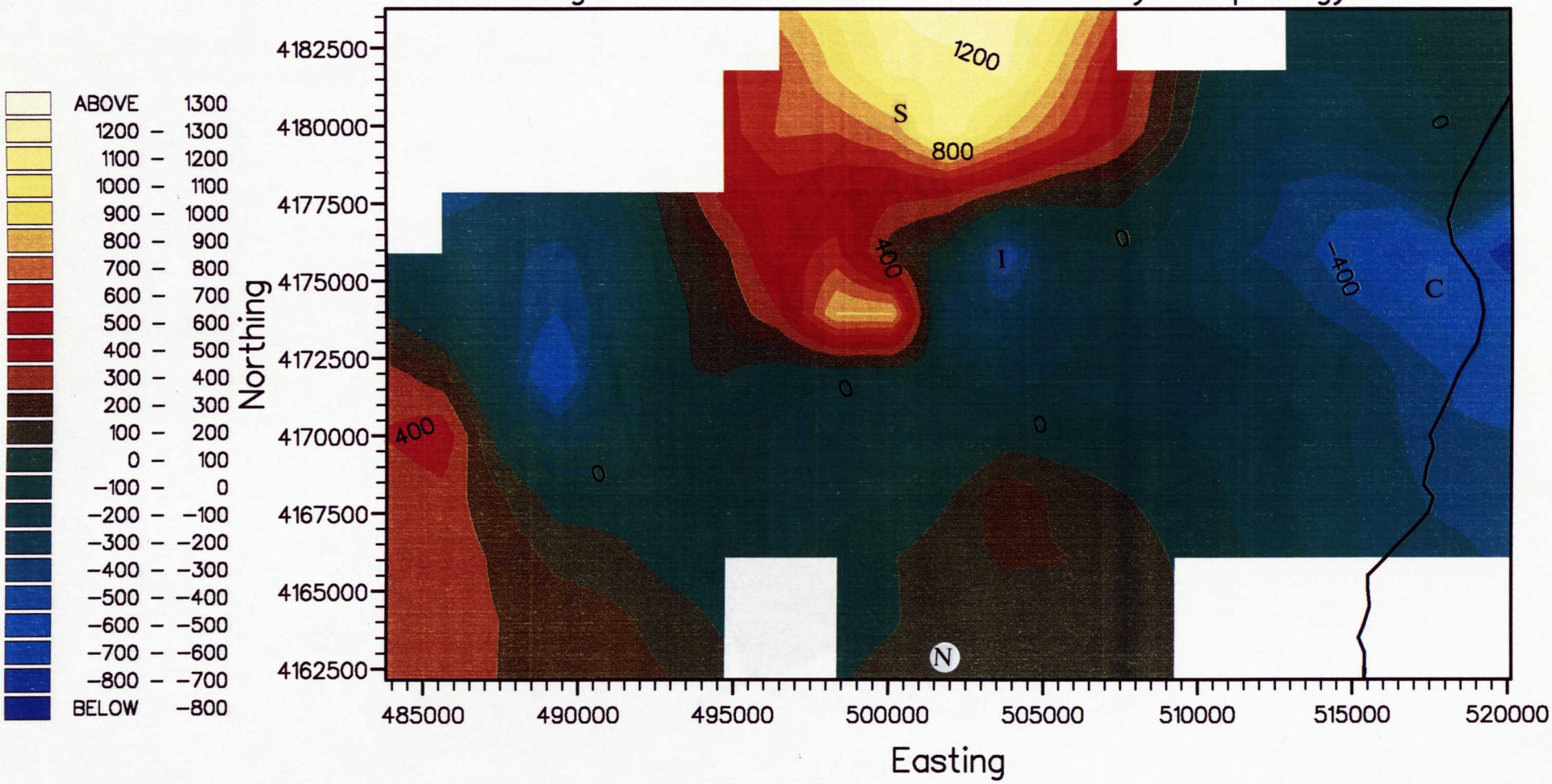

Figure 6.12c: 3–D model of sub–Etnean sediments
View from the SW

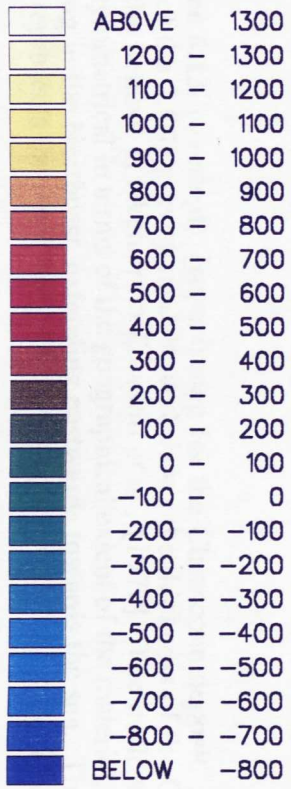

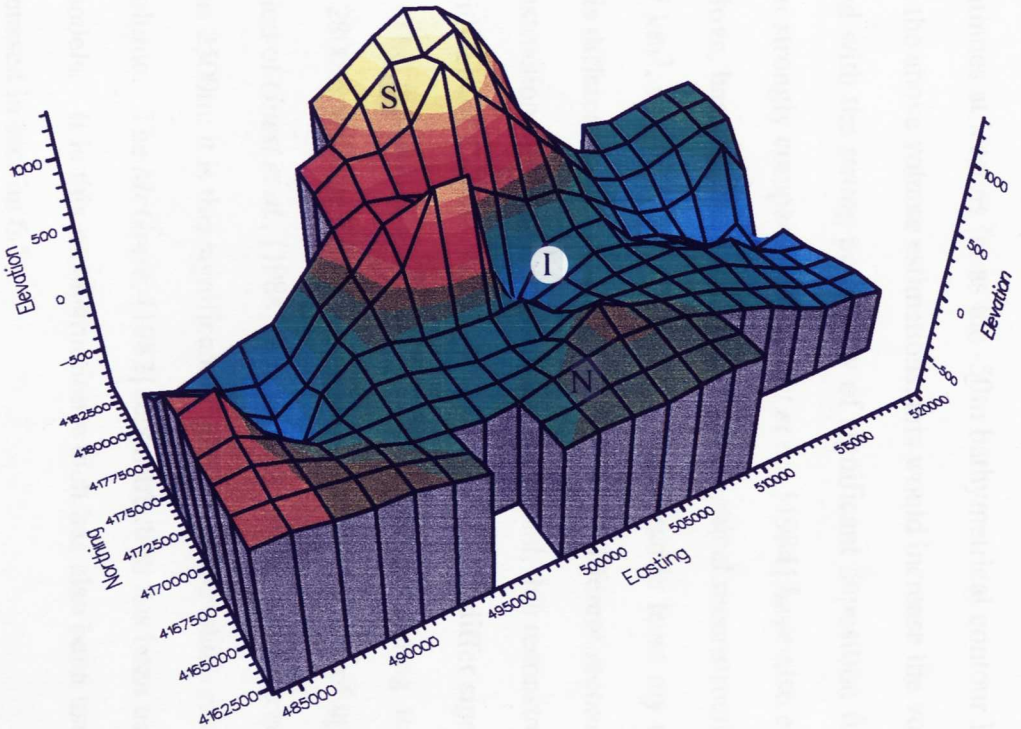

The significantly smaller volume of the Chiancone deposit agrees with the hypothesis that a significant proportion of material is deposited offshore. *Guest et al.*, [1984] indicate that the Chiancone continues at least as far as the -50m bathymetrical contour line, which is not taken into account in the above volume estimations, this would increase the volume significantly, and when combined with the strong possibility of significant deposition further offshore the two volumes appear strongly comparable. *Guest et al.*, [1984] have also estimated the volume of the Valle del Bove, based on their own palaeogeographical reconstruction, they give values in the region of 7 km^3, as can be seen this differs significantly from my own estimated volume. The bulk of this difference can be accounted for by the different reconstructions used; for this study the reconstruction of *McGuire*, [1982] has been used, this reconstruction agrees in general morphology with that of *Coltelli et al.*, [1994], both of which differ significantly from *Guest et al.*, [1984]. The maximum elevation of the region according to *McGuire*, [1982] is approximately 2800m, with the Trifoglietto centre reaching heights of up to 2600m, while under the reconstruction of *Guest et al.*, [1984] the maximum elevation of the area before the formation of the Valle was 2500m; it is this significant height difference which causes the large difference in estimated volume. The *McGuire*, [1982] reconstruction has been used as it agrees with the more recent models. It is this reconstruction which has also been used in the finite element modelling, discussed in section 6.7

Figure 6.13. (overleaf). Isopach map for the Chiancone deposit. This map is based on the results of the 2.5-D gravity models, and shows the thickness of the Chiancone deposit; the outline of the deposit is taken from *Romano et al.*, [1979]. The basic shape is of a trough of material, asymmetrical in terms of the geographical extent of the material, the thickest part of the deposit being in the Northeast, extending eastwards towards the sea. The right hand boundary of the map represents the coast line. Axes are marked with the local grid references.

Figure 6.13: Isopach map for the Chiancone deposit

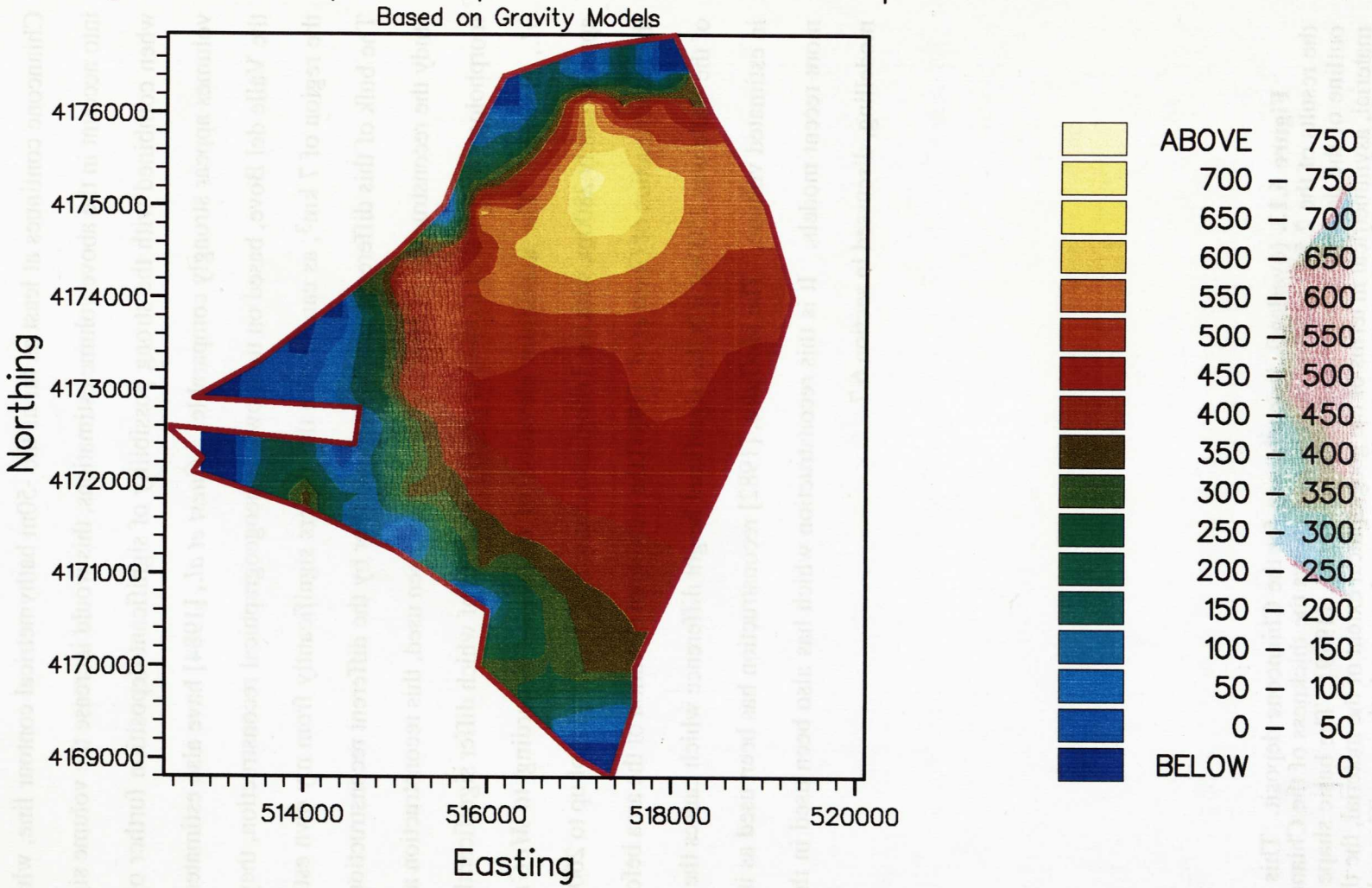

6.6. 3-D Modelling:

The 3-D modelling has been limited to the major features of the 2.5-D models and as such considers only the bodies which are strongly 3-dimensional in shape (i.e. bodies which are circular or of small half strike) and located on the upper flanks, thus the Chiancone has not been modelled. This decision was made on the basis of complexity of the modelling and also on the information to be gained. It was decided that little extra would be gained by modelling the Chiancone in 3-D, but that the increase in detail would be very important for the intrusives of the upper parts of the volcano.

The observed data are entered as a list consisting of: grid reference, elevation and gravity values for each station, while the model is entered as a list of bodies and the co-ordinates (grid reference and elevation) of their vertices. The output is in the form of calculated gravity values for each observed point. In order to check the fit between calculated and observed, the output files have been plotted in map form using UNIMAP.

The 3-D modelling has been concentrated on the bodies labelled as I_1, I_2 and I_3 only, as these appear as the major features of the 2.5-D models and show the strongest 3-D shape, i.e. they are limited in extent and are sub-circular in shape. Each body is built as a series of flat lying slices described by a series of vertices. For each body, each slice must have the same number of vertices, thus for body I_1 each slice has 8 vertices, giving the model an angular appearance. Also included in the modelling was the low density material of the summit region (i.e. the scoria), as without this the calculated anomalies were significantly too positive. This material is not shown in figure 6.15 as it is relatively unimportant and the diagram becomes too complex and interpretation difficult.

The 3-D modelling was begun when the 2.5-D models were considered finished, as the 2.5-D results were used as the starting point. Considerable care has been taken to ensure any changes in the 3-D model have been carried back over to the 2.5-D model, this interactive step adding an extra constraint to the process.

Figure 6.14 shows the calculated and the observed gravity values for each station. As large amounts of material have not been included in the modelling (e.g. the sedimentary

basement and the surface volcanics) the actual values of the calculated anomalies do not fit the observed. However the shape of the calculated anomaly in the area of the Valle del Bove and, to a lesser extent, the summit region does fit the observed data very closely. It is this fit of shape that is considered as the important feature as this shows that the geometry of the system is correct and as the geometry has been kept consistent with the 2.5-D models, and these show good agreement between calculated and observed, it is considered that these models are also a "good fit".

6.6.1. Model Description:

Figure 6.15 shows several views of the resultant 3-D model, the orientations shown were chosen as those giving the best impression of the shape and structure of the bodies. The map view of figure 6.15a gives the overall summary view, showing the location of the bodies in relation to the significant features of the volcano. As can be seen, the summit region is underlain by a large (approximately 4 km across), almost circular structure of relatively high density (2750 kg m^{-3}), the body I_3 in the 2.5-D models, the perspective views show that this body is itself underlain by a pipe-like feature, I_2 (density = 2800 kg m^{-3}). The top of the body I_3 lies at 2350m, which is approximately 900 m below the summit craters. The larger body in the area of the southern wall of the Valle del Bove is much greater in size (8 km long axis, 5 km short axis) as well as density (2950 kg m^{-3}) and is approximately 700m below the surface at its highest point. It is this body which causes the large positive gravity and the seismic velocity anomaly of this area.

Figure 6.14 (overleaf). Contour map for the calculated versus the observed gravity values for the 3-D modelling. The colour pattern represents the observed data; the contour lines the calculated. The axes are marked with the local grid references. N = Nicolosi; R = Riposto. Gaps result from the chosen search radius of 2 km.

Figure 6.14: Calculated vs. Observed for the 3–D modelling

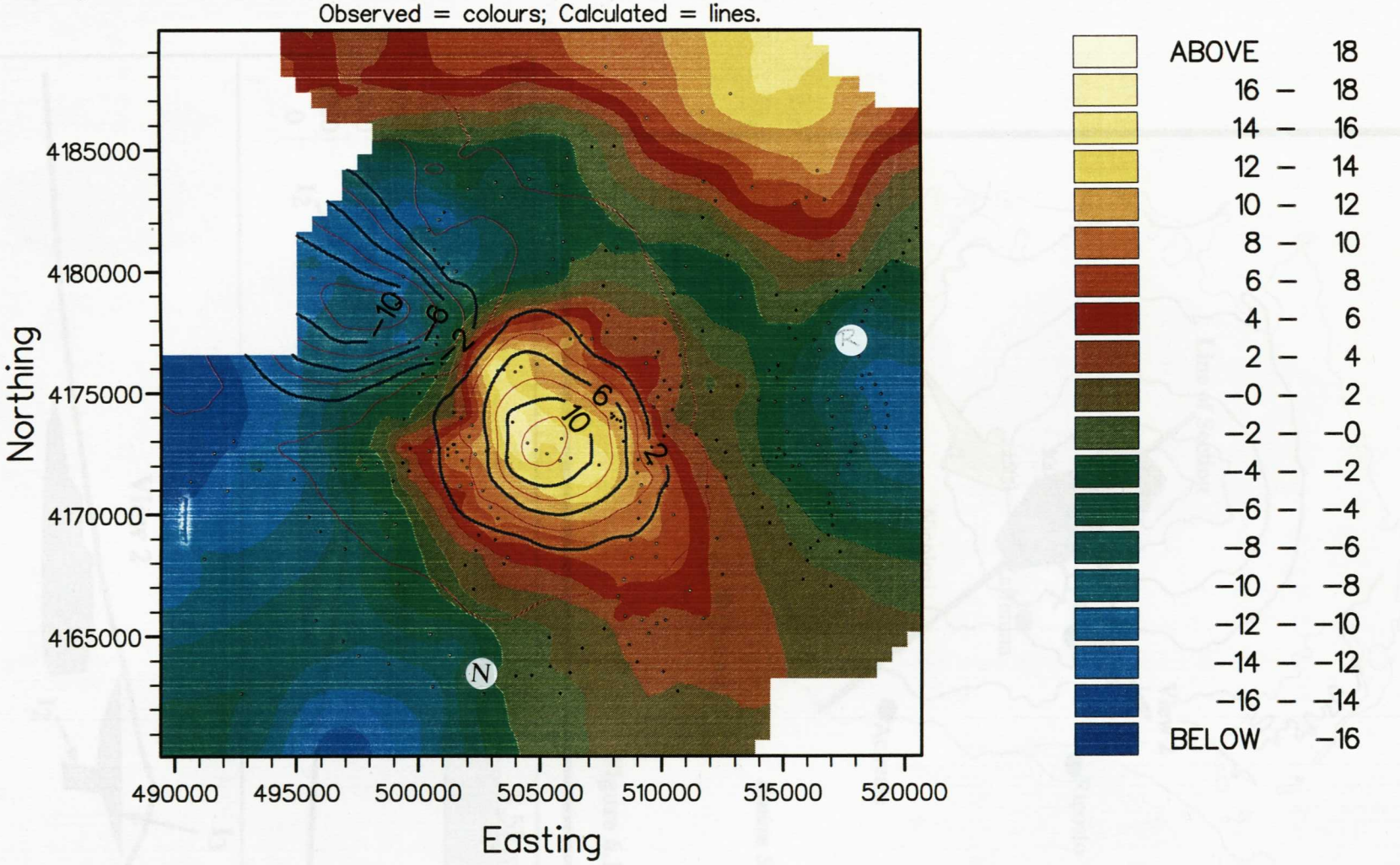

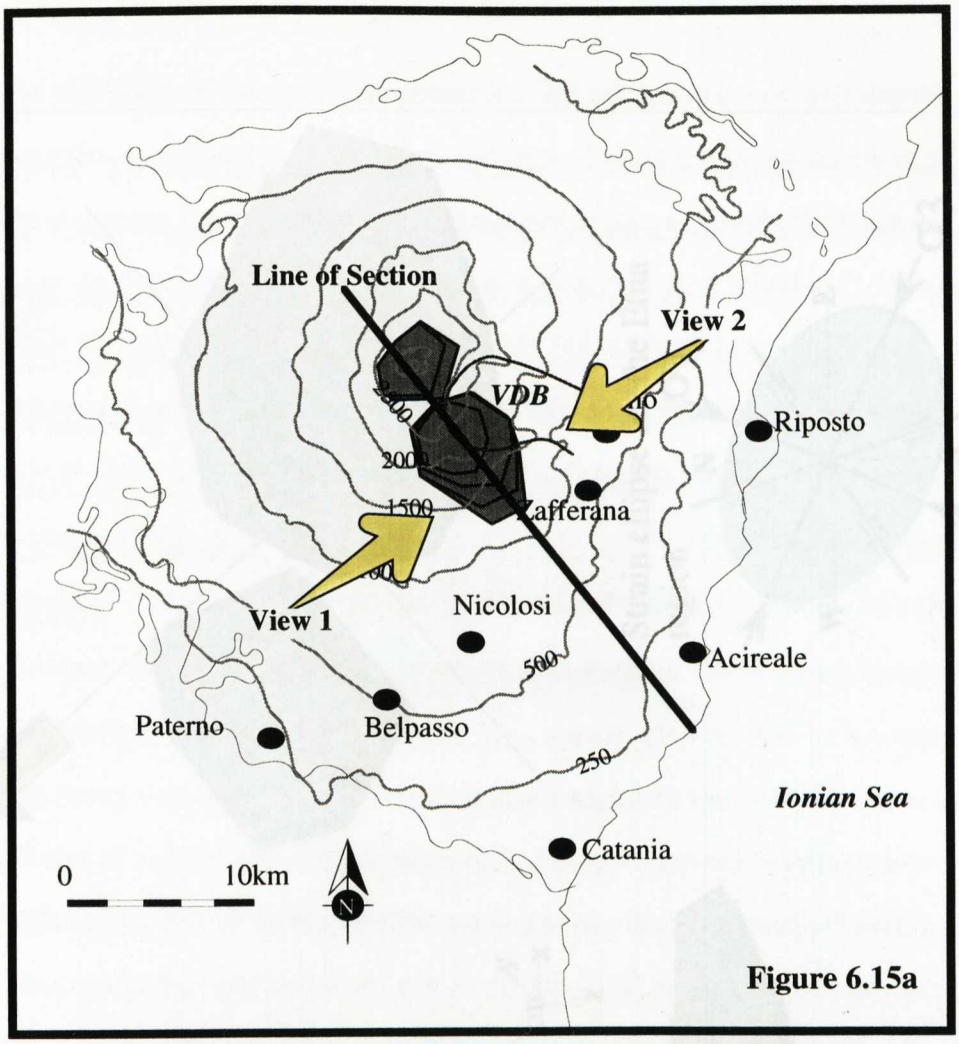

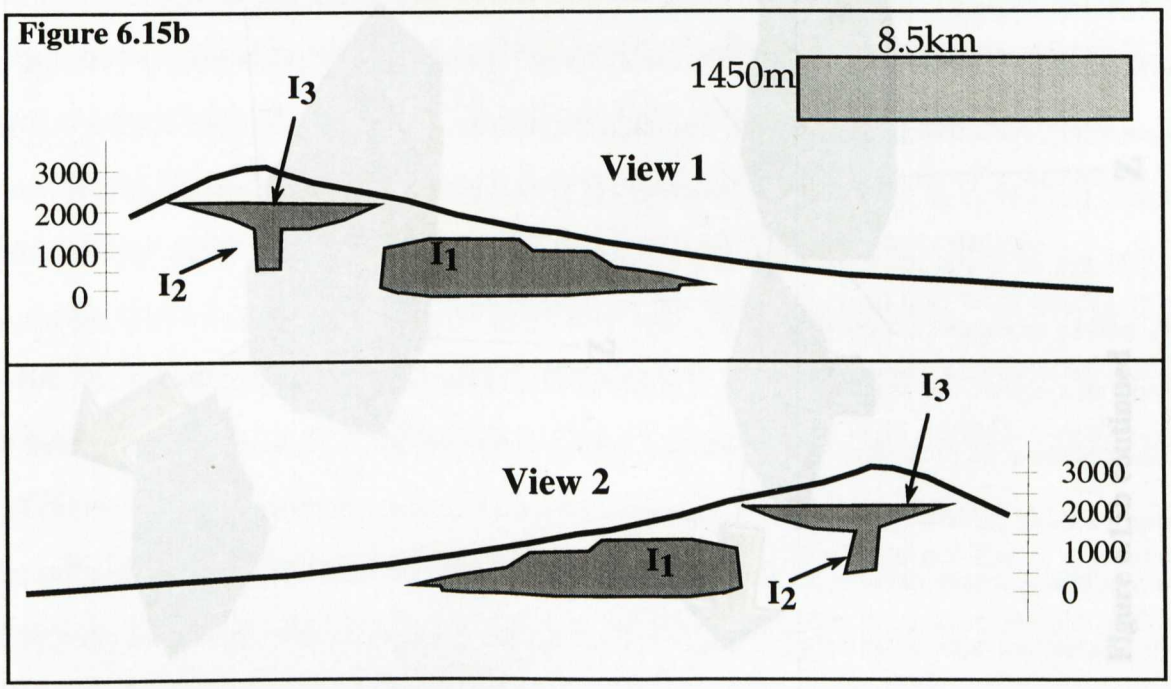

Figure 6.15. 3-D gravity models.
a. Map view, showing the location of the modelled bodies in relation to the topography. VDB = Valle del Bove. Line of section referes to the profile of figure b, as do views 1 and 2.
b. Perspective views together with the strain ellipse for the region. The various views of the bodies allow the 3-dimensional relationships to be clearly seen. Labelling as for the 2.5-D profiles. North is indicated by the arrows. Approximate scale bars are shown. The horizontal and vertical dimensions for body I_1 are shown by the box in the cross section views.

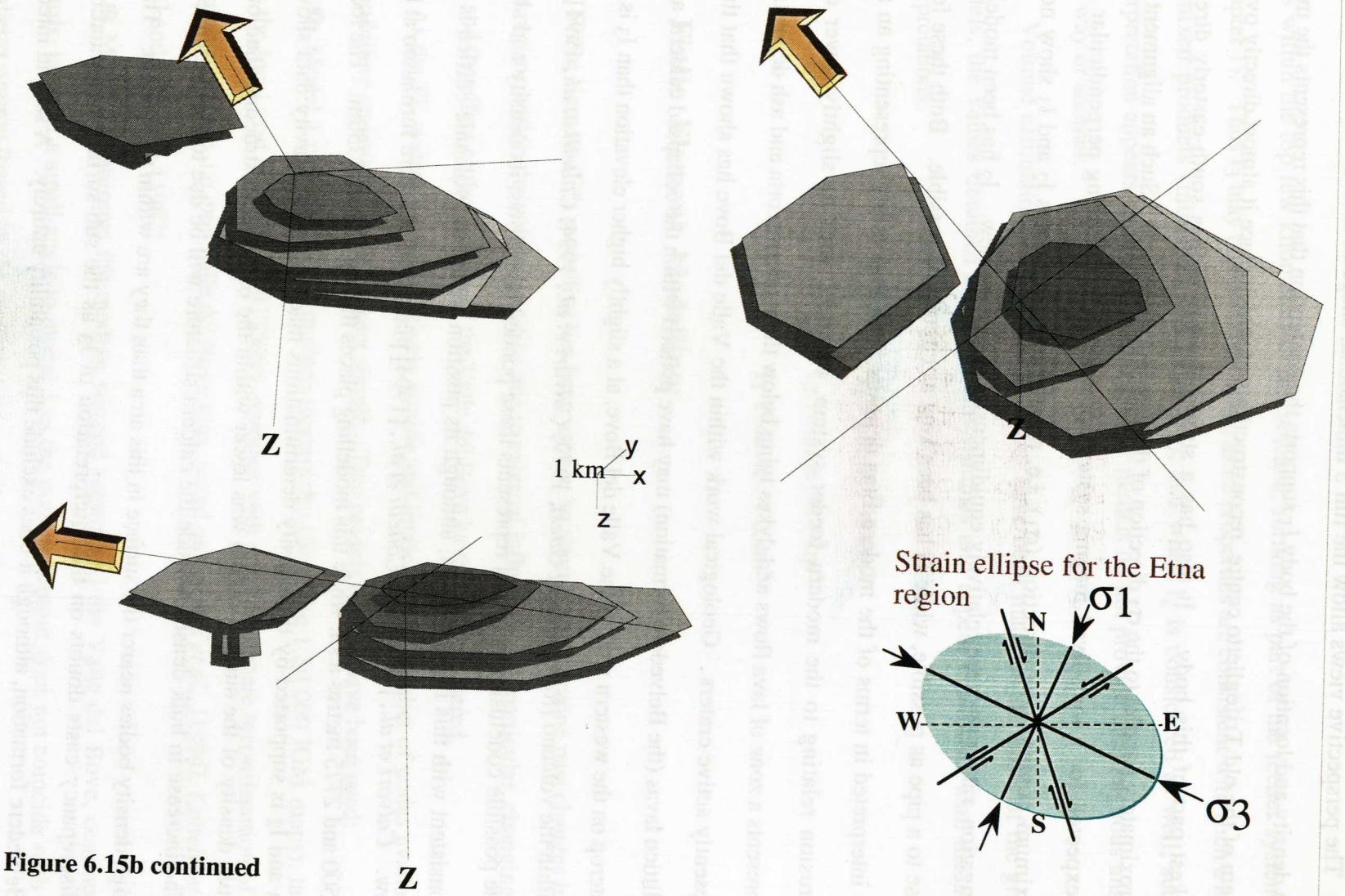

Figure 6.15b continued

The perspective views allow the full 3 dimensional shape of the bodies to be seen. The high density and location of the body I_1 supports the contention that this represents the magma system of the old Trifoglietto centre, reconstructions of which place it almost directly over the thickest part of this body. It also has a strong elongation in a south-easterly direction, approximately parallel to the σ_3 direction of the regional stress field. Such an alignment could be expected for a long-lived magma system, preferentially intruding perpendicular to the maximum compressive direction (σ_1), i.e. parallel to σ_3. Bodies I_2 and I_3 show no such elongation, rather they are relatively equidimensional in plan view. I_2 has been modelled as close to a pipe as possible, while I_3 has been kept as circular as possible. Both these features are interpreted in terms of the modern Etna deposits, with I_2 possibly representing an area of intrusion relating to the modern feeder system, while I_3, with its slightly lower density represents a zone of lava flows and dykes lying below the modern scoria and ash deposits of the presently active craters. Geological work within the Valle del Bove has shown that the post-Ellittico lavas (the Belvedere formation) may have ponded within the collapsed caldera, and now outcrop on the western wall of the Valle del Bove, at a slightly higher elevation than I_3 is located within the volcano [*Romano and Guest,* 1979; *Calvari et al.*, 1994; *Coltelli et al.*, 1994]. Thus one possible conclusion is that I_3 represents these ponded lava flows; its density and shape are consistent with this interpretation, although its position within the volcanic edifice is slightly low. *Calvari et al.*, [1994] and *Coltelli et al.*, [1994] place the Belvedere formation at between 2500 and 2775 metres a.s.l. while this modelling places the top of I_3 at 2350m. The location of I_3 and I_2 is supported by the density determinations made from the gravity data showing the bulk density of the summit region was lower within the old caldera structure than outside it. The increase in bulk density outside the caldera structure will be due to the presence of these high density bodies nearer the surface in this area than they are within the caldera. This height discrepancy casts doubts on the interpretation of I_3 as the sub-surface continuation of the Belvedere formation, although it does exclude this possibility entirely. A second interpretation results from the recent work of *Dobran and Coniglio* [1996] as well as earlier models such as that of *Wadge* [1977]. In essence these models suggest the formation of an area of dykes and

sills within the top few kilometres of the volcano, forming as part of the feeder system (see Chapter 1). Thus I_3 may represent this zone, as its properties are consistent with such a region of mixed products (intrusives and extrusive), and when I_2 is considered as well, such an interpretation appears stronger. These gravity models do not provide unambiguous answers one way or another.

Volume estimations of these three bodies have been made on the basis of the gravity models, the values obtained are maximum volumes and appear consistent with the above interpretations:

I_1 Volume : 38 km^3

I_2 Volume : 0.4 km^3

I_3 Volume : 4.2 km^3

6.7. Finite Element Modelling:

Finite element (FE) modelling has been used in an attempt to determine past changes in the stress regime within the volcanic edifice due to external influences. In particular, changing sea level and the effect of the creation of the Valle del Bove have been considered.

As the FE system used is relatively simple and limited in the number of nodes available, the modelling undertaken has been kept simple. Two models of Etna have been used:

❶ Model 1 is based on the modern topography (from the 1:50 000 IGM maps), taken along the local grid reference of 4175000, together with an approximate reconstruction of the Trifoglietto volcano, i.e. pre-Valle del Bove Etna, based on *Calvari et al.*, [1994], *Coltelli et al.*, [1994] and *McGuire*, [1982].

❷ Model 2 represents the modern summit region and the Valle del Bove, continuing seawards, taken at a small angle to model 1 as the present summit does not coincide with the Trifoglietto summit (based on the reconstruction used).

This small angle between the two models results in a slight difference in the shapes of the structures shown. The location of both profiles on the modern topographic map of Etna are shown in figure 6.16a.

Both models have been extended to 50 km from the summit and to a depth of 30 km below sea-level in order to greatly reduce the edge effects in the resultant stress field models. Edge effects generally arise from the boundaries of the models being fixed in space, that is, the base of the model is held fixed in the vertical (y) direction, while the sides are fixed in the horizontal (x) direction. These boundary conditions are necessary in order to reduce the number of unknowns down to manageable levels, and their effect is kept to a minimum by extending the models to large distances. The FE method used here assumes plain strain, thus both models are 2-D only, being infinite in the third direction (i.e. they are an infinite ridge).

The models consist of three bodies and the sea; the three bodies are:

1. The sub-Etna basement.
2. Etnean volcanics
3. The large intrusive body, I_1.

I_1 has been included as the size and density of this body are sufficiently large to affect the stress patterns within the volcano at such a scale as to be important.

The finite element modelling system used, ELCUT, is limited to 250 nodes, thus spacing is relative coarse and variable across the model, the densest network of nodal points is within the volcanic edifice, with the spacing increasing towards the bottom corners (figure 6.16). The physical properties of each body (table 6.6) are taken from *Birch*, [1966] and are based on average values for the various rock types. The volcanics are assumed to be similar in properties to volcanic ash, as the loose and relatively unconsolidated surface lavas would behave in a similar way to ash material. Also the older, buried volcanics are likely to be a highly heterogeneous mixture of ash and lava flows, and thus have properties closer to ash than solid basalt. The sediments have been given properties somewhere between sandstones and limestones, while the body I_1 has properties of massive basalt or gabbro (the physical properties (Young's modulus and Poissons ratio) are very similar for these two materials). All these properties are only approximations and the real situation is likely to be much more complex, with physical properties changing within a unit, possibly over very short distances. It is possible that the material making up I_1 was either hot or even partly liquid during the time span considered in the pre-Valle del Bove models, however given the relatively shallow level this

body sits at (1-2 km below the surface if the Trifoglietto centre is 2500m high) it is unlikely that it would be entirely molten, rather it is possibly a zone of solid material mixed with limited amounts of hot molten material. Thus the physical properties of the body as a whole may still be close to those of solid basalt, however on a small scale they may vary considerably.

Table 6.6. Physical Properties used in the Finite Element Modelling.

Unit	Young's Modulus, E (GPa)	Poissons Ratio, υ	Density (kg m^{-3})
Volcanics	10	0.15	2400
Sediments	57	0.22	2670
Intrusive (I_1)	70	0.25	2950

The geometry of the models are based on the results of the gravity models, thus the volcano/basement interface closely approximates to the contact as shown in figures 6.9 to 6.11. The shape of body I_1 is similarly constrained. Sea-level for the pre-Valle del Bove situation has been assumed at 100m below the present day level based on *Fairbanks*, [1989]. This assumes a time of approximately 15 000 year B.P.

Only static (non-time varying) stresses have been considered, therefore the results are effectively a snapshot of the stress field at a given time in the volcano's history. The scenarios considered in this modelling represent major events in the volcano's history, events which may have had a considerable effect on the volcano's behaviour. Thus the situations considered are:

❶ Pre-Valle del Bove model:

- stress pattern present due to gravity (reference stress field).
- stress pattern due to increase in sea-level by 100m .
- the effect of a significant ice layer on the summit region.

Figure 6.16. Finite Element Model mesh. The upper diagrams show the entire model, 100km in length by 30km depth (the base is 30km below sea-level; the summit approximately 3000m above sea-level). The lower diagrams are enlargements of the edifice itself. For both models the spacing is approximately 700m inside the edifice, increasing to several kilometres at the corners. Relative spacing is given by the circles, which show the spacing in the region of the node at the centre.

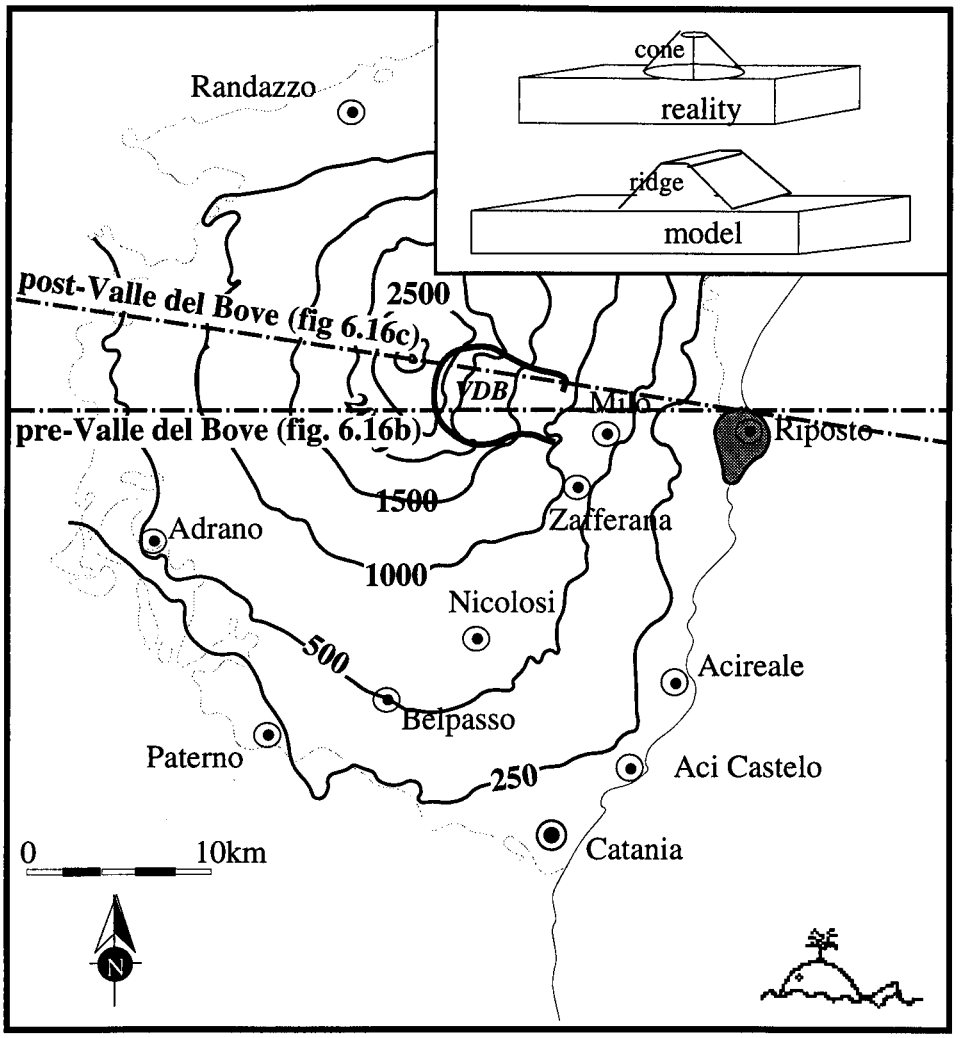

Figure 6.16a. Location of the two Finite Element modelling profiles. The profile for the pre-Valle del Bove situation is placed so as to cut through the approximate location of the Trifoglietto centre; that of the present day cuts through the modern summit region. Contours are in metres. VDB = Valle del Bove; thin grey line = limit of volcanics. The shaded area represents the Chiancone deposit. The insert shows the difference between the models and reality in terms of geometry of the 2-D ridge.

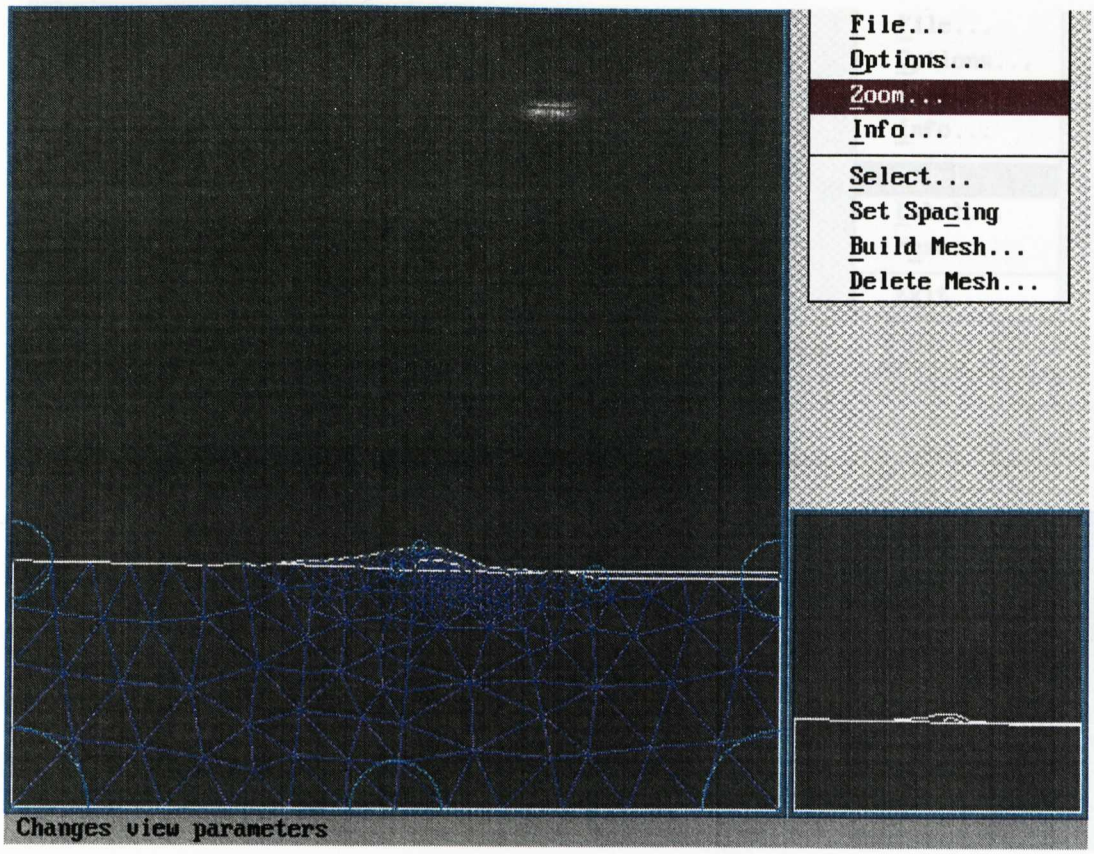

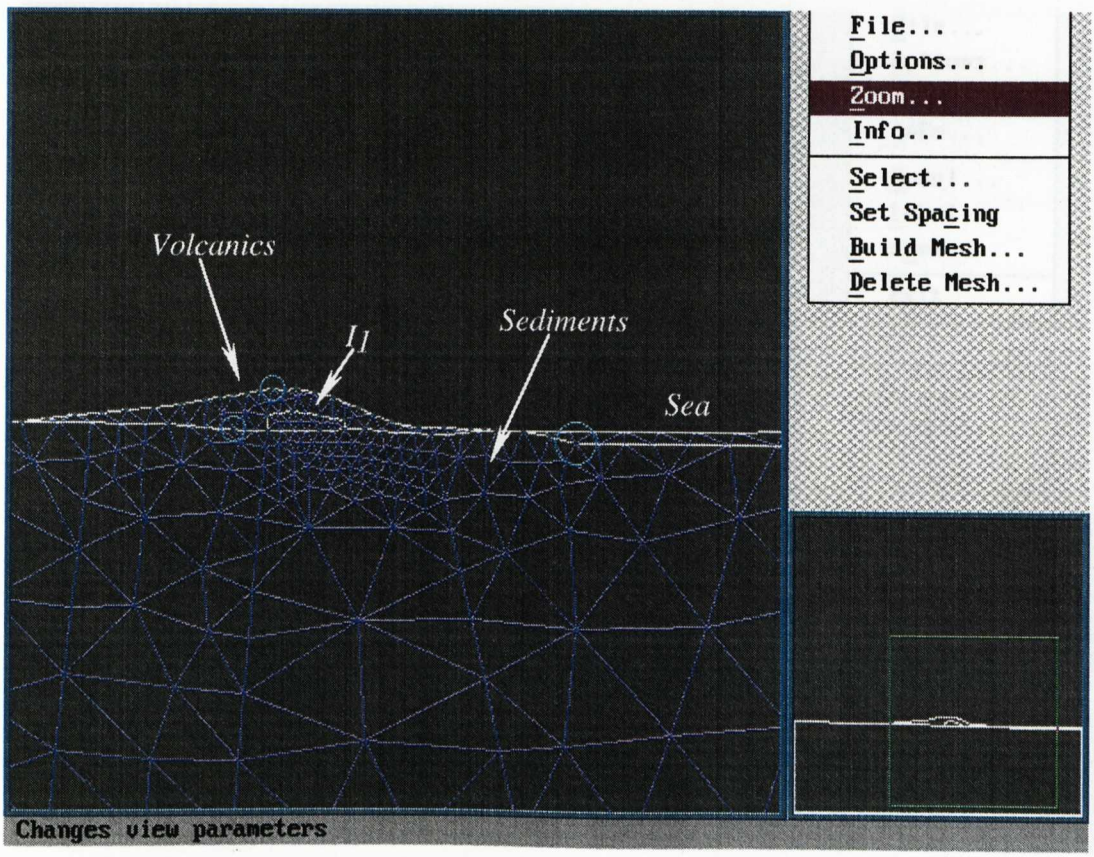

Figure 6.16b. Pre-Valle del Bove model.

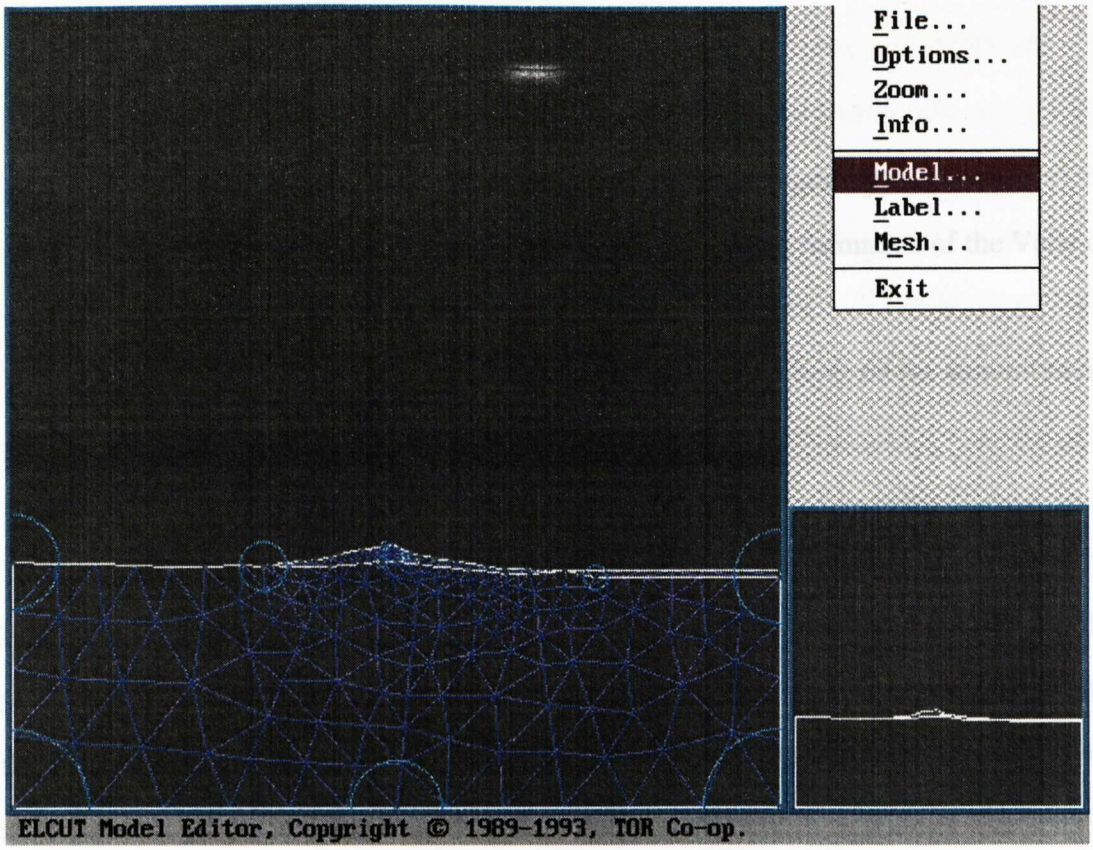

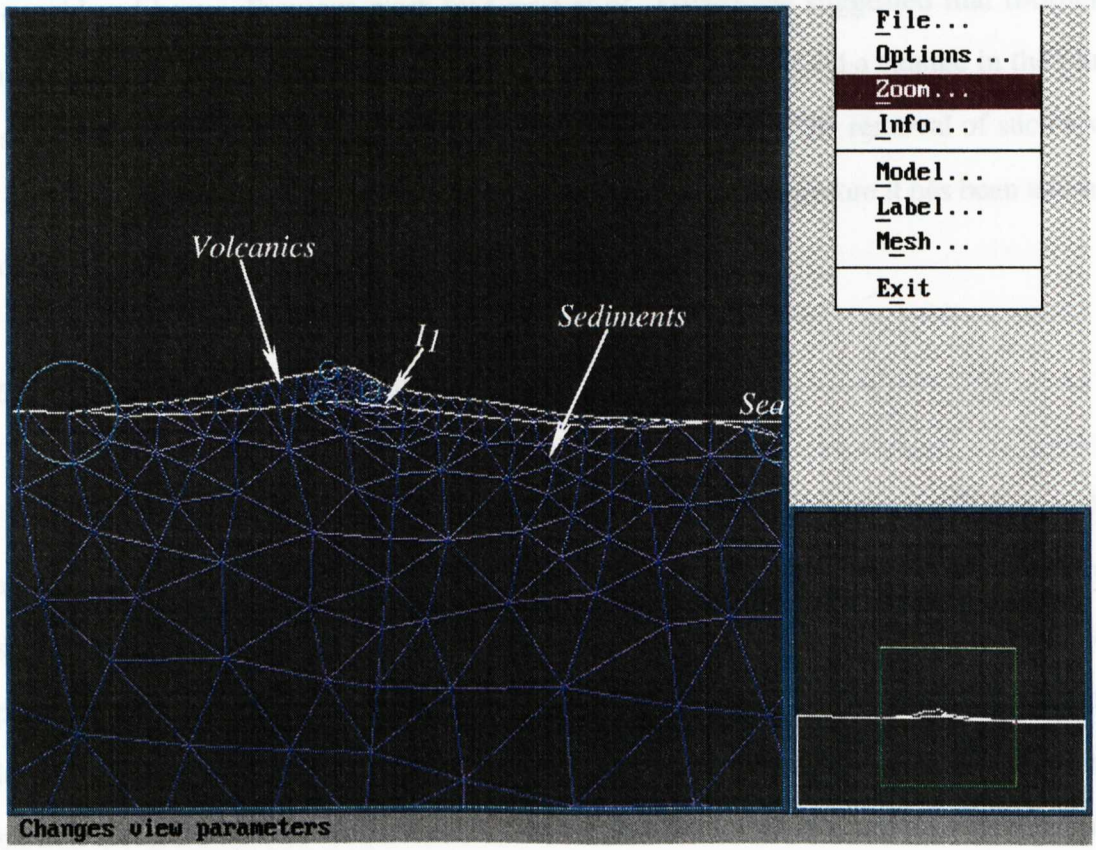

Figure 6.16c. Post-Valle del Bove model.

❷ Post-Valle del Bove model (modern situation):

- reference stress field (due to gravity).
- stress field resulting from the formation of the Valle del Bove.
- the effect of a significant ice layer on the summit region plus a drop in sea-level.

These situations have been chosen on the basis of the following rationale: *Neri et al.*, [1995] have suggested the possibility of significant areas of ice build-up (up to 37 km^2) being present on Etna's summit during previous glaciations, such ice build-ups generally coinciding with sea-level change. Changing sea-level may affect the volcano in numerous ways - changing erosion patterns, groundwater systems and stress fields - however it is only the latter case which is considered here. Previous work by *Guest et al.*, [1984] has suggested that following the formation of the Valle del Bove the change in the stress field caused a change in the plumbing system, preventing high level magma chambers from forming. The removal of such a volume of mass is likely to have a significant affect on the volcano and therefore it has been attempted to model this situation.

6.7.1. Imposed Stress Fields:

ELCUT allows for the imposition of stresses in a number of ways, each being useful for a particular situation. For this study body-forces, surface-forces and normal pressures have been used. Body-forces apply the stress to every part of the body, thus they are a good approximation for gravity, while surface-forces represent a force acting along a surface. Normal pressure is similar to surface force but allows the magnitude of the stress to vary with position along the surface in question. The forces used for each situation modelled are listed below:

❶ Pre-Valle del Bove model (figure 6.16a; 6.17):

The effect of gravity is determined by the use of body forces proportional to the density of each body. The three bodies in the model and the sea have all been given downward acting forces equal to: $g\rho$, where ρ is the density in kg m^{-3} and g is the gravitational acceleration (9.8m s^{-2}). This is equivalent to the force of gravity acting on each cubic metre. For both of the other scenarios modelled, the forces have been calculated as normal pressures, given by the equation:

$$\text{Pressure} = g\rho h$$

Where h = the thickness of the ice/change in sea-level.

No drop in sea-level is included in the ice model as the sea-level already represents the level at the glacial maximum (-100m). In the case of the sea-level change, the pressure used varies with position, thus for a 100m rise in sea-level, at the modern contour line of 0m the force is zero, reaching a maximum at the present 100m below sea-level line (i.e. the assumed level of the 0m contour at the time). The ice limit is taken as the 2300m contour line after *Neri et al.*, [1995].

❷ Post-Valle del Bove model (figures 6.16b; 6.18):

The gravity induced stress field for this case has been determined in an identical manner to the pre-Valle del Bove situation, as has the effect of a significant ice layer. Here the ice limit is the 2500m contour, and as such a build up of ice would be expected to coincide with a drop in sea-level, this is included. Modelling the formation of the Valle del Bove is a more complex problem than simple sea-level change or ice build-up. The formation of the Valle represents the removal of considerable mass from the side of the volcano, in the modelling of this both the amount of material and the time scale of movement are important; it is the rate of stress change that may be expected to have the greater effect than the magnitude of the change. For the purposes of the modelling it has been assumed that the material was removed in a single movement - this is due to the static nature of ELCUT. This assumption is acceptable if the Valle formed in a short time period (e.g. a few thousand years), as the volcano would be unlikely to fully equilibrate over this time scale, and therefore it effectively sees the movement as sudden,

and simultaneous, however for a greater time span the effect of the imposed stresses changes will be reduced. Two approaches to this problem have been used, the first uses an upward acting surface force in the area of the Valle del Bove, i.e. a surface force of 24000 N m^{-2} acting upwards (positive y direction) has been imposed on the present day floor of the Valle; the second recreates the pre-Valle topography and imposes an upward acting body force on the material occupying the Valle, i.e. a force of 24000 N m^{-3} acting in the positive y direction (upwards) has been imposed on this body. The value of 24000 has been used assuming a bulk density of approximately 2400 kg m^{-3} for the material The second case may be more realistic as the use of a surface force does not take into account the thickness of material removed, however the reliability of the reconstruction of the Valle del Bove is low, thus both of these models are only approximations and the real situation will be of much greater complexity. Here all movement is instantaneous and vertical, neither of which are strictly true, also the 2 dimensional nature of ELCUT means that we are removing a ridge of material rather than scraping out a basin, as would be more realistic. This final simplification may have the largest effect of all as likely edge effects on the Northern and Southern walls are ignored, as are any focusing of stresses which may occur at the corners of the real Valle.

6.7.2. Model Results:

The results of the FE work are best seen pictorially as the patterns of the stresses are the significant feature. ELCUT allows significant post-processing, and thus for numerous stress orientations to be observed, however for the purpose of clarity, only stresses acting along the three axis, x,y,z, are shown, with x and z representing the horizontal directions and y the vertical. The orientations of the three axes are shown in the figures 6.17 and 6.18. The sign convention in ELCUT is for a negative number to represent a more compressive force. For all the stress diagrams (6.17 and 6.18) the diagrams show the stress patterns for the three axes directions, x, z, y.

The influences of these imposed forces will vary depending on the time over which they act and their magnitude. Rapid changes in stresses will have a much greater effect than slow

changes, however no attempt is made here to assess the rates of the imposed changes as ELCUT is a static system. The magnitude at which a stress will influence the behaviour of a volcano is a difficult number to assess, thus for the discussion of the individual models the magnitudes are ignored. However an indication of the significance of the stress fields modelled may be given by the hypothesised link between Earth tides and volcanic eruptions. There is a limited amount of evidence to suggest that the changing stresses due to the tidal cycle influence the behaviour of volcanoes. Links between activity and tides have been seen for a number of volcanoes, such as Campi Flegrei caldera [*Berrino and Corrado* 1991], Pavlof Volcano, Alaska [*McNutt and Beavan* 1981], Hawaiian volcanoes [*Shimozuru* 1987] and Etna [*Patanè et al.,* 1994]. The stresses due to tides are of the order of 10^3 N m^{-2} [*Baker* 1984]; magnitudes of stresses greater than this should therefore have an observable influence on the volcanic system.

6.7.2.1. Model 1: Pre-Valle del Bove:

Figure 6.17a shows the reference state, i.e. the effect of imposing gravity only on the model. As can be seen in figure 6.17a, the stress field is horizontal for all three directions, the uneven nature of some of the contours is due to the mesh pattern, and thus is an artefact of the limited number of nodes. For the other situations investigated this gravity field has first been removed before the addition of the imposed stress, this was done as the magnitude of the gravity stresses are several times larger than those due to the imposed changes, and, as the system is relatively course, the numerical rounding errors in the calculations of the gravity-induced stress field may approach the magnitude of the stress changes being modelled.

Figure 6.17b represents a 100m rise in sea-level, in order to aid interpretation the area of the volcano has been magnified. The stress pattern shown by these figures is as one might expect - concentrations of compressive stresses on the coast, focused at the new 0m contour. Such concentrations of stress will have important effects on the volcano. The Timpe Fault system lies approximately in this area of high stress, such concentrations of compressive stresses may cause the faults to lock, acting against small scale creep, leading to the greater chance of catastrophic movement (i.e. large earthquakes). The stresses produced are

insignificant to fracture the rock (10^7 N m^{-2} is needed to fracture basalt, A. Pullen, pers. comm., while 10^5 N m^{-2} is produced here), but they still represent a significant increase in the stresses acting on the faults. The Timpe faults have been considered as an important mechanism of transferring movement from the summit region downslope [*Stewart et al.*, 1993], thus locking them could have major effects further up slope. It is unknown if the Timpa Fault system was present at the time of the formation of the Valle del Bove but as it is the landward continuation of the Malta Escarpment then it is likely that they to have been part of Etna's Eastern Flank for a considerable length of time. The stability of the Flank must also be affected by this loading at the base, such basal compression is likely to prevent small scale creep from occurring, thus as forces up-slope are still attempting to push the slope outwards (e.g. magma intrusion in the summit region) a build up of stress will occur, leading to the increased likelihood of a catastrophic slope failure. This may be offset by a likely change in groundwater movements, with compression increasing the piezomatic pressure and thus having a lubricating effect. The relative importance of these forces is impossible to judge based on these models.

The effect of a build up of 10m of ice on the summit region (figure 6.17c) is as might be expected - the development of a zone of compression immediately below the ice layer. The 10m thickness was arbitrarily chosen as a likely amount, based on personal observations of 2-3m of snow being present in modern winters, in reality ice may be expected to build to much greater thicknesses and therefore these results represent minimum effects. A surprising result is the transmission of this compression through the volcano into the sediments below. How much of this transfer of stress is an artefact of the large difference in physical properties in the model is uncertain, but as the properties used represent reasonable approximations to the real situation, some of this transference must be real. A zone of compression in this region is likely to have important effects on the transport of magma within the volcano. Compression in the summit region is likely to increase the possibility of flank eruptions, sidewards movement now being easier than upwards, while the compression occurring at the sediment/volcano contact might be expected to prevent magma moving into the volcano itself. Such an effect would lead to large amounts of magma being stored at depth, possibly building basal intrusive complexes, leading to the strong possibility of large, more violent eruptions, as the magma will only rise once the

volatile pressure is greater than the confining pressure. Large, explosive eruptions in Etna's past have been linked to palaeoclimatic conditions, with cold, wet conditions allowing the build up of snow and the development of high level ground waters, eruptions under these conditions would be phreatic to phreatomagmatic in nature [*Duncan et al.*, 1984], however the stress patterns of figure 6.17c suggest that the larger eruption at times of colder conditions may have been assisted by the large build up of magma at depth, possibly preventing degassing and encouraging fractionation, once the magma pressure became greater than the confining pressure, the magma would have risen rapidly, driven by large volumes of volatiles, encountering snow and ice at the surface, thus causing large explosive eruptions.

6.7.2.2. Model 2: Post-Valle del Bove:

The stress pattern present due to gravity is very similar to that for the pre-Valle del Bove situation; again the irregularities in the patterns are due to the mesh spacing (figure 6.18a). As for above, the effects of gravity were removed before the other situations modelled. Figure 6.18b shows the stress due to an accumulation of 10m of ice in the summit region, the resultant pattern of stress is very similar to that for the pre-Valle model, again compressive stresses build up under the ice and are transmitted through to the underlying sediments. In a similar manner to the pre-Valle situation, such stress patterns might be expected to encourage Flank eruptions, and the ponding of magma at depth.

The effect of the Valle del Bove's formation is shown in figure 6.18c. The first three diagrams have been created by modelling the Valle's formation using an upwardly directed surface force of 24000 N m^{-2}, while the final diagram compares these results with those calculated by using a body to re-fill the Valle and applying an upward body force of 24000 N m^{-3}. The resultant pattern of stresses are very similar, with large concentrations of tensional stresses around the body I_1 and the volcano/sediment contact. Tension in this region may produce two effects: 1. increase the likelihood of intrusive activity in the area of tension; 2. increase movement along the volcano/sediment contact - the tension effectively lubricating the surface. Tension in the area of the Valle floor is expected and may result in a preference for

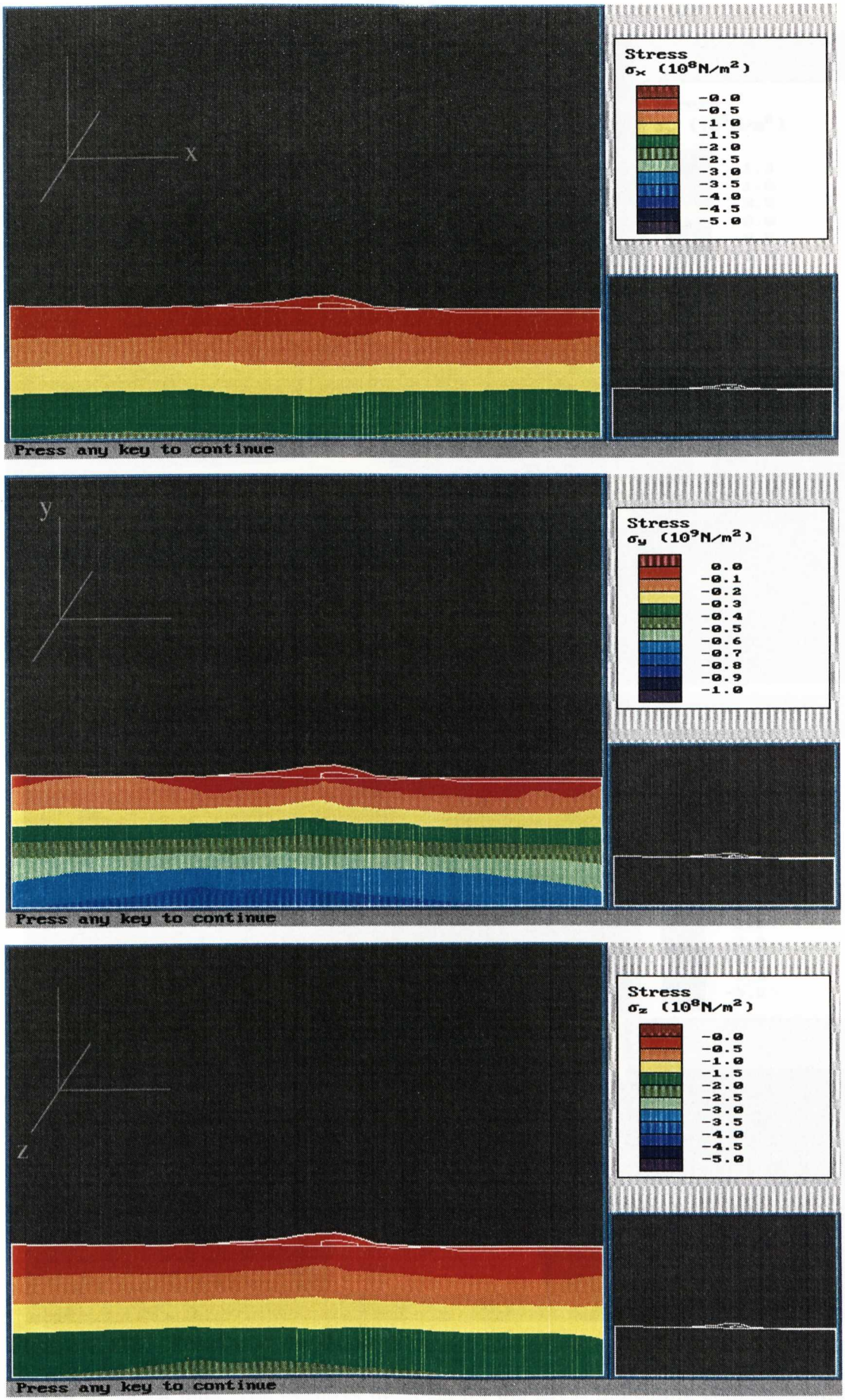

Figure 6.17a. Results of the Finite Element modelling - pre-Valle del Bove model, showing the reference gravity field. These figures are the result of applying gravity to the mesh structure of figure 6.16a. The resultant stress fields are essentially horizontal, irregularities are due to the mesh spacings. For all parts of this figure the stresses acting along the three axes , x, y, z, are shown (σ_x, σ_y, σ_z), as indicated by the axis within each diagram.

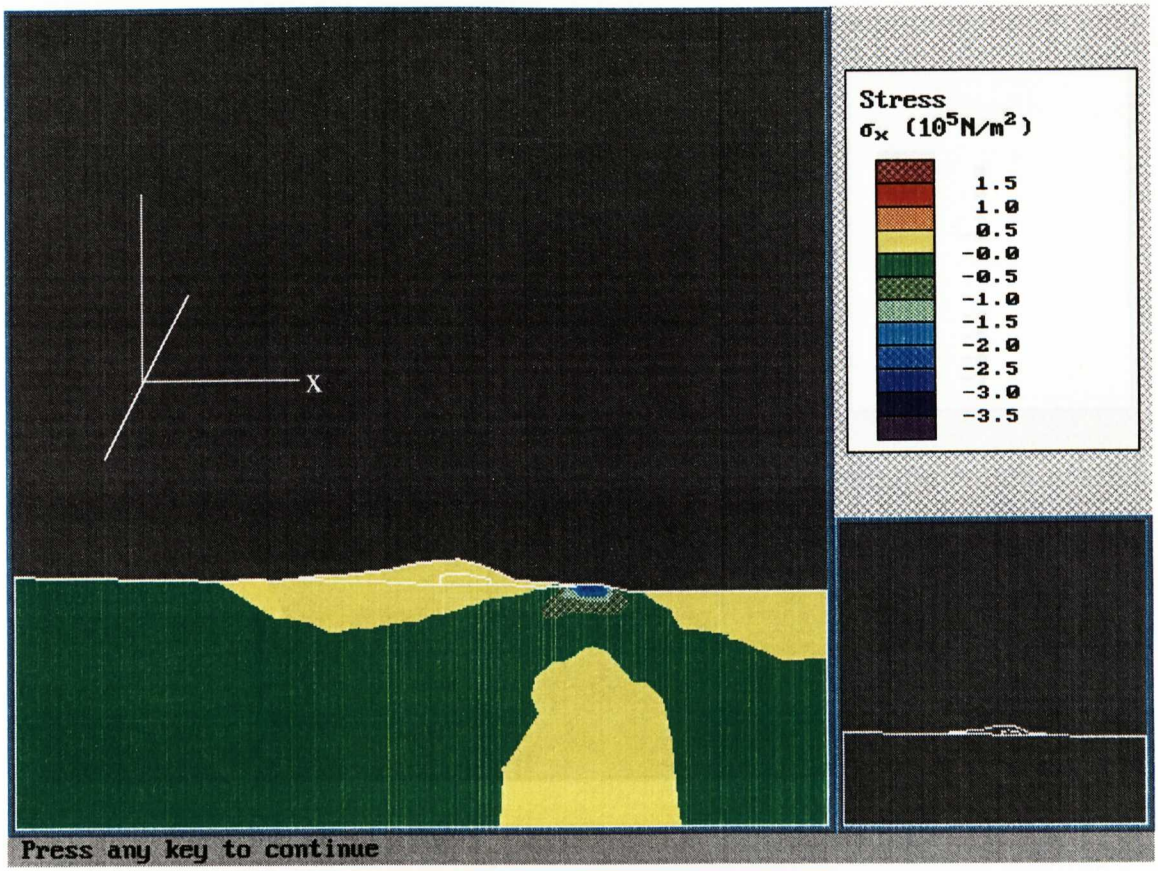

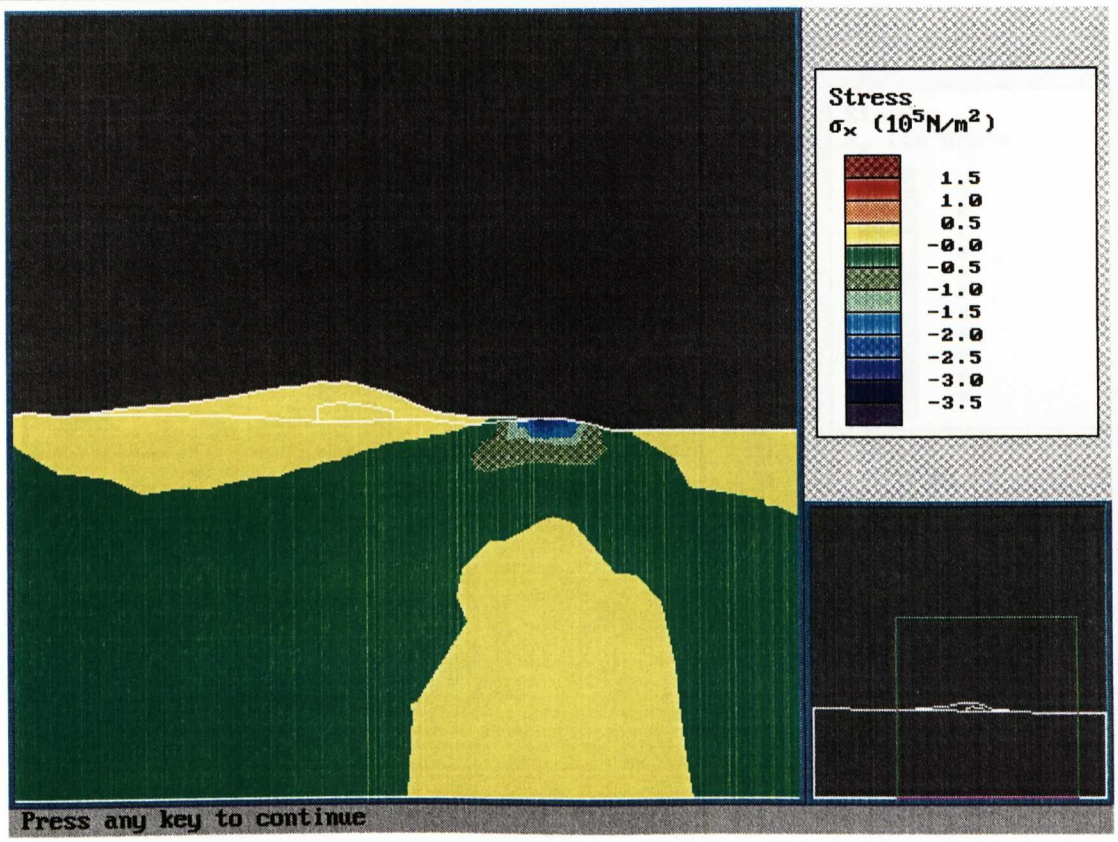

Figure 6.17b. Results of the Finite Element modelling - pre-Valle del Bove model showing the effect of a 100m sea-level rise. The principle stress concentrations are in the area of the coast line. The negative numbers for the stress indicating compression, thus compression occurs at the surface and slight tension at depth. For all parts of this figure the stresses acting along the three axes , x, y, z, are shown (σ_X, σ_Y, σ_Z), as indicated by the axis within each diagram. The lower part of each diagram shows an enlargement of the edifice itself.

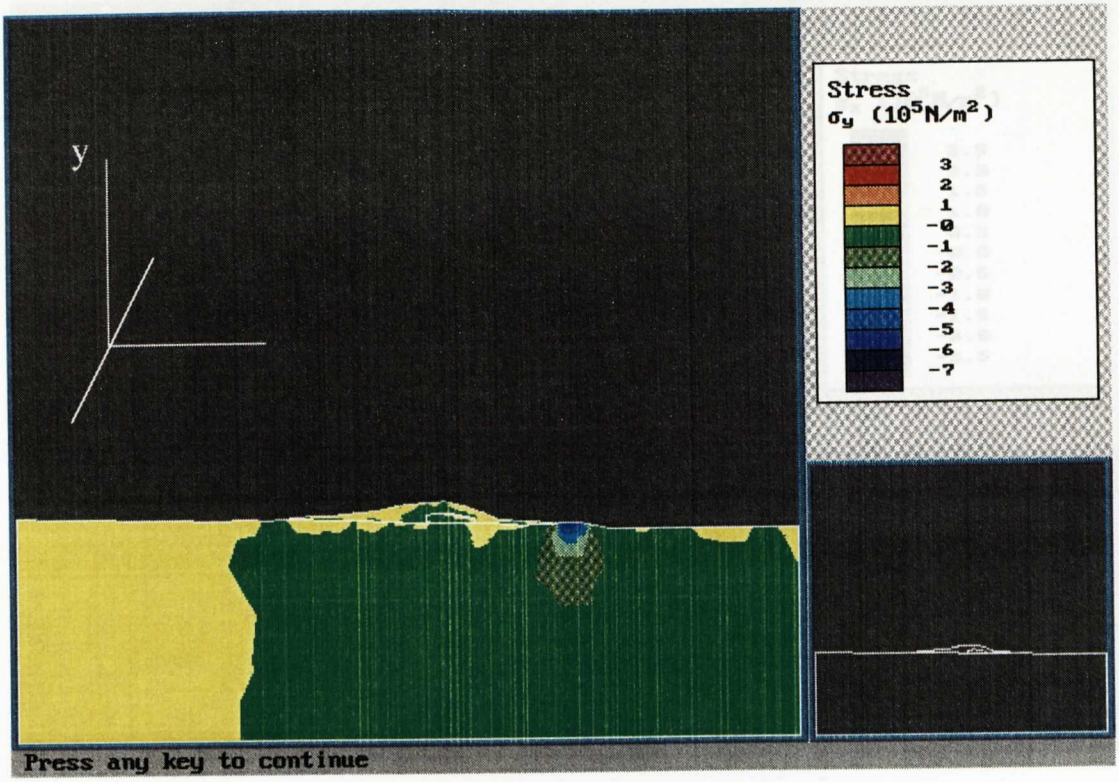

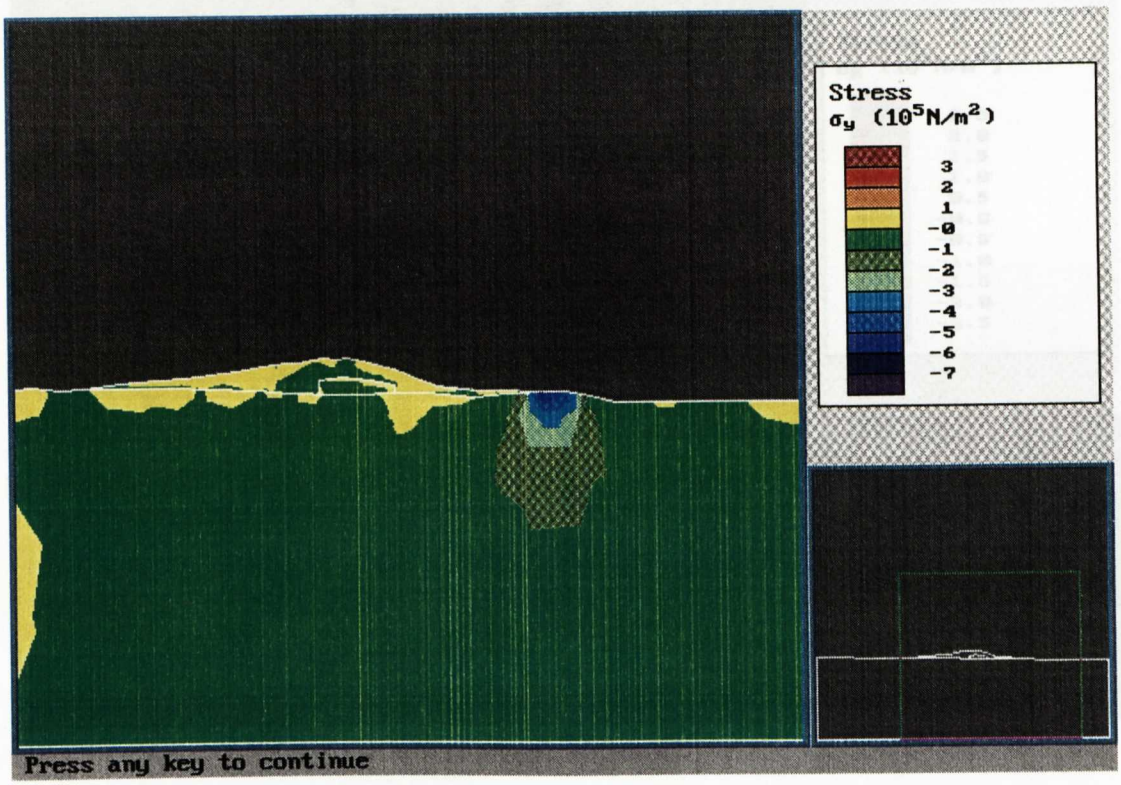

Figure 6.17b continued.

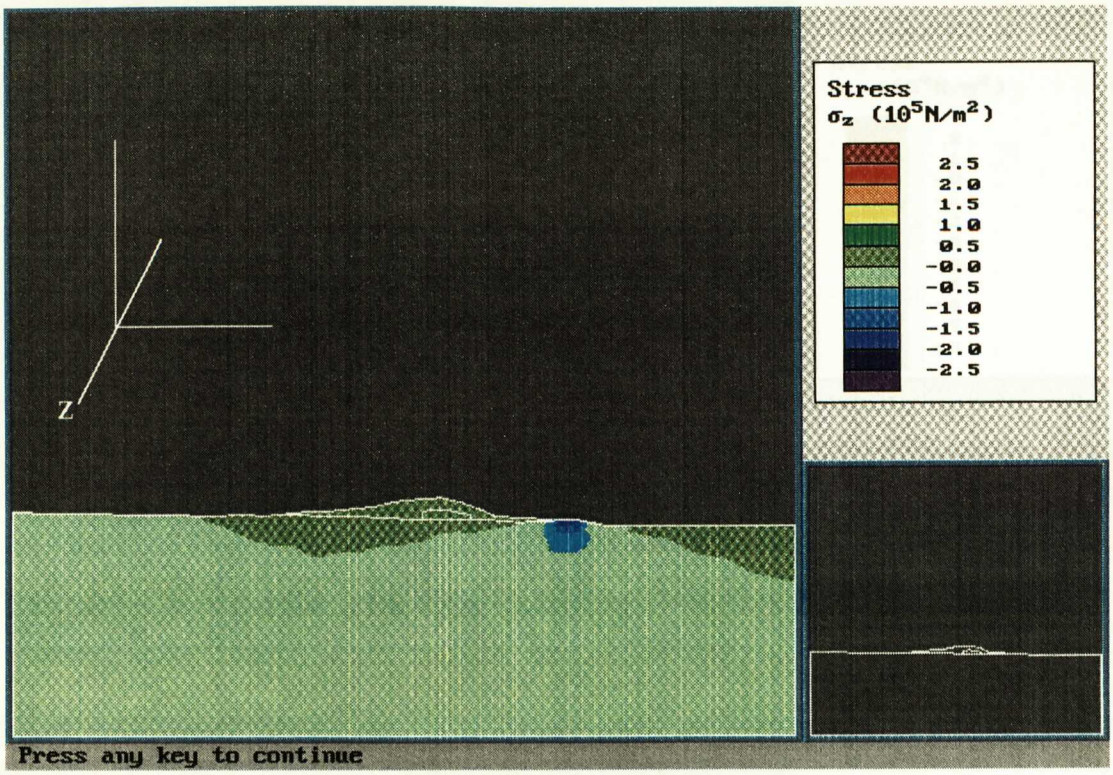

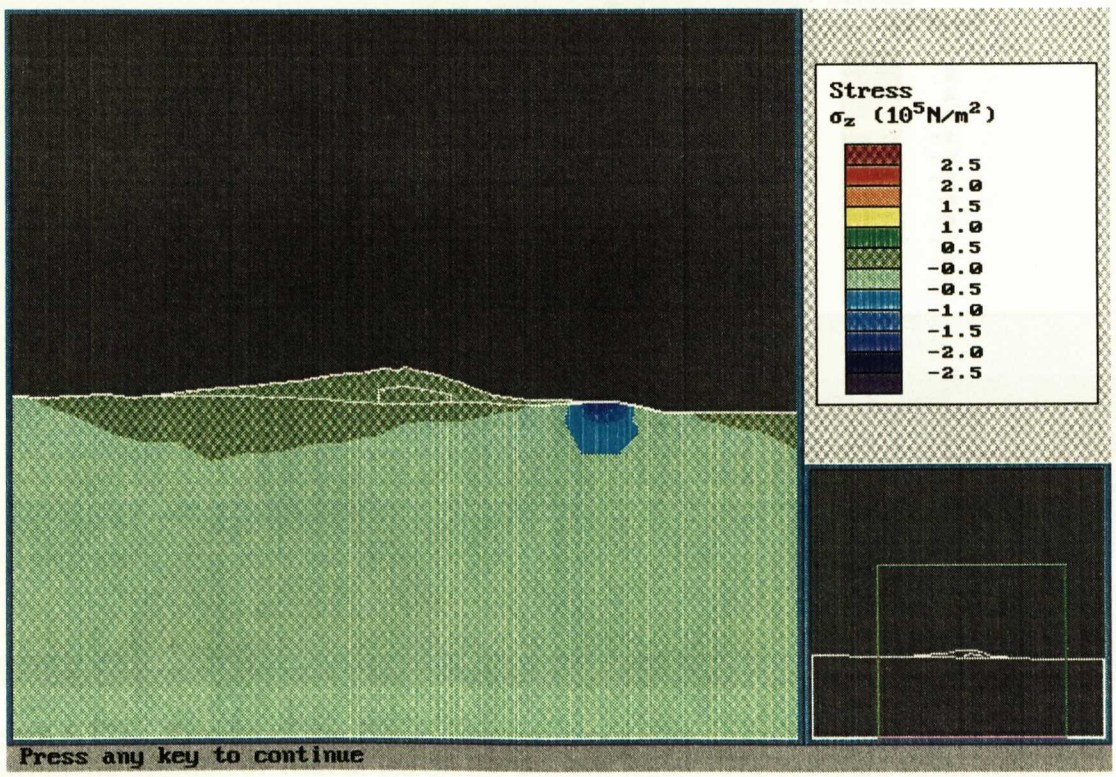

Figure 6.17b continued.

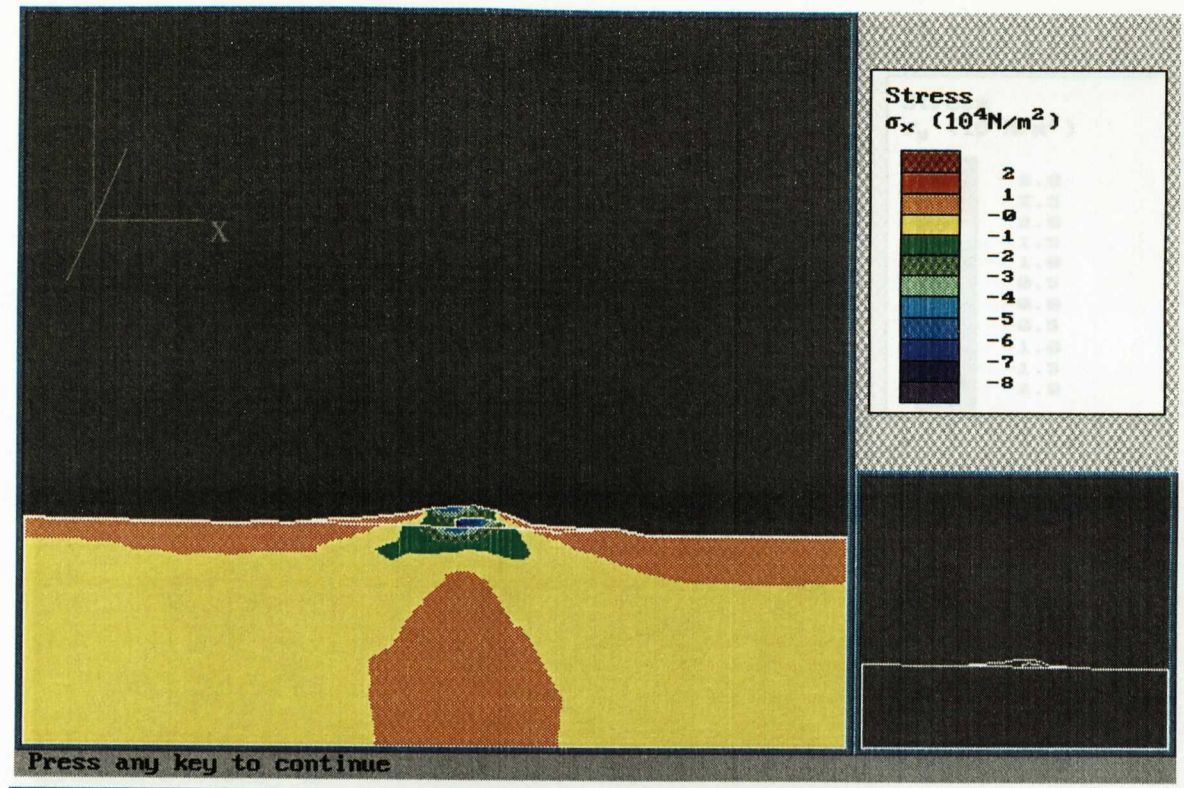

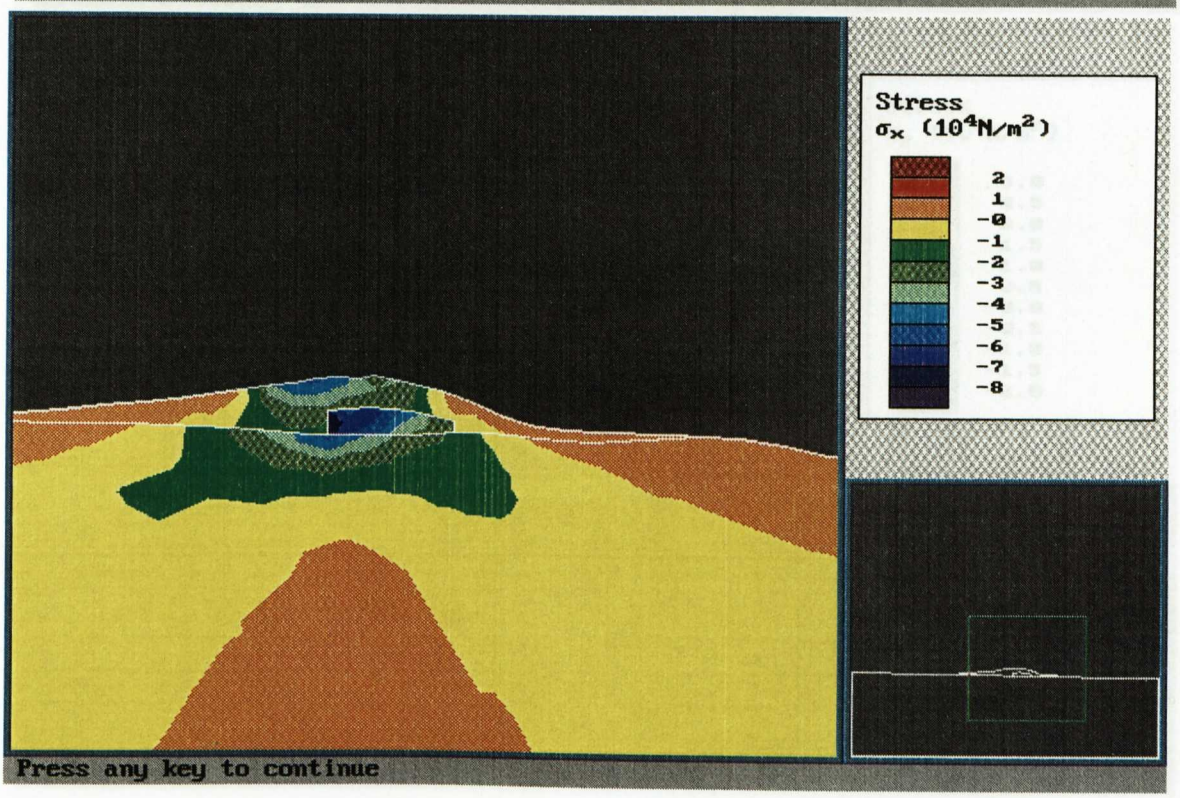

Figure 6.17c. Results of the Finite Element modelling - pre-Valle del Bove model, showing the addition of 10m of ice on the summit region. The resultant stress patterns shows a strong degree of compressive stress in the summit region. This compressive stress has been transmitted through the volcanics into the underlying sediments. For all parts of this figure the stresses acting along the three axes , x, y, z, are shown (σ_X, σ_Y, σ_Z), as indicated by the axis within each diagram. The lower part of each diagram shows an enlargement of the edifice.

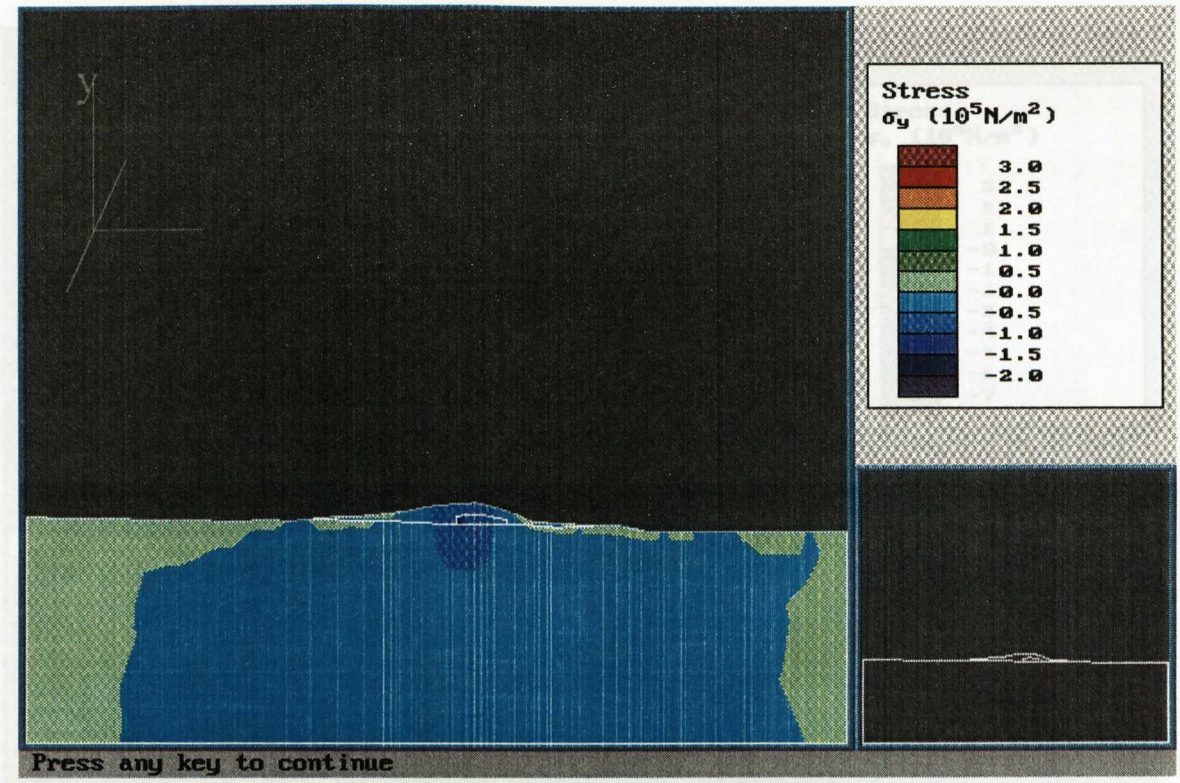

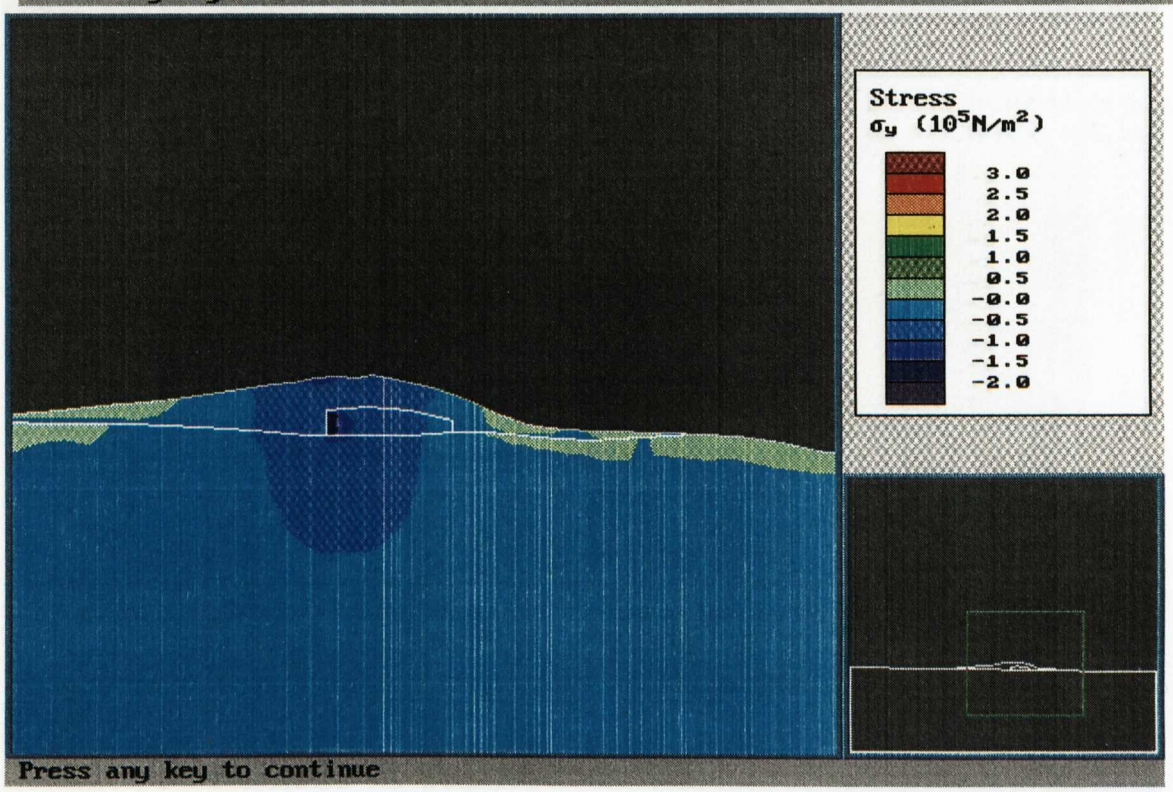

Figure 6.17c continued

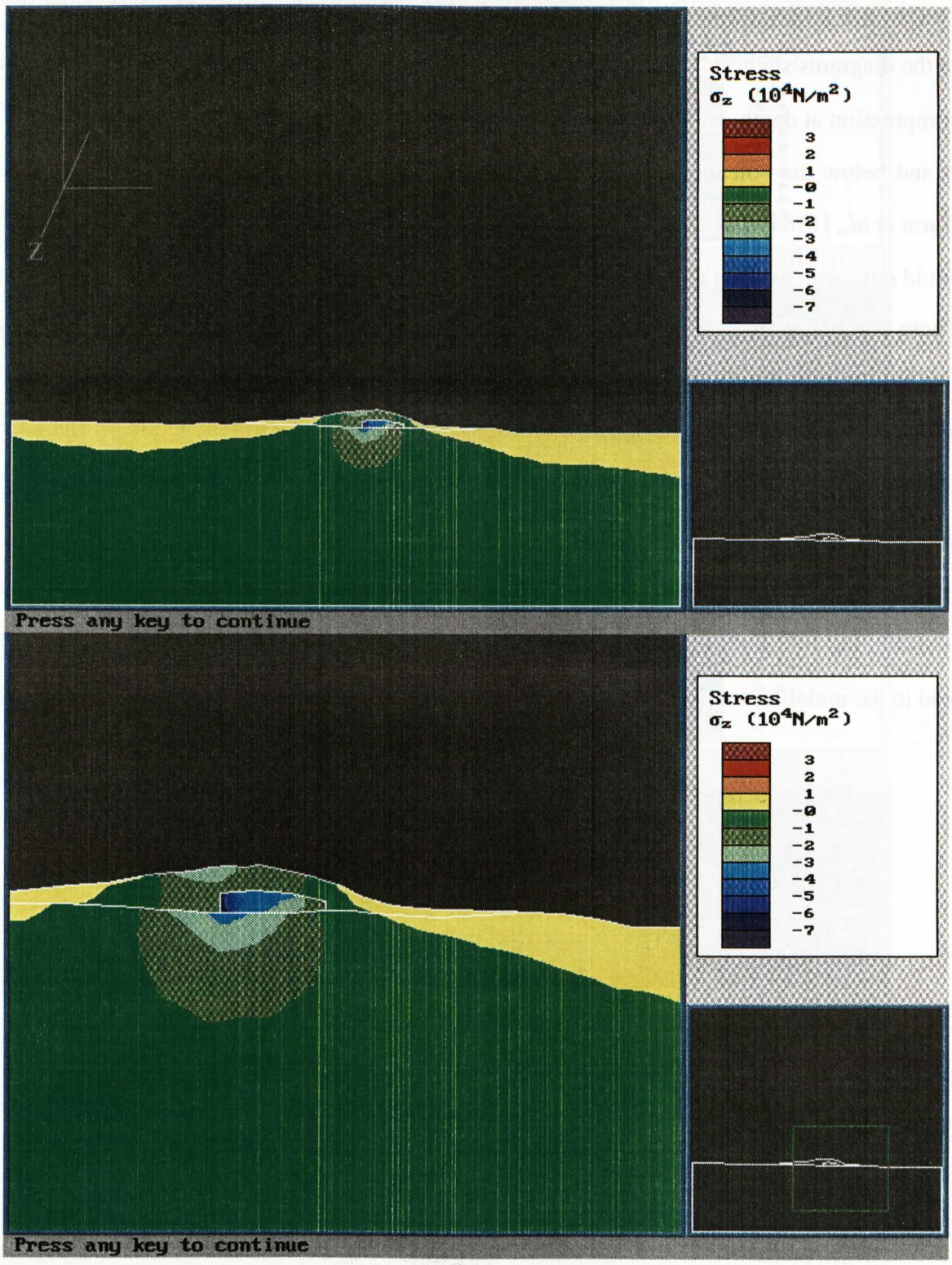

Figure 6.17c continued

eruptions in this area and/or an increase in the instability of the Valle's walls. The pattern of σ_x in the diagrams suggests the possibility of a pumping action occurring, with a slight increase in compression at depth, and an increase in tension near the surface. The concentration of tension at and below the volcano/sediment interface does not entirely agree with the observations of *Guest et al.*, [1984] that after the formation of the Valle del Bove shallow level magma chambers could not form, as such a zone of tension would be an ideal level at which magma could pond. These two points may be interpreted as indicating that the build up in tension allows magma to rise to a shallow level, with the tension in the upper slopes, though small, being sufficient to allow the magma to continue to the surface. By effectively placing the whole of the Eastern Flank and the summit region under tension, the formation of the Valle del Bove will have had a major influence on the stability of this area. The effect of such tension is to act as a lubricant on any slip planes, this would include the sediment/volcanic contact and the Timpa Faults. It is possible, but by no means certain, that such a regime of tension may have been the force that lead to the initial formation of the Timpe faults.

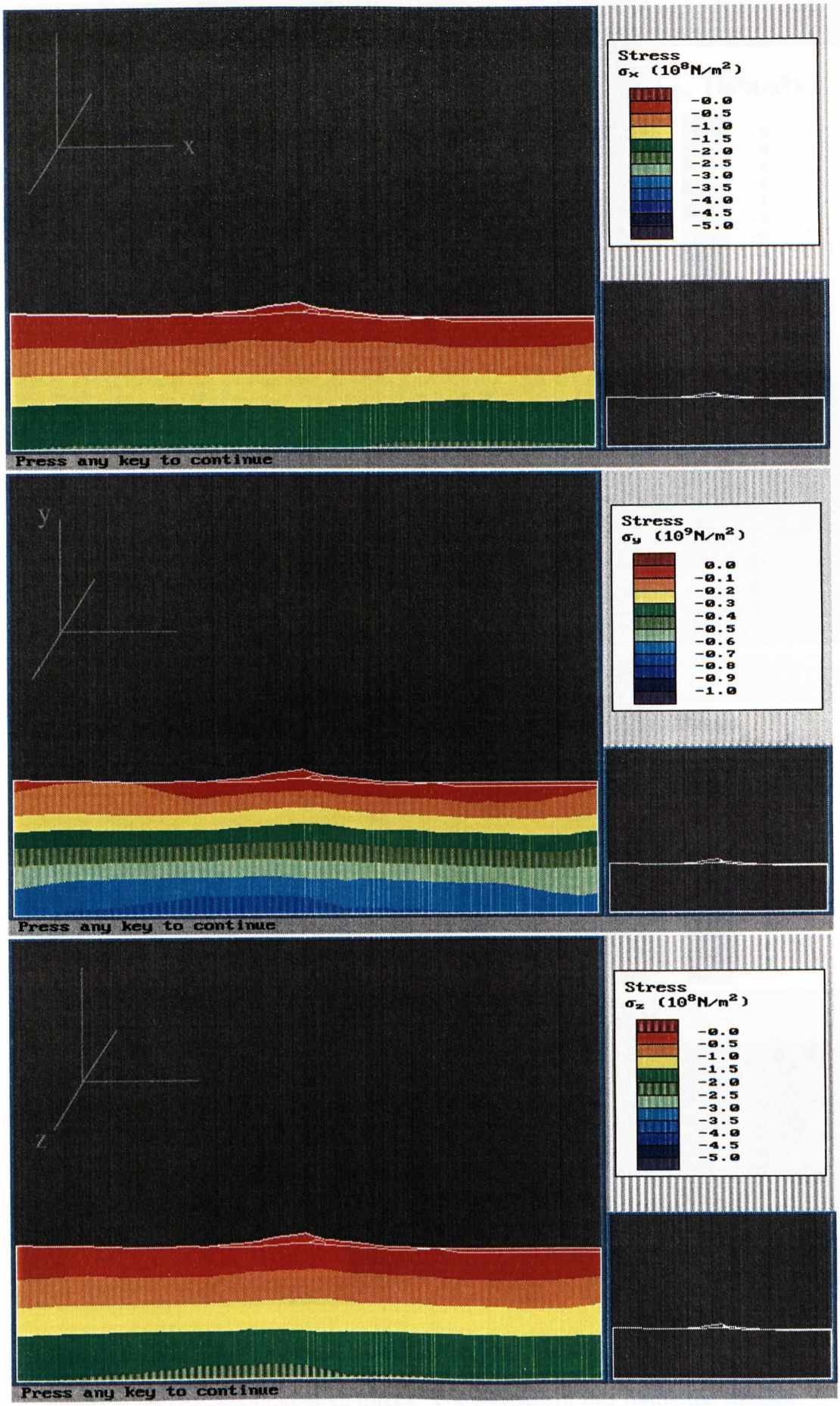

Figure 6.18a. Gravitational Stress Field for the post-Valle del Bove situation. The axes indicate in which direction the stresses are acting

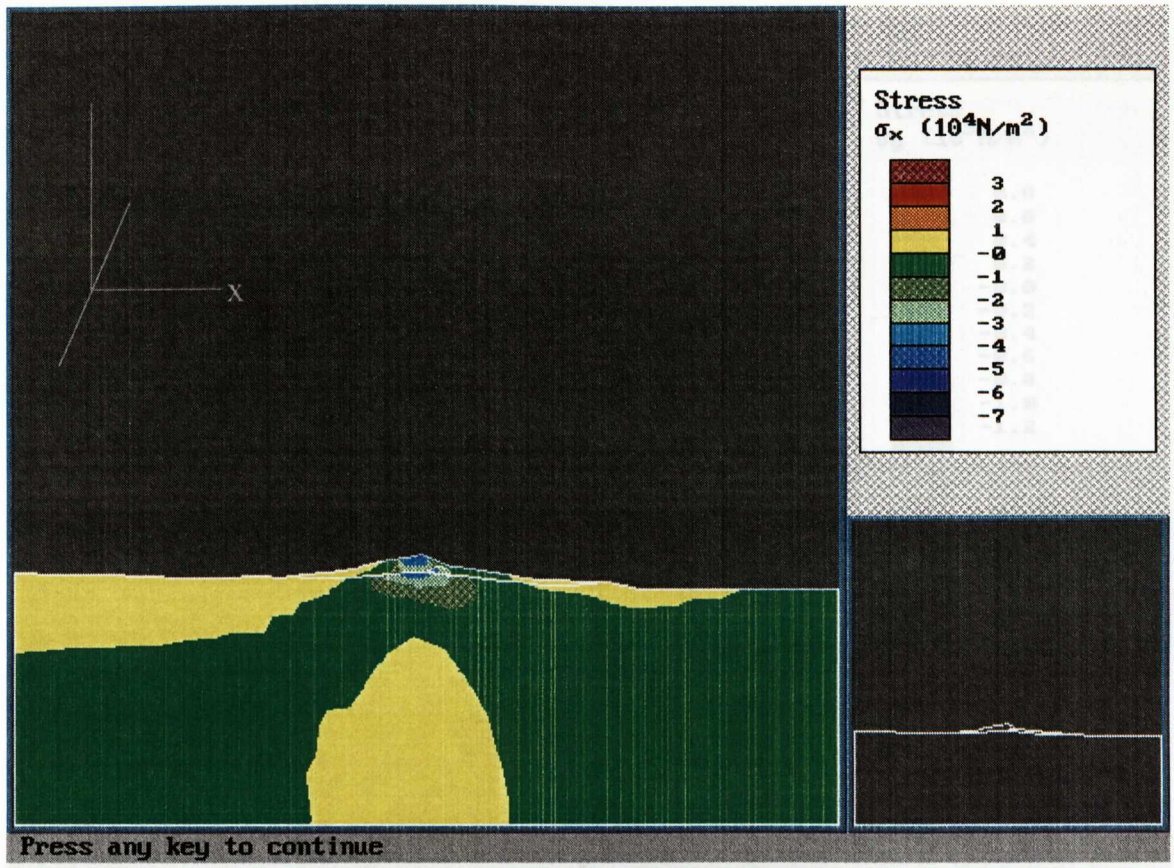

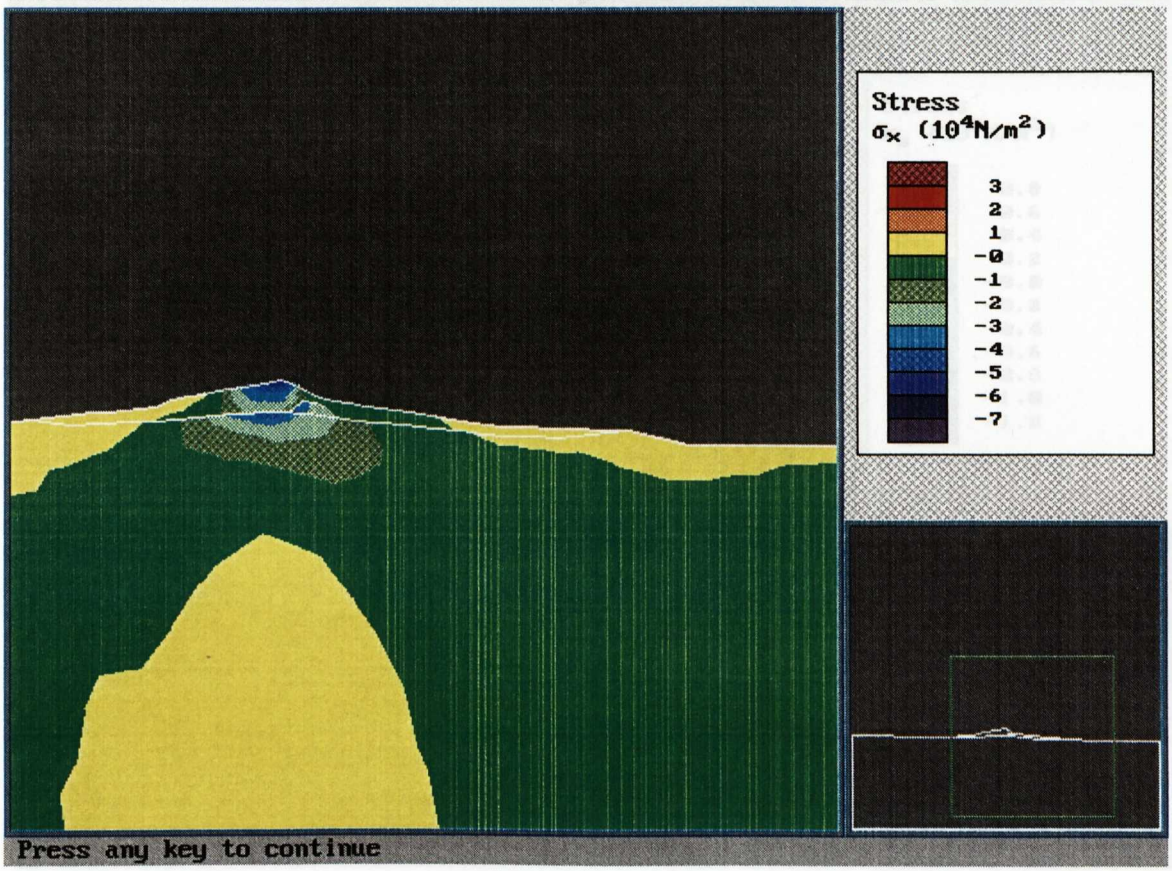

Figure 6.18b: Finite element modelling results - post-Valle del Bove situation. This figure shows the effect of 10m of ice on the present day summit. Negative numbers represent compressive forces. For all parts of this figure the stresses acting along the three axes , x, y, z, are shown (σ_x, σ_y, σ_z), as indicated by the axis within each diagram. The lower part of each figure shows an enlargement of the edifice itself.

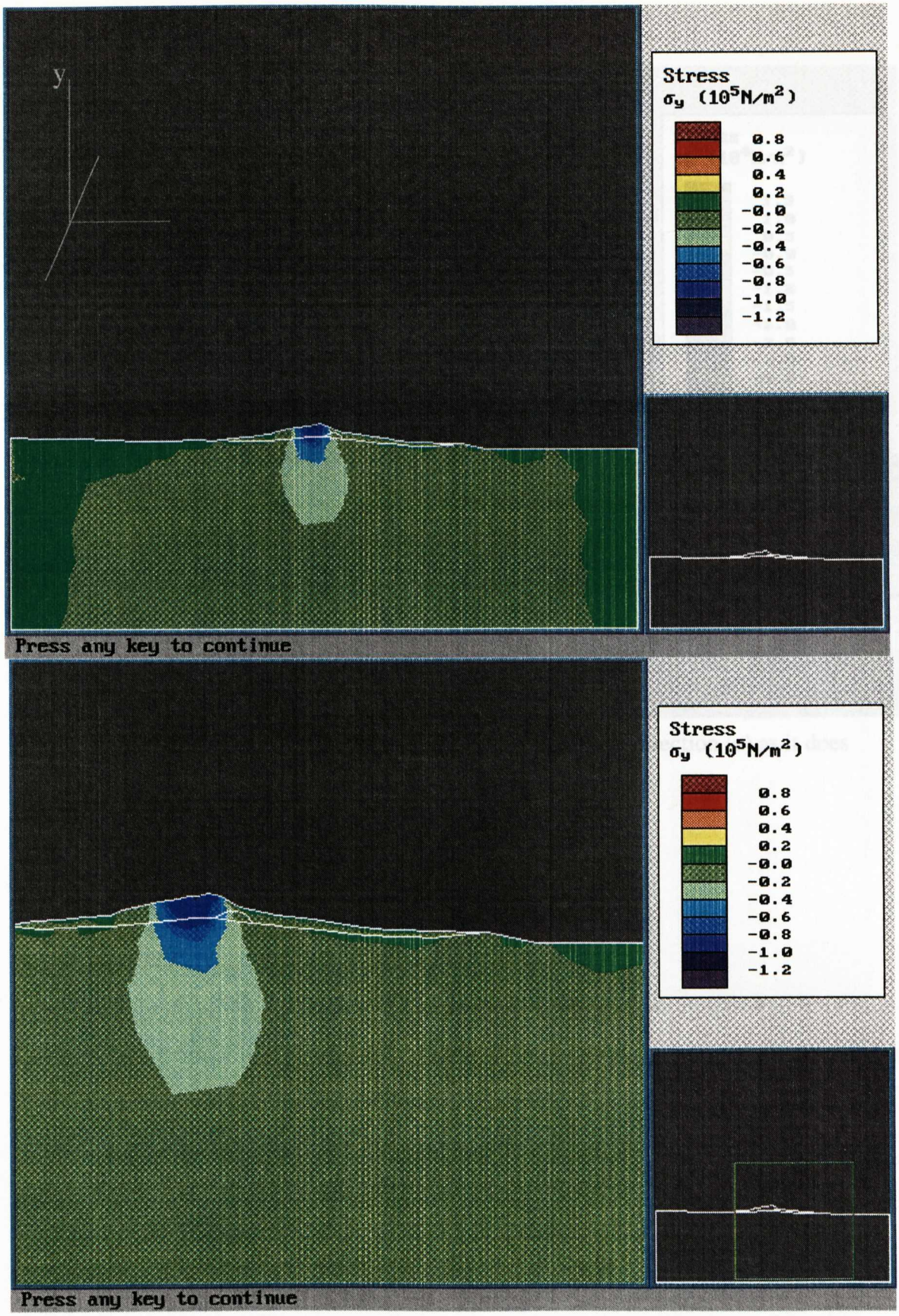

Figure 6.18b continued.

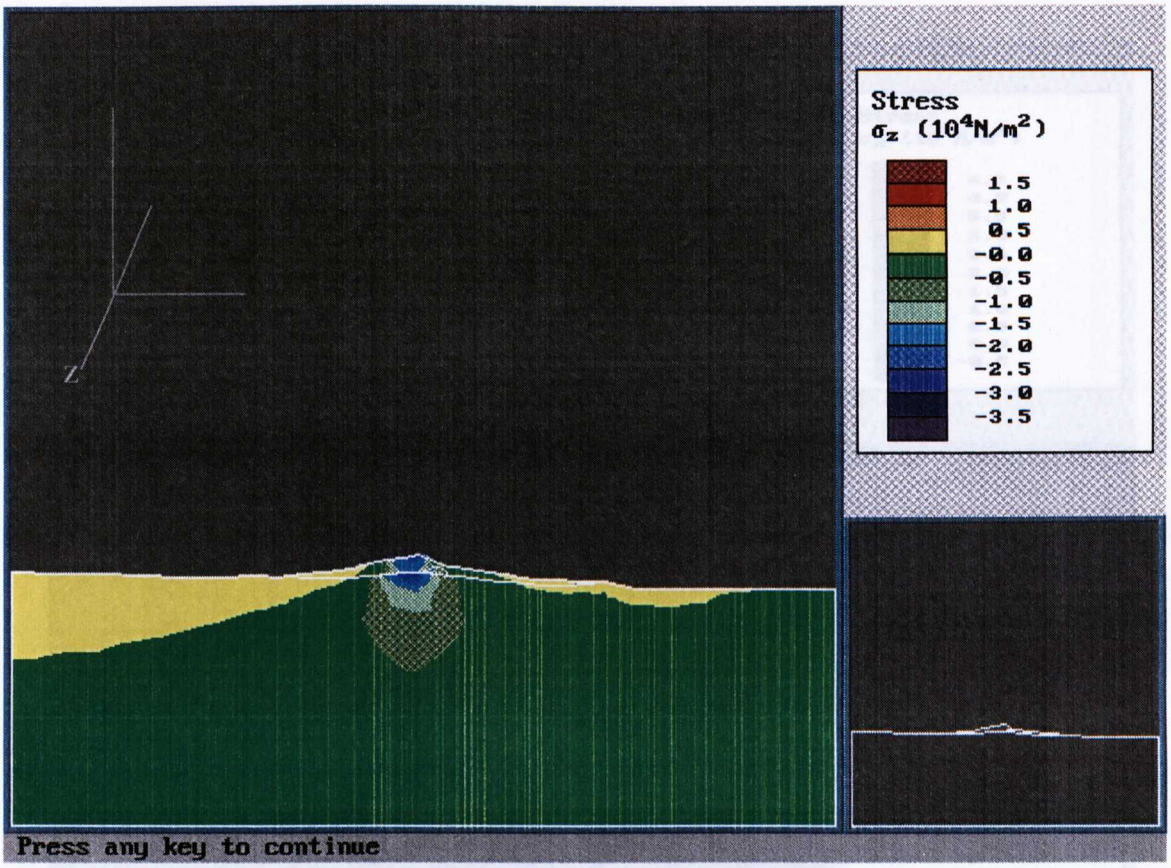

Figure 6.18b continued. No enlargement is shown for this direction (z) as it does not differ significantly from the pattern for the x direction.

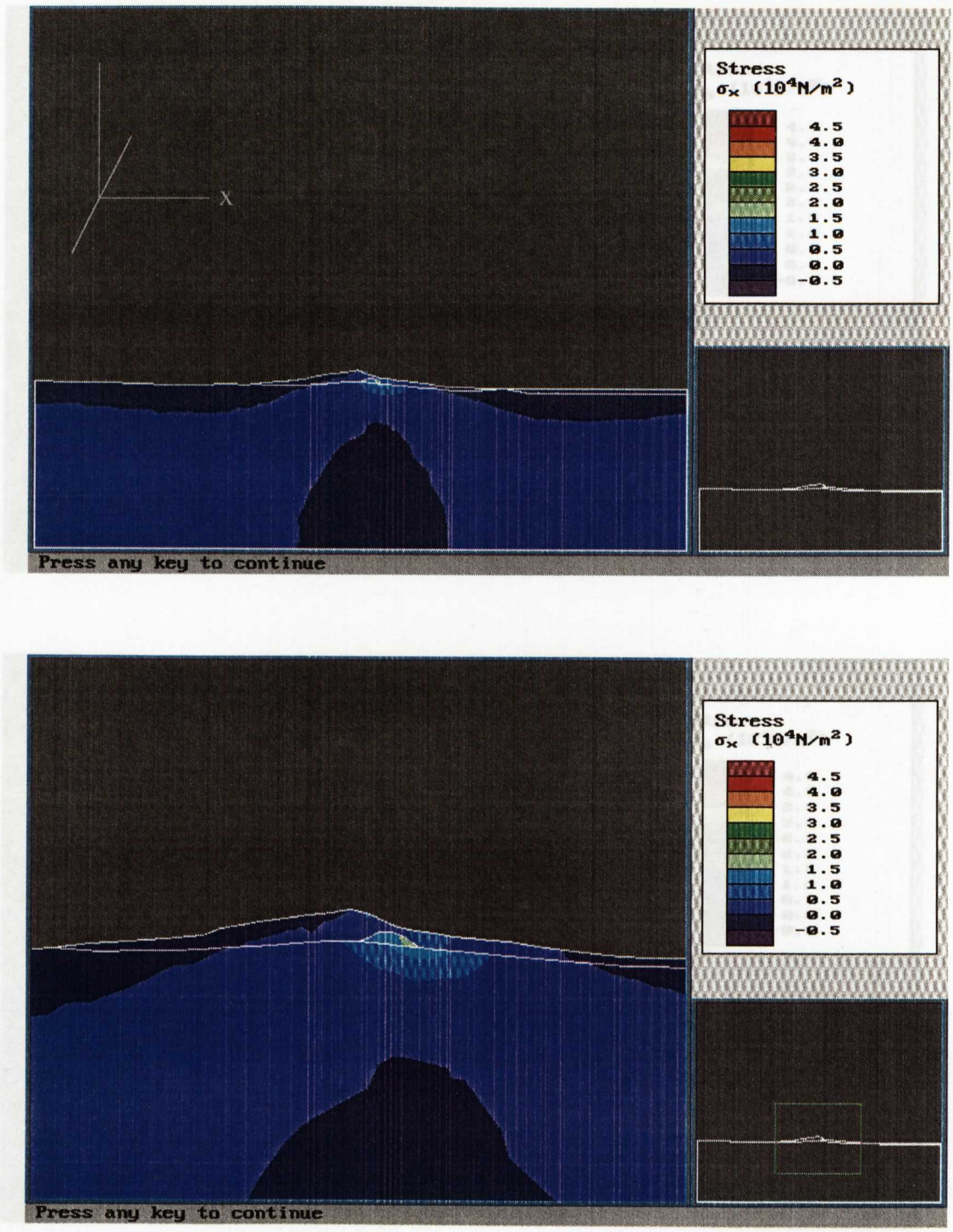

Figure 6.18c: The effect of the creation of the Valle del Bove. The first three diagrams show the result of modelling the removal of the Valle as an upward acting surface force (stress directions are given by the axes). Large amounts of surface tension are created, such tension would be expected to significantly alter the behaviour of the volcano. The final diagram shows the effect of modelling this formation of the Valle by the use of a body force, removing an area of the model representing the pre-Valle topography (only the stress in the x direction are shown). As can be seen the different approach to the model has had little effect on the patterns of the predicted stress changes but does alter the magnitude of the change significantly.

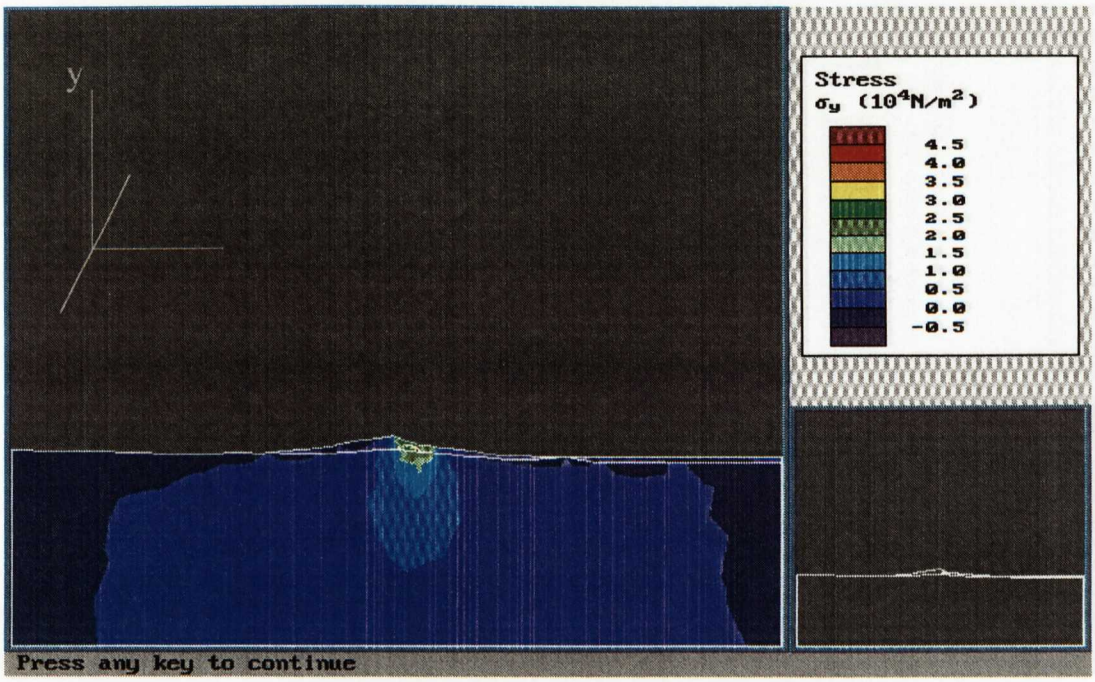

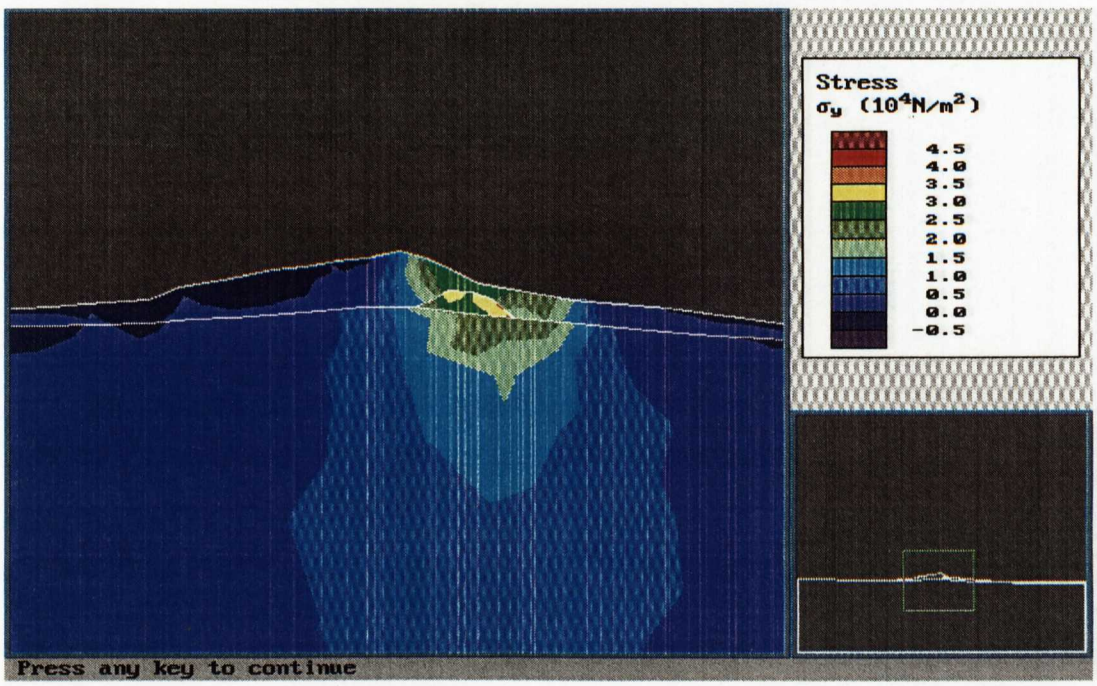

Figure 6.18c. continued

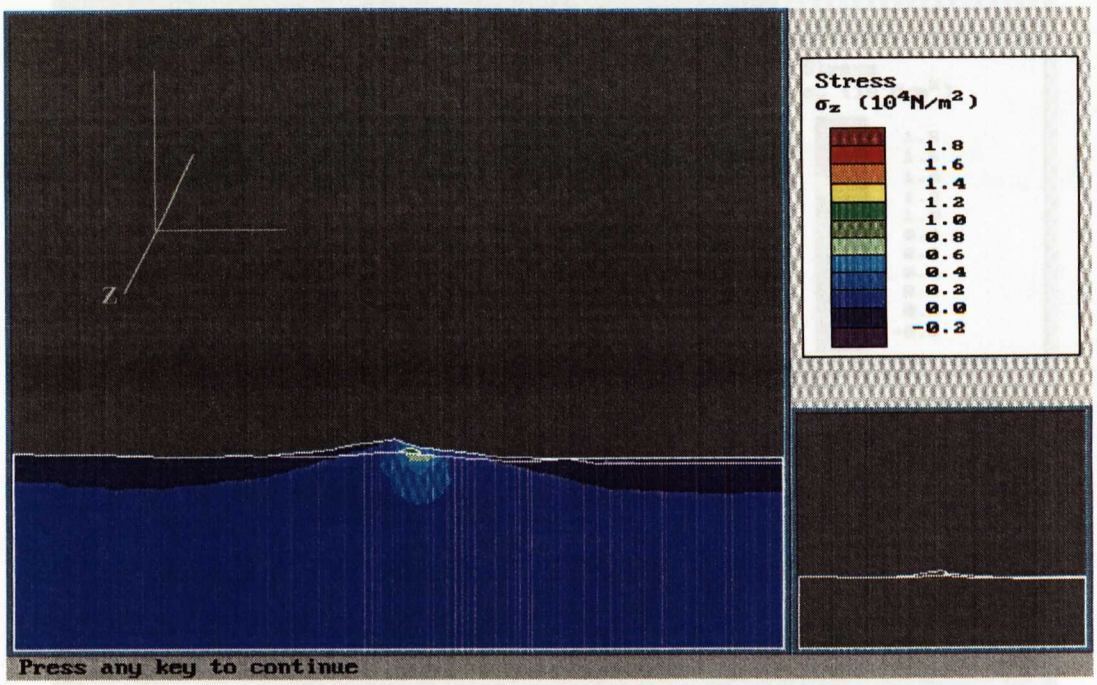

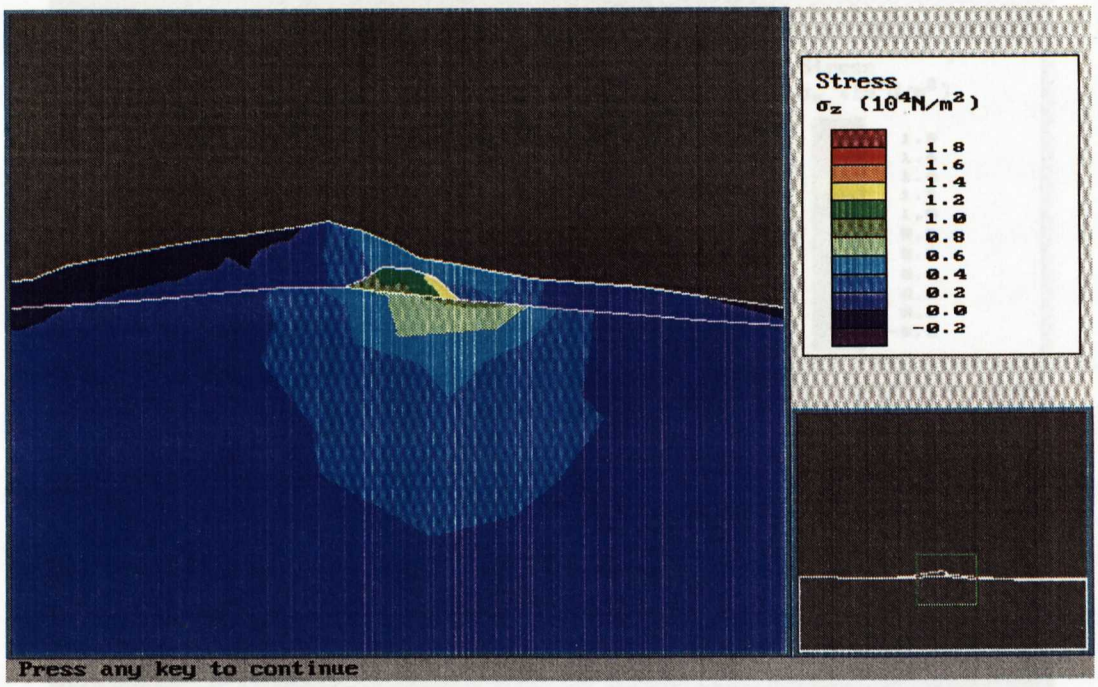

Figure 6.18c. continued

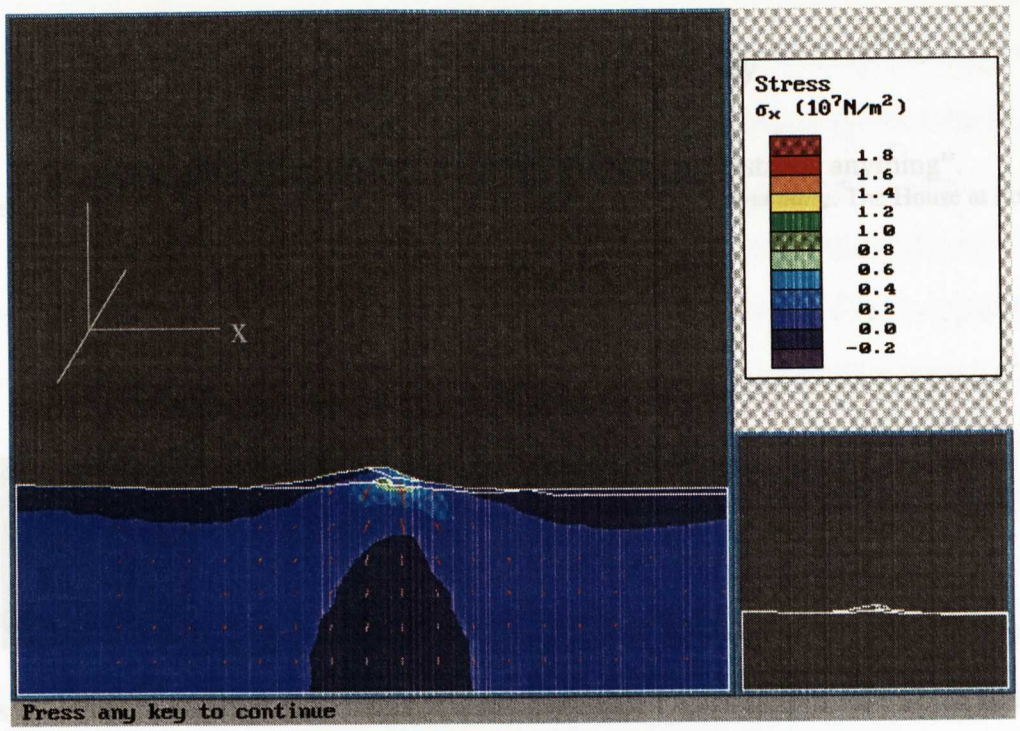

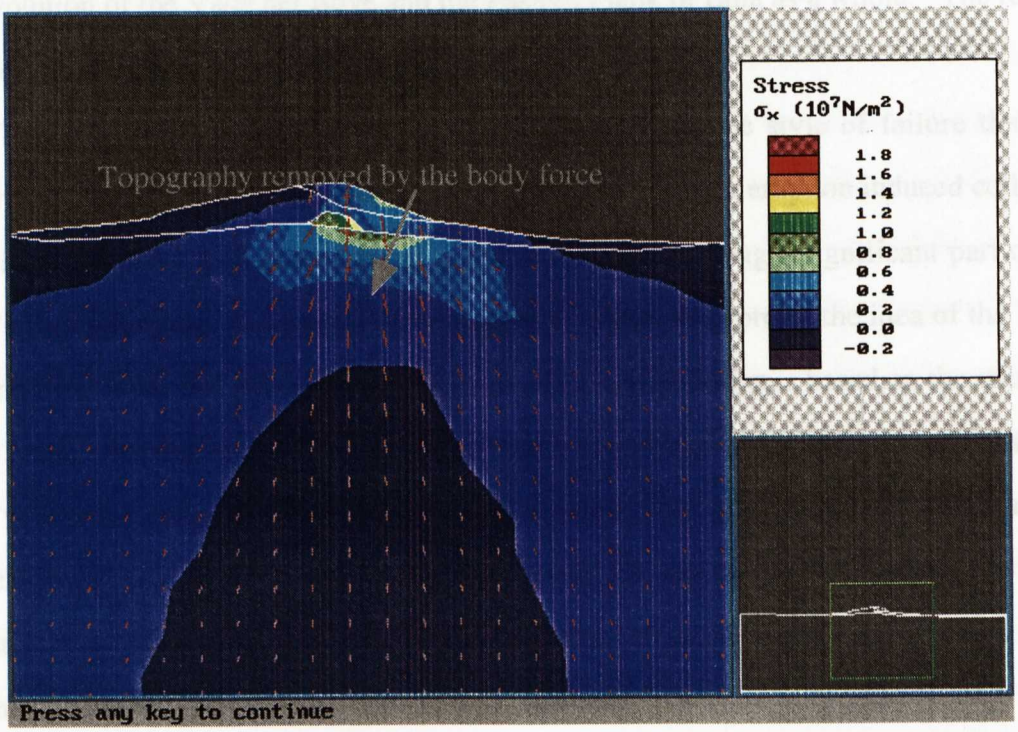

Figure 6.18c continued: As for the preceeding diagrams but the removal of the Valle del Bove is modelled using a body force. The red lines give the direction of the principle stress tensor.

Chapter 7 Conclusions and Implications

"Rabbit's clever," said Pooh thoughtfully.
"Yes," said Piglet, "Rabbit has Brain".
There was a long silence.
"I suppose", said Pooh, "that that's why he never understands anything".
-an exchange between Pooh and Piglet in, *In which Piglet does a very grand thing*. The House at Pooh corner.

7.1. Summary of Results:

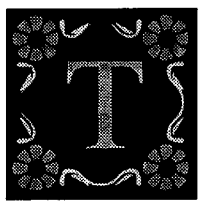

his study consists of a number of different parts whose individual results are brought together within this chapter to construct a detailed picture of the structure and evolution of the Valle del Bove and the Eastern Flank of Etna as a whole. The results obtained with each technique are summarised below.

The evolution of the Valle del Bove will depend on the style of failure that has occurred, possible scenarios include slides, topples and volcanic eruption induced collapse. Most authors appear to discount major volcanic activity as being a significant part of the Valle's formation (e.g. *Habesch,* 1985; Chapter 1), rather they prefer the idea of the Valle forming by erosion and gravitational collapse. This interpretation is based on the structure of the Valle with side-parallel fault systems and a narrowing of the Valle towards its exit. Once volcanic eruption is discounted we must consider what other styles of failure may be applicable and what scale of collapse is appropriate; i.e. whether the collapse of the Valle was sudden with large amounts of material removed simultaneously or if it was a more piecemeal collapse with continuous small scale failures.

The palaeomagnetic data (Chapter 2) were collected in an attempt to distinguish the movement style on the basis of rotation of material about some axis (either horizontal or vertical or both). Geological studies of the dykes within the Valle show they are almost all near vertical and exhibit several groups of orientations, these groupings have been used as age divisions (e.g. *McGuire*, 1982; *McGuire*, 1983). The fact that the majority of dykes are vertical or near vertical (>75° dip) suggests that rotation about a vertical axis may not be

significant, however this would not preclude rotation about a horizontal axis. Analysis of this data shows that the dykes within the upper parts of the Valle del Bove have not undergone rotation (within 10° in the vertical and 20° degrees in the horizontal). This in turn indicates that rotation about any axis of material in the upper parts of the Valle is not the main failure method but it does not rule out translational movement. On this basis the most likely style of collapse is as some form of a topple (rock topple or debris topple; table 1.2). Assuming that the Valle formed by a number of discrete events, each individual slide may include some rotational failure, but the slope has a whole has not significantly rotated.

A GPS network was established in an attempt to detect any present day movement in the area of the Valle del Bove, however the results are inconclusive (Chapter 3 and 5). There appears to have been a small amount of movement of the stations Milo Top, Monte Pomiciaro and Monte Fontane downslope (towards the East) but the amount (up to 22mm) is indistinguishable from the error in the co-ordinates of these points (figure 5.1). Published results suggest that the Eastern Flank as a whole is moving eastwards at a rate of up to 3 cm yr^{-1} [*SCIENCE*, 1994], this value is for the town of Milo. This movement forms the basis of the volcano-tectonic models proposed for Etna (e.g. *Borgia et al.*, 1992; *Lo Giudice and Rasà,* 1992) showing the Eastern Flank as a detached zone, bounded by the Northeast and Southern rift zones. Thus the results of this study give similar values for the movement of Milo as previously published studies.

The most significant results have come from the gravity and magnetic modelling (Chapter 6), which allow for the development of a detailed structural model for the Eastern Flank and provide possible constraints on the local morphology at significant times in Etna's evolution. The body I_3 in the models may be ponded lavas under the summit craters which suggests that after the collapse of the Ellittico caldera, Leone lavas were able to build up on the caldera floor. A maximum thickness of 650m is given by the modelling. This appears to imply the presence of a topographical barrier in the area now occupied by the Valle del Bove, as without this, the lavas would have had no obstacle preventing them from flowing out in to the Valle (figure 1.5b shows a possible reconstruction). A similar build up could occur if effusion rates for the flows were low (<10 $m^3 s^{-1}$). *Pieri and Baloga* [1986] show that the area covered by a lava flow is directly related to the effusion rate, small effusion rate = small area. If such an eruption continued for some time the thickness of the resultant

deposits could be expected to build up to a considerable thickness but cover a limited area, thus allowing for the development of a flow field 650m thick without the requirement of ponding. *Coltelli et al.,* [1994] show evidence for the lava flows of Ellittico flowing around a feature which is no longer present, and they interpret this as evidence for the presence of a topographical barrier in the area of the Southern part of the Valle del Bove, possibly the old Trifoglietto centre. Thus, this supports the ponding hypothesis for the formation of I_3. The biggest problem with this interpretation is the height difference between the exposed Ellittico lavas and this body. Combined with the presence of an obvious pipe below I_3 (body I_2), this elevation difference makes the second interpretation of I_3 as a zone of dyking, representing the high level magma storage system for Etna, the preferred hypothesis. Thus Etna's feeder system appears to consist of a pipe extending, sub-vertically, from some depth (indeterminate from the gravity models) to approximately 1750m, where it intersects a zone of dykes/sills which then feed eruptions (figure 7.1). Such a zone of dyking may allow for limited short term storage, allow some degassing and crystallisation but not differentiation, this would be in agreement with petrological and gas studies (e.g. *Knutson and Green,* [1975] and *Wadge and Guest* [1981]). Summit eruptions are likely to be feed almost directly from the sub-vertical pipe, possibly via a number of branches (e.g. bodies I_4 and I_5), while eccentric eruptions may be fed directly from a deep source, such as the low velocity zone of *Sharp et al.,* [1980].

Reconstructions of basement structures derived from the gravity modelling support previous models for the shape of the sub-Etnean sediments, and show that they slope eastwards, thus possibly providing the slide-plane on which the Eastern Flank is moving. The exact nature of the material making up this basement is unclear. The gravity models assume that the material is sedimentary, i.e. sandstone or limestone, based on the regional geology, however some studies suggest that immediately below the volcanics themselves are Quaternary marine clays, the thickness and extent of which is undetermined [*Borgia et al.*, 1992; *Stewart et al.*, 1993]. The resistivity models of *Loddo et al.,* [1989] suggest that these clays are not continuous below Etna, rather they are present only in limited areas (see figure 6.8). Therefore these clays have not been included in the computer modelling due to

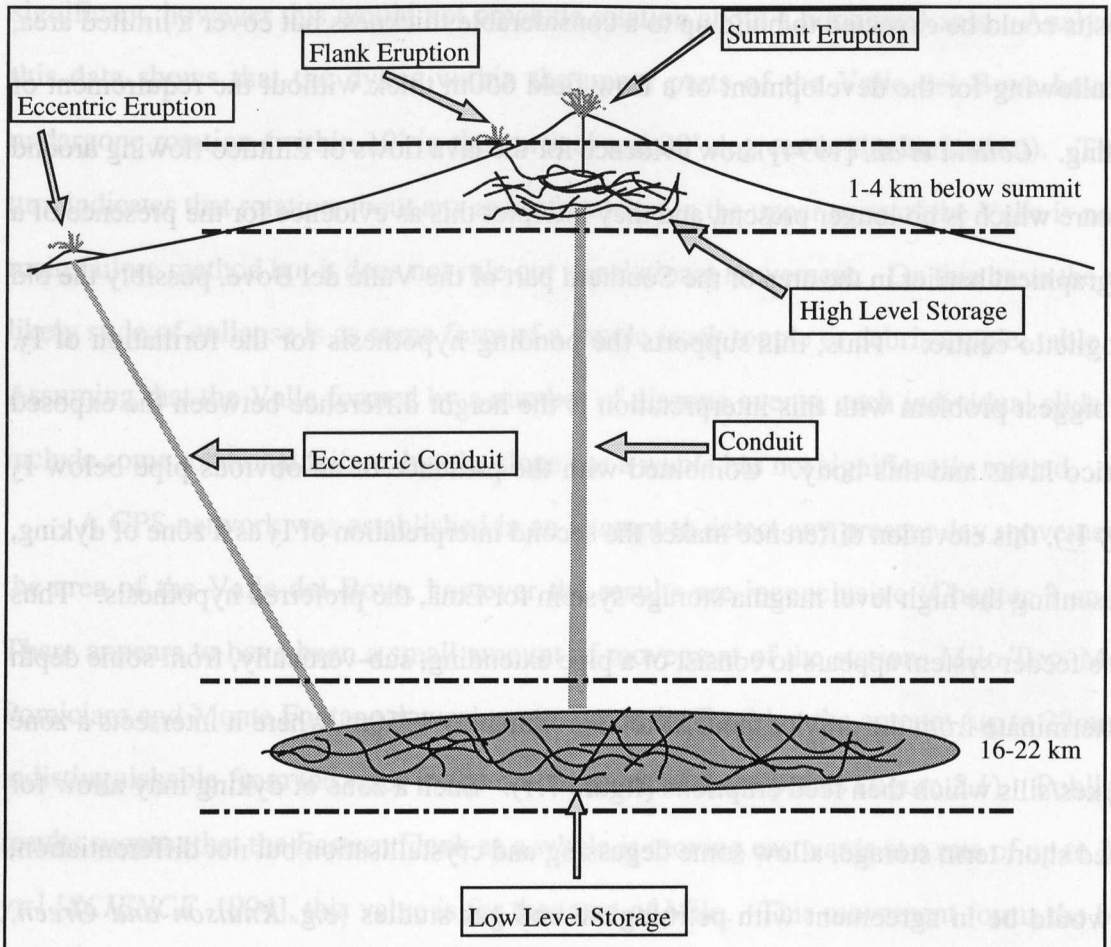

Figure 7.1. The Etnean magmatic system. *Sharp et al.,* [1980] suggest that the deep storage occurs as a series of magma fulled cracks at around 20km depth. Magma rises from this area to a shallow region at 1-4 km depth (based on the models of Chapter 6), where it forms an area of dykes and sills. Eccentric eruptions are fed directly from the deeper system.

the large uncertainties regarding their thickness and extent. It is likely that they would differ very little from the other sediments modelled in terms of density and thus the likely over-estimation of the thickness of the Etnean lavas is considered small. The gravity models have also allowed for the estimation of the volume of the Chiancone deposit and show that it is comparable to the Valle del Bove (9.7 km^3 and 13.2 km^3 respectively).

Finite element modelling (chapter 6) has been used to determine how environmental changes occurring around and on a volcano may have considerable influence on its behaviour. Two principle influences have been modelled: i. climate change; ii. the removal of mass (i.e. the formation of the Valle del Bove). The change in the stress fields associated with the formation of the Valle del Bove suggest that the removal of material has resulted in a positive-feedback system being established, with tension in the upper parts of the volcano

and within the region where the mass has been removed leading to the increased likelihood of further collapses occurring. Climatic changes such as the build up of ice or a change in sea-level will be highly variable in their effects depending on the scale, timing and point of impact. The point of impact implies the location on the volcano at which the stress change is focused, for example, a change in sea-level produces compression at the coast while a build up of an ice cap produces compression at the summit. From the finite element work it is clear that changing environmental factors may have a considerable effect on the stress pattern within the volcanic edifice. Sea-level variations will produce a significant change in the stress patterns both on the slopes of the edifice where the sea directly laps on-shore and within the volcano, and thus will alter the behaviour of the system. Similarly a build up of ice in the summit region shows a transference of stresses throughout the edifice, and thus will have a large effect on the whole volcanic system.

The main results of this work are summarised as :

❶ No significant rotation is associated with the formation of the Valle del Bove;

❷ Movement of the Eastern Flank and the lower parts of the Valle del Bove may be occurring at rates of up to 2 to 3 cm yr^{-1}, although the average rate is much lower;

❸ Several large high density bodies underlie Etna, possibly representing the shallow magmatic system;

❹ Below the Etnean volcanics lie sedimentary layers which slope in an Easterly direction;

❺ The Chiancone deposit and the Valle del Bove have comparable volumes;

❻ Changing climatic conditions will have altered the stress patterns within the volcano, possibly affecting its eruptive behaviour.

❼ The stress changes associated with the formation of the Valle del Bove are self-reinforcing due to the creation of tension in the walls of the resultant failure scar.

7.2. Structure and Evolution of the Valle del Bove:

Investigating the structure of the Valle del Bove is the main aim of this study. Combining several techniques together has allowed a number of aspects of the Valle's structure and evolution to emerge. A vast and bewildering array of, often contradictory,

models and interpretations of the Valle have been published (e.g. *Borgia et al.*, 1992; *Chester et al.*, 1985; *Gresta et al.*, 1990; *Guest et al.*, 1984; *Kieffer*, 1970; *Lo Giudice et al.*, 1982; *McGuire*, 1982; *McGuire*, 1983; *McGuire et al.*, 1991; *McGuire et al.*, 1990; *Rasà et al.*, 1982). The main results that can be derived from this vast amount of published material are the uncertainties and assumptions concerning the Valle's structure and history. A summary of the present state of knowledge may be that the Valle most likely formed by the gradual, piecemeal, collapse of an area of the Eastern Flank, the scale of the individual collapses and their timing are unknown. The final collapse which gave the Valle its present size must have occurred during the eruptive period known as the Mongibello (<34 000 years), that is in the relatively recent past based on the distribution of eruptive products for the Ellittico and younger centres. The material removed from the Valle was deposited in the form of debris flows and alluvial deposits which now form the Chiancone.

The results of this study do not provide all the answers, but they do provide more constraints as well as better information on which to build new models. The gravity and magnetic modelling support the formation of the present day Valle as a post-Ellittico event; this suggests a maximum age of approximately 5000 years. The location, thickness and volume of the Chiancone deposit strongly supports the interpretation of the Valle del Bove being the source area. If the Chiancone is fault controlled, and thus has slowly increased in depth with time, this supports the piecemeal model for the formation of the Valle. As new centres built up, the Valle was able to enlarge. The presence of such a structure would be likely to be a self-reinforcing process, the removal of material from the side of the early volcano creating tension in the upper parts of the flank and thus encouraging the removal of more material (c.f. the Finite Element (FE) modelling). The cause of the initial collapse is unknown but it may have resulted from some change in environmental factors such as sea-level. The FE work of this study (chapter 6) shows that the stress changes associated with a rise in sea-level could affect the stability of a slope, as well as the variation in sea-level altering the erosion patterns significantly.

The location and shape of the Valle may, in part, result from the orientation of the tectonic stress regime in this area, with the Valle lying between the two rift zones (figure 1.4c; *Borgia et al.*, 1992). The shape of the body I_1 in the gravity models (interpreted as an intrusive complex related to the Trifoglietto centre) shows an orientation and elongation

(figure 6.15) which indicates that the present day stress field is the similar to that present during the activity of the Trifoglietto centre (80 000 to 34 000 yrs. B.P.). This interpretation is based on the elongation of this body (I_1) being parallel to the direction of regional extension (σ_3) for the present day stress field. Such stress fields would have been conducive to the formation of a proto-Valle del Bove in the same way as the present Valle appears related to the regional stress pattern, suggesting that the Trifoglietto centre had very similar structures to the present day volcano.

The body I_1 is centred under the Southern wall of the Valle del Bove which may be an indicator that this wall is controlled by this sub-surface body rather than other structural features. Such a large dense body which sits within both the sediments and the volcanics may act as a stabilising influence effectively holding up the volcanics due to its greater mass and strength. Thus it acts as the Southern limit of the Valle. No evidence is seen to suggest that this body is acting so as to stabilise the entire Flank.

The gravity model across the Valle floor (profile C-C', figure 6.10) shows that there has been a considerable amount of infill of "modern" volcanic products, that is material with a density similar to the bulk density of the modern lava flows. Underlying these deposits the model shows lower density volcanics, interpreted as a typical mixture of lavas and pyroclastics as seen in the summit region of the modern volcano, possibly weathered or altered, the weathering processes decreasing the density. It is impossible to be certain about the composition of these two layers, however the surface of the Valle is made up of a large number of historic lava flows and scoria cones (i.e. the 2400 kg m^{-3} (modern volcanics) layer in profile C-C'). It is more difficult to be certain of the composition of the lower density material, but its structure and its lack of variability supports the interpretation of older weathered, but essentially in situ, volcanics. We would expect the deposits of either major slope movements or violent caldera-producing volcanic eruptions to be of much greater variability due to their violent formation. Such deposits may also be expected to contain pockets of very low density material such as scree or ash deposits, although whether these would be of a scale detectable by gravity is uncertain. This apparent lack of variability and low density regions support the interpretation of a gentle, piecemeal collapse as the mechanism for the formation of the Valle del Bove as opposed to a major violent volcanism induced collapse.

The future of the Valle del Bove and Etna itself is difficult to determine directly from this work, however if we consider the past movements of the Valle del Bove area and its present day relationship to the summit region it is possible to infer possible scenarios. The present day head wall of the Valle (the Western wall) sits 1 km due East of the summit craters and, as this area will be a region of tension, we should see a concentration of eruptive events near or on the wall. The models of *McGuire et al.*, [1990] support this, showing that the presence of the Valle causes a change in the direction of dykes during emplacement. Also the fractures and eruptive fissures of the last major eruptive episode (1989 to 1993) ran parallel to the Western Wall [*Calvari et al.*, 1994]. It is not difficult to envisage a situation where intrusion of large volumes of magma behind the wall causes an acceleration in movement such that a large collapse occurs. Such a collapse could expose the summit feeder systems and may trigger an explosive eruption. If I_3 does represent the shallow magmatic system, its proximity to the Valle walls is a mater of concern, however there is little evidence to suggest that this area represents a permanent zone of magma storage, rather it is an area in which magma may sit immediately prior to an eruption. Given the dynamic state of the Etnean feeder system, with generally small volumes, as derived from repeated microgravity measurements [*Rymer et al.,* 1994; *Rymer et al.*, 1993], it seems improbable that any eruption resulting from such a major collapse would be as devastating as, for example, the flank failure driven 1980 eruption of Mt. St. Helens. Thus the likely consequence of a failure of the Valle del Bove's Western wall would be the emplacement of small to moderate volumes of material into the Valle del Bove itself. Such a collapse might be expected to be contained within the upper reaches of the Valle del Bove. Larger collapses and any involving magmatic material would be expected to continue towards the East and thus pose a hazard to the surrounding populations. An eruption induced collapse would be likely to produce large volumes of ash and this would constitute a major hazard. The tools are available for modelling these scenarios and thus prediction of the hazards.

7.3. The Structure of the Eastern Flank:

The gravity and magnetic modelling of this study provide new and more detailed models of the structure of this Flank than has been available to date (chapter 6). While past

geophysical studies have highlighted areas containing anomalous structures, no detailed modelling has been previously attempted in order to identify the causative bodies. The modelling of the study has thus provided the necessary structural information to understand the behaviour and evolution of this Flank.

In general, past work has suggested that the morphology of the sediments underlying Etna consists of an easterly sloping surface which is relatively simple in structure, with the eastwards slope strongly influencing the behaviour of the Flank as a whole. The new models of this study show a similar structure but with detailed features which complicate the situation. The final model (figure 6.12) shows the same eastward slope of the earlier works but superimposed on this are several other structures, most importantly the basin infilled by the Chiancone deposit and the depression due to the presence of the large intrusive body underlying the Valle del Bove. These features produce a more complex picture but illustrate that the easterly slope will increase the instability of the overlying volcanic material. No information on mechanisms or slip planes can be determined from these models, but a reasonable interpretation would be that slippage occurs on the volcanic/sediment contact as this would represent a plane of weakness. *Borgia et al.,* [1982] propose that the Eastern Flank is sliding on the Quaternary marine sediments. However, as the geophysical evidence suggests that these sediments are not present everywhere [*Loddo et al.,* 1989], this can not be entirely true. It is possible that the lower most layers of the volcanics and the upper most sediments are weathered and thus are likely to be clay rich and therefore the contact between them will be a zone of weakness.

The size of the basin occupied by the Chiancone deposit makes it an important feature on this flank. Its depth (up to 700m) and steepness makes it unlikely that it has been a stable area during the volcano's early growth. It is unlikely that it was present in this form for the entire history of the formation of the Valle del Bove (the source of the Chiancone). As it is bounded on its western side by the Timpa Fault system, the possibility exists that this basin is a fault

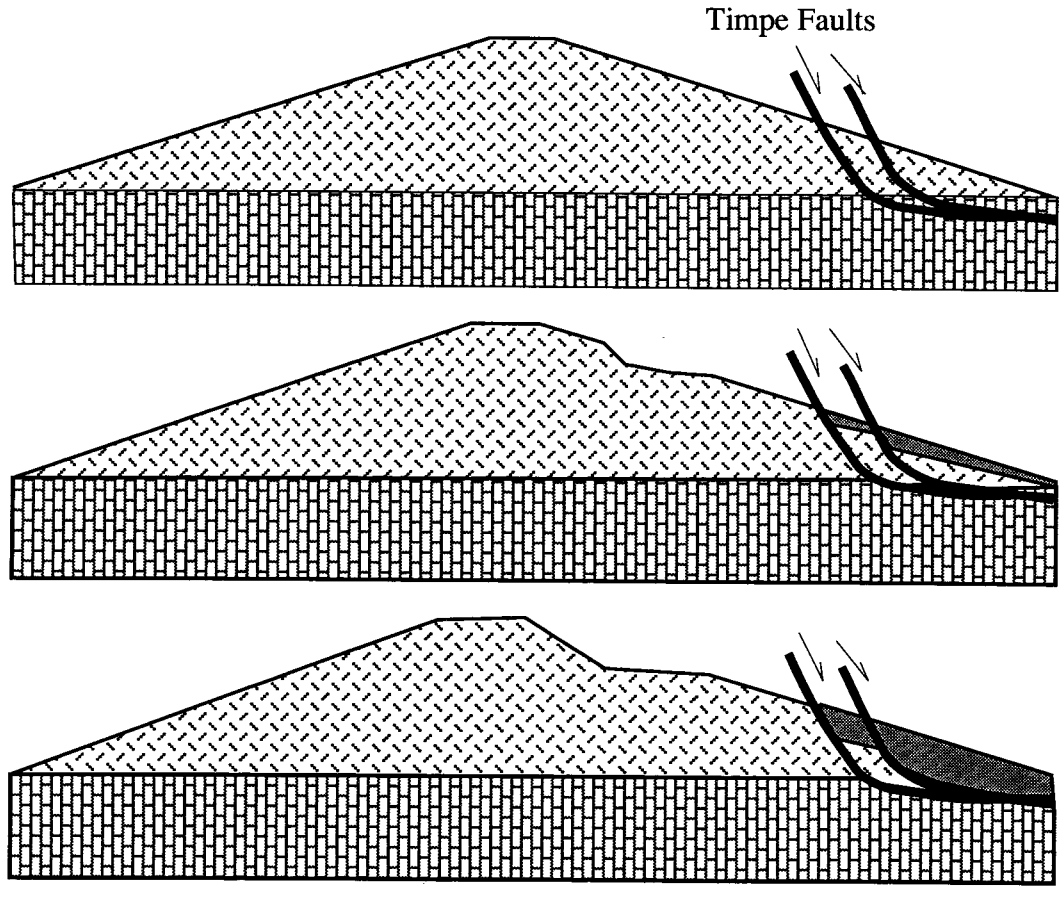

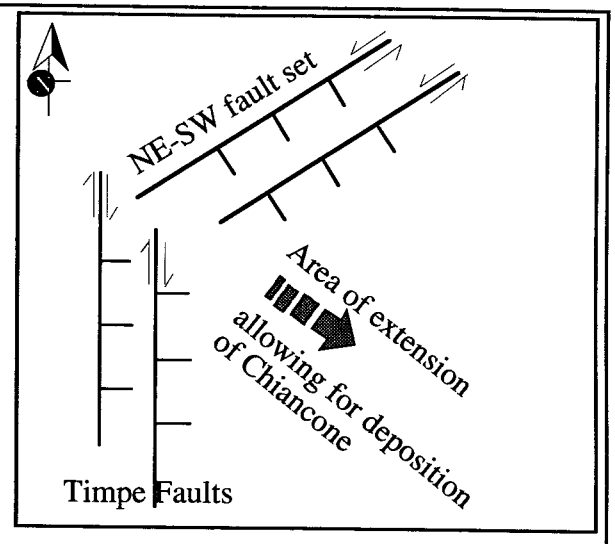

Figure 7.2. Cartoon illustrating the formation of the Timpe Fault system and the Chiancone. Progressive movement on the faults causing a deepening of the basin in which the Chiancone is then deposited as the Valle del Bove grows. The insert shows *Lanzafame et al.,* [1996] interpretation of the area around the Chiancone based on structural information. Sense of strike-slip movement is shown by the arrows, dip-slip by teeth on the downthrown side

controlled structure, which has progressively deepened through time, allowing the deposition of increasing volumes. The Timpa Faults are downthrown to the East and have no clear gravitational expression, however this lack of expression may be illusionary. The boundary to the Chiancone does have a slight expression and has been modelled; if this boundary represents the Timpa Faults they also have therefore been modelled. Figure 7.2 shows a cartoon illustrating the formation of the Chiancone by progressive movement on the Timpa Fault system. The shape of the faults as shown are illustrative only. The recent work of *Lanzafame et al.,* [1996] add support to this argument, with the zone of extension within the intersection of the two fault systems being the basin now occupied by the Chiancone. This NE-SW fault set appear to relate to the Messina fault. The shape of the Chiancone (steeply sloping in the North, shallower in the West, figure 6.13) may result from the relative geometry of these fault systems. It is clear from the local geological maps that the Timpe faults are well separated (in an East-West sense) [*Romano et al.,* 1979], thus the boundary of the Chiancone formed by these faults appears shallow. In turn the steepness of the Northern boundary implies that either the movement on the NE-SW faults is greater than for the Timpe faults or that these faults are closer together. Only detailed surface mapping of the area will solve resolve this.

7.4. Environmental Influences:

One of the main aims of the Finite Element (FE) modelling was to determine the effect that changing climatic and environmental factors may have on the behaviour of the volcano (chapter 6). As Etna has been active throughout the late Quaternary, it has seen large changes in sea-level as well as the build up of ice and changing precipitation levels. It is not possible to model all influences but major changes such as sea-level fluctuations and the appearance/disappearance of ice caps are easily dealt with in Finite Element modelling.

Figure 7.3 shows a summary of the FE modelling of section 6.7. The largest draw-back in this work has been the simplification in terms of the physical properties as well as the structures. This simplification results in uncertainties with regard to the magnitude of the stress fields produced and thus uncertainty in interpretation of their likely effect on the volcano. Therefore figure 7.3 summarises only the stress patterns, ignoring the magnitude,

and thus removes some of this uncertainty. However while the pattern of stresses and their magnitude are important, the rate of change in the stress field is possibly the most significant aspect, i.e. the effect of a 100m sea-level change occurring over 1000 years will be much greater than if it occurred over 10 000 years. A similar argument holds for a build-up of ice. Past sea-level changes in the Etna region [*SEAVOLC*, 1996] have been both fast and slow, producing very different responses in the volcano; no attempt is made to asses the rate of change in the FE modelling used in this study.

The major effects of a sea-level rise are shown in figure 7.3 and can be summarised as:

- Compression in the coastal area (i.e. along the coast);
- Tension at depth;
- Tension under the central parts of the volcano;
- Changes in the lubrication of fault surfaces due to changes in the water table.

Tension within the central areas of the edifice will encourage movement of material outwards while the compression on the coast will act so as to prevent this movement, this will then cause a build up of stresses. In general movement up slope is likely to be transferred further down the volcano by small scale creep. However a build up of compressive stresses within the lower slopes of the volcano will prevent this. This will cause a build of stresses further up the flank. Thus when failure does occur it will be on a large scale and possibly catastrophic. The occurrence of small scale creep allows for the gradual release of stresses and thus will stop major movements occurring. If this creep no longer occurs then the likelihood of major movement is increased.

The effect of an ice build-up and/or a sea-level drop would be somewhat different. Here the major effects can be summarised as:

- Tension in the coastal areas;
- Tension at depth;
- Compression in the central parts of the edifice.

This scenario would result in the increased possibility of small scale movements in coastal areas due to the build up of tension, while the combination of tension at depth and compression within the volcano would encourage intrusive rather than extrusive activity.

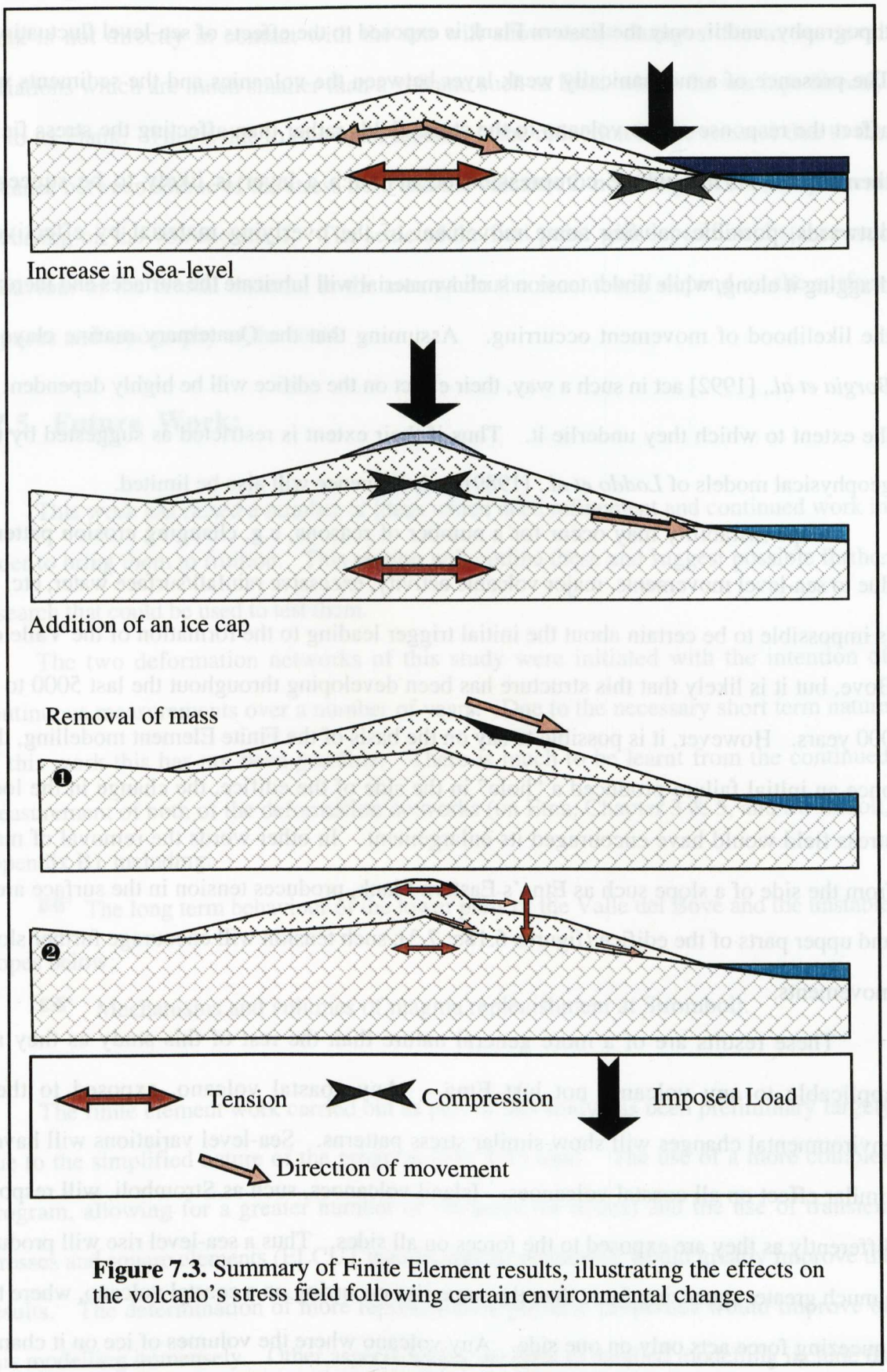

Figure 7.3. Summary of Finite Element results, illustrating the effects on the volcano's stress field following certain environmental changes

In all cases the movement which occurs following such changes in conditions will be limited to the Eastern Flank due to: i. buttressing on the Western Flank by the surrounding topography, and ii. only the Eastern Flank is exposed to the effects of sea-level fluctuations. The presence of a mechanically weak layer between the volcanics and the sediments will affect the response of the volcano to the stress fields rather than affecting the stress fields themselves. Thus where compression occurs such a layer is likely to be squeezed outwards, possible causing some movement of the overlying material by effectively dragging it along, while under tension such a material will lubricate the surfaces and increase the likelihood of movement occurring. Assuming that the Quaternary marine clays of *Borgia et al.*, [1992] act in such a way, their effect on the edifice will be highly dependent on the extent to which they underlie it. Thus if their extent is restricted as suggested by the geophysical models of *Loddo et al.*, [1989] their influence will also be limited.

Slope instability may occur for a number of reasons, e.g. changing erosion patterns due to sea-level movements, major volcanic activity, excessive rainfall/surface water, etc. It is impossible to be certain about the initial trigger leading to the formation of the Valle del Bove, but it is likely that this structure has been developing throughout the last 5000 to 10 000 years. However, it is possible to say on the basis of the Finite Element modelling, that once an initial failure produced a "hole" in the side of the edifice, the change in the local stress field would have encouraged its enlargement. In other words the removal of mass from the side of a slope such as Etna's Eastern Flank, produces tension in the surface areas and upper parts of the edifice (figures 6.18c; 7.3); such tension will encourage further slope movements.

These results are of a more general nature than the rest of this study as they are applicable to any volcano, not just Etna. Any coastal volcano, exposed to these environmental changes will show similar stress patterns. Sea-level variations will have a similar effect on all coastal volcanoes. Island volcanoes, such as Stromboli, will respond differently as they are exposed to the forces on all sides. Thus a sea-level rise will produce a much greater squeezing force than the same rise occurring on a coastal volcano, where the squeezing force acts only on one side. Any volcano where the volumes of ice on it change will show similar response and stress patterns to these models. The difficulty is in deciding at what point a volcano stops being a coastal volcano or when a layer of snow is too thin to

affect stress patterns. For the latter it is difficult to be certain of the limits without detailed modelling, but for the former we can make reasonable assumptions. A volcano where its flank is not directly in contact with the sea will show stress changes due to sea level variations which are much smaller than a volcano such as Etna, where the sea laps directly on to its Flank. This is due to two main factors, 1. the reduction in the stresses due to the distance between source of the stress field and the volcano; 2. no change in erosion patterns occurring on the volcano itself. The scale of the first point will depend on distance and behaviour of the crustal material in the area while the second will depend on the surface deposits and topography of the coast.

7.5. Future Work:

This work has raised a number of ideas which need refinement and continued work in order to bring them to fruition. This section will outline these and suggest possible further research that could be used to test them.

The two deformation networks of this study were initiated with the intention of continuous measurements over a number of years. Due to the necessary short term nature of this work this has not been possible. There is much to be learnt from the continued measurement of both of the deformation networks (on Etna, Chapter 3 & 5, and Stromboli, appendix B), including:

- The long term behaviour of the lower parts of the Valle del Bove and the unstable slopes below;
- Mechanisms and volumes of magma replenishment at Stromboli.

The finite element work carried out as part of this study has been preliminary largely due to the simplified nature of the program (ELCUT) used. The use of a more complex program, allowing for a greater number of elements (or nodes) and the use of transient stresses and square elements (ELCUT uses triangular elements), would greatly improve the results. The determination of more representative physical properties would improve on this modelling immensely. Other aspects which are open to detailed modelling include the dynamics of any collapse of the Western wall of the Valle del Bove and the hazard

implications. The work carried out here is seen as a starting point, with the expectation of further work taking over where this has left off.

APPENDICES HAVE NOT BEEN SCANNED ON INSTRUCTION FROM THE UNIVERSITY

References:

Akin, J. E.,(1986), **Finite element analysis for undergraduates.** pp. 319, Academic Press Ltd., London.

Armienti, P., F. Barberi, F. Innocenti, M. Pompilio, R. Romano, and L. Villari, (1984). Compositional variation in the 1983 and other recent Etnean lavas: insights on the shallow feeding system. *Bull. Volcanol., 47 (4/2),* 995-1007.

Baker, T. F., (1984), Tidal deformations of the Earth., *Sci. Prog. Oxf., 69,* 197-233.

Balde, M., C. Aiken, D. Ziegler, S. Cates, and W. Gosnold, (1991), Large scale, detailed gravity survey in North Dakota positioned using Global Positioning System (GPS) technology., *EOS, 72*(17), 90.

Barnett, C. T., (1976), Theoretical modelling of the magnetic and gravitational fields of an arbitrarily shaped three-dimensional body., *Geophysics, 41*(6), 1353-1364.

Berrino G., and G. Corrado (1991) Tidal signal in the recent dynamics of Campi Flegrei caldera (Italy). *J. Volcanol. Geotherm. Res. 48,* 93-101.

Bianchi, R., A. Coradini, C. Federico, G. Giberti, P. Lanciano, J. P. Pozzi, G. Sartoris, and R. Scandone, (1987), Modelling of surface deformation in volcanic areas: The 1970-1972 and 1982-1984 crises of Campi Flegrei., *J. Geophys. Res., 92*(B13), 14,139-14,150.

Birch, F., (1966), Compressibility; Elastic Constants., in *Handbook of Physical Constants.*, Memoir 97, edited by S. P. Clark, The Geological Society of America., New York.

Borgia, A., (1994), Dynamic basis of volcanic spreading., *J. Geophys. Res., 99*(B9), 17791-17804.

Borgia, A., L. Ferrari, and G. Pasquare, (1992), Importance of gravitational spreading in the tectonic and volcanic evolution of Mount Etna, *Nature, 357,* 231—235.

Brouke, R. A., W. E. Zürn, and L. B. Slichter, (1972), Lunar tidal acceleration on a rigid Earth., *Geophys. Monogr. Ser. Am. Geophys. Un., 16,* 319-324.

Burnett, D. S. (1987), **Finite Element Analysis, from concepts to applications.** ,pp. 844, Addison-Wesley Publishing Co., Reading, Massachusetts.

Calvari, S., M. Coltelli, M. Neri, M. Pompilio, and V. Scribano, (1994a), The 1991-1993 Etna eruption: chronology and lava flow-field evolution. *Acta Vulcanologica, 4,* 1-14.

Calvari, S., G. Groppelli, and G. Pasquare, (1994b), Preliminary geological data on the south-western wall of the Valle del Bove, Mt. Etna, Sicily., *Acta Vulconologica, 5,* 15-30.

Cardaci, C., M. Coviello, G. Lombardo, G. Patané, and R. Scarpa, (1993), Seismic tomography of Etna volcano., *J. Volcanol. Geotherm. Res., 56,* 357-368.

Caupano, P., R. Continiso, P. Gasparini, and G. Gaudiosi,(1993), Deep crustal structure of Sicily (South Italy) from Gravity, Aeromagnetic and Seismic data. in *EUG VII,* vol. 1, pp. 107-108, Terra nova, Strasbourg, France.

Chester, D. K., A. M. Duncan, J. E. Guest, and C. R. J. Kilburn (1985), **Mount Etna: The Anatomy of a Volcano** pp. 404, Chapman and Hall, London.

Collinson, D. W. (1983), **Methods in rock magnetism and palaeomagnetism** Chapman and Hall, London.

Coltelli, M., V. H. Garduno, M. Neri, G. Pasguare, and M. Pompilio, (1994), Geology of the Northern Wall of the Valle del Bove, Mt. Etna (Sicily)., *Acta Vulcanologica, 5,* 55-68.

Delaney, P. T., and D. D. Pollard, (1982), Solidification of basaltic magma during flow in a dykes, *Am. J. Sci., 282,* 856-885.

Dieterich, J. H., and R. W. Decker, (1975), Finite element modelling of surface deformation associated with volcanism., *J. Geophys. Res., 80,* 4094-4102.

Dobran, F and S. Coniglio, (1996), Magma ascent and simulations of Etna's erupitons aim at internal system definition. *J. Geophys. Res., 101(B1),* 713-731.

Dodson, M. A., and E. McClelland-Brown, (1980), Magnetic Blocking temperatures of single domain grains during slow cooling, *J. Geophys. Res., 85,* 2625-2637.

Duncan, A. M., D. K. Chester, and J. E. Guest, (1984), The quaternary stratigraphy of Mount Etna, Sicily: the effects of differing paleoenvironments on styles of volcanism., *Bull. Volcanol., 47*(3), 497-516.

Elwell, S. J.,(1995), Deformation monitoring on Mount Etna using GPS. BE(Hons) Thesis Nottingham Trent University.

Emery, J. J., (1978), Simulation of slope creep., in *Rockslides and Avalanches, 1: Natural Phenoma.*, edited by B. Voight, pp. 669-687, Elsevier Scientific Publishing Co., Amsterdam.

EPOCH,(1993), Slope stability at Mount Etna. EPOCH programm final report. Commission of the European Communities.

Fairbanks, R. G., (1989), A 17000-year glacio-eustatic sea level record: influence of glacial melting rates on the Younger Dryas event and deep-ocean circulation., *Nature, 342*, 637-642.

Fisher, R. A., (1953), Dispersion on a sphere., *Proc. R. Soc. Lond., A217*, 295-305.

Francis, P., C. Oppenheimer, and D. Stevenson, (1993), Endogenous growth of persistently active volcanoes., *Nature, 366*, 554-557.

Francis, P., and S. Self, (1987), Collapsing volcanoes, *Sci. Am., 256*, 73-79.

Gillot, P. Y., G. Kieffer, and R. Romano, (1994), The evolution of Mount Etna in the light of potassium-argon dating., *Acta Vulcanologica, 5*, 81-87.

GVN (1994a), Global Volcanism Network Bullitan July 1994 Vol 19(7):10-11.

GVN (1994a), Global Volcanism Network Bullitan October 1994 Vol 19(10):15-16.

Gresta, S., V. Longo, and A. Viavattene, (1990), Geodynamic behaviour of eastern and western sides of Mount Etna., *Tectonophysics, 179*, 81-92.

Gresta, S., A. Montalto, and G. Patanè, (1991), Volcanic tremor at Mount Etna (January 1984—March 1985): its relationship to the eruptive activity and modelling of the summit feeding system., *Bull.Volcanol., 53*, 309—320.

Griffiths, A. J. (1983), **Palaeomagnetism of Mount Etna.** MSc(Hons) Thesis Imperial College, London.

Guest, J. E., D. K. Chester, and A. M. Duncan, (1984), The Valle del Bove, Mount Etna: Its origin and relation to the stratigraphy and structure of the volcano., *J. Volcanol. Geotherm. Res., 21*, 1-23.

Guest, J. E., and J. B. Murray, (1979), An analysis of hazard from Mount Etna volcano, *J. Geol. Soc. Lond., 136*, 347-354.

Habesch S.M., (1985), **The volcanic geology of the Eastern Flanks of Mount Etna, Sicily.** PhD Thesis, University of Liverpool.

Hallinan, S. (1991), **Gravity studies of the Guayabo Caldera and the Miravalles geothermal field, Costa Rica.** PhD Thesis The Open University.

Hallinan, S. (1993), Nonchaotic collapse at funnel calderas: gravity study of the ring fractures at Guayabo caldera, Costa Rica. *Geology, 21*, 367-370.

Hammer, S., (1939), Terrain Corrections for Gravimeter Stations, *Geophyscis, 4*, 184-194.

Hansen, M. J., (1984), Strategies for classification of Landslides, in *Slope Instability*, edited by D. Brunsden and D. B. Prior, pp. 1-23.

Hirn, A., A. Nercessian, M. Spain, F. Ferrucci, and G. Wittlinger, (1991), Seismic heterogeneity of Mount Etna: structure and activity., *Geophy. J. Int., 105*, 139-153.

Hofmann-Wellenhof, B., H. Lichtenegger, and J. Collins (1993), **GPS Theory and Practice.** pp. 326, Springer-Verlag, Wien.

Jakosky, B. M., (1986), Volcanoes, the stratosphere and climate. *J. Volcanol. Geotherm. Res., 28*, 247-255.

Kearey, P., and M. Brooks (1984), **An Introduction to Geophysical Exploration.**, pp. 296, Blackwell Scientific Publications, Oxford.

Kieffer, G., (1979), L'activite de l'Etna pendant les derniers 20 000 ans. *C.R. Acad. Sci. Paris, 288,* 1023-1026.

Kieffer, G. (1983) L'évolution structurale de l'Etna (Sicile) et les modalités du contrôle tectonique et volcano-tectonic de son activité. Faits et hypothèses apres les éruptions de 1978 et 1979. *Rev. Geogr. Phys. Grol. Dyn., 24(2),* 129-152.

Klerkx, J. (1970), La caldera de la Valle del Bove: sa signatication dans l'evolution de l'Etna (Sicilie). *Bull. Volcanol. 24,* 726-737.

Klerkx, J., and P. Evrard, (1970), Les Anomalies gravimetriques de l'Etna (Sicile) et l'evolution du Trifoglietto. *Annales de la Soc. Geo. Bel., 93*, 145-147.

Kuntson, J. and T.H. Green (1975), Experimental duplication of a high pressure megacryst/cumulate assemblage in a near saturated hawaiite. *Contrib. Mineral. Petrol. 52,* 121-132.

Labaume, P., J. C. Bousquet, and G. Lanzafame, (1990), Early deformations at a submarine compressive front: the Quartnernary Catania foredeep south of Mt. Etna, Sicily, Italy., *Tectonophysics, 177*, 349-366.

Lanzafame G., M. Neri and D. Rust (1996), Active tectonics affecting the eastern flank of Mount Etna: structural interactions at a regional and local scale. *Abstracts volume,* Etna: 15 years on meeting. Cheltenham.

Leica (1992), **Wild GPS - System 200 Technical Reference Manual.** , Leica, Heerbrugg, Switzerland.

Leick, A. (1990), **GPS satellite surveying.** , John Wiley & Sons. Inc.

Lénat, J.-F., P. Vincent, and B. P., (1989), The off-shore continuation of an active basaltic volcano: Piton de la Fournaise (Réunion Island, Indian Ocean); Structural and geomorphological interpretation of Sea Beam mapping., *J. Volcanol. Geotherm. Res., 36,* 1-36.

Levi S., H. Andmasson, R.A. Duncan, Kristansson, P.-Y. Gillot and S.P. Jakobsson, (1990). Late pleistocene geomagnetic excursions in Icelandic lavas: confirmation of the Laschamp excursion. *Earth Planet. Sci. Lett., 96:* 443-457.

Lin, X., F. Wang, J. Lu, and X. Li, (1992), The application of GPS to the high-precision gravity survey in the neritic area., *Geophysical and Geochemical Exploration, 16*(3), 168-173.

Lipman, P. W., W. R. Normark, J. G. Moore, J. B. Wilson, and C. E. Gutmacher, (1988), The giant submarine Alika debris slide, Mauna Loa, Hawaii., *J. Geophys. Res., 93*(B5), 4279-4299.

Lo Giudice, E., G. Patanè, R. Rasa, and R. Romano, (1982), The structural framework of Mt. Etna, *Memorie Della Societa Geologica Italiana, 23,* 125—158.

Lo Giudice, E., and R. Rasà, (1992), Very shallow earthquakes and brittle deformation in active volcanic areas: the Etna region as an example. *Tectonophysics, 202,* 257-268.

Loddo, M., D. Patella, R. Quarto, G. Ruina, A. Tramacere, and G. Zito, (1989), Application of gravity and deep dipole geoelectrics in the volcanic area of Mt Etna (Sicily). *J. Volcanol. Geotherm. Res., 39,* 17-39.

Lyell, C., 1858. On the strucutre of lavas which have consolidated on steep slopes with remarks on the origin of Etna and on the theory of the centres of elevation. *Phil. trans. R. Soc. London 148,* 703-786.

McCormick, M. P., L. W. Thomason, and C. R. Trepte, (1995), Atmospheric effects of the Mt. Pinatubo eruption., *Nature, 373,* 399-404.

McGuire, W. J., (1982), Evolution of the Etna volcano: information from the southern wall of the Valle del Bove Caldera., *J. Volcanol. Geotherm. Res., 13*, 241-271.

McGuire, W. J., (1983), Prehistoric dyke trends on Mount Etna; Implications for magma transport and storage., *Bull. Volcanol., 46*(1), 9-22.

McGuire, W. J., J. B. Murray, A. D. Pullen, and S. J. Saunders, (1991), Ground deformation monitoring at Mount Etna; evidence for dyke emplacement and slope instability, *Journal of the Geological Society, London, 148*, 577—583.

McGuire, W. J., and A. D. Pullen, (1989), Location and orientation of eruptive fissures and feeder-dykes at Mount Etna; influence of gravitational and regional tectonic stress regimes., *J. Volcanol. Geotherm. Res., 38*, 325-344.

McGuire, W. J., A. D. Pullen, and S. J. Saunders, (1990), Recent dyke—induced large scale block movement at Mount Etna and potential slope failure, *Nature, 343*(6256), 357—359.

McNutt S.R. and R.J. Beavan (1981), Volcanic earthquakes at Pavlof Volcano correlated with the soild Earth tide. *Nature 294*, 615-618.

Marhino de Carvalho, J. Jr. and W. Erwes, (1977) **Reduction tables and diagrams for barometric measurements with Thommen altimeters.** Revue Thommen AG Thommen Instrument Dept., CH-4437 Waldenberg, Switzerland,

Mogi, K., (1958), Relation between the eruptions of various volcanoes and the deformations of the ground surfaces around them, *Bulletin of the Earthquake Research Institute, Tokyo, 36*, 99—134.

Murray, J.B., (1990), High-level magma transport at Mount Etna volcano, as deduced from ground deformation measurements. in *Magma transport and Storage*, edited by M.P. Ryan. Wiley & Sons Ltd.

Murray, J. B., and A. D. Pullen, (1984), Three—dimensional model of the feeder conduit of the 1983 eruption of Mt. Etna volcano from ground deformation measurements, *Bull.Volcanol., 47*(4), 1145—1163.

Neri, M., G. Orombelli, G. Pasquarè, and M. Pelfini,(1995), Possible existence and extent of a late-Pleistocene glacier on Mt. Etna. in *Project Seavolc - Sea-level change and the stability and activity of coastal and island volcanoes. Final Report. Environment programme contract EV5V-CT92-0170.*, Commission of the European Communities.

Neumann, R., P. Evrard, and S. Coron, (1985), Interpretation des travaux magnetiques et gravimetriques a l'Etna., *Bolletino Geophysica Teorica ed Applcata, 27*(106), 125-152.

Nunnari, G., and G. Puglisi, (1994), The global positioning system as a useful technique for measuring ground deformations in volcanic areas., *J. Volcanol. Geotherm. Res., 61*, 267-280.

Nunnari, G., and G. Puglisi, (1995), GPS - monitoring volcanic deformation from space., in *Monitoring active volcanoes: Strategies, procedures and techniques.*, edited by B. McGuire, C. Kilburn and J. Murray, pp. 151-181, UCL Press Ltd., London.

Ogniben, L., (1966), Lineamenti idrogeological dell'Etna, *Rivista Mineraria Siciliana, 101-102*, 151-174.

Ottosen, N., and H. Petersson (1992), **Introduction to the finite element method.** pp. 410, Prentice Hall, London.

Patanè G., A. Frasca, A. Agodi and S. Imposa (1994), Earth tides and Etnean volcanic eruptions: an attempt at correlation of the two phenomena during the 1983, 1985 and 1986 eruptions. *Earth Planet. Int. 87,* 123-135.

Patrascu, S., C. Panaiotu, M. Seclaman, and C. E. Panaiotu, (1994), Timing of rotational motion of Apuseni Mountains (Romania); palomagnetic data from Tertiary magmatic rocks., *Tectonophysics, 233*(3-4), 163-176.

Paul, A., J. P. Gratier, and J. Boudon, (1987), A nummerical model for simulating deformation of Mount St. Helens Volcano., *J. Geophys. Res., 92*(B10), 10,299-10,312.

Pedley, R. C. (1991), **GRAVMAG, Interactive 2.5D Gravity and Magnetic Modelling Program; User Manual**. British Geological Survey, Keyworth, Nottingham.

Perrin, M., M. Prevot, and F. Bruere, (1994), Rotation of the Oman Ophiolite and initial location of the ridge in the hotspot reference frame., *Tectonophysics., 229*(1-2), 31-42.

Pieri D.C. and S.M. Baloga (1986), Eruption rate, area, and length relationships for some Hawaiian lava flows. *J. Volcanol. Geotherm. Res. 30*, 29-45.

Piper, J. (1987), **Palaeomagnetism and the continental crust.** Open University Press, Milton Keynes.

Rampino, M. R., S. Self, and R. W. Fairbridge, (1979), Can rapid climatic change cause volcanic eruptions?, *Science, 206*, 826-829.

Rasa, R., R. Romano, and E. Lo Giudice, (1982), A structural survey of Mt. Etna on a morphological basis, *Memorie Della Societa Geologica Italiana, 23*, 117—124.

Rittmann, A. (1963), Vulkanismus and Tektonik des Ätna. *Geol. Rundsch., 53* 788-800.

Rittmann, A. (1973), Structure and evolution of Mount Etna. *Philos. Trans. R. Soc. London, Ser. A, 274,* 5-15.

Rolph, T. C., and J. Shaw, (1986), Variations of the geomagnetic field in Sicily., J. *Geomag. Geoelectr., 38*, 1269-1277.

Romano, R., (1982), Succession of the volcanic activity in the Etnean area, *Memorie Della Societa Geologica Italiana, 23*, 27—48.

Romano, R. and J.E. Guest (1979), Volcanic geology of the simmit and northern flank of Mount Etna, Sicily. *Boll. Soc. Geol. Ital., 98* 189-215.

Romano, R., C. Sturiale and F. Lentini (1979), Carta Geological del Monte Etna. *CNR Prog. Fin. Geodinamica* 1:50 000.

Rymer, H., (1989), A contribution to precision microgravity data analysis using Lacoste and Romberg gravity meters, *Geophys. J. Int., 97*, 311-322.

Rymer, H., (1994), Microgravity change as a precursor to volcanic activity., *J. Volcanol. Geotherm. Res., 61*, 311-328.

Rymer, H., and G. C. Brown, (1986), Gravity fields and the interpretation of volcanic structures: Geological discrimination and temporal evolution, *J. Volcanol. Geotherm. Res., 27*, 229-254.

Rymer, H., G. C. Brown, F. Ferrucci, and J. Murray, (1994), Dyke intrusion mechanisms on Etna 1989-1992 and microgravity precursors to eruption., *Acta Vulcanologica, 4*, 109-114.

Rymer, H., J. B. Murray, G. C. Brown, F. Ferrucci, and W. J. McGuire, (1993), Mechanisms of magma eruption and emplacement at Mt Etna between 1989 and 1992., *Nature, 361*, 439—441.

Sandberg, C. H., (1958), Terrain corrections for an inclined plane in gravity computations., *Geophysics, 23*(4), 701-711.

Sanderson, T.J.O., G. Berrino, G. Corrado and M. Grimaldi (1983), Ground deformation and gravity changes accompanyinh the March 1981 eruption of Mount Etna. *J. Volcanol. Geotherm. Res., 16,* 299-315.

Saribudak, M., M. Sanver, C. Sengor, and N. Gorur, (1991), Paleomagnetic evidence for substantial rotation of the Almacik Flake within the North Anatolian fault zone, NW Turkey., *Eos, 72*(17), 104.

SCIENCE,(1994), Volcanic deformation and tidal gravity effects at Mount Etna, Sicily. , EC Science programme.

Scott, S.C., (1983), Variations in lava composition during the March 1981 of Mount ETna and the implications of a compositional comparison with earlier historic eruptions. *Bull. Volcanol., 46(4),* 393-412.

SEAVOLC,(1996), Sea-level change and the stability and activity of coastla and island volcanoes. in *Environment Programme Contract EV5V-CTV92-0170,* Commission of the European Communities.

Self, S., M. R. Rampino, and J. J. Barbera, (1981), The possible effects of large 19th and 20th century volcanic eruptions on zonal and hemispheric surface tempreatures., *J. Volcanol. Geotherm. Res., 11,* 41-60.

Sharp, A. D. L., P. M. Davis, and F. Gray, (1980), A low velocity zone beneath Mount Etna and magma storage, *Nature, 287,* 587—591.

Shimozuru, D., (1987), Tidal effects on Hawaiian Volcanism, in: *Volcanism in Hawaii.* edited by R.W. Decker, T.L. Wright, P.H. Stauffer. U.S.G.S. Profesional Paper 1350.

Skeels, D. C., (1967), What is residual gravity?, *Geophysics, 32*(5), 872-876.

Soengkono, S. (1990), Geophysical study of the Western Taupo Volcanic Zone. PhD Thesis, University of Auckland, New Zealand.

Stacey, F. D. (1969), **Physics of the Earth.** John Wiley & Sons. Inc., New York.

Stewart, I., W. McGuire, C. Vita-Finzi, C. Firth, R. Holmes, and S. Saunders, (1993), Active faulting and neotectonic deformation on the eastern flank of Mount Etna, Sicily., *Z. Geomorph., 94,* 73-94.

Tanguy, J. C., (1970), An archaeimagnetic study of Mt. Etna: The magnetic direction recorded in lava flows subsequent to the twelfth century., *Archaeometry, 12*(2), 115-128.

Tanguy, J.-C., (1981), Les eruptions historiques de l'Etna: chronologie et localisation. *Bull.Volcanol. 44,* 585-640.

Tanguy J.-C., and G. Kieffer, G. (1977), the 1974 eruption of Mount Etna. *Bull. Volcanol., 40,* 1-14.

Telford, W. M., L. P. Geldart, and R. E. Sheriff (1990), **Applied Geophysics.** Cambridge University Press, Cambridge.

UNIRAS (1989), **AGL/Interpolations: user guide and reference manual, ISG 129.** UNIRAS, Soborg, Denmark.

UNIRAS (1990), **Unimap 2000: user manual Version 6, ISG 141.** UNIRAS, Soborg, Denmark.

Vaglisindi, C., (1950), A review of three papers in Italian by Emiliani, C. *J. Geol., 58,* 284-285.

van Wyk de Vries, B.,(1995), The Effect of Volcanoes on Rifting. in *IUGG XXI General assembly,* AGU, Boulder, Colorado.

Voight, B., R. J. Janda, H. Glicken, and P. M. Douglass, (1983), Nature and mechanics of the Mount St. Helens rockslide-avalanche of 18 May 1980., *Géotechnique, 33,* 243-273.

Voight, B., and B. A. Kennedy, (1978), Slope failure of 1967-1969, Chuquicamata Mine, Chile., in *Rockslides and Avalanches 2.*, edited by B. Voight, pp. 595-632.

Wadge, G. (1977), The storage and release of magma on Mount Etna. *J. Volcanol. Geotherm. Res., 2* 361-387.

Wadge, G. (1980), Flank fissures on Etna and the surface expressions of magmatic conduits. *U.K. Research on Mount Etna 1977-79.* The Royal Society, p.27-30.

Wadge, G. and J.E. Guest (1981), steady state magma discharge at ETna, 1977-81. *Nature, 255,* 385-387.

Wallmann, P. C., G. A. Mahood, and D. D. Pollard, (1988), Mechanical models for correlation of ring-fracture eruptions at Pantelleria, Straits of Sicily, with glacial sea-level drawdown., *Bull. Volcanol., 50,* 327-339.

Williams, D. L., and C. Finn, (1985), Analysis of gravity data in volcanic terrain and gravity anomalies and subvolcanic intrusions in the Cascade Range, U.S.A, and at other selected volcanoes. *Society of Exploration Geiophysicists.*

Yokoyama, I. (1974), Geomagnetic and gravity anomalies in volcanic areas. In: *Physical Volcanology.*, edited by L. Civetta, P. Gasparini, G. Luongo, A. Ropolla.